2007

Large eddy simulation of turbulent heat transfer in stationary and rotating square ducts

Zhaohui Qin
Iowa State University

Large eddy simulation of turbulent heat transfer in stationary and rotating square ducts

by

Zhaohui Qin

A dissertation submitted to the graduate faculty

in partial fulfillment of the requirements for the degree of

DOCTOR OF PHILOSOPHY

Major: Mechanical Engineering

Program of Study Committee:
Richard H. Pletcher, Major Professor
Francine Battaglia
Michael G. Olsen
Tom I-P. Shih
John C. Tannehill

Iowa State University

Ames, Iowa

2007

DEDICATION

To my wife, Jialin Shen

TABLE OF CONTENTS

LIST OF TABLES

LIST OF FIGURES

CHAPTER 1. INTRODUCTION

1.1 Motivation

Turbulent flow (or turbulence) is one of the most challenging unresolved problems in classical physics. Typically, turbulent flow refers to the motions in fluids that are highly complex, irregular, and three-dimensional. Turbulent flows are very common (in fact, much more common than laminar flows) and can be seen frequently in our daily life. The examples include vortices which keep forming and breaking in rapids, the wave-like surface deformations in the wakes of a boat, the many whirls in a wind in which the small ones rotate fallen leaves gently while the huge ones may make a violent destruction. Turbulent flow can transport mass, momentum and energy more efficiently than laminar flow which is preferred in some situations like the mixing of fuel and air in internal combustion engines; however, the turbulent motion usually corresponds to higher drag, which along with its irregularity and complexity makes it unpopular in lots of cases such as aircraft design. Whether we want to enhance it or suppress it, a deep understanding of the physics of turbulent flow is always needed.

The modern attack on the turbulence problem has a history of 120 years starting from the famous experiment of Reynolds in 1883. However, up to now, due to the difficulty of solving the nonlinear three-dimensional Navier-Stokes equations, analytical solutions of turbulent flows are still rare and cannot meet the enormous requirement of engineering applications. Although experimental studies relieve this dilemma to some extent, they are usually costly and restricted by measurement techniques. The last two decades saw the rapid development of computers, and computational fluid dynamics (CFD) became a more and more important tool to give us insights into the phenomena and mechanisms of turbulence. Now, the role of computational simulation is multifold: it can carry out "numerical experiments" at a much

lower cost compared with real experiments; it can be used to visualize flow structures, uncover new flow features, verify theoretical analysis, aid engineering designs and much more. It is safe to say that computational simulation is now an indispensable component in the fluid mechanics research, and both industry and academia will benefit more and more from its growing capability.

The most common methods which CFD tools utilize to compute turbulent flow can be roughly put into four categories:

- Reynolds-averaged method based on the Reynolds-averaged Navier-Stokes equations (RANS). Since these equations are not closed themselves, some closure methods must be introduced to close the problem.

- Large eddy simulation (LES). The basic idea of this method is that only the large scale motions are computed explicitly while the small scale motions are modeled. This method is the focus of this thesis and more remarks will be given shortly.

- Direct numerical simulation (DNS), in which the Navier-Stokes equations are solved directly without any models and all scales of motions are resolved. To achieve such a resolution, sufficiently fine grids have to be used (the grid number is of the order of 9/4 power of Reynolds number).

- Combinations of methods mentioned above. For example, the detached eddy simulation (DES) employs the RANS method in the vicinity of solid walls while using LES away from the walls and into the main stream.

In the above four types of methods, DNS is regarded as the most accurate, and DNS results are usually used to verify and validate the other methods. However, since DNS has to use extremely fine grids to resolve all motion scales, it requires exceptionally large computational resources, especially for high Reynolds numbers, which severely limits its application. The RANS method is usually inexpensive, but its accuracy suffers much because of the uncertainty of the closure models. LES, which costs much less than DNS, but provides almost the same capability, can be thought of as an ideal compromise of accuracy and economy.

In LES, a spatial filtering (or averaging) operation is applied to the governing equations

and the filtered quantities correspond to the motions of scales larger than the filter size (so called "large scales" or "large eddies"). Usually, the filter size is the same as the grid size. The filtered equations are solved in a time accurate manner. Since in turbulent flows, the turbulent fluctuations and viscous dissipation occur on a range of scales from the geometrical scale down to the Kolmogorov scale, which is much smaller than the grid size in LES, the information about the motions smaller than the grid size (so called "subgrid scale" or briefly, SGS) should be given. In the filtered equations, the effects of these subgrid scale motions are reflected in the so called subgrid scale stress and subgrid scale heat flux terms, which should be modeled. More details will be given in later chapters.

The main motivations of this research are

- to extend the LES capability to turbulent duct flows subject to heat transfer and system rotation. It is hoped that the present research will provide useful information to engineering applications such as film cooling for turbine blades;
- to improve our understanding of the physics of the turbulent duct flows under rotation.

1.2 Objectives

The four main objectives of this thesis are listed below and discussed in more detail subsequently.

- Incorporate the Navier-Stokes characteristic boundary condition (NSCBC) into the lower-upper symmetric Gauss-Seidel (LU-SGS) scheme to solve the filtered governing equations.
- Investigate the thermally developing turbulent duct flow under strong heating.
- Study the turbulent heat transfer in square ducts rotating about a spanwise axis.
- Analyse the velocity field and instability of rotating duct flow.

1.2.1 Incorporate NSCBC into LU-SGS Scheme

Despite its many advantages, unfortunately, the application of LES has been largely limited to simple geometries. One important reason of this restriction is because most applications of LES (and DNS, in fact) has relied on spatially periodic boundary conditions. Applications

of non-periodic inflow and outflow boundary conditions which can at the same time sustain a realistic turbulence level and cause small numerical errors are still scarce. Perhaps the characteristic boundary condition (CBC) is a good choice. This method has been widely used in CFD. A practical three-dimensional CBC called Navier-Stokes characteristic boundary conditions (NSCBC) which was first developed by Thompson (1987, 1990) is especially fit for our purpose. It can be expected that combining NSCBC with LES can greatly extend the application of LES to complex geometries. However, from the search of literature one can find that such endeavors are very rare, and more unusual are reports of the details of such combinations. The reason may lie in an important feature of NSCBC: it has to be incorporated into the original numerical scheme rather than being used separately (Anderson, 1995). Since most LES and DNS codes use very sophisticated schemes, such incorporations usually become very complex and tricky. In this thesis, details of the incorporation of NSCBC into the lower-upper symmetric Gauss-Seidel (LU-SGS) scheme are given.

Another limitation of LES related to the periodic boundary condition is that it can be hardly used in thermally developing compressible flows with strong heating or cooling. The reason is that strong heating or cooling will change the properties (density, viscosity, thermal conductivity, etc.) of the compressible flow significantly, thus, the mean and fluctuations of the velocity field at the exit will be much different from those at the inlet which invalidates the periodic assumption. For example, in strongly heated internal gas flows, the turbulence downstream may undergo a reverse transition to a laminar-like state which is sometimes referred to as relaminarization. Such flows are of practical interest but beyond the ability of LES with periodic boundary conditions. Using the NSCBC technique, however, we are able to carry out such calculations without special difficulties.

A further improvement to the current NSCBC strategy is a so called "vanishing inviscid flux derivative" method which is designed for the possible separation inside a heated rotating duct when the buoyancy force is an opposing one. In this situation, the streamwise velocity in some regions of the duct cross section will become negative (flow reversal) beyond the separation point. This means some information from the outside of the domain has to be given

so that the flow field at these regions can be solved. This is, of course, a tough job since such information is usually unknown. To avoid such a situation, one can add an insulated buffer zone to the exit so that the flow field can recover to the "normal" form. However, this method can be awkward in two senses. First, the length of the buffer zone has to be determined in a trial-and-error manner which is usually time consuming; second, the length of the buffer zone changes with the problem parameters so that the whole calculation has to begin from the very beginning rather than starting from the data obtained for a slightly different case. The current "vanishing inviscid flux derivative" method, which is similar to the FLARE approximation for boundary layer flow (Tannehill et al. 1997), enables us to compute the flow reversal without a buffer zone and all those difficulties along with it.

1.2.2 Investigate the Thermally Developing Turbulent Duct Flow under Strong Heating

As mentioned above, in strongly heated internal gas flows significant property variations can arise. A reverse transition from turbulent to laminar state can occur. Such flows can find their applications in gas-cooled nuclear reactors, nuclear propulsion systems, turbine blades and so on. A comprehensive understanding of forced convection heat transfer with strongly varying properties is crucial to these applications. Apart from the importance in engineering applications, the research also justifies itself in the sense that it may help to clarify the concerns about the validity of the extensively used law-of-the-wall for both velocity and temperature.

The present thesis considers the hydrodynamically developed turbulent air flow thermally developing in a four-wall-heated square duct. The magnitude of heating is large enough to cause significant property variations. From a search of the literature it seems no prior LES (nor DNS) work of this class of flows has been reported.

1.2.3 Study the Turbulent Heat Transfer in Spanwise Rotating Square Ducts

Turbulent flow and related heat transfer inside a square duct rotating about an axis perpendicular to one of the walls (see Fig. 1.1) has many engineering applications such as internal

cooling of turbine blades and automobile brakes. One of the primary concerns in these applications is the heat transfer coefficients on each wall of the duct. The complexity of this class of flows is largely due to the mutual influence between velocity field and temperature field through the effects of the Coriolis and centrifugal buoyancy forces.

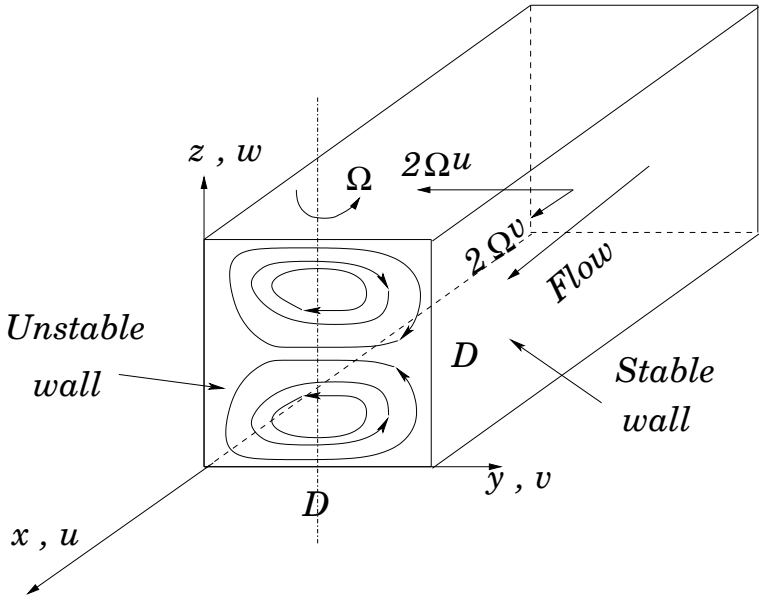

Figure 1.1 Flow in a rotating square duct

Although extensive experiments and numerical simulations based on the RANS method have been carried out on this topic, relatively few DNS and LES results are available. In the limited DNS/LES literature, most of the focus was on the fully developed region. In the present research the hydrodynamically developed turbulent air flow thermally developing in a four-wall-heated rotating square duct is simulated over a wide range of Reynolds number, rotation number and Grashof number. Numerous aspects of the flow including mean velocity, secondary flow pattern, turbulent kinetic energy, temperature fluctuation intensity, local temperature distributions and shear stress distributions, local and wall-averaged Nusselt numbers are investigated. A delicate mechanism through which the Coriolis and centrifugal forces affect the mixed convection is found to be able to explain much of the phenomena observed.

1.2.4 Analyze the Velocity Field and Instability of Rotating Duct Flow

To reach a better understanding of the physics of rotating duct flow, it is desired to theoretically determine the velocity field in a rotating square duct. A secondary flow pattern is formed due to the effects of the Coriolis force (see Fig. 1.1). This pattern includes two types of boundary layers which are of great importance in the study of rotating fluid flows, namely the Ekman layer and the Stewartson layer. A linear Stewartson layer solution, a non-linear Ekman layer solution and a local similarity assumption are combined together to give the velocity field.

The secondary flow pattern can be composed of either one pair or two pairs of rotating vortices. One may be curious about the factors that determine the pair numbers. An instability analysis is carried out to obtain a criterion of marginal stability. There are several other instability phenomena that occur at different locations in the duct under different situations. These instabilities are also explored theoretically in the present thesis.

One reason why the instability analysis is important is that the mean velocity profile changes due to such instabilities. Our results may contribute to the understanding of the non-linear interaction processes between mean flow and disturbances.

1.3 Review of Turbulent Flows in Rotating Ducts

This section gives a brief literature review of previous researches that have been conducted on turbulent rotating duct flows. This review is intended to provide background information on this topic. More specific references will be cited in the appropriate chapters later.

The main application of the rotating duct flows is for cooling of turbine blades. To achieve a high power-to-weight ratio, increasing inlet temperatures is preferred in gas turbine design. This high inlet temperature usually exceeds the temperature which the blade material can resist. Therefore a sophisticated cooling system is needed to protect the blades from melting. A widely used method for this purpose is to draw low temperature air from the compressor as coolant and circulate it through passages inside the blades to provide internal cooling. Also the circulating air can exit from specific holes on the blade surface for film cooling. Typically the internal coolant passages are straight ducts connected by 180 degree bends and ribs are usually

installed to the duct walls to enhance heat transfer. Besides the heat transfer performance, minimizing pressure loss is also crucial to achieve an efficient cooling since the coolant flow is driven by the turbine itself.

To understand the flow and heat transfer in the rotating internal coolant passages, numerous investigations have been carried out. These investigations can be put into three categories: experiments, numerical simulations and theoretical analyses.

1.3.1 Experiments

The early experiments on rotating duct flows and closely related rotating channel flows were focused on the measurements of pressure drop and integral parameters like heat transfer coefficients.

Though it is hard to find out who did the first experiment of this type, the work of Johnston et al. (1972) on turbulent rotating channel flows can be regarded as a milestone. They used hydrogen bubbles and dye injection to visualize the suppression and enhancement of turbulence on the stable and unstable sides of the channel. Their experiments also showed the cellular structure in the unstable side of the channel. Mårtensson et al. (2002) investigated the influence of rotation on the pressure drop in both square and rectangular ducts. They also studied the effects of the angle between the rotation vector and the main axis of the duct. The range of Reynolds number of their experiments was from 5,000 to 30,000 and the rotation number was from 0 to 1.0.

The experimental data on the details of the flow field are difficult and costly to obtain under rotation conditions. As a consequence, such data were limited until recently. Bons and Kerrebrock (1998) used particle image velocimetry (PIV) to measure the mean velocity of the turbulent flows in a rotating square duct with Reynolds number from 8,000 to 10,000 and rotation number from 0 to 0.3. Liou et al. (2003) reported laser-Doppler velocimetry (LDV) measurements of both mean velocity and turbulent fluctuations in a rotating two pass duct with Reynolds number fixed at 10,000 and rotation numbers up to 0.2.

The effects of rotation on heat transfer have been studied extensively. Morris and Ayhan

(1979) were first to incorporate the effect of centrifugal buoyancy to explain the observed heat transfer phenomena in a rotating circular tube. Medwell et al. (1991) did experiments on a rotating circular tube flow and gave the axial distributions of Nusselt number as well as temperature. Morris and Ghavami-Nasr (1991) carried out experiments on a rotating rectangular channel and studied the effects of Reynolds number and rotation number on the heat transfer coefficients. Wagner et al. (1991a, 1991b) systematically investigated the influences of Reynolds number, rotation number, density ratio and flow direction on the heat transfer in rotating cooling passages. Han et al. (1992, 1993, 1994) performed experiments on rotating square ducts under three different thermal boundary conditions, namely uniform wall temperature, uniform wall heat flux and uneven wall temperatures. They found that the constant wall heat flux condition gave a higher Nusselt number on both stable and unstable sides than the constant wall temperature case with otherwise the same conditions.

Most heat transfer experiments mentioned above used thermocouples so that the results were discrete and regional averaged values. The measurements of the details of the temperature field inside a rotating cooling passage, and the details of flow field, were not available till very recently. Liou et al. (2001) used transient liquid crystal thermometry (TLCT) technology to perform detailed measurements of the heat transfer coefficient in a rotating square duct.

1.3.2 Numerical Simulations

Most numerical studies on rotating turbulent duct flows were based on the RANS methods, for example, the work of Iacovides and Launder (1991), Prakash and Zerkle (1992), Tekriwal (1994), Tolpadi (1994), Bo et al. (1995), Dutta et al. (1996), Hwang et al. (1998), Lin et al. (2001) and Belhoucine et al. (2004). Relatively few DNS or LES studies are available. Kristoffersen and Andersson (1993) did direct numerical simulations of fully developed turbulent flow in a rotating channel. The Reynolds number was 2900 and the rotation number varied from 0 to 0.5. Their simulation showed an appreciable region in the mean velocity profile with slope of twice the angular velocity, which was in accordance with the experiments of Johnston et al. (1972). Also their results revealed the nearly complete suppression of turbulence in the

vicinity of the stable side at high rotation number. Alvelius (1999) also carried out a DNS study for rotating channel flows in his PhD thesis.

Gavrilakis (2004) performed DNS for fully developed turbulent flows in a rotating square duct. He simulated both the common cases with rotation axis parallel to the wall and the tilted rotating cases in which the rotation axis was parallel to the diagonal. The Reynolds number was fixed at 4,500 and the rotation numbers were 0.0133 and 0.0266. Mårtensson et al. (2004) carried out a DNS study very similar to that of Gavrilakis. In this work, the Reynolds number was 4,400 and rotation number was up to 0.77. They also simulated the tilted rotating duct cases. These two studies are the only available DNS results for rotating ducts according to the author's knowledge.

Tafti and Vanka (1991) used LES to simulate the turbulent flow in a rotating channel. The streamwise velocity, and the formation of spanwise roll cells were major concerns in this study. This point will be further discussed in the next section. Piomelli and Liu (1995) also did LES simulations of rotating channel flows and in this work they proposed a "localized dynamic SGS model" which will be used in this thesis. Pallares and Davidson (2000) did LES of turbulent flows in rotating channels and in a stationary square duct. Their results agreed with the DNS of Alvelius (1999) very well. Pallares and Davidson (2002) did LES of turbulent heat transfer in both stationary and rotating square ducts. In this study, the rotating duct flows were assumed to be hydrodynamically and thermally fully developed. A uniform heat flux condition was applied at the four walls. It was found that the turbulence level was strongly affected by the centrifugal buoyancy forces. The overall Nusselt numbers and the turbulence levels were not greatly influenced by the thermal boundary conditions. Murata and Mochizuki (1999, 2001, 2004) did a series of LES studies of turbulent heat transfer in rotating duct flows in which the effects of cross section aspect ratio, ribs and 180 degree turns were explored. Sewall and Tafti (2005) studied the flow and heat transfer in the developing region of a rotating ribbed turbine blade cooling channel. The Reynolds number was 20,000, the rotation number was 0.3 and four buoyancy parameters were calculated: 0.0, 0.25, 0.45 and 0.65. Their results were found to be in very good agreement with previous experimental results.

It should be noticed that all these recent LES researches did not take into account the effects of coolant property variations, which can hardly be justified in heat transfer situations. Salinas Vázquez and Métais (2002) performed LES for a compressible turbulent square duct flow under heating. Lee et al. (2004) did LES to explore the effects of rotation on the heat transfer in compressible turbulent channel flows. However, no LES of rotating turbulent duct flow with property variations has been reported.

1.3.3 Theoretical Analysis

The theoretical analyses of the rotating duct flows are quite limited. One reason may be, as Greenspan indicated in the preface of his classical text book *The theory of the rotating fluids* and quoted here, this problem lies in a field which is still "in the process of rapid and diverse growth" (Greenspan, 1968).

Two boundary layers of central importance in internal rotating flows are the Ekman layer and the Stewartson layer, bearing the names of their discoverers (Ekman, 1905; Stewartson, 1957). Both of these layers appear in rotating pipe flows. Benton and Boyer (1966) studied the flow in a rapidly rotating conduit of arbitrary cross-section. They treated the boundary layer around the periphery as an Ekman layer and the cross sections which have a finite part of their boundaries parallel to the axis of rotation (for example, the situation which is the focus of the present thesis) were excluded because of singularities. Bennetts and Hocking (1973) developed a nonlinear Ekman condition based on the local similarity assumption. The same authors used this condition with some modifications in examining the pressure-induced flows at high rotation numbers (Bennetts and Hocking, 1974). Smirnov (1978) developed a drag formula for rapidly rotating rectangular ducts. Smirnov also gave an explicit expression for the flow field with the linear theory. All of these authors considered only laminar flows. An attempt to obtain a drag formula for the turbulent rotating duct was recently attempted (Pallares et al., 2005), however, only the Ekman layers were considered and the drag formula was a half-empirical one.

For the instability analysis of rotating channel flow, Taylor (1923) was the first one who

treated the instability problem in viscous flow both theoretically and experimentally. Due to the interests of relating the origin of turbulence with instability of laminar flows, this topic has been extensively studied since then. Details of the development can be seen in books of Lin (1955), Chandrasekhar (1961) and Drazin and Reid (2004). Lezius and Johnston (1976) studied the stability of rotating laminar and turbulent channel flows using the method of Chandrasekhar and obtained good agreement with their experiments. Kheshgi and Scriven (1985) analyzed fully developed viscous flow through a rotating square duct with a given pressure gradient using the finite element method. In this work, critical Rossby numbers were obtained through extensive computational simulations of different combinations of Rossby number and Ekman number. It can be seen that the secondary flow pattern and critical Rossby numbers are very different between rotating channels and ducts. Such differences may be attributed to the effects of the Ekman layer. Busse (1968) gave a theoretical description for infinitesimal non-axisymmetric disturbances of a shear flow caused by differential rotation. His method was inspired and then generalized by the work of Greenspan (1968). An Orr-Sommerfeld type equation can be obtained from Busse's treatment. However, Busse restricted himself in the limit to an infinite Reynolds number (Rayleigh stability equation). Until now, there is no available stability analysis for the rotating duct flows according to the author's best knowledge.

1.4 Dissertation Organization

The dissertation is organized in the following way:

Chapter 2 describes the governing equations, the filtering procedure, the sub-grid scale (SGS) models and the finite volume formulations which were used in the current large eddy simulations (LES). This chapter highlights the different SGS models and boundary conditions.

The details of the process of incorporating Navier-Stokes characteristic boundary conditions (NSCBC) into the lower-upper symmetric Gauss-Seidel (LU-SGS) scheme will be presented in Chapter 3. The validity of this strategy is verified through simulation of several benchmark flows.

The results of thermally developing turbulent stationary duct flows under different heating are reported in Chapter 4. The counterpart of the rotating duct flows are given in Chapter 5. In Chapter 4, the effects of strong heating on the flow field, turbulent intensity and pressure loss are emphasized. In Chapter 5, the effects of Coriolis and centrifugal buoyancy forces are the main interests of the research and are stressed.

Chapter 6 is dedicated to the theoretical aspect of this subject. First the velocity field of the fully developed incompressible laminar flow inside a rotating square duct is investigated and then an instability analysis is carried out.

The conclusions of this research, as well as recommendations for future work can be found in Chapter 7.

CHAPTER 2. GOVERNING EQUATIONS AND NUMERICAL SCHEMES

In this chapter, the non-dimensional compressible filtered Navier-Stokes equations used for LES are derived. The sub-grid scale models required to close the equations are described. The numerical schemes used to solve the resultant equations are then presented.

2.1 Governing Equations

The compressible Navier-Stokes equations can be written in vector form as

$$\frac{\partial \mathbf{U}^*}{\partial t^*} + \frac{\partial \mathbf{F}^*{}_i}{\partial x_i^*} = \mathbf{S}^*. \tag{2.1}$$

The vector quantities are

$$\mathbf{U}^* = \begin{bmatrix} \rho^* \\ \rho^* u_1^* \\ \rho^* u_2^* \\ \rho^* u_3^* \\ \rho^* E^* \end{bmatrix}; \quad \mathbf{F}^*{}_i = \begin{bmatrix} \rho^* u_i^* \\ \rho^* u_i^* u_1^* - \sigma_{i1}^* \\ \rho^* u_i^* u_2^* - \sigma_{i2}^* \\ \rho^* u_i^* u_3^* - \sigma_{i3}^* \\ \rho^* E^* u_i^* - u_j^* \sigma_{ij}^* + q_i^* \end{bmatrix}. \tag{2.2}$$

In the above vectors, E^* is the total specific energy, that is the sum of the specific internal energy and the specific kinetic energy: $E^* = e^* + \frac{1}{2} u_i^* u_i^*$. The stress tensor is given as

$$\sigma_{ij}^* = -p^* \delta_{ij} + 2\mu^* (S_{ij}^* - \frac{1}{3} S_{kk}^* \delta_{ij}), \tag{2.3}$$

where δ is the Kronecker delta and S_{ij}^* is the strain rate tensor

$$S_{ij}^* = \frac{1}{2} (\frac{\partial u_i^*}{\partial x_j^*} + \frac{\partial u_j^*}{\partial x_i^*}). \tag{2.4}$$

The heat flux q_i^* is determined by Fourier's law:

$$q_i^* = -k^* \frac{\partial T^*}{\partial x_i^*}. \tag{2.5}$$

The source term $\mathbf{S}^*$ is $\mathbf{0}$ if there is no external force fields, otherwise it will contain the force terms, actual or fictional (apparent). For example, if the coordinates are attached to a rotating frame, the fluid flow will feel both Coriolis forces and a centrifugal force which should be included in $\mathbf{S}^*$. In LES and DNS, it is very common to apply periodic boundary conditions to some dimensions of the computational domain. If such a boundary condition is used in the flow direction, a forcing function equivalent to the mean pressure force has to be employed in the source term to drive the flow.

The ideal gas model is used to close the above equations since air is the working fluid in most of the film cooling applications. The equation of state for the ideal gas model is

$$p^* = \rho^* R^* T^*, \tag{2.6}$$

where R^* is the gas constant. And for an ideal gas the specific internal energy is $e^* = c_v^* T^*$.

The properties μ^* and k^* are the molecular dynamic viscosity and thermal conductivity, respectively. Both of them are functions of temperature that can be derived from molecular dynamics theory (eg. *Lectures on gas theory* of L. Boltzmann). For simplicity, the power law will be used throughout this research, that is, both μ^* and k^* are proportional to the 0.71 power of the absolute temperature T^*.

The above dimensional equations (denoted by asterisks) can be non-dimensionalized with respect to appropriate dimensional reference quantities as described below

$$\begin{array}{lll} x_i = \frac{x_i^*}{L_{ref}} & t = \frac{t^*}{L_{ref}/U_{ref}} & u_i = \frac{u_i^*}{U_{ref}} \\ p = \frac{p^*}{\rho_{ref} U_{ref}^2} & \rho = \frac{\rho^*}{\rho_{ref}} & T = \frac{T^*}{T_{ref}} \\ e = \frac{e^*}{U_{ref}^2} & \mu = \frac{\mu^*}{\mu_{ref}} & k = \frac{k^*}{k_{ref}} \\ c_v = \frac{c_v^*}{U_{ref}^2/T_{ref}} & c_p = \frac{c_p^*}{U_{ref}^2/T_{ref}} & R = \frac{R^*}{U_{ref}^2/T_{ref}}. \end{array} \tag{2.7}$$

In this research, the hydraulic diameter is chosen as the reference length L_{ref}. U_{ref}, T_{ref}, ρ_{ref} are the mean values of corresponding quantities at the duct inlet. μ_{ref} and k_{ref} are the values of corresponding properties at T_{ref}.

Using the above definitions, the non-dimensional form of the governing equations is

$$\frac{\partial \mathbf{U}}{\partial t} + \frac{\partial \mathbf{F}_i}{\partial x_i} = \mathbf{S}, \tag{2.8}$$

with

$$\mathbf{U} = \begin{bmatrix} \rho \\ \rho u_1 \\ \rho u_2 \\ \rho u_3 \\ \rho E \end{bmatrix}; \quad \mathbf{F}_i = \begin{bmatrix} \rho u_i \\ \rho u_i u_1 - \sigma_{i1} \\ \rho u_i u_2 - \sigma_{i2} \\ \rho u_i u_3 - \sigma_{i3} \\ \rho E u_i - u_j \sigma_{ij} + q_i \end{bmatrix}. \tag{2.9}$$

The non-dimensional stress tensor, strain rate tensor and heat flux vector are

$$\sigma_{ij} = -p\delta_{ij} + \frac{2\mu}{Re}(S_{ij} - \frac{1}{3}S_{kk}\delta_{ij}), \tag{2.10}$$

$$S_{ij} = \frac{1}{2}(\frac{\partial u_i}{\partial x_j} + \frac{\partial u_j}{\partial x_i}), \tag{2.11}$$

$$q_i = -\frac{c_p \mu}{PrRe}\frac{\partial T}{\partial x_i}. \tag{2.12}$$

Re is the Reynolds number and Pr is the Prandtl number. Their definitions are

$$Re = \frac{\rho_{ref} U_{ref} L_{ref}}{\mu_{ref}}, \tag{2.13}$$

$$Pr = \frac{\mu^* c_p^*}{k^*}. \tag{2.14}$$

2.2 Filtering

Large eddy simulation resolves only the large scales and models the small scales of the flow. To separate the effects of the large-scale and small scale motions, a filtering operation should be applied to the Navier-Stokes equations. The filtering operation is defined as

$$\bar{f}(\mathbf{x}, t) = \int G(|\mathbf{r}|\,; \Delta) f(\mathbf{x} - \mathbf{r}, t) d\mathbf{r}, \tag{2.15}$$

where integration is over the entire flow domain, and the specified filter function G satisfies the normalization condition

$$\int G(|\mathbf{r}|\,; \Delta) d\mathbf{r} = 1. \tag{2.16}$$

Several filter functions have been applied to LES such as the sharp Fourier cut-off filter, Gaussian filter, box filter, top-hat filter, etc. In the present thesis, the top-hat filter is used, which is defined as

$$G(|\mathbf{r}|\,;\Delta) = \begin{cases} 1/\Delta & \text{if } |\mathbf{r}| \leq \Delta/2 \\ 0 & \text{if } |\mathbf{r}| > \Delta/2 \end{cases} \tag{2.17}$$

where Δ is the filter width. This filter is a very natural choice when finite-volume or finite-difference methods are used because by setting Δ the same as the grid resolution this filtering process reduces to an average over a control volume. Since our tacit understanding about the value of a variable at one control volume is indeed the average value of this variable over the control volume, this is by itself a top-hat filtering process and no more *explicit* filtering is needed!

In the present research, an anisotropic rectangular grid with grid spacings Δ_1, Δ_2, and Δ_3 in the three coordinate directions was used in most of the cases; then the filter width Δ was taken to be $\Delta = (\Delta_1\Delta_2\Delta_3)^{1/3}$ as suggested by Deardorff (1970).

As a result of the filtering operation, the flow field can be viewed as being decomposed into two components:

$$f = \bar{f} + f', \tag{2.18}$$

where $\bar{f}$ is the filtered scale, or large scale, or resolved scale component; and f' is the small scale, or unresolved scale, or subgrid scale component. This looks analogous to the Reynolds decomposition. An important difference, however, is that LES uses a spatial average rather than a temporal average in the filtering procedure. As a result, the filtering operation and differentiating with respect to time commute, i.e.,

$$\frac{\partial \bar{f}}{\partial t} = \overline{\frac{\partial f}{\partial t}}. \tag{2.19}$$

However, the filtering operation and differentiation with respect to position do not commute in general unless the filter width is constant, and the commutation error is second order in filter width (Ghosal and Moin, 1995). To avoid this difficulty, one can filter only in the homogeneous directions. If the numerical scheme is of second order, however, the filtering operation can be treated to commute with the differentiation with respect to position.

If the filtering operation is applied to the nondimensional governing equations (Eq. (2.8) and Eq. (2.9)), terms like $\overline{\rho u_i}$, $\overline{\rho u_i u_j}$ and $\overline{\rho u_i T}$ appear. To simplify the equations, Favre filtering (Favre, 1983) is introduced to give

$$\tilde{f} = \frac{\overline{\rho f}}{\bar{\rho}}. \tag{2.20}$$

Thus, the variables can be decomposed in another way besides Eq. (2.18):

$$f = \tilde{f} + f'', \tag{2.21}$$

where $\tilde{f}$ is the resolved component and f'' is the unresolved component. Using Favre filtering, we have

$$\overline{\rho u_i} = \bar{\rho}\tilde{u}_i; \quad \overline{\rho u_i u_j} = \bar{\rho}\widetilde{u_i u_j}; \quad \overline{\rho u_i T} = \bar{\rho}\widetilde{u_i T}. \tag{2.22}$$

The Favre filtered continuity and momentum equations can be easily derived (assuming the source term $\mathbf{S} = \mathbf{0}$):

$$\frac{\partial \bar{\rho}}{\partial t} + \frac{\partial(\bar{\rho}\tilde{u}_j)}{\partial x_j} = 0, \tag{2.23}$$

$$\frac{\partial(\bar{\rho}\tilde{u}_i)}{\partial t} + \frac{\partial(\bar{\rho}\tilde{u}_i\tilde{u}_j)}{\partial x_j} = \frac{\partial \bar{\sigma}_{ij}}{\partial x_j} - \frac{\partial \tau_{ij}}{\partial x_j}, \tag{2.24}$$

in which

$$\bar{\sigma}_{ij} = \overline{-p\delta_{ij} + \frac{2\mu}{Re}(S_{ij} - \frac{1}{3}S_{kk}\delta_{ij})} = -\bar{p}\delta_{ij} + \overline{\frac{2\mu}{Re}(S_{ij} - \frac{1}{3}S_{kk}\delta_{ij})}$$

$$\approx \hat{\sigma}_{ij} = -\bar{p}\delta_{ij} + \frac{2\bar{\mu}}{Re}(\tilde{S}_{ij} - \frac{1}{3}\tilde{S}_{kk}\delta_{ij}), \tag{2.25}$$

$$\tau_{ij} = \bar{\rho}(\widetilde{u_i u_j} - \tilde{u}_i\tilde{u}_j). \tag{2.26}$$

The approximation made in Eq. (2.25) is due to the weak correlation between μ and derivatives of velocity (Cebeci and Smith, 1974). Compared with the original momentum equations, the filtered form has one more term associated with the so-called subgrid scale (SGS) stress tensor τ_{ij} which represents the effect of the small-scale motions. The strain rate tensor is

$$\tilde{S}_{ij} = \frac{1}{2}(\frac{\partial \tilde{u}_i}{\partial x_j} + \frac{\partial \tilde{u}_j}{\partial x_i}). \tag{2.27}$$

The deduction of the filtered equation for conservation of total energy is somewhat more complex. First, the thermal energy equation is used

$$\frac{\partial(\rho c_v T)}{\partial t} + \frac{\partial(\rho c_v T u_j)}{\partial x_j} = \sigma_{ij}\frac{\partial u_i}{\partial x_j} - \frac{\partial q_j}{\partial x_j}. \tag{2.28}$$

Applying the filtering operation to the above equation leads to

$$\frac{\partial(\bar{\rho} c_v \tilde{T})}{\partial t} + \frac{\partial(\bar{\rho} c_v \tilde{T}\tilde{u}_j)}{\partial x_j} = \overline{\sigma_{ij}\frac{\partial u_i}{\partial x_j}} - \frac{\partial \bar{q}_j}{\partial x_j} - \frac{\partial \phi_j}{\partial x_j}, \tag{2.29}$$

in which $\phi_j = \bar{\rho} c_v(\widetilde{Tu_j} - \tilde{T}\tilde{u}_j)$ is the SGS heat flux. Notice the specific heat c_v is regarded as a constant since the ideal gas model is used. The filtered heat flux $\bar{q}_j$ can be approximated as

$$\bar{q}_j = -\overline{\frac{c_p \mu}{PrRe}\frac{\partial T}{\partial x_j}} \approx \hat{q}_j = -\frac{c_p \bar{\mu}}{PrRe}\frac{\partial \tilde{T}}{\partial x_j} \tag{2.30}$$

by assuming the correlation between viscosity and temperature derivative is weak. If we expand the filtered momentum equation, Eq. (2.24), we can obtain

$$\bar{\rho}\frac{\partial \tilde{u}_i}{\partial t} + \tilde{u}_i\left[\frac{\partial \bar{\rho}}{\partial t} + \frac{\partial(\bar{\rho}\tilde{u}_j)}{\partial x_j}\right] + \bar{\rho}\tilde{u}_j\frac{\partial \tilde{u}_i}{\partial x_j} = \frac{\partial \bar{\sigma}_{ij}}{\partial x_j} - \frac{\partial \tau_{ij}}{\partial x_j}, \tag{2.31}$$

and the term inside the square brackets vanishes due to continuity (Eq.(2.23)) . Multiplying Eq. (2.31) by $\tilde{u}_i$ and adding to the filtered internal energy equation, Eq. (2.29), gives

$$\begin{aligned} &\frac{\partial(\bar{\rho} c_v \tilde{T})}{\partial t} + \frac{\partial(\bar{\rho} c_v \tilde{T}\tilde{u}_j)}{\partial x_j} + \\ &\bar{\rho}\frac{\partial(\frac{1}{2}\tilde{u}_i\tilde{u}_i)}{\partial t} + \bar{\rho}\tilde{u}_j\frac{\partial(\frac{1}{2}\tilde{u}_i\tilde{u}_i)}{\partial x_j} = \\ &\overline{\sigma_{ij}\frac{\partial u_i}{\partial x_j}} - \frac{\partial \bar{q}_j}{\partial x_j} - \frac{\partial \phi_j}{\partial x_j} + \\ &\tilde{u}_i\frac{\partial \bar{\sigma}_{ij}}{\partial x_j} - \tilde{u}_i\frac{\partial \tau_{ij}}{\partial x_j}. \end{aligned} \tag{2.32}$$

The filtered continuity equation, Eq.(2.23), is then multiplied by $\frac{1}{2}\tilde{u}_i\tilde{u}_i$ and added to Eq. (2.32) and results in

$$\begin{aligned} &\frac{\partial(\bar{\rho} c_v \tilde{T})}{\partial t} + \bar{\rho}\frac{\partial(\frac{1}{2}\tilde{u}_i\tilde{u}_i)}{\partial t} + \frac{1}{2}\tilde{u}_i\tilde{u}_i\frac{\partial \bar{\rho}}{\partial t} + \\ &\frac{\partial(\bar{\rho} c_v \tilde{T}\tilde{u}_j)}{\partial x_j} + \bar{\rho}\tilde{u}_j\frac{\partial(\frac{1}{2}\tilde{u}_i\tilde{u}_i)}{\partial x_j} + \frac{1}{2}\tilde{u}_i\tilde{u}_i\frac{\partial(\bar{\rho}\tilde{u}_j)}{\partial x_j} = \\ &\overline{\sigma_{ij}\frac{\partial u_i}{\partial x_j}} - \frac{\partial \bar{q}_j}{\partial x_j} - \frac{\partial \phi_j}{\partial x_j} + \tilde{u}_i\frac{\partial \bar{\sigma}_{ij}}{\partial x_j} - \tilde{u}_i\frac{\partial \tau_{ij}}{\partial x_j}. \end{aligned} \tag{2.33}$$

By combining terms we have

$$\frac{\partial(\bar{\rho}\hat{E})}{\partial t} + \frac{\partial(\bar{\rho}\hat{E}\tilde{u}_j)}{\partial x_j} = \overline{\sigma_{ij}\frac{\partial u_i}{\partial x_j}} - \frac{\partial \hat{q}_j}{\partial x_j} - \frac{\partial \phi_j}{\partial x_j} + \tilde{u}_i\frac{\partial \hat{\sigma}_{ij}}{\partial x_j} - \tilde{u}_i\frac{\partial \tau_{ij}}{\partial x_j}, \tag{2.34}$$

where $\hat{E} = \tilde{e} + \frac{1}{2}\tilde{u}_i\tilde{u}_i$ and $\bar{\sigma}_{ij}$ and $\bar{q}_j$ are replaced by their approximations $\hat{\sigma}_{ij}$ and $\hat{q}_j$ respectively. This equation can be rewritten as

$$\frac{\partial(\bar{\rho}\hat{E})}{\partial t} + \frac{\partial(\bar{\rho}\hat{E}\tilde{u}_j)}{\partial x_j} = \frac{\partial(\tilde{u}_i\hat{\sigma}_{ij})}{\partial x_j} - \frac{\partial \hat{q}_j}{\partial x_j} - \frac{\partial \phi_j}{\partial x_j} - \alpha - \epsilon, \tag{2.35}$$

where

$$\begin{aligned} \alpha &= \tilde{u}_i\frac{\partial \tau_{ij}}{\partial x_j}; \\ \epsilon &= \overline{\sigma_{ij}\frac{\partial u_i}{\partial x_j}} - \hat{\sigma}_{ij}\frac{\partial \tilde{u}_j}{\partial x_j}. \end{aligned} \tag{2.36}$$

For the present work, α and ϵ are neglected which is appropriate when Mach number is less than 0.2 (Vreman et al. 1995). The last governing equation, the equation of state, can be easily filtered: $\bar{p} = \bar{\rho}R\tilde{T}$.

Thus, the filtered governing equations can be written in vector form as

$$\frac{\partial \mathbf{U}}{\partial t} + \frac{\partial \mathbf{F}_i}{\partial x_i} = \mathbf{S}, \tag{2.37}$$

with

$$\mathbf{U} = \begin{bmatrix} \bar{\rho} \\ \bar{\rho}\tilde{u}_1 \\ \bar{\rho}\tilde{u}_2 \\ \bar{\rho}\tilde{u}_3 \\ \bar{\rho}\hat{E} \end{bmatrix}; \quad \mathbf{F}_i = \begin{bmatrix} \bar{\rho}\tilde{u}_i \\ \bar{\rho}\tilde{u}_i\tilde{u}_1 - \hat{\sigma}_{i1} + \tau_{i1} \\ \bar{\rho}\tilde{u}_i\tilde{u}_2 - \hat{\sigma}_{i2} + \tau_{i2} \\ \bar{\rho}\tilde{u}_i\tilde{u}_3 - \hat{\sigma}_{i3} + \tau_{i3} \\ \bar{\rho}\hat{E}\tilde{u}_i - \tilde{u}_j\hat{\sigma}_{ij} + \hat{q}_i + \phi_i \end{bmatrix}, \tag{2.38}$$

in which the SGS stress tensor τ_{ij} and SGS heat flux ϕ_j have to be modeled to close the system of equations. These models are called subgrid scale (SGS) models.

2.3 Subgrid Scale Model

The role of SGS models in LES is analogous to the turbulence models for the Reynolds averaged Navier-Stokes (RANS) equations. Because the LES uses spatial average and the SGS

terms represent the effects of the small-scale motion which is, by and large, isotropic, the SGS models have an advantage of being more universal than RANS models.

Numerous SGS models have been used in LES. A recent review of SGS modeling techniques can be found in Meneveau and Katz (2000).

The filtered strain rate tensor is

$$\tilde{S}_{ij} = \frac{1}{2}(\frac{\partial \tilde{u}_i}{\partial x_j} + \frac{\partial \tilde{u}_j}{\partial x_i}). \tag{2.39}$$

The magnitude of the filtered strain rate tensor is defined as

$$\tilde{\mathcal{S}} = (2\tilde{S}_{ij}\tilde{S}_{ij})^{1/2}. \tag{2.40}$$

Both of these quantities are widely used in SGS models. The SGS stress tensor, τ_{ij} can be decomposed into two parts, the anisotropic part and the isotropic part as

$$\tau_{ij} = \bar{\rho}(\widetilde{u_i u_j} - \tilde{u}_i\tilde{u}_j) = \tau^a_{ij} + \frac{1}{3}\tau_{kk}\delta_{ij}. \tag{2.41}$$

The most widely used SGS modeling approach is the eddy viscosity methodology which assumes the anisotropic part of the SGS stress tensor to be proportional to the filtered rate of strain:

$$\tau^a_{ij} = -2\mu_t(\tilde{S}_{ij} - \frac{1}{3}\tilde{S}_{kk}\delta_{ij}). \tag{2.42}$$

The above equation includes the $\tilde{S}_{kk}$ term due to the flow compressibility.

The isotropic part τ_{kk} is negligible compared to the thermodynamic pressure as Moin et al. (1991) and Spyropoulos and Blaisdell (1995) indicated. Vreman et al. (1995) and Dailey (1997) observed that the calculation was unstable if the isotropic part was not neglected. In the present work, τ_{kk} is neglected. Then the question left is how to determine the eddy viscosity μ_t. The simplest model is that proposed by Smagorinsky (1963), which also forms the basis for the more advanced dynamic models.

2.3.1 Smagorinsky Model

By analogy to the Prandtl's mixing-length hypothesis, the eddy viscosity is modeled as

$$\mu_t = \bar{\rho}\mathcal{L}_s^2\tilde{\mathcal{S}} = \bar{\rho}C_s\Delta^2\tilde{\mathcal{S}}, \tag{2.43}$$

where $\mathcal{L}_s$ is the Smagorinsky length scale and C_s is the Smagorinsky coefficient which is a positive constant in this model. It is easy to see the shortcoming of this model: the Smagorinsky coefficient should in fact depend on factors like flow regimes, distance to the walls, grid scales, etc., so it cannot be a constant. For example, in laminar flow or close to a solid wall, this coefficient should be zero. Though it is possible to modify the Smagorinsky coefficient formula to take these factors into account, the dynamic model which will be discussed shortly is considered as more satisfactory because the dynamic model can determine the appropriate local Smagorinsky coefficient without any *a priori* parameters.

2.3.2 Dynamic Model

The dynamic model was proposed by Germano et al. (1991). It assumes that inside a proper size neighborhood of any point within a flow field, the Smagorinsky coefficient is the same. To exploit this assumption, a test filter has to be introduced besides the grid filter. As mentioned in the last section, the grid filter width is $\Delta = (\Delta_1\Delta_2\Delta_3)^{1/3}$ where Δ_i is the grid spacing in the ith direction. The operation of grid filtering is defined as

$$\bar{f}(\mathbf{x},t) = \int G(|\mathbf{r}|\,;\Delta) f(\mathbf{x}-\mathbf{r},t)d\mathbf{r}. \tag{2.44}$$

The LES equations are intended to be solved for $\bar{f}$ (or with Favre average, $\tilde{f}$), though this filtering is not explicitly performed. The test filter has filter width $\hat{\Delta}$, which is typically taken to be twice Δ. The test filtering operation is similarly defined as

$$\hat{f}(\mathbf{x},t) = \int G(|\mathbf{r}|\,;\hat{\Delta}) f(\mathbf{x}-\mathbf{r},t)d\mathbf{r}. \tag{2.45}$$

However, the test filtering is deemed to be applied to the *filtered* flow field rather than the original un-filtered one since the latter is unknown. And this test filtering operation should be *explicitly* performed. We first show how to calculate the local Smagorinsky coefficient C_s "dynamically".

The subgrid scale and subtest scale stresses based on the single- and double-filtering operations are defined as

$$\tau_{ij} = \bar{\rho}\widetilde{u_i u_j} - \bar{\rho}\tilde{u}_i\tilde{u}_j = \overline{\rho u_i u_j} - \frac{\overline{\rho u_i}\,\overline{\rho u_j}}{\bar{\rho}};$$

$$T_{ij} = \widehat{\overline{\rho u_i u_j}} - \frac{\widehat{\overline{\rho u_i}}\,\widehat{\overline{\rho u_j}}}{\hat{\bar{\rho}}} = \widehat{\bar{\rho} u_i u_j} - \frac{\widehat{\bar{\rho}\tilde{u}_i}\widehat{\bar{\rho}\tilde{u}_j}}{\hat{\bar{\rho}}}. \tag{2.46}$$

According to the Smagorinsky model, the anisotropic part of the SGS stress is determined by

$$\tau_{ij}^a = \tau_{ij} - \frac{1}{3}\tau_{kk}\delta_{ij} = -2\mu_t(\tilde{S}_{ij} - \frac{1}{3}\tilde{S}_{kk}\delta_{ij}) = -2\bar{\rho}C_s\Delta^2\tilde{\mathcal{S}}(\tilde{S}_{ij} - \frac{1}{3}\tilde{S}_{kk}\delta_{ij}) = C_s\beta_{ij}. \tag{2.47}$$

Similarly, the subtest scale stress is modeled as

$$T_{ij}^a = T_{ij} - \frac{1}{3}T_{kk}\delta_{ij} = -2\hat{\mu}_t(\hat{\tilde{S}}_{ij} - \frac{1}{3}\hat{\tilde{S}}_{kk}\delta_{ij}) = -2\hat{\bar{\rho}}C_s\hat{\Delta}^2\hat{\tilde{\mathcal{S}}}(\hat{\tilde{S}}_{ij} - \frac{1}{3}\hat{\tilde{S}}_{kk}\delta_{ij}) = C_s\alpha_{ij}, \tag{2.48}$$

where $\hat{\tilde{S}}_{ij} = \frac{1}{2}(\frac{\partial\hat{\tilde{u}}_i}{\partial x_j} + \frac{\partial\hat{\tilde{u}}_j}{\partial x_i})$. An identity due to Germano (1992) is obtained by

$$\mathcal{L}_{ij} = T_{ij} - \hat{\tau}_{ij} = \widehat{\bar{\rho}\tilde{u}_i\tilde{u}_j} - \frac{\widehat{\bar{\rho}\tilde{u}_i}\widehat{\bar{\rho}\tilde{u}_j}}{\hat{\bar{\rho}}}. \tag{2.49}$$

Thus, we have

$$\mathcal{L}_{ij}^a = \mathcal{L}_{ij} - \frac{1}{3}\mathcal{L}_{kk}\delta_{ij} = C_s\alpha_{ij} - \widehat{C_s\beta_{ij}} \approx C_s(\alpha_{ij} - \hat{\beta}_{ij}). \tag{2.50}$$

Notice both $\mathcal{L}_{ij}^a$ and $\alpha_{ij} - \hat{\beta}_{ij}$ are known in terms of $\tilde{u}_i$ and $\tilde{u}_j$. This information can be used to determine the value of C_s. Of course, a single C_s cannot satisfy the total of six independent components of $\mathcal{L}_{ij}^a$. However, as Lilly (1992) showed, the sum of the squares of the error can be minimized by contracting both sides of Eq. (2.50) with $\alpha_{ij} - \hat{\beta}_{ij}$ to yield:

$$C_s = \frac{\left\langle \mathcal{L}_{ij}^a(\alpha_{ij} - \hat{\beta}_{ij}) \right\rangle}{\left\langle (\alpha_{mn} - \hat{\beta}_{mn})(\alpha_{mn} - \hat{\beta}_{mn}) \right\rangle}, \tag{2.51}$$

where $\langle\cdot\rangle$ denotes a spatial averaging procedure along the homogeneous directions of the flow. Such a procedure is necessary to ensure the stability of LES calculations.

The SGS heat flux vector, ϕ_j, can be modeled similarly. First, the subtest scale heat flux Q_j is defined following ϕ_j as

$$\begin{aligned} \phi_j &= c_v(\widehat{\bar{\rho}\tilde{T}\tilde{u}_j} - \bar{\rho}\tilde{T}\tilde{u}_j) = c_v(\overline{\rho T u_j} - \frac{\overline{\rho T}\,\overline{\rho u_j}}{\bar{\rho}}); \\ Q_j &= c_v(\widehat{\overline{\rho T u_j}} - \frac{\widehat{\overline{\rho T}}\,\widehat{\overline{\rho u_j}}}{\hat{\bar{\rho}}}) = \widehat{\bar{\rho}\tilde{T}\tilde{u}_j} - \frac{\widehat{\bar{\rho}\tilde{T}}\widehat{\bar{\rho}\tilde{u}_j}}{\hat{\bar{\rho}}}. \end{aligned} \tag{2.52}$$

Then the heat fluxes are modeled as

$$\begin{aligned} \phi_j &= -\frac{c_v\mu_t}{Pr_t}\frac{\partial\tilde{T}}{\partial x_j} = \frac{\chi_j}{Pr_t}; \\ Q_j &= -\frac{c_v\hat{\mu}_t}{Pr_t}\frac{\partial\hat{\tilde{T}}}{\partial x_j} = \frac{\zeta_j}{Pr_t}, \end{aligned} \tag{2.53}$$

where Pr_t is the turbulent Prandtl number to be determined dynamically. μ_t and $\hat{\mu}_t$ are the same as those defined in Eqs. (2.47) and (2.48). The identity relating the two heat fluxes is

$$\mathcal{M}_j = Q_j - \hat{\phi}_j = c_v(\widehat{\bar{\rho}\tilde{T}\tilde{u}_j} - \frac{\widehat{\bar{\rho}\tilde{T}}\widehat{\bar{\rho}\tilde{u}_j}}{\hat{\bar{\rho}}}) = \frac{\zeta_j - \hat{\chi}_j}{Pr_t}. \tag{2.54}$$

Thus, we have

$$Pr_t = \frac{\langle(\zeta_j - \hat{\chi}_j)(\zeta_j - \hat{\chi}_j)\rangle}{\langle\mathcal{M}_n(\zeta_n - \hat{\chi}_n)\rangle}, \tag{2.55}$$

where $\langle\cdot\rangle$ still denotes a spatial averaging along the homogeneous directions of the flow. This dynamic model was successfully used by Wang and Pletcher (1996), Xu et al. (2004) and many other authors.

Now a new problem arises: what if there is no homogeneous direction at all? In fact it is the case for lots of situations including the developing flow in a square duct. A solution to this problem is the so called localized dynamic model which was developed by Ghosal et al. (1995). Here we describe a simpler version due to Piomelli and Liu (1995).

2.3.3 Localized Dynamic Model

Equation (2.50) is recast in the form

$$\mathcal{L}^a_{ij} = C_s\alpha_{ij} - \widehat{C^*_s\beta_{ij}}, \tag{2.56}$$

where C^*_s is an estimate of the coefficient and assumed to be known. In the present research, the value at the previous time-step is used as C^*_s. The initial value of C_s is set to the Smagorinsky constant. Since C^*_s is known, C_s can be obtained by

$$C_s = \left\langle \frac{(\mathcal{L}^a_{ij} + \widehat{C^*_s\beta_{ij}})\alpha_{ij}}{\alpha_{mn}\alpha_{mn}} \right\rangle, \tag{2.57}$$

where $\langle\cdot\rangle$ is an averaging performed locally over the test filter volume.

The turbulent Prandtl number is determined similarly:

$$Pr_t = \left\langle \frac{\zeta_n\zeta_n}{(\mathcal{M}_j + \widehat{\chi_j/Pr^*_t})\zeta_j} \right\rangle. \tag{2.58}$$

2.4 Finite Volume Based Numerical Scheme

2.4.1 Integral Form of Equations

Though the conserved variables $(\bar{\rho}, \bar{\rho}\tilde{u}_i, \bar{\rho}\tilde{E})$ are often used as dependent variables, primitive variables $(\bar{p}, \tilde{u}_i, \tilde{T})$ are preferable at low Mach numbers since under such situations computing the pressure from the equation of state with codes using the conserved variables can result in significant roundoff errors (Shuen et al., 1992).

We choose the set of variables $\mathbf{W} = (\bar{p}, \tilde{u}_1, \tilde{u}_2, \tilde{u}_3, \tilde{T})^T$ as the primitive variables, and the governing equations (2.37) can be recast in terms of $\mathbf{W}$ as

$$\frac{\partial \mathbf{U}}{\partial \mathbf{W}} \frac{\partial \mathbf{W}}{\partial t} + \frac{\partial \mathbf{F}_i}{\partial x_i} = \mathbf{S}. \tag{2.59}$$

By replacing density with pressure and temperature and then multiplying by the gas constant throughout, the terms in the above equation become

$$\mathbf{U} = \begin{bmatrix} \bar{p}/\tilde{T} \\ \bar{p}\tilde{u}_1/\tilde{T} \\ \bar{p}\tilde{u}_2/\tilde{T} \\ \bar{p}\tilde{u}_3/\tilde{T} \\ \bar{p}\hat{E}/\tilde{T} \end{bmatrix}; \quad \mathbf{F}_i = \begin{bmatrix} \bar{p}\tilde{u}_i/\tilde{T} \\ \bar{p}\tilde{u}_i\tilde{u}_1/\tilde{T} - R\hat{\sigma}_{i1} + R\tau_{i1} \\ \bar{p}\tilde{u}_i\tilde{u}_2/\tilde{T} - R\hat{\sigma}_{i2} + R\tau_{i2} \\ \bar{p}\tilde{u}_i\tilde{u}_3/\tilde{T} - R\hat{\sigma}_{i3} + R\tau_{i3} \\ \bar{p}\tilde{u}_i\hat{E}/\tilde{T} - R\tilde{u}_j\hat{\sigma}_{ij} + R\hat{q}_i + R\phi_i \end{bmatrix}, \tag{2.60}$$

where

$$\begin{aligned} \hat{E} &= c_v\tilde{T} + \frac{1}{2}(\tilde{u}_k\tilde{u}_k); \\ \hat{\sigma}_{ij} &= -\bar{p}\delta_{ij} + \frac{2\bar{\mu}}{Re}(\tilde{S}_{ij} - \frac{1}{3}\tilde{S}_{kk}\delta_{ij}); \\ \tilde{S}_{ij} &= \frac{1}{2}(\frac{\partial \tilde{u}_i}{\partial x_j} + \frac{\partial \tilde{u}_j}{\partial x_i}); \\ \tau_{ij} &= -2\mu_t(\tilde{S}_{ij} - \frac{1}{3}\tilde{S}_{kk}\delta_{ij}); \\ \hat{q}_i &= -\frac{c_p\bar{\mu}}{PrRe}\frac{\partial \tilde{T}}{\partial x_i}; \\ \phi_i &= -\frac{c_v\mu_t}{Pr_t}\frac{\partial \tilde{T}}{\partial x_i}. \end{aligned} \tag{2.61}$$

It is usually advantageous to split the flux vector $\mathbf{F}_i$ into three parts, namely, the inviscid

part $\mathcal{F}_i$, the viscous part $\mathbb{F}_i$ and the subgrid-scale part $\mathscr{F}_i$. They are defined as

$$\mathbf{F}_i = \mathcal{F}_i - \mathbb{F}_i + \mathscr{F}_i. \tag{2.62}$$

$$\mathcal{F}_i = \begin{bmatrix} \bar{p}\tilde{u}_i/\tilde{T} \\ \bar{p}\tilde{u}_i\tilde{u}_1/\tilde{T} + R\bar{p}\delta_{i1} \\ \bar{p}\tilde{u}_i\tilde{u}_2/\tilde{T} + R\bar{p}\delta_{i1} \\ \bar{p}\tilde{u}_i\tilde{u}_3/\tilde{T} + R\bar{p}\delta_{i1} \\ \bar{p}\tilde{u}_i\hat{H}/\tilde{T} \end{bmatrix}; \quad \mathbb{F}_i = \begin{bmatrix} 0 \\ R\hat{V}_{i1} \\ R\hat{V}_{i2} \\ R\hat{V}_{i3} \\ R\tilde{u}_j\hat{V}_{ij} - R\hat{q}_i \end{bmatrix}; \quad \mathscr{F}_i = \begin{bmatrix} 0 \\ R\tau_{i1} \\ R\tau_{i2} \\ R\tau_{i3} \\ R\phi_i \end{bmatrix}, \tag{2.63}$$

in which the stress tensor $\hat{\sigma}_{ij}$ is decomposed into two parts: pressure tensor $-\bar{p}\delta_{ij}$ and the viscous stress tensor $\hat{V}_{ij} = \frac{2\bar{\mu}}{Re}(\tilde{S}_{ij} - \frac{1}{3}\tilde{S}_{kk}\delta_{ij})$. The contribution of pressure is included in the inviscid flux. Note the use of specific total enthalpy $\hat{H} = \hat{E} + R\tilde{T} = c_p\tilde{T} + \frac{1}{2}(\tilde{u}_k\tilde{u}_k)$.

By integrating throughout a control volume Ω and using the Gauss divergence theorem, Eq. (2.59) becomes

$$\int_\Omega [T]\frac{\partial \mathbf{W}}{\partial t}d\Omega + \oint_{\partial\Omega} \mathbf{F}_i\vec{e}_i \cdot d\vec{S} = \int_\Omega \mathbf{S}d\Omega, \tag{2.64}$$

where $[T] = \frac{\partial \mathbf{U}}{\partial \mathbf{W}}$ is the time derivative Jacobian matrix listed in Appendix A, $\partial\Omega$ is the bounding surface of the control volume Ω, $\vec{e}_i$ is the unit vector in the ith direction and $\vec{S}$ is the surface area vector which points in the surface normal direction.

In the rest of this thesis, the overheads denoting the filtered variables such as $\overline{(\cdot)}$, $\tilde{(\cdot)}$, $\hat{(\cdot)}$ will be dropped for simplicity. However, their meanings should not be confused with the original unfiltered variables.

2.4.2 Finite Volume Method and Integral Approximation

The above integral form of the governing equations will be discretized and solved in a finite volume framework that has the advantage that it can be easily implemented in complex geometries. The solution domain is divided into rectangular control volumes. The conserved equations and conservation principles are applied to each control volume. The Cartesian hexahedral control volumes are used in the present thesis and a typical control volume with its six neighboring volumes is depicted in Fig. 2.1. Note that the solution variables are stored at the geometric centers of the control volumes. And we will always align the coordinates

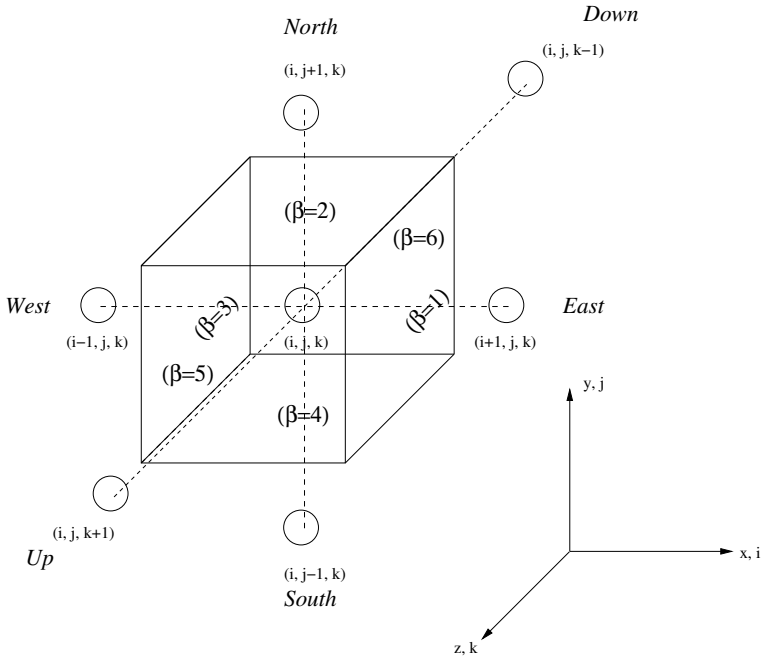

Figure 2.1 Main control volume (i,j,k) with its six neighboring control volumes

with the directions as shown in Fig. 2.1. The indices 1, 2 and 3 in the above equations are also always assigned to the x, y and z coordinates as well as u, v and w velocity components, respectively. Every control volume has six surfaces that are labeled by numbers from one to six denoting the east, north, west, south, up and down surfaces correspondingly.

The volume integrals in Eq. (2.64) are then approximated using the mean value theorm as

$$\int_\Omega [T]\frac{\partial \mathbf{W}}{\partial t}d\Omega \approx \left([T]\frac{\partial \mathbf{W}}{\partial t}\right)_{i,j,k}\Omega_{i,j,k};$$
$$\int_\Omega \mathbf{S}d\Omega \approx \mathbf{S}_{i,j,k}\Omega_{i,j,k}. \tag{2.65}$$

This suggests that the solution variables stored at the volume center are assumed to be the average values for the control volume and this indeed agrees with the implication of the implicit grid filtering process described in section 2.2.

The surface integral is approximated as

$$\oint_{\partial\Omega} \mathbf{F}_l \vec{e}_l \cdot d\vec{S} \approx \mathbf{C}(\mathbf{W}), \tag{2.66}$$

where

$$\mathbf{C}(\mathbf{W}) = \sum_{\beta=1}^{6} \mathbf{F}_{l\beta} n_{\beta l} S_{\beta}. \tag{2.67}$$

In the above equation the summation convention does not hold for index β which denotes the six surfaces of the control volume. $\mathbf{F}_{l\beta}$ is the value of $\mathbf{F}_l$ on the βth surface of the control volume; $n_{\beta l}$ is the projection of the unit outward normal $\vec{n}_\beta$ of the βth surface $\vec{S}_\beta$ in the l direction; The surface area vector $\vec{S}_\beta = S_\beta \vec{n}_\beta$, where S_β is the magnitude.

The inviscid flux vector on a surface between two control volumes, say the east/west (E/W) surface between (i, j, k) and $(i + 1, j, k)$, is evaluated as

$$\mathcal{F}_{l1} = \mathcal{F}_l \left(\mathbf{W}_{i+1/2,j,k} \right), \tag{2.68}$$

where $\mathbf{W}_{i+1/2,j,k}$ is the value of solution variables on the E/W surface which can be obtained by Eq. (2.73). To compute the viscous and subgrid-scale fluxes, the gradients of $\mathbf{W}$ at the control volume surfaces have to be calculated. The method will be given shortly.

With these approximations, Eq. (2.64) becomes

$$[T]\frac{d\mathbf{W}}{dt}\Omega + \mathbf{C}(\mathbf{W}) = \mathbf{S}\Omega, \tag{2.69}$$

which is an algebraic equation and every function in it depends solely on $\mathbf{W}$ of the main control volume and its six neighboring volumes.

2.4.3 Gradients

To calculate the viscous and subgrid-scale flux vectors, the gradients of u, v, w and T at the control volume surfaces have to be computed. The face based approach is used in this work and the gradients are calculated and stored on the faces of the control volumes.

The gradients of a scalar ϕ are calculated with the Gauss divergence theorem on an auxiliary control volume Ω' as

$$\int_{\Omega'} \nabla\phi d\Omega' = \int_{\partial\Omega'} \phi d\vec{S}'. \tag{2.70}$$

And this equation can be approximated as

$$\nabla\phi\Omega' \approx \sum_{\beta'=1}^{6} \left(\phi \vec{S}' \right)_{\beta'}, \tag{2.71}$$

where β' denotes the six surfaces of the auxiliary control volume.

The auxiliary control volume is constructed such that its faces coincide with the volume centers of the *two* main control volumes whose interface stores the gradients. For example,

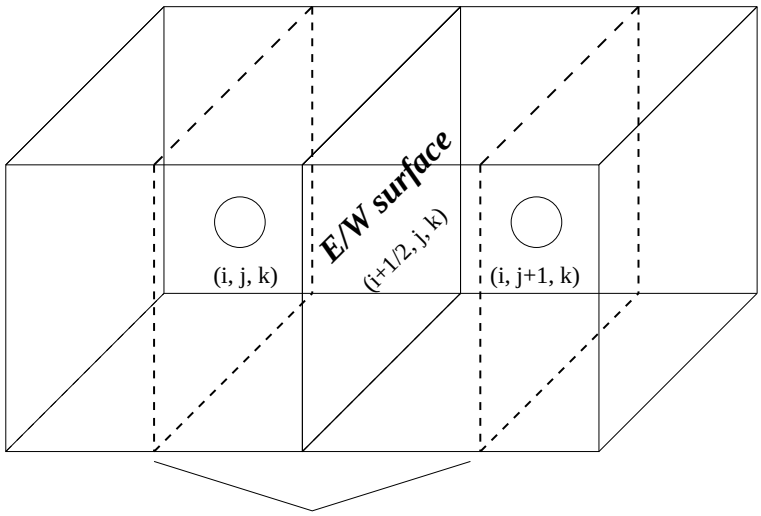

Figure 2.2 Auxiliary control volume for calculation of gradients on east/west (E/W) surfaces of main control volumes

the auxiliary control volume used to calculate the gradients on the east/west (E/W) faces of the main control volume (i, j, k) and $(i+1, j, k)$ is shown in Fig. 2.2. Thus, the volume of the auxiliary control volume is given by

$$\Omega' = \frac{1}{2}(\Omega_{i,j,k} + \Omega_{i+1,j,k}). \tag{2.72}$$

Since we assume the gradient on the surface $(i+1/2, j, k)$ should be the average value over the auxiliary control volume, it can be easily found from Eq. (2.71) that

$$\phi_{i+1/2,j,k} = \alpha_x \phi_{i,j,k} + (1-\alpha_x)\phi_{i+1,j,k}, \tag{2.73}$$

where

$$\alpha_x = \frac{x_{i+1,j,k} - x_{i+1/2,j,k}}{x_{i+1,j,k} - x_{i,j,k}}. \tag{2.74}$$

And the x derivative of ϕ at the E/W surface is

$$\left(\frac{\partial \phi}{\partial x}\right)_{i+1/2,j,k} = \frac{\phi_{i+1,j,k} - \phi_{i,j,k}}{x_{i+1,j,k} - x_{i,j,k}}. \tag{2.75}$$

The determination of the derivatives in the y and z directions at the E/W surface is a little more complex. According to Eq. (2.71), we have

$$\left(\frac{\partial\phi}{\partial y}\right)_{i+1/2,j,k} = \frac{(\phi S)_N - (\phi S)_S}{\Omega'}, \tag{2.76}$$

where subscripts N and S, respectively, denote the north and south surfaces of the *auxiliary* control volume, or alternatively, surfaces $(i+1/2, j+1/2, k)$ and $(i+1/2, j-1/2, k)$. In the same spirit of Eq. (2.73), the values of ϕ on the north and south surfaces of the *main* control volumes can be obtained:

$$\begin{aligned}
\phi_{i,j+1/2,k} &= \alpha_y^+ \phi_{i,j,k} + (1-\alpha_y^+)\phi_{i,j+1,k};\\
\phi_{i+1,j+1/2,k} &= \alpha_y^+ \phi_{i+1,j,k} + (1-\alpha_y^+)\phi_{i+1,j+1,k};\\
\phi_{i,j-1/2,k} &= \alpha_y^- \phi_{i,j-1,k} + (1-\alpha_y^-)\phi_{i,j,k};\\
\phi_{i+1,j-1/2,k} &= \alpha_y^- \phi_{i+1,j-1,k} + (1-\alpha_y^-)\phi_{i+1,j,k}.
\end{aligned} \tag{2.77}$$

where

$$\begin{aligned}
\alpha_y^+ &= \frac{y_{i,j+1,k} - y_{i,j+1/2,k}}{y_{i,j+1,k} - y_{i,j,k}};\\
\alpha_y^- &= \frac{y_{i,j,k} - y_{i,j-1/2,k}}{y_{i,j,k} - y_{i,j-1,k}}.
\end{aligned} \tag{2.78}$$

Since both $\phi_{i,j+1/2,k}$ and $\phi_{i+1,j+1/2,k}$ contribute to $(\phi S)_N$ in Eq. (2.76), the value of ϕ on the north and south surfaces of the *auxiliary* control volume should be determined with an area weighting

$$\begin{aligned}
\phi_{i+1/2,j+1/2,k} &= (1-\alpha_x)\phi_{i,j+1/2,k} + \alpha_x \phi_{i+1,j+1/2,k};\\
\phi_{i+1/2,j-1/2,k} &= (1-\alpha_x)\phi_{i,j-1/2,k} + \alpha_x \phi_{i+1,j-1/2,k}.
\end{aligned} \tag{2.79}$$

The difference between the above equation and Eq. (2.73) should be recognized. With these results, the derivative of ϕ in the y direction on the E/W surface is

$$\left(\frac{\partial\phi}{\partial y}\right)_{i+1/2,j,k} = \frac{\phi_{i+1/2,j+1/2,k} - \phi_{i+1/2,j-1/2,k}}{y_{i,j+1/2,k} - y_{i,j-1/2,k}}. \tag{2.80}$$

In the same manner, the derivative of ϕ in z direction on the E/W surface can be obtained. With the above formalae all flux terms on each control volume surface in Eq. (2.67) can be determined.

2.4.4 Time Derivative Preconditioning

Eq. (2.69) can be solved by common compressible solvers using time marching. A problem related with the solving procedure is that the convergence speed of the compressible solvers becomes very slow at low Mach numbers. This is due to the large differences in the magnitude of system eigenvalues. Eq. (2.59) can be written as

$$[T]\frac{\partial \mathbf{W}}{\partial t} + [A]\frac{\partial \mathbf{W}}{\partial x} = \mathbf{S} - \left[\frac{\partial(\mathbb{F}_1 + \mathscr{F}_1)}{\partial x} + \frac{\partial \mathbf{F}_2}{\partial y} + \frac{\partial \mathbf{F}_3}{\partial z}\right], \tag{2.81}$$

where

$$[A] = \frac{\partial \mathcal{F}_1}{\partial \mathbf{W}}. \tag{2.82}$$

The five eigenvalues of matrix $[T]^{-1}[A]$ are $(u + c, u - c, u, u, u)$ where u is the convective speed and c is the local sound speed. As the Mach number tends to zero, the sound speed goes to infinity and the system is singular. To compute flows at low Mach numbers, one could adopt a fully incompressible scheme. On the other hand, we can modify the compressible formulation so that it will work well for the low Mach number situations. This technique is called "preconditioning" which has been investigated by many researchers such as Turkel (1987), Feng and Merkle (1990), Choi and Merkle (1993), etc. In the current research, the preconditioning method developed by Pletcher and Chen (1993) is used. This involves adding a pseudo-time derivative to the governing equation Eq. (2.69):

$$[\Gamma]\frac{\partial \mathbf{W}}{\partial \tau}\Omega + [T]\frac{d\mathbf{W}}{dt}\Omega + \mathbf{C}(\mathbf{W}) = \mathbf{S}\Omega, \tag{2.83}$$

in which $[\Gamma]$ is the preconditioning matrix and τ is the pseudo time. $[\Gamma]$ is obtained by multiplying the first column of $[T]$ by the gas constant, R, as shown in Appendix A. Now the characteristic of the system is controled by the differences in the eigenvalues of matrix $[\Gamma]^{-1}[A]$, which are much closer to each other than was the case for the original system. As a result, the convergence is improved dramatically for the numerical scheme.

2.4.5 LU-SGS Scheme

Now we describe the numerical scheme used to solve Eq. (2.83), namely, the lower-upper symmetric Gauss-Seidel (LU-SGS) scheme. This approach was originally developed by Yoon

and Jameson (1987) for the Euler and Navier-Stokes equations without preconditioning. Later on Rieger and Jameson (1988) extended it to solve three-dimensional cases. Dailey (1997) applied the scheme to solve the preconditioned Navier-Stokes equations in a finite volume framework. There are several features highlighting the LU-SGS scheme when it is used for a preconditioned system like Eq. (2.83).

First, since a pseudo time step is introduced in Eq. (2.83), the solving process is a dual time marching one. That is, iterating in pseudo time for each step in physical time. When the pseudo time step iterations converge, the governing equations are regarded as being satisfied at this specific physical time step and the program goes ahead to the next physical time step. The whole process will stop when the desired physical time has been reached. This is why the preconditioning can work: the iteration happens for pseudo time steps and the "real" time derivative is only updated with the results of the latest pseudo time step. Thus, the characteristic of the system is only controled by $[\Gamma]^{-1}[A]$.

Second, in practice the pseudo time step $\Delta\tau$ is set to be so large that the pseudo time derivative $[\Gamma]\frac{\Delta \mathbf{W}}{\Delta\tau}$ is extremely small and is ignored without calculation, in fact. However, it is still by every means a pseudo time marching method, only with a negligible pseudo time derivative.

Third, as expected, an *L-D-U* decomposition is needed for the coefficient matrix to facilitate the pseudo time iterations.

Beginning with Eq. (2.83), the flux term $\mathbf{C}(\mathbf{W})$ is split into two parts:

$$\mathbf{C}(\mathbf{W}) = \sum_{\beta=1}^{6} \mathcal{F}_{l\beta} n_{\beta l} S_\beta - \sum_{\beta=1}^{6} (\mathbb{F} - \mathscr{F})_{l\beta} n_{\beta l} S_\beta = \mathbf{E}(\mathbf{W}) - \mathbf{V}(\mathbf{W}), \tag{2.84}$$

where $\mathbf{E}(\mathbf{W})$ is the inviscid flux term and $\mathbf{V}(\mathbf{W})$ includes the viscous and subgrid-scale flux contributions. In the present research the inviscid flux is calculated at each pseudo time step while the viscous and subgrid-scale fluxes are lagged as the values of the previous pseudo time step.

The pseudo time derivative is discretized with a first-order Euler backward difference, and the physical time derivative is discretized with a second-order three point backward difference,

which gives

$$[\Gamma]\frac{\mathbf{W}^{m+1}-\mathbf{W}^{m}}{\Delta\tau}\Omega+[T]\frac{3\mathbf{W}^{n+1}-4\mathbf{W}^{n}+\mathbf{W}^{n-1}}{2\Delta t}\Omega+\mathbf{E}(\mathbf{W}^{n+1})=\mathbf{S}^{m}\Omega+\mathbf{V}(\mathbf{W}^{m}), \quad (2.85)$$

where m denotes the pseudo time step and n the physical time step. As mentioned above, the solution at physical time step $n+1$ can be regarded as being obtained if the pseudo time iterations converge. Thus, $\mathbf{W}^{n+1}$ can be substituted by $\mathbf{W}^{m+1}$ in the iterations. The inviscid flux vector is linearized as

$$\mathbf{E}(\mathbf{W}^{m+1})\approx\mathbf{E}(\mathbf{W}^{m})+\sum_{\beta=1}^{6}\left[([A]_{\beta}n_{\beta x}+[B]_{\beta}n_{\beta y}+[C]_{\beta}n_{\beta z})S_{\beta}(\mathbf{W}^{m+1}-\mathbf{W}^{m})_{\beta}\right], \quad (2.86)$$

where

$$[A]=\left(\frac{\partial\mathcal{F}_1}{\partial\mathbf{W}}\right)^{m};\quad [B]=\left(\frac{\partial\mathcal{F}_2}{\partial\mathbf{W}}\right)^{m};\quad [C]=\left(\frac{\partial\mathcal{F}_3}{\partial\mathbf{W}}\right)^{m}. \quad (2.87)$$

These inviscid flux Jacobians $[A]$, $[B]$ and $[C]$ are given in Appendix A. Consequently, Eq. (2.85) can be written in a "delta"form as

$$\frac{\Omega}{\Delta\tau}\Delta\mathbf{W}+[\Gamma]^{-1}[T]\frac{3\Omega}{2\Delta t}\Delta\mathbf{W}+[\Gamma]^{-1}\sum_{\beta=1}^{6}([A]_{\beta}n_{\beta x}+[B]_{\beta}n_{\beta y}+[C]_{\beta}n_{\beta z})S_{\beta}\Delta\mathbf{W}_{\beta}=-\mathcal{R}^{m}, \quad (2.88)$$

where

$$\begin{aligned}\Delta\mathbf{W}&=\mathbf{W}^{m+1}-\mathbf{W}^{m};\\ \mathcal{R}^{m}&=[\Gamma]^{-1}\mathbf{R}^{m};\\ \mathbf{R}^{m}&=\mathbf{S}^{m}\Omega-\mathbf{C}(\mathbf{W}^{m})-[T]\frac{3\mathbf{W}^{m}-4\mathbf{W}^{n}+\mathbf{W}^{n-1}}{2\Delta t}\Omega.\end{aligned} \quad (2.89)$$

As mentioned before, the pseudo time step $\Delta\tau$ is set to be very large so that the first term in the left hand side can be ignored. With the arrangements of control volumes and coordinates shown in Fig. 2.1, Eq. (2.88) can be simplified as

$$\begin{aligned}&[\Gamma]^{-1}[T]\frac{3\Omega}{2\Delta t}\Delta\mathbf{W}+[\Gamma]^{-1}[([A]\Delta\mathbf{W}S)_1-([A]\Delta\mathbf{W}S)_3\\ &+([B]\Delta\mathbf{W}S)_2-([B]\Delta\mathbf{W}S)_4+([C]\Delta\mathbf{W}S)_5-([C]\Delta\mathbf{W}S)_6)]=-\mathcal{R}^{m}.\end{aligned} \quad (2.90)$$

Equation (2.88) can also be used for non-Cartesian hexahedral volumes, for example, Xu (2003).

The Jacobian matrices can be modified as

$$[A] = [\Gamma][\tilde{A}]; \quad [B] = [\Gamma][\tilde{B}]; \quad [C] = [\Gamma][\tilde{C}]. \tag{2.91}$$

The terms on the surfaces can be approximated as

$$\begin{aligned}
([A]\Delta\mathbf{W})_1 &= ([\Gamma][\tilde{A}]\Delta\mathbf{W})_1 \approx ([\Gamma][\tilde{A}]^+\Delta\mathbf{W})_{i,j,k} + ([\Gamma][\tilde{A}]^-\Delta\mathbf{W})_{i+1,j,k};\\
([A]\Delta\mathbf{W})_3 &= ([\Gamma][\tilde{A}]\Delta\mathbf{W})_3 \approx ([\Gamma][\tilde{A}]^+\Delta\mathbf{W})_{i-1,j,k} + ([\Gamma][\tilde{A}]^-\Delta\mathbf{W})_{i,j,k};\\
([B]\Delta\mathbf{W})_2 &= ([\Gamma][\tilde{B}]\Delta\mathbf{W})_2 \approx ([\Gamma][\tilde{B}]^+\Delta\mathbf{W})_{i,j,k} + ([\Gamma][\tilde{B}]^-\Delta\mathbf{W})_{i,j+1,k};\\
([B]\Delta\mathbf{W})_4 &= ([\Gamma][\tilde{B}]\Delta\mathbf{W})_4 \approx ([\Gamma][\tilde{B}]^+\Delta\mathbf{W})_{i,j-1,k} + ([\Gamma][\tilde{B}]^-\Delta\mathbf{W})_{i,j,k};\\
([C]\Delta\mathbf{W})_5 &= ([\Gamma][\tilde{C}]\Delta\mathbf{W})_5 \approx ([\Gamma][\tilde{C}]^+\Delta\mathbf{W})_{i,j,k} + ([\Gamma][\tilde{C}]^-\Delta\mathbf{W})_{i,j,k+1};\\
([C]\Delta\mathbf{W})_6 &= ([\Gamma][\tilde{C}]\Delta\mathbf{W})_6 \approx ([\Gamma][\tilde{C}]^+\Delta\mathbf{W})_{i,j,k-1} + ([\Gamma][\tilde{C}]^-\Delta\mathbf{W})_{i,j,k},
\end{aligned} \tag{2.92}$$

where

$$\begin{aligned}
[\tilde{A}]^{\pm} &= \frac{1}{2}([\tilde{A}] \pm \left|\lambda_{[\tilde{A}]}\right|[I]);\\
[\tilde{B}]^{\pm} &= \frac{1}{2}([\tilde{B}] \pm \left|\lambda_{[\tilde{B}]}\right|[I]);\\
[\tilde{C}]^{\pm} &= \frac{1}{2}([\tilde{C}] \pm \left|\lambda_{[\tilde{C}]}\right|[I]).
\end{aligned} \tag{2.93}$$

λ is the maximum eigenvalues of the corresponding flux Jacobian matrix and $[I]$ is the identity matrix. From the above equations, it is obvious that

$$\begin{aligned}
[\Gamma][\tilde{A}]^+ - [\Gamma][\tilde{A}]^- &= \left|\lambda_{[\tilde{A}]}\right|[\Gamma];\\
[\Gamma][\tilde{B}]^+ - [\Gamma][\tilde{B}]^- &= \left|\lambda_{[\tilde{B}]}\right|[\Gamma];\\
[\Gamma][\tilde{C}]^+ - [\Gamma][\tilde{C}]^- &= \left|\lambda_{[\tilde{C}]}\right|[\Gamma].
\end{aligned} \tag{2.94}$$

Equations (2.93), (2.94) are substituted into Eq. (2.90). The result is written as

$$([L] + [D] + [U])\Delta\mathbf{W} = -\mathcal{R}, \tag{2.95}$$

where

$$[L] = -[\Gamma]^{-1}_{i,j,k}\left[([\Gamma][\tilde{A}]^+)_{i-1,j,k}S_3 + ([\Gamma][\tilde{B}]^+)_{i,j-1,k}S_4 + ([\Gamma][\tilde{C}]^+)_{i,j,k-1}S_6\right];$$

$$
\begin{aligned}
[D] &= ([\Gamma]^{-1}[T])_{i,j,k}\frac{3\Omega}{2\Delta t} + [\Gamma]^{-1}_{i,j,k}\Big[([\Gamma][\tilde{A}]^{+})_{i,j,k}S_1 - ([\Gamma][\tilde{A}]^{-})_{i,j,k}S_3 \\
&+([\Gamma][\tilde{B}]^{+})_{i,j,k}S_2 - ([\Gamma][\tilde{B}]^{-})_{i,j,k}S_3 + ([\Gamma][\tilde{C}]^{+})_{i,j,k}S_5 - ([\Gamma][\tilde{C}]^{-})_{i,j,k}S_6\Big]; \qquad (2.96)\\
[U] &= -[\Gamma]^{-1}_{i,j,k}\Big[([\Gamma][\tilde{A}]^{-})_{i+1,j,k}S_1 + ([\Gamma][\tilde{B}]^{-})_{i,j+1,k}S_2 + ([\Gamma][\tilde{C}]^{-})_{i,j,k+1}S_5\Big].
\end{aligned}
$$

It can be observed that the matrix $[L]$ only depends on the lower points while $[U]$ only depends on the upper points. Note Eq. (2.95) is written in this way for brevity, in fact $\Delta\mathbf{W}$ should be incorporated into each term with appropriate values. For example,

$$
[L]\Delta\mathbf{W} = -[\Gamma]^{-1}_{i,j,k}\Big[([\Gamma][\tilde{A}]^{+}\Delta\mathbf{W})_{i-1,j,k}S_3 + ([\Gamma][\tilde{B}]^{+}\Delta\mathbf{W})_{i,j-1,k}S_4 + ([\Gamma][\tilde{C}]^{+}\Delta\mathbf{W})_{i,j,k-1}S_6\Big]. \qquad (2.97)
$$

The same understanding also holds for the following Eqs. (2.100) and (2.101).

Due to Eq. (2.95) and the fact that for Cartesian grids,

$$
S_1 = S_3 = S_{13}; \quad S_2 = S_4 = S_{24}; \quad S_5 = S_6 = S_{56}, \qquad (2.98)
$$

we have

$$
[D] = ([\Gamma]^{-1}[T])_{i,j,k}\frac{3\Omega}{2\Delta t} + \Big[(\Big|\lambda_{[\tilde{A}]}\Big|)_{i,j,k}S_{13} + (\Big|\lambda_{[\tilde{B}]}\Big|)_{i,j,k}S_{24} + (\Big|\lambda_{[\tilde{C}]}\Big|)_{i,j,k}S_{56}\Big]\,[I]. \qquad (2.99)
$$

Due to the nature of the preconditioning matrix we chose, the product $[\Gamma]^{-1}[T]$ is a diagonal matrix so the matrix $[D]$ is also diagonal. To efficiently solve Eq. (2.95), it can be approximated as

$$
([L] + [D])[D]^{-1}([D] + [U])\Delta\mathbf{W} = -\mathcal{R}, \qquad (2.100)
$$

and solved in three steps as follows:

$$
\begin{aligned}
&\text{Step 1}: \textit{let } \mathbf{X} = [D]^{-1}([D] + [U])\Delta\mathbf{W}, \textit{ then}\\
&\qquad ([L] + [D])\mathbf{X} = -\mathcal{R}.\\
&\qquad \textit{Thus, } \mathbf{X} = [D]^{-1}(-\mathcal{R} - [L]\mathbf{X});\\
&\text{Step 2}: \textit{since } [D]^{-1}([D] + [U])\Delta\mathbf{W} = \mathbf{X}, \textit{ we have} \qquad (2.101)\\
&\qquad \Delta\mathbf{W} = \mathbf{X} - [D]^{-1}[U]\Delta\mathbf{W};\\
&\text{Step 3}: \mathbf{W}^{m+1} = \mathbf{W}^{m} + \Delta\mathbf{W}.
\end{aligned}
$$

In step 1, the calculation is carried out on $i+j+k = constant$ planes from the lower corner, $(i,j,k) = (1,1,1)$, to the upper corner, $(i,j,k) = (ni, nj, nk)$, of the grid, where ni, nj, nk are the number of control volumes in the x, y, and z directions, respectively. Through this manner, $[L]\mathbf{X}$ are always known during the process and this is why it can be put on the right hand side of the equation. Similarly, $[U]\Delta\mathbf{W}$ is also always known during the sweeping from upper corner to lower corner in step 2 and moved to the right hand side. Since $[D]$ is diagonal, the inversion of $[D]$ in the above steps requires only a trivial amount of work and this is one reason that the LU-SGS scheme is so efficient compared to other implicit schemes. For the LU-SGS scheme, boundary conditions are handled by setting $\Delta\mathbf{W} = 0$ at ghost volumes and explicitly setting $\mathbf{W}$ at the beginning of each iteration. More details are given in the following section.

2.5 Boundary Conditions

Boundary conditions are enforced by using "ghost" volumes, as depicted in Fig. 2.3. The ghost volumes are images of the corresponding near boundary control volumes, that is, they are symmetrically located with respect to the boundary. According to Eq. (2.73), we have

$$\phi_b = \frac{1}{2}(\phi_{nb} + \phi_g), \tag{2.102}$$

where ϕ_b is the value of variable ϕ at the boundary, ϕ_{nb} the value at the near boundary control volume and ϕ_g the value at the ghost volume. Since ϕ_{nb} is updated in each iteration, ϕ_g can be set up at the beginning of the next iteration according to ϕ_{nb} so that a certain boundary value ϕ_b can be enforced. Sometimes it is the normal derivative which is enforced at the boundary. In such cases, Eq. (2.75) should be used to determine the ghost volume values:

$$\phi_g = \phi_{nb} + \left(\frac{\partial\phi}{\partial n}\right)_b \Delta l, \tag{2.103}$$

where Δl is the distance between the volume centers.

Some most commonly used boundary conditions in DNS and LES are described here as examples.

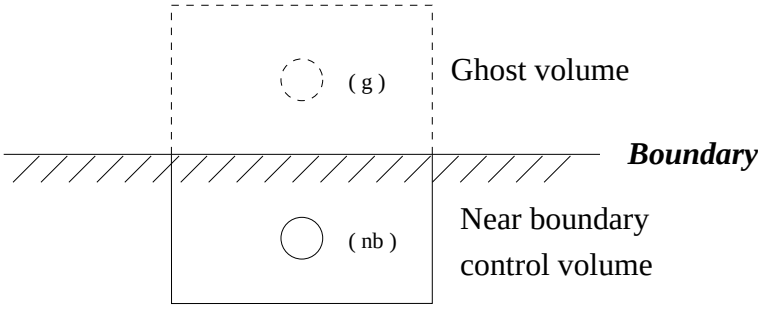

Figure 2.3 Ghost volumes for boundary conditions

2.5.1 Solid Wall Boundary Conditions

On solid walls, the no slip condition has to be enforced for all velocity components as

$$u_g = -u_{nb}; \quad v_g = -v_{nb}; \quad w_g = -w_{nb}. \tag{2.104}$$

The pressure condition at a solid wall is set as $p_g = p_{nb}$ to fulfill the approximate boundary condition $\partial p/\partial n = 0$.

For cases involving heat transfer, two different temperature conditions can be applied at a solid wall: fixed wall temperature or fixed wall heat flux. A desired wall temperature, T_w, is enforced by setting $T_g = 2T_w - T_{nb}$. To enforce a fixed non-dimensional wall heat flux, q_w, at the wall, the temperature at the ghost volume is given by

$$T_g = T_{nb} + \frac{q_w RePr}{\mu_w}\Delta l. \tag{2.105}$$

Note here the definition of q_w is different from that of Eq. (2.10). The non-dimensional *wall* heat flux q_w is given in terms of the dimensional quantities as

$$q_w = \frac{q_w^*}{\rho_{ref} U_{ref} T_{ref} c_p^*}. \tag{2.106}$$

2.5.2 Periodic Boundary Conditions

Periodic boundary conditions have been extensively used in DNS and LES of incompressible or constant property flows. This condition is especially suitable for fully developed homogeneous flow since the flow fields at inflow and outflow are considered as statistically the same provided they are apart from each other far enough. A simple example is the fully developed

flow in an uniform isothermal pipe. For periodic boundary conditions, the computational domain can be thought of as repeating itself infinitely. With the method of ghost volumes, this can be done by copying values of the variables of the near outflow/inflow boundary control volume to the ghost volume at the inflow/outflow boundary. This idea is shown in Fig. 2.4

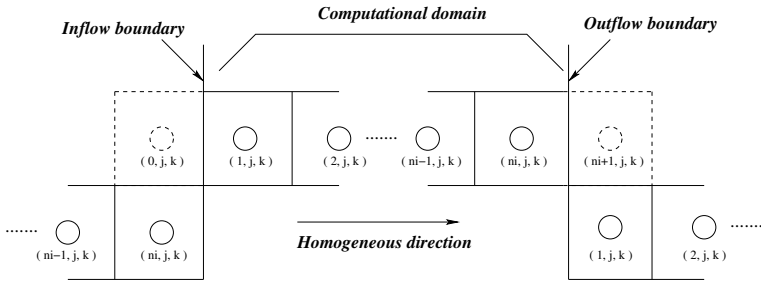

Figure 2.4 Periodic boundary conditions

in which the flow direction is the x direction. And the periodicity suggests that at inflow

$$\begin{aligned}(\rho u)_g &= (\rho u)_{0,j,k} = (\rho u)_{ni,j,k};\\ v_g &= v_{0,j,k} = v_{ni,j,k};\\ w_g &= w_{0,j,k} = w_{ni,j,k};\\ T_g &= T_{0,j,k} = T_{ni,j,k}.\end{aligned} \tag{2.107}$$

However, the pressure is not periodic in the flow direction due to the negative, linear streamwise pressure gradient which drives the flow. A common practice is to decompose the pressure into pressure gradient term and periodic pressure term as

$$p(x, y, z, t) = \beta x + p_p(x, y, z, t), \tag{2.108}$$

where β is the streamwise pressure gradient. Since the pressure gradient term is much smaller than the periodic pressure term for moderate Reynolds numbers, the pressure p may be replaced with p_p in the governing equations and at the same time the pressure gradient enters the right hand side of the u-momentum equation as a "forcing function". This forcing function is determined by requiring that the mean mass flow rate reach a desired constant $\left(\frac{\dot{m}}{A_c}\right)^0$. Following the approach of Benocci and Pinelli (1990), β is calculated dynamically at each

physical time step as

$$\beta^{n+1} = \beta^n - \frac{1}{\Delta t}\left[\left(\frac{\dot{m}}{A_c}\right)^0 - 2\left(\frac{\dot{m}}{A_c}\right)^n + \left(\frac{\dot{m}}{A_c}\right)^{n-1}\right], \tag{2.109}$$

where A_c is the cross-flow area.

Though widely used and proven robust, the periodic boundary conditions have some obvious shortcomings. First, it cannot be used for the developing flows; second, it should not be used in the heat transfer cases with property variations, including density variations, since the periodicity assumptions are no longer valid for pressure, temperature, and velocity; third, it can hardly be applied to non-uniform geometries, for example, the flow past a backward facing step; four, it cannot be used if the flow is intrinsically non-homogeneous, for example, free shear or jet flows. The second problem can be cleared up by the step-periodic boundary conditions which will be mentioned below. However, different strategies should be tried before the other problems can be solved. This issue will be discussed in the next chapter.

2.5.3 Step-periodic Boundary Conditions

For cases with property variations due to the heat addition or even pressure changes when an ideal gas equation of state is used to determine the density, the temperature and properties change continually. As a result, the velocity and temperature are no longer periodic. Dailey (1997) had found that the following conditions held approximately in the downstream region ($x > 5$) of a two-dimensional, constant heat flux channel:

$$\begin{aligned} (\rho u)(0,y) &= (\rho u)(L_x,y); \\ v(0,y) &= v(L_x,y); \\ w(0,y) &= w(L_x,y); \\ p_p(0,y) &= p_p(L_x,y); \\ T(0,y) &= T(L_x,y) - \Delta T_x, \end{aligned} \tag{2.110}$$

where L_x is the length of the channel in the streamwise direction and the temperature difference ΔT_x is given by integrating the energy equation.

CHAPTER 3. INCORPORATION OF NSCBC INTO LU-SGS SCHEME

3.1 Introduction

A large number of direct and large eddy simulations have used periodic boundary conditions in one or more directions. With the assumption of periodicity, the computational domain is thought of as being repeated infinitely. This condition can be easily applied and has been proven robust. However, the periodicity assumption cannot be justified in a wide range of situations. As indicated in the last chapter, such situations include the developing flows, heat transfer cases with property variations, non-uniform geometries, free shear or jet flows and more. It is also very common in flow simulations that only a limited computational domain is considered due to the computer resource limit. This means that one has to "cut off" the domain which is not of primary interest. In such cases artificial computational boundaries are introduced where the domain is truncated and artificial boundary conditions (ABC) should be applied there. Abundant amounts of literature have dealt with this subject for more than 20 years. It has been shown that a good ABC should lead to a well-posed mathematical problem. To explore this aspect in detail is beyond the scope of this thesis, and the interested reader is referred to reviews by Givoli (1991), Tsynkov (1998), Hagstrom (1999) and Colonius (2004). A noteworthy comment is that a well-posed ABC does not always give satisfactory numerical results. For instance, Oliger and Sundstrom (1978) proved that imposing the pressure on a subsonic compressible outflow was a well-posed problem. However, it is well known that such a crude boundary condition gives rise to strong reflections in the flow which can cause the numerical solution to oscillate or even blow up (Anderson, 1995).

Another way to define ABC is the concept of non-reflecting boundary conditions (NRBC) which inhibit the reflection of disturbances on the boundary. As just mentioned, many mathe-

matically sound boundary conditions are not *numerically* feasible for reasons of wave reflections which cause the solution to oscillate or even blow up. The physics behind this numerical phenomenon is that, the mathematically sound boundary conditions, fixed pressure at a subsonic compressible outflow for example, are usually only good for the *steady-state*. In an unsteady flow, finite compression and expansion waves travel up and down the stream. As a result, all the flow variables, including pressure, fluctuate with time. Thus, though totally proper as the flow approaches the steady-state, the boundary condition may be physically improper during the unsteady process. Since numerical simulations are essentially initial-boundary value problems, which means the satisfactory final solution can only be reached by improving from somewhat unsatisfactory initial guess, all numerical simulations are "unsteady" processes in this view and proper time-accurate boundary conditions are needed so that the final solution can be reached smoothly. In simulations of turbulent flows, this need is more imperative because turbulence is intrinsically irregular and fluctuating. Without boundary conditions that can fluctuate appropriately with time, the numerical simulation of turbulence can hardly reflect the real physics, let alone giving reasonable results.

One way to obtain such boundary conditions follows from the classical method of characteristics solution (Hedstrom, 1979). It is based on the fact that a hyperbolic system can be decomposed into wave modes propagating along the characteristic directions, which can be going into or out of the computational domain. The outgoing waves are completely determined by the interior solution and no boundary condition can be applied to them. It is waves entering the domain from outside its boundary, together with the state in the interior, that determines the time evolution of the system. For the case of one-dimensional flow, it is possible to locally identify and decouple the outgoing and incoming waves. Then, we can enforce the boundary condition we wish on the incoming waves. Boundary conditions obtained this way are named characteristic boundary conditions (CBC).

Since the waves reflected back from the boundary will cause numerical problems, it is attractive to cancel all waves entering the computational domain. Early work of Hedstrom (1979) and Thompson (1987) use this principle. However, this non-reflecting boundary con-

dition may violate the physics. For instance, there should exist one incoming wave that enters the computational domain through a subsonic outflow boundary and should not be suppressed. From this consideration, Rudy and Strikwerda (1980) improved this method to find a partially non-reflecting boundary condition. They gave a way to specify the static pressure through the outflow boundary of a subsonic flow. This method was adopted in Poinsot and Lele (1992). A notable physical explanation and improvement of this method has been made by Liu (2006). Finally, Thompson (1990) derived a force-free boundary condition, which sets to zero the sum of all forces acting on the fluid in the direction normal to the boundary, so that a fluid element at the boundary is simply advected outward at the fluid velocity.

The method initiated by Thompson (1987, 1990), which will be called Navier-Stokes characteristic boundary condition (NSCBC), was further developed by Poinsot and Lele (1992). Both of these authors based their method on the local one-dimensional inviscid (LODI) assumption, which presumes the one-dimensional characteristic analysis can be performed in multidimensional cases by ignoring the transverse and viscous terms. Of course, this assumption is not exact and becomes a defect of the method for the lack of true multidimensionality. Kim and Lee (2000, 2004) overcame this problem by treating the transverse and viscous terms as source terms in the characteristic analysis.

Besides the NSCBC method, other numerical boundary conditions have been proposed. These proposals include the perfectly matched layer (Berenger, 1994; Hu, 1996), the fringe method (Spalart, 1988), the spatial windowing method (Guo et al., 1994), the super-grid-scale model (Colonius and Ran, 2002), etc.

This chapter will be devoted to showing how the NSCBC method can be incorporated into the LU-SGS scheme. Through a literature search it appears that the application of NSCBC in LES and DNS is still not widespread. Some limited examples are Ravikanth and Pletcher (2002) and Yahyaoui et al. (2001). The reason is that NSCBC has to be incorporated into the original numerical scheme rather than being used separately (Anderson, 1995). The LES and DNS codes tend to use very sophisticated numerical algorithms which makes such incorporations somewhat complex and tricky. Hopefully the current presentation will help in

some measure.

3.2 Navier-Stokes Characteristic Boundary Conditions

3.2.1 Transformation to Characteristic Form

The starting point of analysis for the development of boundary conditions is Eq. (2.81).

$$[T]\frac{\partial \mathbf{W}}{\partial t} + [A]\frac{\partial \mathbf{W}}{\partial x} = \mathbf{S} - \left[\frac{\partial(\mathbb{F}_1 + \mathscr{F}_1)}{\partial x} + \frac{\partial \mathbf{F}_2}{\partial y} + \frac{\partial \mathbf{F}_3}{\partial z}\right] = \mathbf{S}^*. \tag{3.1}$$

Recall that $[T]$ is the transformation matrix between the conservative and the primitive variables. $[A]$ is the inviscid flux Jacobian which is $[A] = \frac{\partial \mathcal{F}_1}{\partial \mathbf{W}}$ and $\mathbf{F}_i$ are the flux vectors. Notice that the highlighting of the x direction in the above governing equation serves only as an example. The choice depends on which direction of wave propagation is of interest. For example, if one wants to impose NSCBC at the outlet of a duct as shown in Fig. 3.1, the equation should be recast in the x direction. If instead one hopes to apply NSCBC to the solid wall,

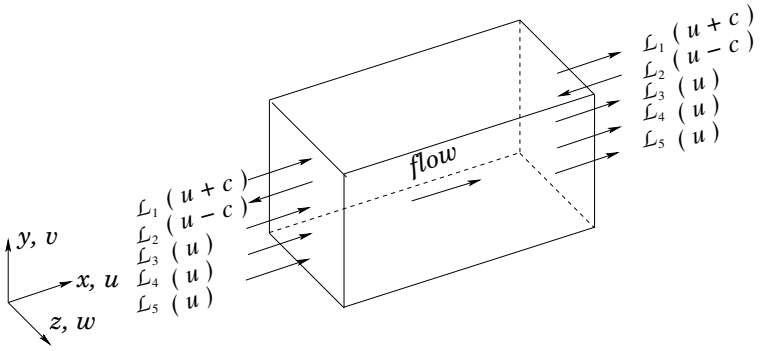

Figure 3.1 Sketch of a square duct for the characteristic analysis

then it is the y and/or z directions which should be modified.

By multiplying by $[T]^{-1}$ the above equation becomes

$$\frac{\partial \mathbf{W}}{\partial t} + [\Pi]\frac{\partial \mathbf{W}}{\partial x} = [T]^{-1}\mathbf{S}^*, \tag{3.2}$$

where $[\Pi] = [T]^{-1}[A]$. Let $[\Pi] = [S][\Lambda][S]^{-1}$, where $[\Lambda]$ is a diagonal matrix with elements that are eigenvalues of $[T]^{-1}[A]$, then the rows of $[S]^{-1}$ are the corresponding eigenvectors.

Multiplying Eq. (3.2) by $[S]^{-1}$, we have

$$[S]^{-1}\frac{\partial \mathbf{W}}{\partial t} + [\Lambda][S]^{-1}\frac{\partial \mathbf{W}}{\partial x} = [S]^{-1}[T]^{-1}\mathbf{S}^*. \tag{3.3}$$

We define

$$[\Xi] = [\Lambda][S]^{-1}, \tag{3.4}$$

and

$$\mathcal{L} = [\Xi]\frac{\partial \mathbf{W}}{\partial x} \tag{3.5}$$

which is the characteristic wave vector. It bears this name because the components of Eq. 3.3 are of the form of a wave equation:

$$l_i\left(\frac{\partial \mathbf{W}}{\partial t} + \lambda_i\frac{\partial \mathbf{W}}{\partial x}\right) = l_i([T]^{-1}\mathbf{S}^*), \tag{3.6}$$

where l_i are rows of $[S]^{-1}$, that is, the left eigenvectors; λ_i are the corresponding eigenvalues. It can be observed that in fact $\mathcal{L}$ is another expression for the convection terms, and each component of $\mathcal{L}$ is either an incoming or an outgoing wave, depending on the sign of its eigenvalue. For an ideal gas, the five eigenvalues are $(u + c, u - c, u, u, u)$ where c is the local sound speed. In a subsonic flow, $|u| < c$, then there should exist at least one incoming wave at the outlet and typically four incoming waves at the inlet, as shown in Fig. 3.1. The outgoing waves can be directly computed from Eq. (3.5) with a one-sided difference that uses grid points on the interior side of the boundary. Though the accuracy of the spatial derivatives is often decreased (centered differences are replaced by one-sided differences in our case), theoretical analysis (Gustafsson, 1975) shows that if the order of approximation near the boundary is equal to the scheme order minus one, the overall accuracy of the scheme is not affected. However, the incoming waves cannot be evaluated this way. This can be explained in terms of numerical evaluation of spatial derivatives. Most numerical schemes are stable for upwind differencing and unstable for downwind differencing. Thus, estimating the incoming waves with one one-sided difference requires downwind differencing and should be avoided. In fact, all incoming waves at a given boundary should be obtained from the choice of the physical boundary conditions imposed on this boundary and the outgoing waves. This process can by symbolically expressed

as

$$\mathcal{L}_i = f(\mathbf{W}_p, \mathcal{L}_o), \tag{3.7}$$

where subscripts i, o, p denote incoming waves, outgoing waves and physical boundary conditions, respectively. Usually we need to use the following equation, which can be easily obtained from Eq. (3.3), to deduce the relation between different $\mathcal{L}_i$s, especially when physical boundary conditions are involved.

$$\frac{\partial \mathbf{W}}{\partial t} + \mathcal{D} = [T]^{-1}\mathbf{S}^*, \tag{3.8}$$

where $\mathcal{D} = [S]\mathcal{L}$.

As a result of the above process, a new matrix $[\Xi']$ can be obtained by replacing some rows of the original matrix $[\Xi]$ with the linear combinations of the other rows. New terms may also be introduced into the source term of the equation. Correspondingly, Eq. (3.3) becomes

$$[S]^{-1}\frac{\partial \mathbf{W}}{\partial t} + [\Xi']\frac{\partial \mathring{\mathbf{W}}}{\partial x} = [S]^{-1}[T]^{-1}\mathring{\mathbf{S}}^{*\prime}. \tag{3.9}$$

Here the accent $\mathring{(\cdot)}$ means the x derivatives have to be evaluated with one-sided differences and the prime added to the source term means some new terms may be introduced.

After the boundary conditions are applied to the incoming waves, the equation can be transformed to the familiar form like Eq. (3.1) by multiplying Eq. (3.9) with $[T][S]$:

$$[T]\frac{\partial \mathbf{W}}{\partial t} + [A']\frac{\partial \mathring{\mathbf{W}}}{\partial x} = \mathring{\mathbf{S}}^{*\prime}, \tag{3.10}$$

where $[A'] = [T][S][\Xi']$ and this equation should be applied to the considered boundary.

3.2.2 Local One-Dimensional Inviscid Assumption

The matrices involved in the procedure described in the last section are listed in Appendix B. Notice they are only valid for the present governing equations, which are for an ideal gas and a gas constant R has been multiplied throughout. With the results shown in Appendix B,

we have

$$\mathcal{L} = \begin{bmatrix} \mathcal{L}_1 \\ \mathcal{L}_2 \\ \mathcal{L}_3 \\ \mathcal{L}_4 \\ \mathcal{L}_5 \end{bmatrix} = \begin{bmatrix} (u+c)\frac{(\gamma-1)T}{2}(\frac{1}{\gamma p}\frac{\partial p}{\partial x} + \frac{1}{c}\frac{\partial u}{\partial x}) \\ (u-c)\frac{(\gamma-1)T}{2}(\frac{1}{\gamma p}\frac{\partial p}{\partial x} + \frac{1}{c}\frac{\partial u}{\partial x}) \\ u\left[\frac{\partial T}{\partial x} - \frac{(\gamma-1)T}{\gamma p}\frac{\partial p}{\partial x}\right] \\ u\frac{\partial v}{\partial x} \\ u\frac{\partial w}{\partial x} \end{bmatrix}; \quad \mathcal{D} = \begin{bmatrix} \mathcal{D}_1 \\ \mathcal{D}_2 \\ \mathcal{D}_3 \\ \mathcal{D}_4 \\ \mathcal{D}_5 \end{bmatrix} = \begin{bmatrix} \frac{p}{T}\frac{\gamma}{\gamma-1}(\mathcal{L}_1 + \mathcal{L}_2) \\ \frac{c}{(\gamma-1)T}(\mathcal{L}_1 - \mathcal{L}_2) \\ \mathcal{L}_4 \\ \mathcal{L}_5 \\ \mathcal{L}_1 + \mathcal{L}_2 + \mathcal{L}_3 \end{bmatrix}. \tag{3.11}$$

And by virtue of Eq. (3.8), $\mathcal{D}$ is related to the time derivatives of the primitive variables which can be subject to physical boundary conditions. One major simplification is reached by using the so-called local one-dimensional inviscid (LODI) assumption, which argues that the source term on the right hand side of Eq. (3.8) can be ignored for the current purpose. In terms of the primitive variables we chose, this LODI system is

$$\frac{\partial p}{\partial t} + \frac{p}{T}\frac{\gamma}{\gamma-1}(\mathcal{L}_1 + \mathcal{L}_2) = 0; \tag{3.12}$$

$$\frac{\partial u}{\partial t} + \frac{c}{(\gamma-1)T}(\mathcal{L}_1 - \mathcal{L}_2) = 0; \tag{3.13}$$

$$\frac{\partial v}{\partial t} + \mathcal{L}_4 = 0; \tag{3.14}$$

$$\frac{\partial w}{\partial t} + \mathcal{L}_5 = 0; \tag{3.15}$$

$$\frac{\partial T}{\partial t} + \mathcal{L}_1 + \mathcal{L}_2 + \mathcal{L}_3 = 0. \tag{3.16}$$

Most physical boundary conditions have a counterpart LODI relation. For example, imposing a constant inlet pressure should be accomplished (from Eq. (3.12)) by setting $\mathcal{L}_2 = -\mathcal{L}_1$ to fix the amplitude variation of the pressure wave entering the domain.

The previous relations may be combined to express the time derivatives of other quantities of interest. For instance

$$\frac{\partial \rho}{\partial t} + \frac{\rho}{T}\left[\frac{1}{\gamma-1}(\mathcal{L}_1 + \mathcal{L}_2) - \mathcal{L}_3\right] = 0; \tag{3.17}$$

$$\frac{\partial(\dot{m}/A_c)}{\partial t} + \frac{\rho c}{T}\left\{\frac{1}{\gamma-1}[(1+\mathcal{M})\mathcal{L}_1 - (1-\mathcal{M})\mathcal{L}_2] - \mathcal{M}\mathcal{L}_3\right\} = 0, \tag{3.18}$$

where $\frac{\dot{m}}{A_c} = \rho u$ is the local mass flow rate and $\mathcal{M} = u/c$ is the local Mach number.

Table 3.1 Number of physical boundary conditions needed for well-posedness of 3-D Euler and Navier-Stokes equations

Boundary Conditions	**Euler**	**Navier-Stokes**
Subsonic inflow	4	4/5
Subsonic outflow	1	4
no-slip wall	-	4

Other forms of LODI relations may be useful when boundary conditions are imposed in terms of gradients. All gradients normal to the boundary may be expressed as functions of the $\mathcal{L}_i$s:

$$\frac{\partial p}{\partial x} = \frac{p\gamma}{T(\gamma-1)}\left[\frac{\mathcal{L}_1}{u+c} + \frac{\mathcal{L}_2}{u-c}\right]; \tag{3.19}$$

$$\frac{\partial u}{\partial x} = \frac{c}{T(\gamma-1)}\left[\frac{\mathcal{L}_1}{u+c} - \frac{\mathcal{L}_2}{u-c}\right]; \tag{3.20}$$

$$\frac{\partial T}{\partial x} = \frac{\mathcal{L}_1}{u+c} + \frac{\mathcal{L}_2}{u-c} + \frac{\mathcal{L}_3}{u}. \tag{3.21}$$

3.2.3 NSCBC Strategy for Euler and Navier-Stokes Equations

In this section we simply copy two tables (Table 3.2, 3.3) from Poinsot and Lele (1992), which list several choices of physical boundary conditions for the 3-D Euler and Navier-Stokes equations. From theoretical studies (Strikwerda, 1977; Oliger and Sundström, 1978), we know a certain number of physical boundary conditions are needed for the well-posedness of these two types of equations. The results are shown in Table 3.1.

We will discuss how the above general theory can be fit to special physical boundary conditions in the subsequent sections.

3.2.4 Subsonic Inflow Boundary Conditions

At a subsonic inflow boundary, four characteristic waves, $\mathcal{L}_1$, $\mathcal{L}_3$, $\mathcal{L}_4$, $\mathcal{L}_5$ are entering the domain while $\mathcal{L}_2$ is leaving the domain. Four physical boundary conditions are needed and many different choices exist. For example, we can impose u, v, w and T which is typical when we wish to control the inlet shear. Note these quantities are not necessarily constants but can

Table 3.2 Physical inflow boundary conditions for 3-D flows for Euler and Navier-Stokes equations

	Euler		**Navier-Stokes**		
	Inviscid conditions	Number of conditions	Inviscid conditions	Viscous conditions	Total number of conditions
			4	0	4
SI 1 No well-posed-ness proof for Euler or NS	u_1 imposed u_2 imposed u_3 imposed T imposed	4	u_1 imposed u_2 imposed u_3 imposed T imposed		Special case: Euler and NS need same conditions
			4	1	5
SI 2 Well-posed for Euler. No proof for NS	u_1 imposed u_2 imposed u_3 imposed ρ imposed	4	u_1 imposed u_2 imposed u_3 imposed ρ imposed	$\frac{\partial \tau_{11}}{\partial x_1} = 0$	
			4	1	5
SI 3 Well-posed for Euler and NS	$u_1 - 2c/(\gamma - 1)$ imposed u_2 imposed u_3 imposed s imposed	4	$u_1 - 2c/(\gamma - 1)$ imposed u_2 imposed u_3 imposed s imposed	$\frac{\partial \tau_{11}}{\partial x_1} = 0$	Did not work (Unstable)
			4	1	5
SI 4 Non-reflecting No proof for Euler and NS	$\mathcal{L}_1 = 0$ $\mathcal{L}_3 = 0$ $\mathcal{L}_4 = 0$ $\mathcal{L}_5 = 0$	4	$\mathcal{L}_1 = 0$ $\mathcal{L}_3 = 0$ $\mathcal{L}_4 = 0$ $\mathcal{L}_5 = 0$	$\frac{\partial \tau_{11}}{\partial x_1} = 0$	

Table 3.3 Physical outflow/wall boundary conditions for 3-D flows for Euler and Navier-Stokes equations

	Euler		**Navier-Stokes**		
	Inviscid conditions	Number of conditions	Inviscid conditions	Viscous conditions	Total number of conditions
			1	3	4
SO 1 Subsonic non-reflecting outflow	p at infinity is imposed	1	p at infinity is imposed	$\frac{\partial \tau_{12}}{\partial x_1} = 0$ $\frac{\partial \tau_{13}}{\partial x_1} = 0$ $\frac{\partial q_1}{\partial x_1} = 0$	
			1	3	4
SO 2 Subsonic reflecting outflow	p is imposed	1	p is imposed	$\frac{\partial \tau_{12}}{\partial x_1} = 0$ $\frac{\partial \tau_{13}}{\partial x_1} = 0$ $\frac{\partial q_1}{\partial x_1} = 0$	
			4	0	4
W 1 Isothermal no-slip wall			$u_1 = 0$ $u_2 = 0$ $u_3 = 0$ $T = cte$		
			3	1	4
W 2 Adiabatic no-slip wall			$u_1 = 0$ $u_2 = 0$ $u_3 = 0$	$q_1 = 0$	
			1	3	4
W 3 Adiabatic slip wall	$u_1 = 0$	1	$u_1 = 0$	$\tau_{12} = 0$ $\tau_{13} = 0$ $q_1 = 0$	

be changing with time. This is common in simulations of turbulence where flow fluctuations should be introduced. Since $\mathcal{L}_2$ is an outgoing wave, it can be calculated by interior points and one-sided differences. The other four unkown incoming waves then are computed from Eqs. (3.13) to (3.16) in terms of $\mathcal{L}_2$ and time derivatives of u, v, w and T, which are known.

3.2.5 Subsonic Outflow Boundary Conditions

For subsonic flow at exit, there is only one incoming wave, namely $\mathcal{L}_2$, which needs special treatment. The conventional method to provide a well-posed problem is to enforce $p = p_\infty$ at the outflow boundary. This treatment will however create acoustic wave reflections which may contaminate the flow solutions. On the other hand, a perfect non-reflecting boundary condition imposed by setting $\mathcal{L}_2 = 0$ is also problematic because there is nothing to prevent the pressure from drifting. A clever solution to this dilemma is the partial-reflecting boundary condition proposed by Rudy and Strikwerda (1980) who modified the LODI relation for pressure, Eq. (3.12), a little

$$\frac{\partial p}{\partial t} + \frac{p}{T}\frac{\gamma}{\gamma - 1}(\mathcal{L}_1 + \mathcal{L}_2) + \alpha(p - p_\infty) = 0, \tag{3.22}$$

where α is an adjustable parameter. From this equation we can find

$$\mathcal{L}_2 = \mathcal{K}(p - p_\infty) - \mathcal{L}_1, \tag{3.23}$$

where $\mathcal{K}$ is determined by $\mathcal{K} = \sigma(1 - \mathcal{M}^2)c/L$. The preferred range for constant σ is $0.2 - 0.5$. L is the characteristic length of the domain and $\mathcal{M}$ is the maximum Mach number in the flow field. A notable physical explanation and improvement of this formula has been made by Liu (2006).

3.2.6 Adiabatic and Isothermal Wall Boundary Conditions

From Table 3.3, it can be seen at an adiabatic wall, all velocity components should vanish and the heat flux is zero. LODI relations (3.13), (3.14), and (3.15) show that $\mathcal{L}_2 = \mathcal{L}_1$ and $\mathcal{L}_4 = \mathcal{L}_5 = 0$. $\mathcal{L}_3$ also is zero because the normal velocity is zero.

For an isothermal wall, it is of interest to observe that $\mathcal{L}_2$ should be equal to $\mathcal{L}_1$ according to Eq. (3.13), however, from Eq. (3.16), $\mathcal{L}_2$ should be equal to $-\mathcal{L}_1$! This obvious contradiction

is due to the improper LODI assumption in this situation: the source term Rq (see Eq. (2.63)) is typically large and cannot be ignored.

3.2.7 Beyond LODI

The local one-dimensional inviscid assumption is in fact a drawback of NSCBC method. The reason is that without considering the source term in Eq. (3.8), the resultant characteristic equations on the boundary are not accurate and may not be able to converge to the exact solution. This will be illustrated in the next section. It is therefore preferred to include the source term in Eq. (3.8) when the relations between $\frac{\partial \mathbf{W}}{\partial t}$ and $\mathcal{D}$ are deduced.

3.2.8 Case Study: Purely Subsonic Isentropic Nozzle Flow

Now we use a simple quasi-one-dimensional flow, namely the purely subsonic isentropic nozzle flow, to show how the above procedure can be implemented. This example is taken from the textbook *Computational fluid dynamics: the basics with applications* of Anderson (1995) which gives more details. The price for using this relatively simple example is that some equations should be deduced again.

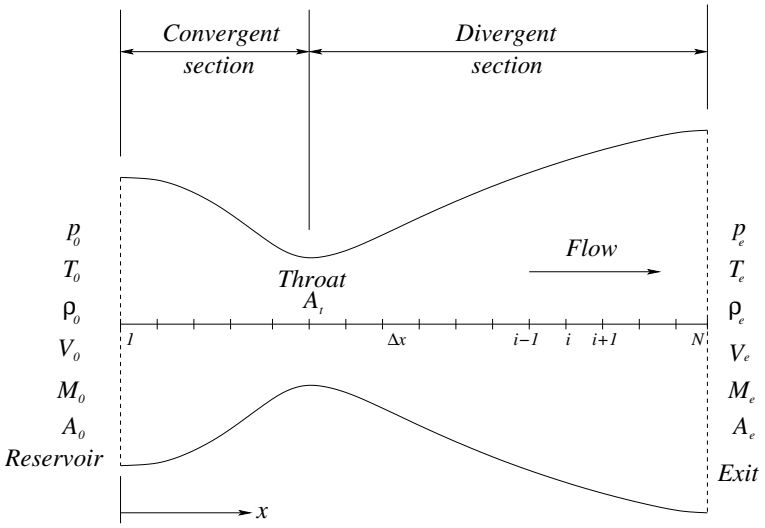

Figure 3.2 Sketch of a convergent-divergent nozzle for the purely subsonic flow solution

The convergent-divergent nozzle sketched in Fig. 3.2 has a specified area distribution as

follows

$$\frac{A}{A_t} = \begin{cases} 1 + 2.2(\frac{x}{L} - 1.5)^2, \ 0 \leq \frac{x}{L} \leq 1.5 \\ 1 + 0.2223(\frac{x}{L} - 1.5)^2, \ 1.5 \leq \frac{x}{L} \leq 3.0 \end{cases} \tag{3.24}$$

where A_t denotes the area of the nozzle throat and L is some reference length. The pressure ratio is $\frac{p_e}{p_0} = 0.9$. According to the exact analytical solution, the flow through the nozzle is still subsonic everywhere; the highest Mach number, which occurs at the throat, is 0.721 and the Mach number at the exit is 0.391.

The nondimensional governing equations are

$$\frac{\partial \mathbf{U}}{\partial t} + [A]\frac{\partial \mathbf{U}}{\partial x} = \mathbf{J}, \tag{3.25}$$

where

$$\mathbf{U} = \begin{bmatrix} \rho \\ V \\ T \end{bmatrix}; \quad [A] = \begin{bmatrix} V & \rho & 0 \\ \frac{T}{\gamma\rho} & V & \frac{1}{\gamma} \\ 0 & (\gamma-1)T & V \end{bmatrix}; \quad \mathbf{J} = \begin{bmatrix} -\rho V \frac{\partial ln\, A}{\partial x} \\ 0 \\ -(\gamma-1)TV\frac{\partial ln\, A}{\partial x} \end{bmatrix}. \tag{3.26}$$

The nondimensional variables are defined as

$$\begin{aligned} T &= \tfrac{T^*}{T_0}, \quad \rho = \tfrac{\rho^*}{\rho_0}, \quad p = \tfrac{p^*}{p_0}, \quad A = \tfrac{A}{A_t}, \\ x &= \tfrac{x^*}{L}, \quad V = \tfrac{V^*}{c_0}, \quad t = \tfrac{t^*}{L/c_0}, \quad c_0 = \sqrt{\gamma R T_0}. \end{aligned} \tag{3.27}$$

The above equations can be solved by using a finite-difference method with the MacCormack scheme. First the x axis along the nozzle is divided into N grid points with uniform spacing Δx. The first point, labeled point 1, is at the nozzle inlet and the last point which is at the nozzle exit is denoted by N. We choose $N = 31$. Suppose point i is an arbitrary grid point, with points $i-1$ and $i+1$ as the adjacent points.

The MacCormack scheme is a predictor-corrector method. We will briefly show the steps. First, consider the predictor step. We have

$$\left(\frac{\partial \mathbf{U}}{\partial t}\right)_i^t = -[A]_i^t \frac{\mathbf{U}_{i+1}^t - \mathbf{U}_i^t}{\Delta x} + \mathbf{J}_i^t. \tag{3.28}$$

The predicted values of $\mathbf{U}_i$ is obtained from

$$\bar{\mathbf{U}}_i^{t+\Delta t} = \mathbf{U}_i^t + \left(\frac{\partial \mathbf{U}}{\partial t}\right)_i^t \Delta t. \tag{3.29}$$

The predicted values of the matrix $[A]$ and the source term $\mathbf{J}$ can be obtained from $\bar{\mathbf{U}}$.

Moving to the corrector step, we have

$$\left(\overline{\frac{\partial \mathbf{U}}{\partial t}}\right)_i^{t+\Delta t} = -[\bar{A}]_i^{t+\Delta t} \frac{\bar{\mathbf{U}}_i^{t+\Delta t} - \bar{\mathbf{U}}_{i-1}^{t+\Delta t}}{\Delta x} + \bar{\mathbf{J}}_i^{t+\Delta t}. \tag{3.30}$$

Therefore, the average time derivative of $\mathbf{U}$ is

$$\left(\frac{\partial \mathbf{U}}{\partial t}\right)_{av} = 0.5 \left[\left(\frac{\partial \mathbf{U}}{\partial t}\right)_i^t + \left(\overline{\frac{\partial \mathbf{U}}{\partial t}}\right)_i^{t+\Delta t} \right], \tag{3.31}$$

and the variables at time $t + \Delta t$ are evaluated by

$$\mathbf{U}_i^{t+\Delta t} = \mathbf{U}_i^t + \left(\frac{\partial \mathbf{U}}{\partial t}\right)_{av} \Delta t. \tag{3.32}$$

The inflow boundary conditions are fixed ρ and T, both equal to 1.0, while V is extrapolated from the interior:

$$V_1 = 2V_2 - V_3. \tag{3.33}$$

At the outlet, the pressure is specified and the other two flow variables should be allowed to float.

$$V_N = 2V_{N-1} - V_{N-2}; \quad T_N = 2T_{N-1} - T_{N-2}; \quad \rho_N = \tfrac{p_N}{T_N}. \tag{3.34}$$

The initial conditions are

$$\begin{cases} \rho = 1.0 - 0.023x; \\ T = 1.0 - 0.009333x; \\ V = 0.05 + 0.11x. \end{cases} \tag{3.35}$$

The distribution of pressure through the nozzle at three different time steps is shown in Fig. 3.3. We can see the numerical solution oscillates enormously at time step 1200. In fact shortly thereafter the solution blows up. This is due to the wave reflection at the downstream boundary. One way to fix this problem is by adding artificial viscosity to the governing equations so that the reflecting waves may be dissipated. This is the method adopted by Anderson (1995). We will try the NSCBC method instead.

Starting from the governing equations (3.25) and (3.26), we have

$$[A] = [S][\Lambda][S]^{-1}, \tag{3.36}$$

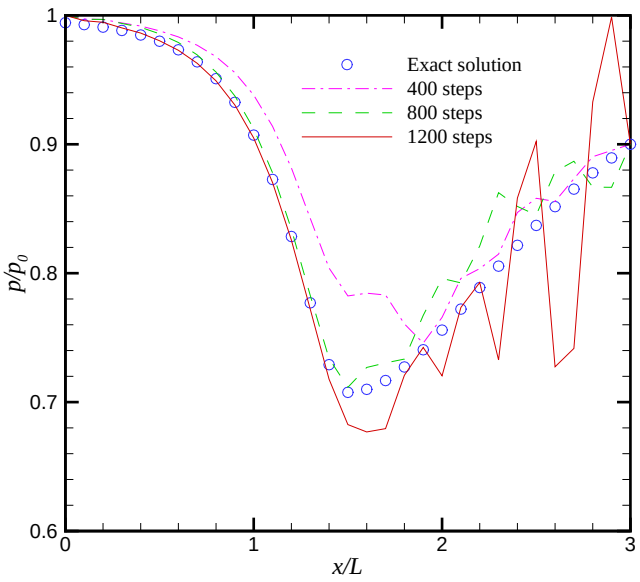

Figure 3.3 Pressure distribution through purely subsonic nozzle at different time steps

where

$$[S] = \begin{bmatrix} \frac{1}{2\gamma c} & -\frac{1}{\gamma T} & \frac{1}{2\gamma c} \\ -\frac{1}{2\gamma\rho} & 0 & \frac{1}{2\gamma\rho} \\ \frac{(\gamma-1)c}{2\gamma\rho} & \frac{1}{\gamma\rho} & \frac{(\gamma-1)c}{2\gamma\rho} \end{bmatrix}, \tag{3.37}$$

and

$$[S]^{-1} = \begin{bmatrix} c & -\gamma\rho & \rho/c \\ (1-\gamma)T & 0 & \rho \\ c & \gamma\rho & \rho/c \end{bmatrix}; \quad [\Lambda] = \begin{bmatrix} V-c & 0 & 0 \\ 0 & V & 0 \\ 0 & 0 & V+c \end{bmatrix}. \tag{3.38}$$

The three characteristic waves are

$$\mathcal{L} = \begin{bmatrix} \mathcal{L}_1 \\ \mathcal{L}_2 \\ \mathcal{L}_3 \end{bmatrix} = \begin{bmatrix} (V-c)c & -\gamma\rho(V-c) & (V-c)\rho/c \\ (1-\gamma)TV & 0 & \rho V \\ (V+c)c & \gamma\rho(V+c) & (V+c)\rho/c \end{bmatrix} \partial_x \begin{bmatrix} \rho \\ V \\ T \end{bmatrix}. \tag{3.39}$$

Then we have

$$\mathcal{D} = \begin{bmatrix} \mathcal{D}_1 \\ \mathcal{D}_2 \\ \mathcal{D}_3 \end{bmatrix} = \begin{bmatrix} \frac{1}{2\gamma c}(\mathcal{L}_1 + \mathcal{L}_3) - \frac{1}{\gamma T}\mathcal{L}_2 \\ \frac{1}{2\gamma\rho}(\mathcal{L}_3 - \mathcal{L}_1) \\ \frac{(\gamma-1)c}{2\gamma\rho}(\mathcal{L}_1 + \mathcal{L}_3) + \frac{1}{\gamma\rho}\mathcal{L}_2 \end{bmatrix}. \tag{3.40}$$

Thus, at the inlet and outlet boundaries we have

$$\frac{\partial \mathbf{U}}{\partial t} + \mathcal{D} = \mathbf{J}, \tag{3.41}$$

which is the appropriate equation for both boundaries.

At the inflow boundary there is one outgoing wave, namely $\mathcal{L}_1$, as well as two incoming waves, $\mathcal{L}_2$ and $\mathcal{L}_3$, which need to be determined. The physical boundary conditions are fixed density and temperature at the inlet. Therefore, from Eq. (3.40), we have

$$\begin{aligned} \mathcal{D}_1 = J_1 = -\rho V \frac{\partial ln\, A}{\partial x}; \\ \mathcal{D}_3 = J_3 = -(\gamma - 1)TV \frac{\partial ln\, A}{\partial x}, \end{aligned} \tag{3.42}$$

at point $i = 1$, which gives

$$\mathcal{L}_3 = -\mathcal{L}_1 - 2\gamma \left(\rho c V \tfrac{\partial ln\, A}{\partial x}\right)_{i=1}; \quad \mathcal{L}_2 = 0. \tag{3.43}$$

Notice the LODI is not used and the source term is included in the formula. Substituting Eq. (3.43) into Eqs. (3.40) and (3.41), we obtain the equation for the inflow boundary, $i = 1$.

At the outflow boundary there are two outgoing waves, namely $\mathcal{L}_2$, $\mathcal{L}_3$, and there is one incoming wave, $\mathcal{L}_1$, which needs to be determined. The physical boundary conditions are fixed pressure at the outlet. Therefore, from Eq. (3.40),we have

$$\begin{aligned} \frac{\partial p}{\partial t} = T\frac{\partial \rho}{\partial t} + \rho\frac{\partial T}{\partial t} = 0; \\ T(-\mathcal{D}_1 + J_1) + \rho(-\mathcal{D}_3 + J_3) = 0, \end{aligned} \tag{3.44}$$

$$\tag{3.45}$$

at point $i = N$, which gives

$$\mathcal{L}_1 = -\mathcal{L}_3 - 2\gamma \left(\rho c V \frac{\partial ln\, A}{\partial x}\right)_{i=N}. \tag{3.46}$$

The above equation can be directly substituted into Eqs. (3.40) and (3.41) to obtain the equation for the outflow boundary. The result is shown in Fig. 3.4. No spurious waves are observed at the outflow boundary, and the steady-state solution matches the exact value very well. It can be derived that at the outflow boundary

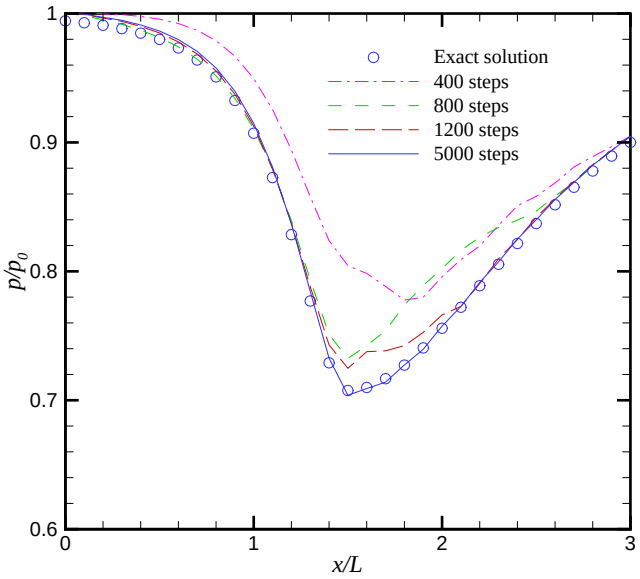

Figure 3.4 Pressure distribution through purely subsonic nozzle at different time steps

$$-\frac{\partial p}{\partial t} = \frac{c}{2}(\mathcal{L}_1 + \mathcal{L}_3) + \gamma p V \frac{\partial ln\ A}{\partial x}. \tag{3.47}$$

Thus, if Eq. (3.46) is used, we have $\frac{\partial p}{\partial t} = 0$. However, if LODI is used, which gives $\mathcal{L}_1 = -\mathcal{L}_3$, then the pressure variation at the outflow will be determined by the differential equation

$$\frac{\partial p}{\partial t} = -\gamma p V \frac{\partial ln\ A}{\partial x}, \tag{3.48}$$

whose behavoir depends on the velocity, which is in turn dependent on pressure. This makes the problem complex and difficult to control.

The last comment is made on the partial-reflecting outflow boundary condition mentioned in section 3.2.5. When this boundary condition is used, along with the reasoning we have

followed until now, we have

$$\frac{\partial p_N}{\partial t} = -\frac{c}{2}\mathcal{K}(p_N - p_\infty), \tag{3.49}$$

which gives

$$\Delta p = \Delta p_0 e^{-\frac{c}{2}\mathcal{K}t}, \tag{3.50}$$

where $\Delta p = p_N - p_\infty$. It can be observed that $\mathcal{K}$ is in fact inverse of a length scale and should be always positive.

3.3 Incorporation of NSCBC into LU-SGS Scheme

In the simulations of developing flows, either hydrodynamically or thermally or both, it is preferred to use characteristic boundary conditions at the outflow to simple extrapolation. The reason is that simple extrapolation of both velocities and pressure neither satisfies the physics nor is able to maintain the correct friction velocity level inside the flow. Another choice is the convective boundary condition which assumes the flow field advects out of the exit with the speed of the mean flow. However, it still leaves the problem of setting up a proper outflow pressure field for compressible flows.

We will use the partial-reflecting outflow boundary condition. The LODI relation is Eq. (3.22):

$$\frac{\partial p}{\partial t} + \frac{p}{T}\frac{\gamma}{\gamma - 1}(\mathcal{L}_1 + \mathcal{L}_2) + \alpha(p - p_\infty) = 0, \tag{3.51}$$

therefore the incoming wave $\mathcal{L}_2$ can be expressed as

$$\mathcal{L}_2 = \mathcal{K}(p - p_\infty) - \mathcal{L}_1. \tag{3.52}$$

As a result, the matrix $[\Xi]$ (see Eq. (3.4)) is changed to $[\Xi']$ in Eq. 3.9 at the outflow boundary. In virtue of Eq. (B.5), we have

$$[\Xi'] = \begin{bmatrix} (u+c)(\gamma-1)T/(2\gamma p) & (u+c)(\gamma-1)T/(2c) & 0 & 0 & 0 \\ -(u+c)(\gamma-1)T/(2\gamma p) & -(u+c)(\gamma-1)T/(2c) & 0 & 0 & 0 \\ -u(\gamma-1)T/(\gamma p) & 0 & 0 & 0 & u \\ 0 & 0 & u & 0 & 0 \\ 0 & 0 & 0 & u & 0 \end{bmatrix} \tag{3.53}$$

and the Jacobian matrix $[A']$ in Eq. (3.10) is therefore

$$[A'] = [T][S][\Xi'] = \begin{bmatrix} \frac{u(\gamma-1)}{\gamma T} & 0 & 0 & 0 & -\frac{pu}{T^2} \\ \frac{c(u+c)+u^2(\gamma-1)}{\gamma T} & \frac{p(u+c)}{T} & 0 & 0 & -\frac{pu^2}{T^2} \\ \frac{uv(\gamma-1)}{\gamma T} & 0 & \frac{pu}{T} & 0 & -\frac{puv}{T^2} \\ \frac{uw(\gamma-1)}{\gamma T} & 0 & 0 & \frac{pu}{T} & -\frac{puw}{T^2} \\ \frac{u\left[c(u+c)+\frac{u^2+v^2+w^2}{2}(\gamma-1)\right]}{\gamma T} & \frac{pu(u+c)}{T} & \frac{puv}{T} & \frac{puw}{T} & -\frac{pu(u^2+v^2+w^2)}{2T^2} \end{bmatrix}. \quad (3.54)$$

Also a new source term is introduced to the right member of Eq. (3.10):

$$\mathbf{S}^{*\prime} = \mathbf{S}^* - \mathbf{S}^\alpha, \quad (3.55)$$

where

$$\mathbf{S}^\alpha = [T][S] \begin{bmatrix} 0 \\ \mathcal{K}(p-p_\infty) \\ 0 \\ 0 \\ 0 \end{bmatrix} = \begin{bmatrix} 1 \\ u-c \\ v \\ w \\ H-uc \end{bmatrix} \cdot \frac{p\mathcal{K}(p-p_\infty)}{T^2(\gamma-1)}. \quad (3.56)$$

Now we turn our attention to the real application of the above modified system. At the outlet, as sketched in Fig. 3.5, the modified system should be applied to the outflow surface,

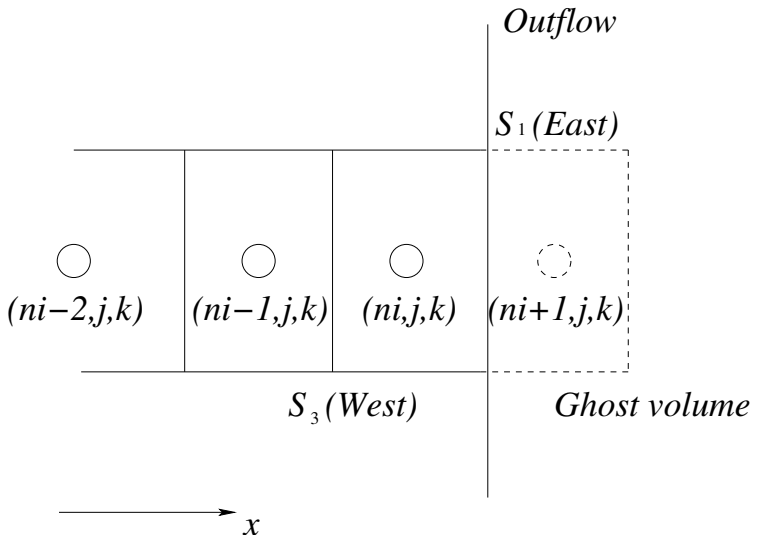

Figure 3.5 Sketch of the outflow boundary

which is the east face of control volume (ni, j, k). For the interior control volumes, the original integral governing equations should be used for all six surfaces. For the near-boundary volume (ni, j, k), however, only five faces of the hexahedron use the original equations since its east surface is subject to the new system. Thus, Eq. 2.90 becomes

$$\begin{aligned}[\Gamma]^{-1}[T]\frac{3\Omega}{2\Delta t}\Delta\mathbf{W} + [\Gamma]^{-1}[([A']\Delta\mathbf{W}S)_1 - ([A]\Delta\mathbf{W}S)_3 \\ +([B]\Delta\mathbf{W}S)_2 - ([B]\Delta\mathbf{W}S)_4 + ([C]\Delta\mathbf{W}S)_5 - ([C]\Delta\mathbf{W}S)_6)] = -\mathcal{R}^m\end{aligned} \tag{3.57}$$

for the near-boundary volume (ni, j, k). As a result, the matrices in the $L-D-U$ decomposition become

$$\begin{aligned}[L] &= -[\Gamma]^{-1}_{ni,j,k}\left[([\Gamma][\tilde{A}]^+)_{ni-1,j,k}S_3 + ([\Gamma][\tilde{B}]^+)_{ni,j-1,k}S_4 + ([\Gamma][\tilde{C}]^+)_{ni,j,k-1}S_6\right]; \\ [D] &= ([\Gamma]^{-1}[T])_{ni,j,k}\frac{3\Omega}{2\Delta t} + [\Gamma]^{-1}_{ni,j,k}\left[([\Gamma][\tilde{A}']^+)_{ni,j,k}S_1 - ([\Gamma][\tilde{A}]^-)_{ni,j,k}S_3\right. \\ &\left.+([\Gamma][\tilde{B}]^+)_{ni,j,k}S_2 - ([\Gamma][\tilde{B}]^-)_{ni,j,k}S_3 + ([\Gamma][\tilde{C}]^+)_{ni,j,k}S_5 - ([\Gamma][\tilde{C}]^-)_{ni,j,k}S_6\right]; \\ [U] &= -[\Gamma]^{-1}_{ni,j,k}\left[([\Gamma][\tilde{A}']^-)_{ni+1,j,k}S_1 + ([\Gamma][\tilde{B}]^-)_{ni,j+1,k}S_2 + ([\Gamma][\tilde{C}]^-)_{ni,j,k+1}S_5\right].\end{aligned} \tag{3.58}$$

Compared with the original matrices, the lower matrix $[L]$ does not change but both the diagonal matrix $[D]$ and the upper matrix $[U]$ do change. In the above equations,

$$\begin{aligned}[\tilde{A}'] &= [\Gamma]^{-1}[A']; \\ [\tilde{A}']^\pm &= \frac{1}{2}([\tilde{A}'] \pm \left|\lambda_{[\tilde{A}']}\right|[I]).\end{aligned} \tag{3.59}$$

One problem is that now the diagonal matrix $[D]$ is no longer diagonal:

$$\begin{aligned}[D] &= ([\Gamma]^{-1}[T])\tfrac{3\Omega}{2\Delta t} + ([\tilde{A}']^+ - [\tilde{A}]^-)S_{13} + (\left|\lambda_{[\tilde{B}]}\right|[I])S_{24} + (\left|\lambda_{[\tilde{C}]}\right|[I])S_{56} \\ &= ([\Gamma]^{-1}[T])\tfrac{3\Omega}{2\Delta t} \\ &\quad +\tfrac{1}{2}\left[([\tilde{A}'] - [\tilde{A}]) + (\left|\lambda_{[\tilde{A}']}\right| + \left|\lambda_{[\tilde{A}]}\right|)[I]\right]S_{13} \\ &\quad +(\left|\lambda_{[\tilde{B}]}\right|[I])S_{24} + (\left|\lambda_{[\tilde{C}]}\right|[I])S_{56},\end{aligned} \tag{3.60}$$

and

$$[\tilde{A}'] - [\tilde{A}] = [\Gamma]^{-1}([A'] - [A]) = \begin{bmatrix} -\frac{u}{R} & -\frac{\gamma p}{R} & 0 & 0 & 0 \\ \frac{uc}{\gamma p} & c & 0 & 0 & 0 \\ 0 & 0 & 0 & 0 & 0 \\ 0 & 0 & 0 & 0 & 0 \\ \frac{uT(1-\gamma)}{\gamma p} & (1-\gamma)T & 0 & 0 & 0 \end{bmatrix}, \tag{3.61}$$

which contains four non-diagonal elements. Since the efficiency of LU-SGS scheme is largely dependent on the easily-done inversion of the diagonal matrix $[D]$, these newly arising non-diagonal elements can totally ruin the scheme. Our treatment to solve this problem is pretty simple: we move the non-diagonal elements of $[D]$ to the corresponding locations of the lower and upper matrices. That is

$$[L'] = [L] + \begin{bmatrix} 0 & 0 & 0 & 0 & 0 \\ \frac{uc}{\gamma p} & 0 & 0 & 0 & 0 \\ 0 & 0 & 0 & 0 & 0 \\ 0 & 0 & 0 & 0 & 0 \\ \frac{uT(1-\gamma)}{\gamma p} & (1-\gamma)T & 0 & 0 & 0 \end{bmatrix}, \tag{3.62}$$

and

$$[U'] = [U] + \begin{bmatrix} 0 & -\frac{\gamma p}{R} & 0 & 0 & 0 \\ 0 & 0 & 0 & 0 & 0 \\ 0 & 0 & 0 & 0 & 0 \\ 0 & 0 & 0 & 0 & 0 \\ 0 & 0 & 0 & 0 & 0 \end{bmatrix}. \tag{3.63}$$

In this way, matrix $[D]$ becomes diagonal again:

$$\begin{aligned}[D'] \quad = \quad & ([\Gamma]^{-1}[T])\tfrac{3\Omega}{2\Delta t} \\ & +(\left|\lambda_{[\tilde{B}]}\right|[I])S_{24}+(\left|\lambda_{[\tilde{C}]}\right|[I])S_{56}, \\ & +\tfrac{1}{2}S_{13}\begin{bmatrix} -\frac{u}{R}+\bar{\lambda}_A & 0 & 0 & 0 & 0 \\ 0 & c+\bar{\lambda}_A & 0 & 0 & 0 \\ 0 & 0 & \bar{\lambda}_A & 0 & 0 \\ 0 & 0 & 0 & \bar{\lambda}_A & 0 \\ 0 & 0 & 0 & 0 & \bar{\lambda}_A \end{bmatrix},\end{aligned} \tag{3.64}$$

where $\bar{\lambda}_A = \left|\lambda_{[\tilde{A}']}\right| + \left|\lambda_{[\tilde{A}]}\right|$. And the new iteration equation for the near-boundary volume (ni, j, k) is

$$([L'] + [D'] + [U'])\Delta\mathbf{W} = -\mathcal{R}', \tag{3.65}$$

in which the prime accent put on the source term denotes that an additional source term (see Eq. (3.56)) is included.

CHAPTER 4. TURBULENT DUCT FLOW WITH AND WITHOUT HEAT TRANSFER

In this chapter, the LES formulation is applied to simulations of turbulent flow through a stationary square duct. The isothermal flows will be calculated first, and then the results of turbulent duct flows with low and high heating are presented. The DNS of Gavrilakis (1992) and that of Huser and Biringen (1993), along with the experimental measurements of Cheesewright et al. (1990) will be compared with the current LES results for the isothermal flows. The heat transfer coefficient for duct flow under heating will be compared with empirical relations.

4.1 Introduction

Turbulent heat transfer in a square duct has many engineering applications, for example, in heat exchangers. Some experiments have been conducted to study the characteristics of the flow and temperature fields in this class of flows. Sparrow et al. (1986) carried out experiments of a hydrodynamically developed turbulent flow developing in a duct heated on one side. They obtained the Nusselt number in fully developed as well as thermal entrance regions. They also found that the one-wall heating condition resulted in relatively long thermal entrance lengths. Hirota et al. (1997) made measurements for forced-convection heat transfer in a four-isothermal-walled square duct. Their measurements showed the similarity between distributions of streamwise turbulent heat flux and temperature fluctuation intensity. Similarity was also found between distributions of the transverse turbulent heat flux and turbulent shear stress. From their results, it was found that the constant turbulent Prandtl number assumption was invalid for duct flow since it became larger as the duct corner was approached.

Liou et al. (2000) visualized the local heat transfer distributions in a sharp turning duct using the transient liquid crystal method.

A significant amount of numerical simulations (Launder and Ying, 1973; Myong, 1991; Rokni and Gatski, 2001; Rokni and Sunden, 2003) based on the Reynolds-averaged Navier-Stokes (RANS) equations have been conducted on this topic. Relatively few direct numerical simulations (DNS) or large eddy simulations (LES) of turbulent heat transfer in a duct are available. The only direct simulation appears to be the work of Piller and Nobile (2002), which provided results on incompressible turbulent duct flow with an imposed temperature difference between the horizontal walls. Their results indicated that secondary motions affect the distributions of local shear stress and wall heat flux rather than global parameters such as friction factor and Nusselt number. Pallares and Davidson (2002) did an LES study of turbulent heat transfer in both stationary and rotating square ducts using an incompressible formulation. The LES research of Vázquez and Métais (2002) on a one-wall-heated duct is the only study which employed the compressible Navier-Stokes equations. They observed stronger secondary flows as well as weaker turbulent fluctuations in the near-wall region in heated duct compared with non-heated duct. These effects were found to be mostly due to the increase of the viscous sublayer thickness and amplification of ejection events near the heated wall.

In strongly heated internal gas flows, the temperature variations result in significant variations in density, molecular viscosity and thermal conductivity. The flows develop continuously downstream and the turbulence may undergo a reverse transition to a laminar-like state which is sometimes referred to as laminarization. Perkins (1975) is the first to measure mean temperature profiles for dominantly forced convection of gases in a vertical pipe with significant property variations at low Mach numbers. Shehata and McEligot (1998) presented the first mean velocity distributions for this situation. Satake et al. (2000) performed DNS for turbulent gas flow in a vertical pipe with property variations. Xu et al. (2004) carried out LES for the same situation. However, there are no LES or DNS results for turbulent flow in a duct with high heating available. The present research tries to give some LES results for the high heating case with an expectation to invite further experimental and numerical work on this

topic.

In turbulent duct flows, Prandtl's secondary flow of the second kind has a significant effect on the transport of heat and momentum. This secondary flow causes distortion of the isolines of mean velocity, temperature, and their fluctuations. Heating changes the structures of the near wall turbulence which in turn changes the mean and fluctuation values as well as Reynolds stress components. Different heating arrangements have different effects.

The present paper deals with the large eddy simulation of hydrodynamically developed turbulent air flow thermally developing in a four-heated-wall square duct at low Mach number. The magnitude of heating simulated can be high enough to cause significant property variations. From a search of the literature it appears that no prior LES (or DNS) work of this class of flows has been reported, mainly due to the non homogeneous nature of the flow. Due to the large variation of properties, the widely used spatially periodic boundary condition does not apply for this situation, although experiments of McEligot et al. (1965) show there exists a "quasi-developed" state far downstream of the entry and the "stepwise" periodic boundary conditions can be used in this region. This "stepwise" periodic boundary conditions have been used in LES of turbulent heat transfer by Dailey et al. (2003) and Xu et al. (2004). In the present study, we use the fully developed turbulent flow in an isothermal duct to generate mean velocity and turbulent fluctuations at the computational inlet and apply Navier-Stokes characteristic boundary conditions (NSCBC) at the outlet. Two thermal boundary conditions, the isothermal wall and the isoflux wall, are considered since it is well known that these two conditions have different effects on the turbulent heat transport. To validate the numerical procedure, we calculated several isothermal cases and compared our results with previous DNS and experimental results. Then heated ducts were simulated and results discussed.

4.2 Isothermal Duct Flows

4.2.1 Flow Configurations and Simulation Details

The computational domain is shown in Fig. 4.1. The size of the computational domain is $24D_h \times D_h \times D_h$ (D_h being the hydraulic diameter), in the x (streamwise), y and z (transverse)

directions, respectively.

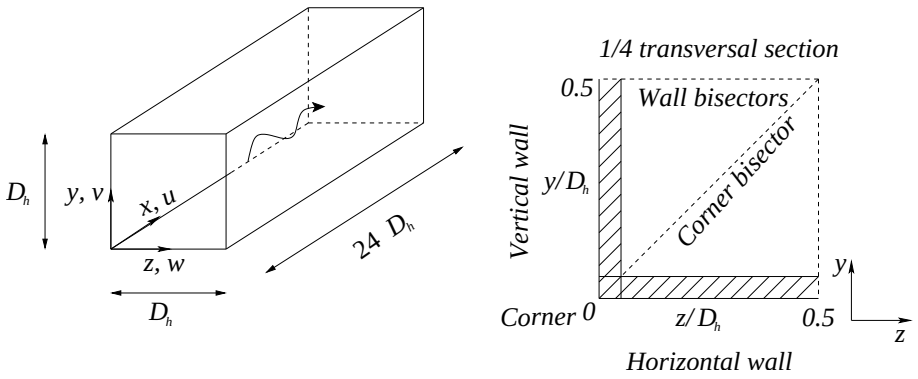

Figure 4.1 Sketch of the computational domain

Vázquez and Métais (2002) showed that the two-point correlations of velocity fluctuations for the isothermal duct is close to zero for $x/D_h = 6.4$. Therefore, a computational domain of streamwise length $24D_h$ was considered to be sufficient. Two sets of grids were used: a coarse grid consisting of $240 \times 40 \times 40$ control volumes and a fine grid with $240 \times 60 \times 60$ control volumes. Both grids were uniformly spaced in the x direction, but the grids were clustered towards the walls using hyperbolic tangent stretching to correctly simulate the near-wall regions. The distribution of the control volumes was identical in the y and z directions, where

$$\begin{aligned} y_i(z_i) &= \frac{1}{2}\left\{1 + \frac{tanh(a\xi_i)}{tanh(a)}\right\} \\ \xi_i &= -1 + 2\frac{i-1}{i_{max}-1} \text{ for i=1,...,}i_{max} \\ a &= \frac{1}{2}ln\left[\frac{1+b}{1-b}\right] \text{ for } 0 \leq b < 1. \end{aligned} \tag{4.1}$$

The parameter b controls the stretching of the grid, and typically $b = 0.7 - 0.95$. In wall units, the minimum and maximum grid spacings in the y and z directions were, respectively, 1.98 and 10.50 for the course grid and 0.91 and 9.12 for the fine grid. The grid spacing in the x direction was $\Delta x^+ = 30.69$ for both grids. The distance in wall units is defined by

$$y^+ = \frac{yu_\tau}{\nu_w}, \tag{4.2}$$

and the friction velocity $u_\tau = \sqrt{\tau_w/\rho_w}$ where τ_w is the shear stress and ρ_w is the fluid density near the wall.

Two cases with Reynolds number $Re_b = 5000$ and $Re_b = 8100$ based on the hydraulic diameter D_h and the bulk velocity u_b were simulated. The Mach number M was taken to be 0.001.

The initial flow field of the isothermal duct was constructed by superimposing a white noise on two laminar Poiseuille profiles sheared along the y and z directions. Uniform pressure and temperature were prescribed.

The boundary conditions at the walls were no-slip, isothermal. Periodic boundary conditions and Navier-Stokes characteristic boundary conditions (NSCBC) were used along the streamwise direction. NSCBC was applied to the duct outlet with a partial-reflecting boundary condition. A periodic inflow generator was needed to provide proper velocity field to the inflow boundary. All velocity components, u, v, w as well as density ρ at the inlet were given by the inflow generator. The pressure at the inflow was extrapolated from the duct interior, and then the inlet temperature was calculated from the extrapolated pressure and the density given by the inflow generator. The computational domain for NSCBC method is shown in Fig. 4.2. Table 4.1 shows a summary of the simulation details.

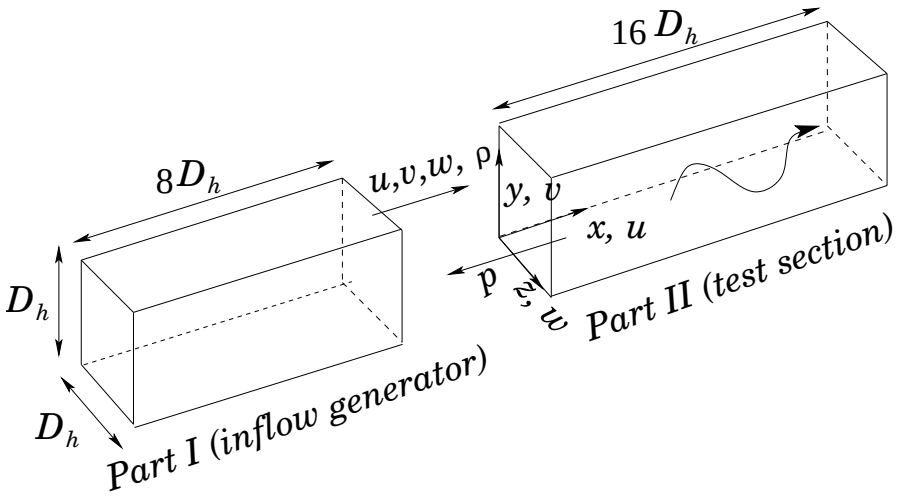

Figure 4.2 Computational domain for NSCBC method

Table 4.1 Simulation details of isothermal duct flows

	Re_b	grid	bc
Case 1	5000	$240 \times 40 \times 40$	Periodic
Case 2	5000	$240 \times 40 \times 40$	Characteristic
Case 3	5000	$240 \times 60 \times 60$	Periodic
Case 4	8100	$240 \times 40 \times 40$	Periodic
Case 5	8100	$240 \times 40 \times 40$	Characteristic

4.2.2 Results for Velocity Statistics

The velocity statistics were compared to the DNS results of Gavrilakis (1992) ($Re_b = 4410$) and Huser and Biringen (1993) ($Re_b = 10320$) and the experimental results of Cheesewright et al. (1990) ($Re_b = 4900$). The flow statistics were collected over 120 time units (D_h/u_b). For the cases with periodic boundary conditions, the mean profile was obtained by averaging in the homogeneous direction (streamwise direction here) and in time. For the cases with characteristic boundary conditions, the mean value was acquired by averaging data at the plane $x/D_h = 14$ in time.

Figures 4.3 and 4.4 shows mean streamwise velocity along the wall bisector $z/D_h = 0.5$. In these figures, the mean velocity profile is normalized by the friction velocity as $u^+ = u/u_\tau$. As shown, very good agreement with the DNS results was achieved. The dash lines in these figures represent the conventional law of the wall through empirical correlations. Very close to the wall is the viscous sublayer which has linear velocity distribution $u^+ = y^+$ and away from the wall is the "log-law" region which is represented by $u^+ = \frac{1}{\kappa} ln y^+ + 5.5$. The von Kármán constant $\kappa = 0.4$. We can see our mean velocity profile is slightly above the log-law. This is because we use a friction velocity defined by a four-wall-averaged shear stress. If we used the local shear stress, the normalized mean velocity profile would move closer to the log-law.

The contours of the mean streamwise velocity and the mean secondary flow vectors in a quarter of a cross-section are shown in Fig. 4.5. The mean secondary flow vectors show there exist two counter-rotating vortices in each corner of the duct. The magnitude of the secondary flow velocity is about $1 - 2\%$ of the bulk velocity. For the $Re_b = 5000$ case, $w_{max}/u_b = 1.9\%$.

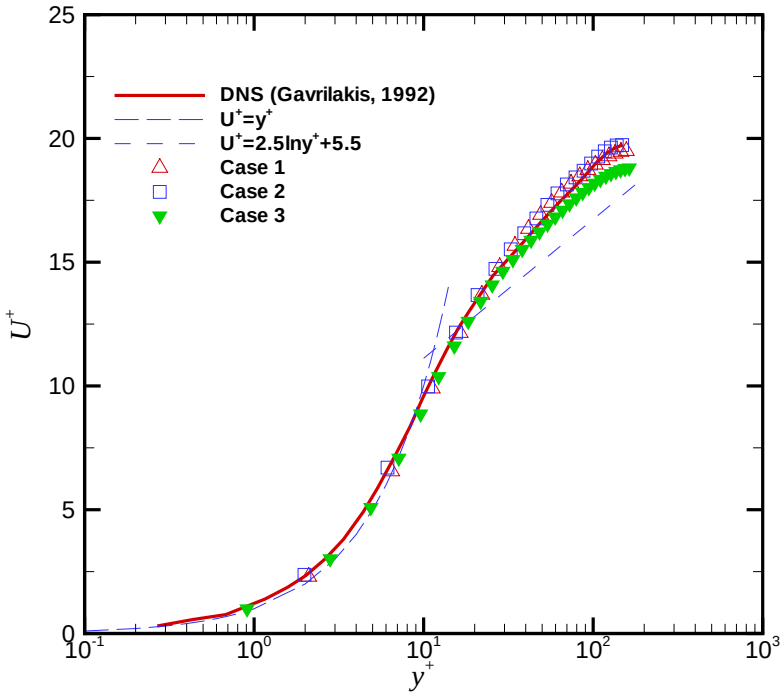

Figure 4.3 Mean velocity profile in wall coordinates, $Re_b = 5000$

Though this secondary flow is rather weak, it has major effects on the momentum and heat transfer processes in the duct. For example, the distortion of the streamwise velocity contours in the vicinity of the corner is due to the momentum transfer by the secondary flows from the duct center toward the corner. In this figure a streamline is highlighted and the corresponding secondary flow impingement and ejection are marked.

The mean and instantaneous secondary flow fields are shown in Fig. 4.6. We can see there are obvious flow variability with the instantaneous field, which is very different than the mean field.

Figures 4.7 and 4.8 show the local wall shear stress (τ/τ^a) distribution. The wall shear stress is normalized by the four-wall-averaged value (τ^a). We can see the results are very sensitive to the Reynolds number. The local wall shear stress exhibits two local maxima located around $z/D_h = 0.2$ and $z/D_h = 0.5$ for the $Re_b = 5000$ case. The maximum located

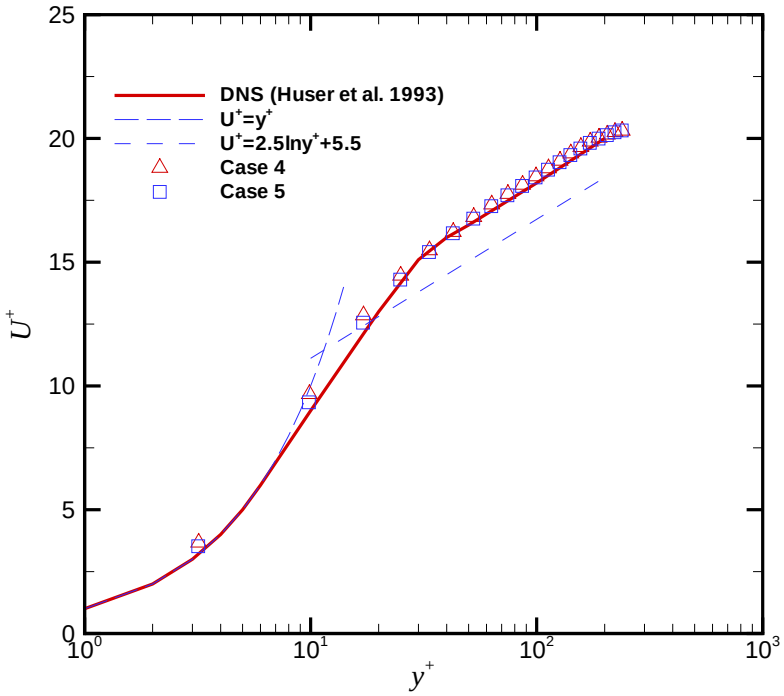

Figure 4.4 Mean velocity profile in wall coordinates, $Re_b = 8100$

at the wall midpoint can be easily understood since the velocity gradient is large there. The coincidence of the location of the other local maximum with the position of the secondary flow impingement suggests a connection between these two phenomena: the impingement brings high-speed fluid from the duct center to the wall which results in a higher velocity gradient. Because the secondary flow ejection has contrary effect, we can expect the local maximum at the wall midpoint to decrease as the secondary flow becomes stronger.

Figures 4.9 and 4.10 show the comparison between the present LES results (case 1, $Re_b = 5000$) and experiment of Cheesewright et al. (1990) ($Re_b = 4900$) for five different z-planes. These mean velocity profiles are normalized by the velocity at the duct center u_c. We can see that their location and magnitude are very well reproduced by LES.

The LES and experimental results of turbulent intensity profiles are compared in Fig. 4.11 and Fig. 4.12 at five different z-planes. The root mean square (r.m.s.) values were obtained

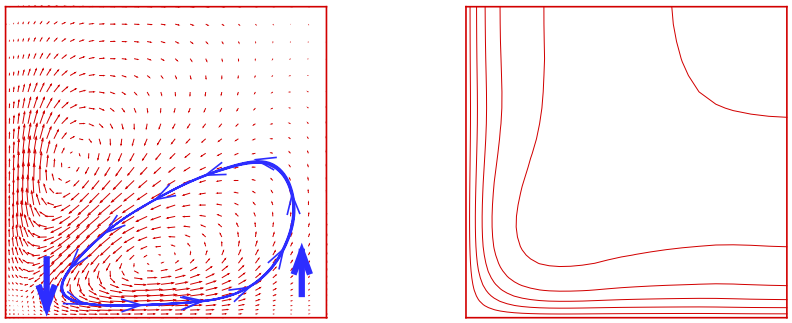

Figure 4.5 Secondary mean flow vectors and iso-contours of the mean streamwise velocity

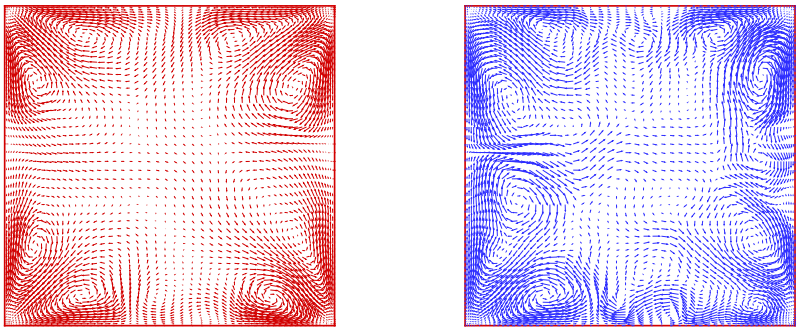

Figure 4.6 Mean and instantaneous secondary flow vectors

by operations like $u'_{rms} = \sqrt{< u'u' >}$, where $u' = u - < u >$ and $< \cdot >$ denotes an average in the x direction and in time. The r.m.s. values at the wall bisector are very much like those of turbulent channel flows. Close to the corner, however, the profiles are totally different due to the presence of walls.

To show the influence of the wall, we can use the anisotropy-invariant map proposed by Lumley and Newman (1977). This map limits *all* possible states of turbulence to a small region enclosed by three curves defined by the anisotropy tensor. The anisotropy tensor b_{ij} is deduced from the Reynolds stress tensor:

$$b_{ij} = \frac{< u'_i u'_j > -\frac{2}{3}k\delta_{ij}}{2k}, \tag{4.3}$$

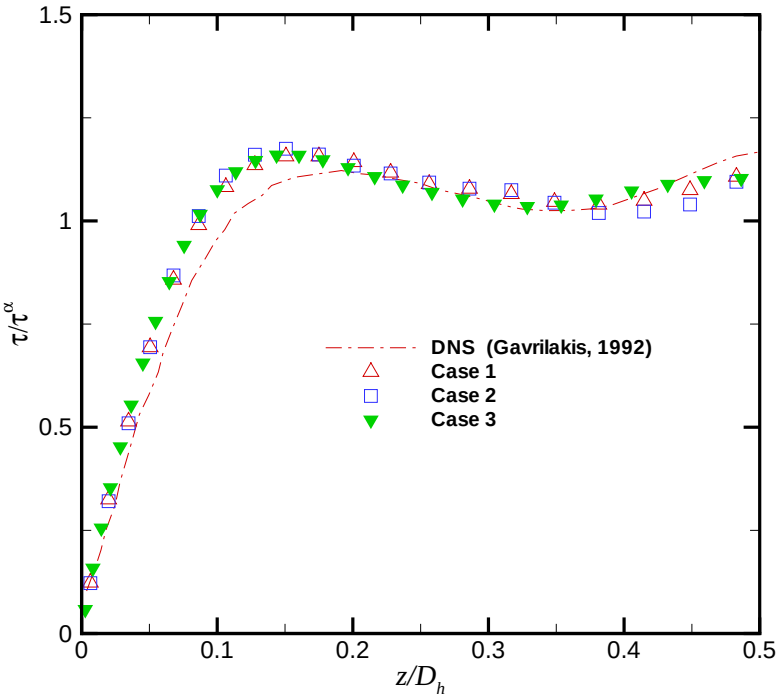

Figure 4.7 Local wall shear stress distribution, $Re_b = 5000$

where $k = \frac{1}{2} < u_i' u_i' >$. The three invariants ($I$, II and III) are given by

$$I = b_{ii}, \quad II = b_{ij} b_{ji}, \quad III = b_{ij} b_{jk} b_{ki}. \tag{4.4}$$

The different turbulent states can be identified by the curves of II as functions of III.

The isotropic turbulence corresponds to $II = III = 0$; the axisymmetric turbulence corresponds to $II = \frac{3}{2}\left(\frac{4}{3}|III|\right)^{\frac{2}{3}}$ and the two-component turbulence corresponds to $II = \frac{2}{9} + 2III$ (see Fig. 4.13). The top of the map represents the most anisotropic state, which is called the one-component turbulence. In this state one of the r.m.s. velocity components dominates the other two. The lowest point of the map is the most isotropic state, which is simply the isotropic turbulence.

Anisotropy invariants II and III along three constant z-planes: $z/D_h = 0.05$, $z/D_h = 0.25$ and $z/D_h = 0.5$ were calculated for case 1. The arrows shown in Fig. 4.13 denote the direction of increasing y. The solid line corresponds to $z/D_h = 0.5$, the dashed line to $z/D_h = 0.25$ and

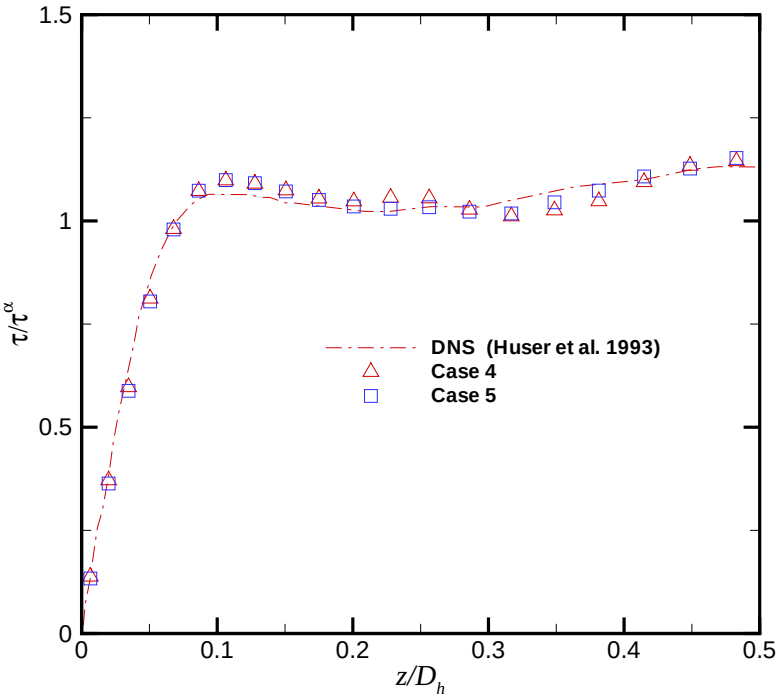

Figure 4.8 Local wall shear stress distribution, $Re_b = 8100$

the dotted line to $z/D_h = 0.05$. We can see at the wall midpoint, i.e. $z/D_h = 0.5$, when the distance from the wall increases the turbulence changes from two-component to one-component and then becomes more and more isotropic as the duct center is approached. However, close to the vertical wall, i.e. $z/D_h = 0.05$, the feature is totally different: the turbulence is highly anisotropic near the corner and becomes more and more like two-component turbulence as the vertical wall midpoint is approached. An instructive conclusion can be drawn: the flow behavior at the duct wall midpoint is similar to those of the channel and circular pipe flows.

Finally, the average friction coefficients are compared with an empirical correlation. The friction coefficient is defined as

$$C_f = \frac{\tau_w}{\frac{1}{2}\rho_b u_b^2}. \tag{4.5}$$

The empirical correlation of Jones (1976) is

$$1/C_f{}^{\frac{1}{2}} = 4log_{10}(2.25Re_bC_f{}^{\frac{1}{2}}) - 1.6, \tag{4.6}$$

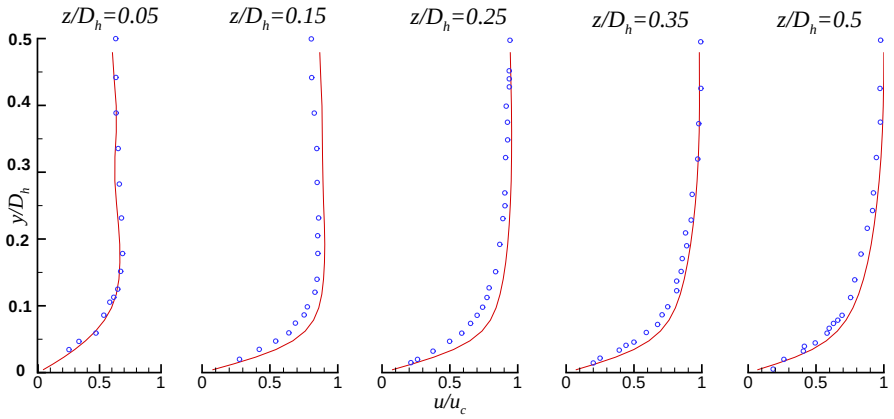

Figure 4.9 Comparison of the present LES mean streamwise velocity (——) with the experimental results of Cheesewright et al. (1990) (○) for five z-planes

Table 4.2 Comparison of friction coefficients of isothermal ducts

	Re_b	grid	bc	C_f	C_f from Jones' correlation	% error
Case 1	5000	$240 \times 40 \times 40$	Periodic	0.00845	0.00904	-6.5
Case 2	5000	$240 \times 40 \times 40$	Characteristic	0.00774	0.00904	-14.3
Case 3	5000	$240 \times 60 \times 60$	Periodic	0.00901	0.00904	-0.3
Case 4	8100	$240 \times 40 \times 40$	Periodic	0.00747	0.00792	-5.7
Case 5	8100	$240 \times 40 \times 40$	Characteristic	0.00740	0.00792	-6.6

and the results are summarized in Table 4.2. It can be seen from Table 4.2 that coarse grids tend to underpredict the friction coefficient. The characteristic boundary condition typically gives somewhat worse prediction than periodic boundary condition but the situation improves for higher Reynolds number.

4.3 Heated Duct Flows

Four heated duct cases were simulated. The computational domain is the same as that given in Fig. 4.2. Two different thermal boundary conditions were investigated. The first thermal condition is to keep all the duct walls at a higher temperature T_w, and the second condition is to maintain a constant wall heat flux q_w. As before, the non-dimensional temperature T_w is

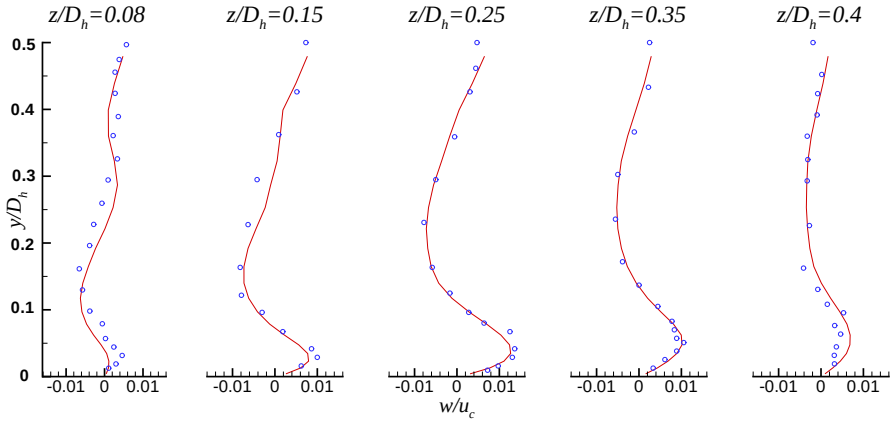

Figure 4.10 Comparison of the present LES mean spanwise velocity (——) with the experimental results of Cheesewright et al. (1990) (∘) for five z-planes

Table 4.3 Simulation details of heated duct flows

	Re_b	grid	bc	q_w	T_w
Case 6	5000	$240 \times 40 \times 40$	Isothermal	–	1.23
Case 7	5000	$240 \times 40 \times 40$	Isothermal	–	2.0
Case 8	5000	$240 \times 40 \times 40$	Isoflux	0.002	–
Case 9	5000	$240 \times 40 \times 40$	Isoflux	0.004	–

normalized by the temperature of the fluid at the entrance and q_w is defined as

$$q_w = \frac{q_w^*}{\rho_{ref} U_{ref} c_p T_{ref}}, \tag{4.7}$$

where q_w^* is the dimensional wall heat flux. These two conditions will be hereafter referred to as isothermal wall and isoflux wall conditions, respectively. The computational details are summarized in Table 4.3.

4.3.1 Streamwise Variation of Integral Parameters

It is somewhat surprising that no analytical or experimental results for thermally developing turbulent flow in rectangular ducts are available. Handbooks for guidance of practical convective heat transfer design like that of Kakaç et al. (1987) suggest that results of circular ducts may be used provided the hydraulic diameter D_h is the same. Since rectangular ducts are

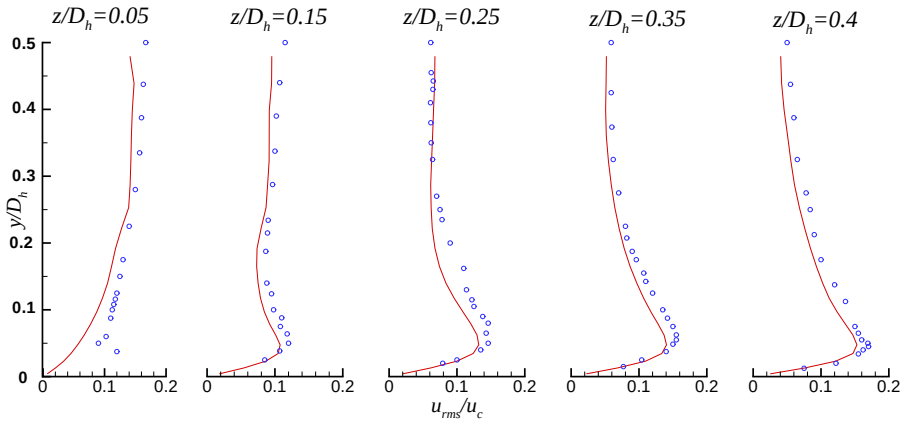

Figure 4.11 Comparison of the present LES u'_{rms} (——) with the experimental results of Cheesewright et al. (1990) (○) for five z-planes

characterized by secondary flows which cause higher temperatures near the corner and there is no such an effect in circular pipes, the results for circular duct flows can only be regarded as an approximation.

Figure 4.14 shows the dimensional streamwise distribution of local Nusselt number. The local Nusselt number is defined as

$$Nu_{loc} = \frac{h_x D_h}{k_b}, \tag{4.8}$$

where h_x is the circumferentially averaged but axially local heat transfer coefficient and k_b is the bulk thermal conductivity.

As mentioned, only analytical and empirical correlations for the circular pipe are available. From the analytical solution to the turbulent thermally developing flow (see §4.2.4 in Kakaç et al., 1987), the local Nusselt number for isothermal (Nu_T) and isoflux (Nu_H) boundary conditions are nearly identical for $Pr \geq 0.7$. The ratio of these two Nusselt numbers $\frac{Nu_H}{Nu_T}$ changes from ≈ 1.04 at $x/D_h = 2$ to ≈ 1.028 at station $x/D_h = 15$. Our results give 1.27 and 1.026, respectively. Several correlations for the Nusselt numbers in the thermal entrance region of a smooth circular duct have been developed. Reynolds et al. (1969) proposed the following correlation:

$$\frac{Nu_{loc}}{Nu_\infty} = 1 + \frac{0.8(1 + 70,000Re^{-3/2})}{x/D_h}, \tag{4.9}$$

where Nu_∞ is the Nusselt number for the fully developed region. This correlation is valid

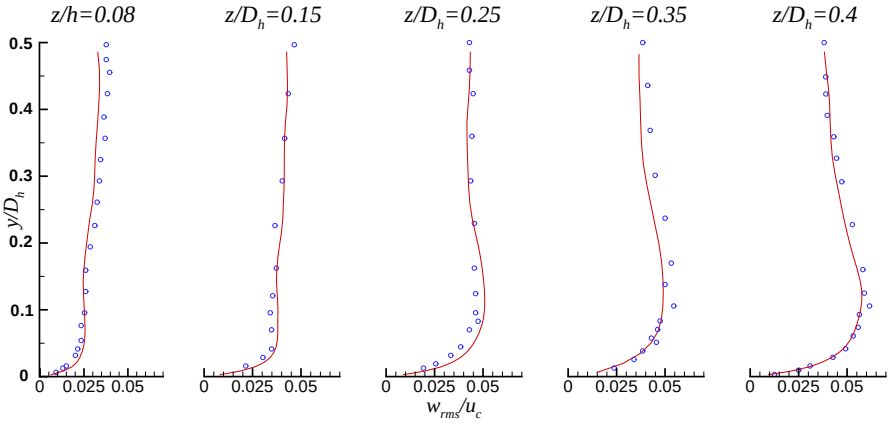

Figure 4.12 Comparison of the present LES w'_{rms} (——) with the experimental results of Cheesewright et al. (1990) (○) for five z-planes

for $x/D_h > 2$, $3000 < Re < 5 \times 10^4$ and $Pr = 0.71$. Kays and Crawford (2005) also gave a correlation of Nusselt number in the thermal entry length of a circular tube under isoflux condition. Since the heating level is high enough to cause considerable property variations, we will choose the correlations taking this effect into account to calculate Nu_∞. Humble et al. (1951) proposed

$$Nu_\infty = 0.023 Re_D^{0.8} Pr^{0.4} (\frac{T_w}{T_b})^{-0.55}. \tag{4.10}$$

The distributions of four-wall averaged wall temperature and bulk temperature are shown in Figs. 4.15 and 4.16.

The comparison between the present LES with the above correlations are summarized in Table 4.4.

As we can observe, the heated square duct cases did not compare favorably with the correlation for a circular pipe. The reason is due to the poor heat transfer performance at the duct corner.

Figure 4.17 shows the surface heat flux distribution for isothermal ducts and surface temperature distribution for isoflux ducts at three streamwise stations. Figure 4.18 shows the variation of the local wall shear stress τ_w around the duct perimeter for heated ducts at different streamwise stations. In these figures, $h = D_h/2$ is the half width of the duct. The local

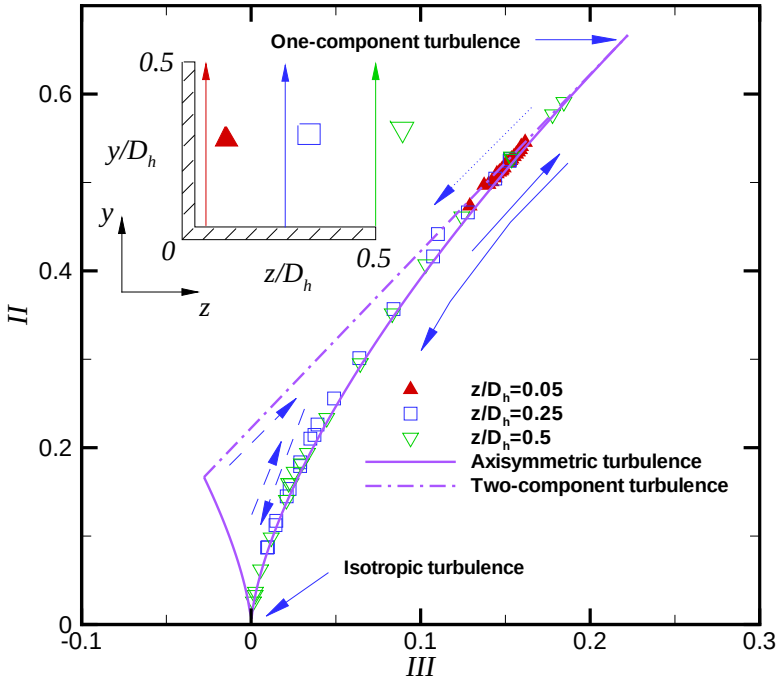

Figure 4.13 Anisotropy invariant map at three different z-planes

wall shear stress is normalized by the local averaged wall shear stress ${\tau_w}^a$. At $x = 2D_h$, the wall shear stress profiles of heated ducts are still very similar to those of the isothermal duct. As streamwise distance increases, the peak value of each heated duct profile gradually increases and shifts from the corner toward the mid-wall. The wall shear stress at the mid-wall, however, gradually decreases at the same time. The higher heating rate results in more shift of the peak value.

The local wall heat flux distributions of isothermal flows (Fig. 4.17) show the same tendency which occurs in the wall shear stress distributions. The positions where the maximum values of wall heat flux and wall shear stress appear also agree with each other. These phenomena can be explained by the behavior of the secondary flows (see Fig. 4.5). Near the mid-wall, as flow goes downstream, the gradually enhanced secondary flows transport hot and slow fluid from the wall to the central area which reduces the gradients of velocity and temperature. As

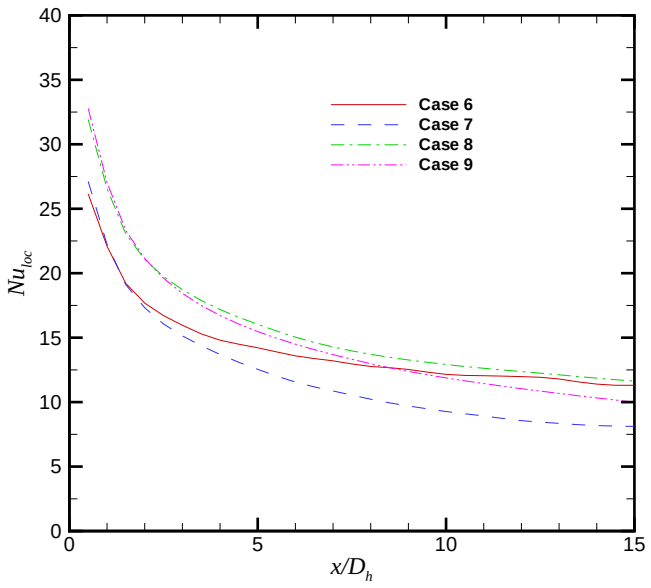

Figure 4.14 Streamwise distribution of local Nusselt number

a result, both local wall shear stress and local wall heat flux decreases at the mid-wall. Around the region $y \approx 0.4h$, the secondary flows bring relatively cold and fast moving fluid from the duct interior toward the wall. This increases velocity and temperature gradients and gives rise to greater local wall shear stress and local wall heat flux.

We can see for the isothermal ducts, the heat flux close to corner is very low and for the isoflux ducts the temperature near corner is very high. Both situations imply impaired heat transfer performance. If we consider the Nusselt number at the middle duct wall rather than the four-wall averaged Nusselt number, we have better agreements between LES and correlations for the isoflux cases as shown in Table 4.5. This can be explained by the fact indicated in the last section, that is, the flow behavior at the duct wall midpoint is similar to those of the channel and circular pipe flows. However, the discrepancy between the present isothermal ducts and correlations cannot be reduced this way. This suggests that for rectangular ducts, different thermal boundary conditions have significant influence on the flows.

To determine the correct Nusselt number distribution, more analytical and experimental research is needed. It is crucial to obtain velocity, eddy viscosity and turbulent Prandtl number

Table 4.4 Comparison of local Nusselt numbers of heated ducts, four-wall averaged values

	Nu_∞	$x/D_h = 8$	% error	$x/D_h = 14$	% error
Case 6	16.29	12.76	–	11.39	–
Reynolds (1969)		18.24	-30.0	17.41	-34.6
Kays (2005)		17.86	-28.5	16.94	-32.8
Case 7	12.47	10.22	–	8.18	–
Reynolds (1969)		13.96	-26.8	13.32	-38.6
Kays (2005)		13.67	-25.2	13.02	-37.2
Case 8	14.45	13.70	–	11.86	–
Reynolds (1969)		16.18	-15.3	15.44	-23.2
Kays (2005)		15.84	-13.5	15.09	-21.4
Case 9	12.47	12.97	–	10.32	–
Reynolds (1969)		13.96	-7.1	13.32	-22.5
Kays (2005)		13.67	-5.1	13.02	-20.7

Table 4.5 Comparison of local Nusselt numbers of heated ducts, middle wall values

	Nu_∞	$x/D_h = 8$	% error	$x/D_h = 14$	% error
Case 8	14.45	17.36	–	14.86	–
Reynolds (1969)		16.18	7.3	15.44	-3.8
Kays (2005)		15.84	9.6	15.09	-1.5
Case 9	12.47	15.16	–	11.94	–
Reynolds (1969)		13.96	8.6	13.32	-10.4
Kays (2005)		13.67	10.9	13.02	-8.3

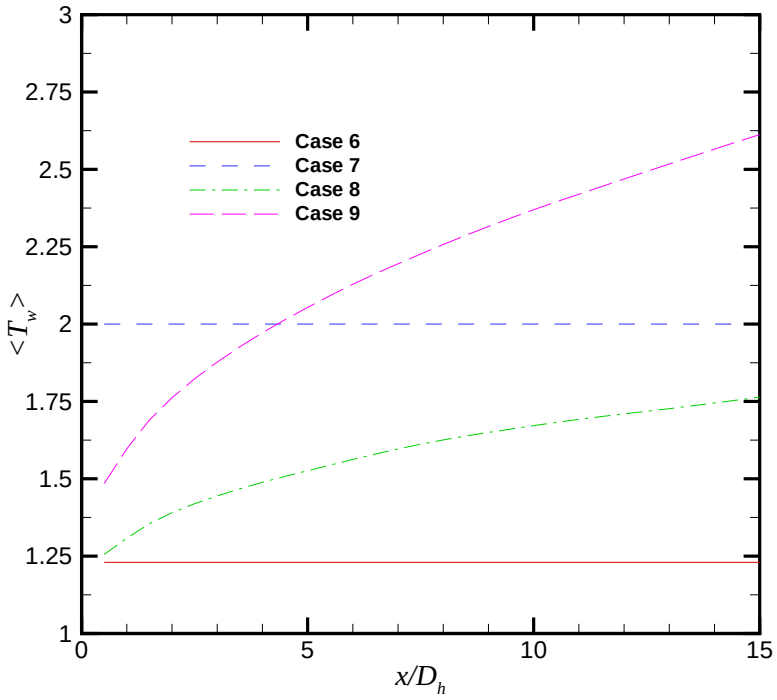

Figure 4.15 Streamwise distribution of four-wall averaged wall temperature

distributions in order to perform an analysis of the turbulent heat transfer problem and this is the business of the next section.

4.3.2 Downstream Statistics

Figures 4.19 and 4.20 show the mean streamwise velocity and mean temperature profiles along the wall bisector at three different downstream locations: $x = 2D_h$, $x = 8D_h$ and $x = 14D_h$. Here the mean velocity and mean temperature are normalized by the local friction velocity and local friction temperature. That is, they are given in wall coordinates. The mean temperature difference θ^+ is given as

$$\theta^+ = \frac{T_w - T}{T_\tau}$$
$$T_\tau = \frac{q_w}{\rho_w c_p u_\tau}. \tag{4.11}$$

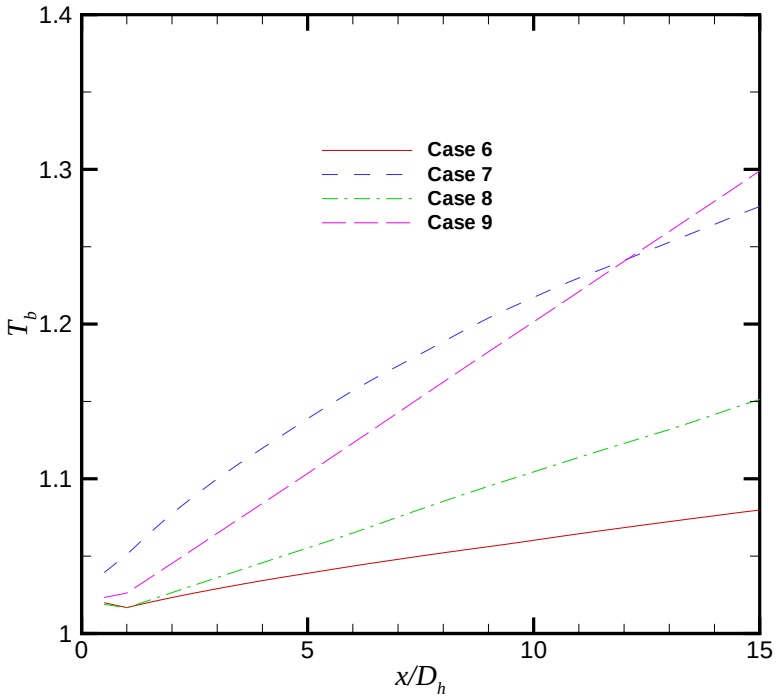

Figure 4.16 Streamwise distribution of bulk temperature

We can discern some general trends from these figures: both velocity and temperature profiles away from the wall (large y^+) depart more from their log-law and approach more closely to the laminar prediction as the flow progresses downstream. This is known as "re-laminarization". A simple explanation is that as temperature increases the molecular viscosity of the gas also increases which results in the drop of the Reynolds number. One may notice the above trend does not always hold, especially in the high-heating isoflux case (Case 9) in which the "tail" of the U^+ profile drops as x/D_h becomes large. The same results have been obtained in the experiments of Shehata and McEligot (1998) carried out in a vertical pipe. This apparent discrepancy may be due to the effects of significant property variations on local friction velocity. With a stronger heating rate, the density decreases while molecular viscosity increases substantially near the wall which causes the local friction velocity to increase

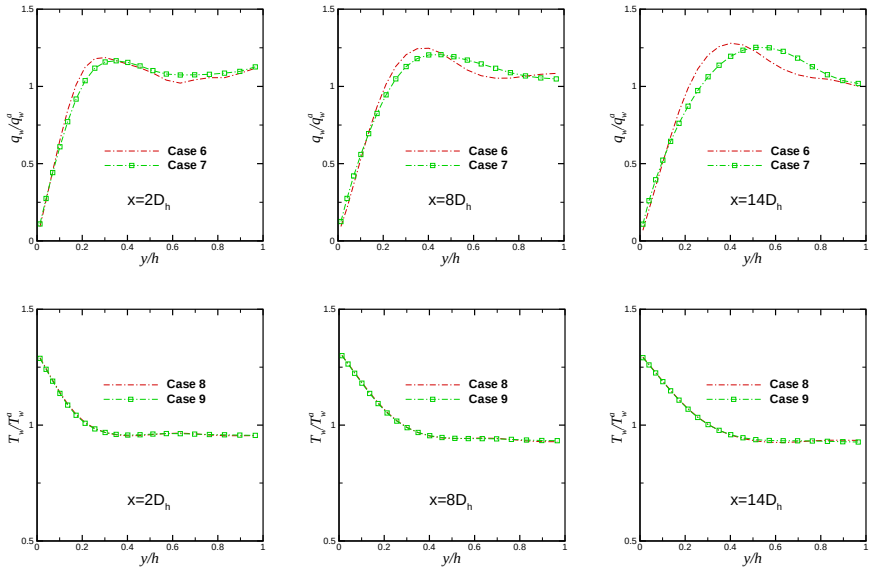

Figure 4.17 Distributions of surface heat flux and surface temperature at three streamwise stations

dramatically. If the central velocity increase cannot offset this increase of friction velocity, an illusive drop of U^+ will be observed.

Huang et al. (1995) suggested to use semi-local coordinates, $U^\star$ or $\theta^\star$ versus $y^\star$ instead of U^+ versus y^+ when large property variations are involved. In these coordinates, local rather than wall values of density and molecular viscosity are used:

$$U^\star = \frac{< u >}{u_\tau{}^\star}; \theta^\star = \frac{T_w - T}{T_\tau{}^\star}$$
$$u_\tau{}^\star = \sqrt{\frac{\tau_w}{\rho(y)}}; T_\tau{}^\star = \frac{q_w}{\rho(y) c_p u_\tau{}^\star}$$
$$y^\star = \frac{\delta_y u_\tau{}^\star}{\nu(y)}. \tag{4.12}$$

Figures 4.21 and 4.22 show the mean streamwise velocity and mean temperature along the wall bisector which is plotted in semi-local coordinates. The velocity profiles then show better consistency with temperature profiles. It can be seen that at the same streamwise location stronger heating rate results in thicker viscous layer which leads to more laminar-like mean temperature profile. For a fixed heating rate, the viscous layer develops in the streamwise direction and results in a trend toward laminarization of the mean profiles.

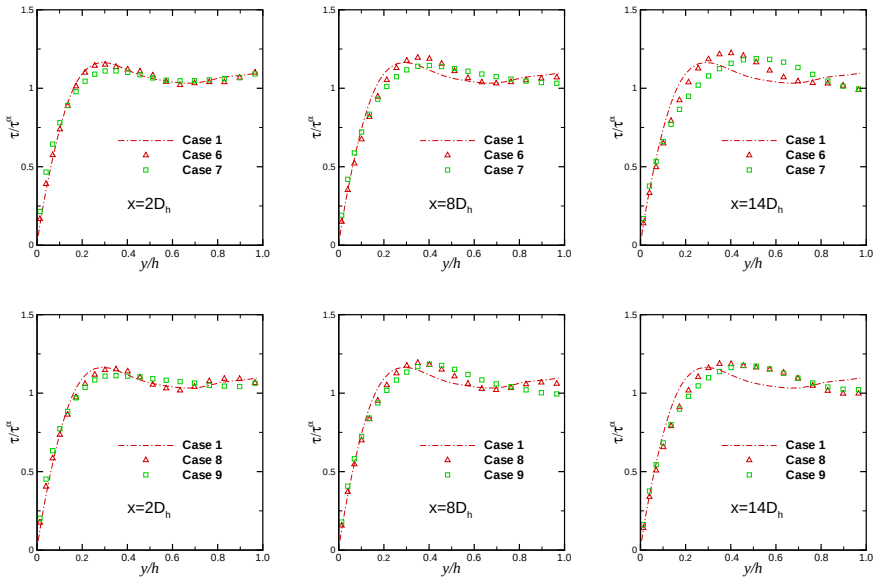

Figure 4.18 Local wall shear stress

It is also of interest to examine the effects of heating on turbulent intensities. The turbulent kinetic energy profiles along the wall bisector are shown in Fig. 4.23. The turbulent kinetic energy is defined as $k = \frac{1}{2} < u_i' u_i' >$. To eliminate any ambiguity that may be caused by property variations, the turbulent kinetic energy is normalized by square of the reference velocity. All profiles increase from zero at the wall to a maximum and then decrease to the centerline. The position of the maximum shifts toward the center as the streamwise distance increases. In the two isoflux cases, the turbulent kinetic energy decreases after station $x = 8D_h$ which implies strong laminarization of the flows. For the isothermal flows, the current domain length is still not long enough to show the damping of the turbulent kinetic energy far downstream. It can be noticed that in the largest heating rate case, case 9, the turbulent kinetic energy at the duct center decreases as x increases which suggests that the viscous sublayer has reached the duct center. It can be observed that at the same streamwise location the turbulent kinetic energy decreases when the heat transfer level is enhanced.

The distributions of the Reynolds stress $< -u'^{+}v'^{+} >$ along the wall bisector are shown in Fig. 4.24. In the two isoflux cases, the Reynolds stress keeps decreasing as the streamwise distance increases. For both isothermal and isoflux conditions, as the heat transfer rate becomes

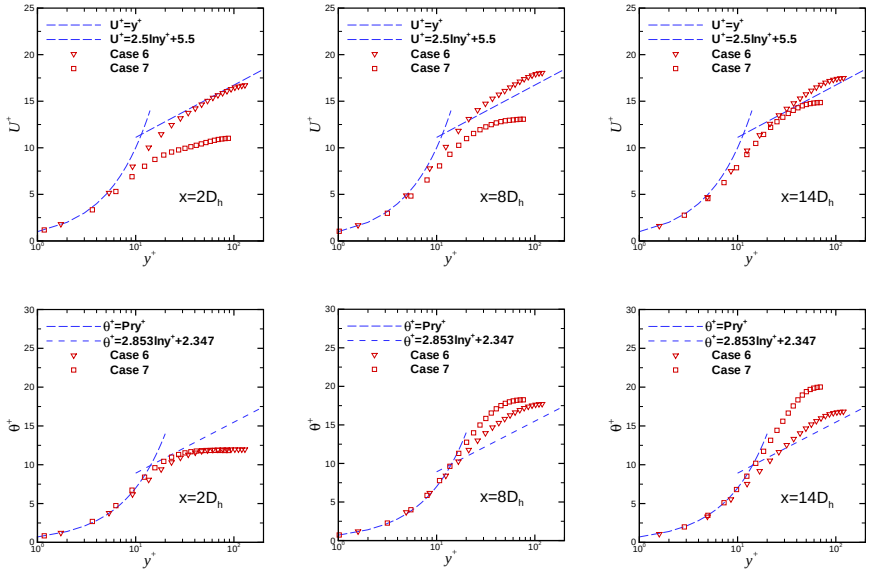

Figure 4.19 Streamwise mean velocity and temperature profiles for heated isothermal ducts along the wall bisector: in wall coordinates

higher, the Reynolds stress at the same streamwise location decreases.

The rms temperature fluctuations normalized by the local averaged friction temperature along the wall bisector are shown in Fig. 4.25. Almost the same features of the turbulent kinetic energy profiles can be found in the temperature fluctuations such as the increase-decrease shape and the shifting of the peak positions. In the isoflux flows, the rms temperature fluctuation at the wall is not zero as in the isothermal flows because the heat conduction in the wall is not taken into account (Kasagi et al., 1989). The rms value at the wall is about $1.8 \sim 2.5$ for scalar transport (Kasagi et al., 1989; Kong et al., 2000; Pallares and Davidson, 2002). In the current study, this value near the inlet is about 1.2. For the higher heating rate isoflux case (case 9), before $x = 8D_h$, the temperature fluctuation profiles are similar to those of corresponding lower heating rate case (case 8); however, after station $x = 8D_h$, the profiles begin to decrease as a result of strong heating. The same trend has been confirmed in the DNS research for strongly heated pipe flow (Satake et al., 2000).

The distributions of the streamwise turbulent heat flux $< -u'T' >$ along the wall bisector are shown in Fig. 4.26. Obvious similarity between the profiles of $< -u'T' >$ and ${T^+}_{rms}$ can

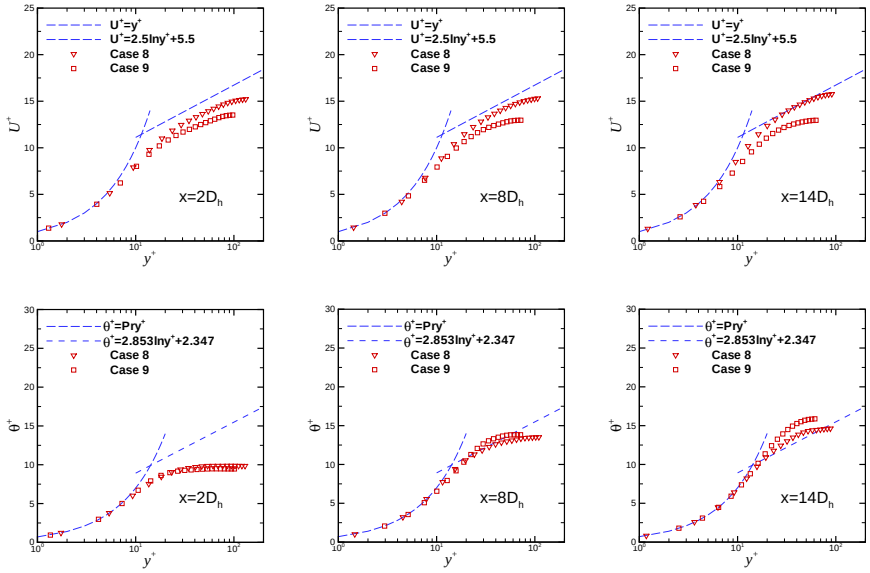

Figure 4.20 Streamwise mean velocity and temperature profiles for isoflux ducts along the wall bisector: in wall coordinates

be observed.

The distributions of the transverse turbulent heat flux $< v'T' >$ along the wall bisector are shown in Fig. 4.27. At a specific streamwise location, both streamwise and transverse turbulent heat fluxes decrease with increasing heat transfer rate.

As indicated by Monin and Yaglom (1971), in the vicinity of the wall, the mean and fluctuating quantities can be expanded by the Taylor series. For both isothermal and isoflux walls, we have

$$\begin{aligned} u' &= a_1 y + a_2 y^2 + \cdots, \\ v' &= b_2 y^2 + b_3 y^3 + \cdots, \end{aligned} \tag{4.13}$$

$$\tag{4.14}$$

and for the isothermal wall,

$$T' = c_1 y + c_3 y^3 + \cdots, \tag{4.15}$$

while for the isoflux wall,

$$T' = d_0 + d_1 y + d_3 y^3 + \cdots, \tag{4.16}$$

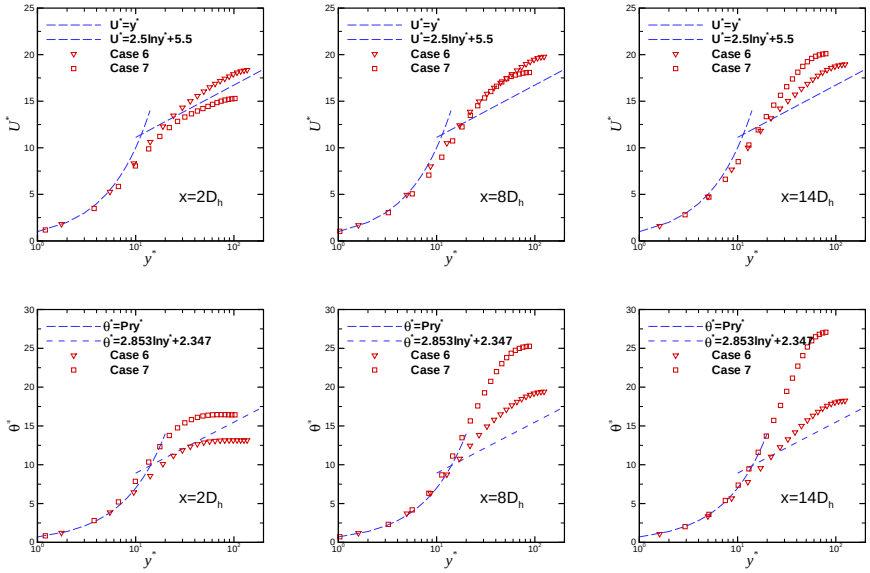

Figure 4.21 Streamwise mean velocity and temperature profiles for heated isothermal ducts along the wall bisector: in semi-local coordinates

where the coefficients a_i, b_i, c_i and d_i are functions of x, z and t. Therefore, the streamwise and transverse turbulent heat fluxes for the isothermal wall are given by

$$< -u'T' > \quad = - < a_1 c_1 > y^2 + \cdots, \tag{4.17}$$

$$< v'T' > \quad =< b_2 c_1 > y^3 + \cdots. \tag{4.18}$$

For the isoflux wall, the streamwise and transverse turbulent heat fluxes are

$$< -u'T' > \quad = - < a_1 d_0 > y + \cdots, \tag{4.19}$$

$$< v'T' > \quad =< b_2 d_0 > y^2 + \cdots. \tag{4.20}$$

The present results are shown in Fig. 4.28, which shows the above equations are valid.

The profiles of the turbulent Prandtl number along $z = 0.5D_h$ are shown in Fig. 4.29. The turbulent Prandtl number is defined as the ratio of turbulent eddy viscosity ν_t to eddy

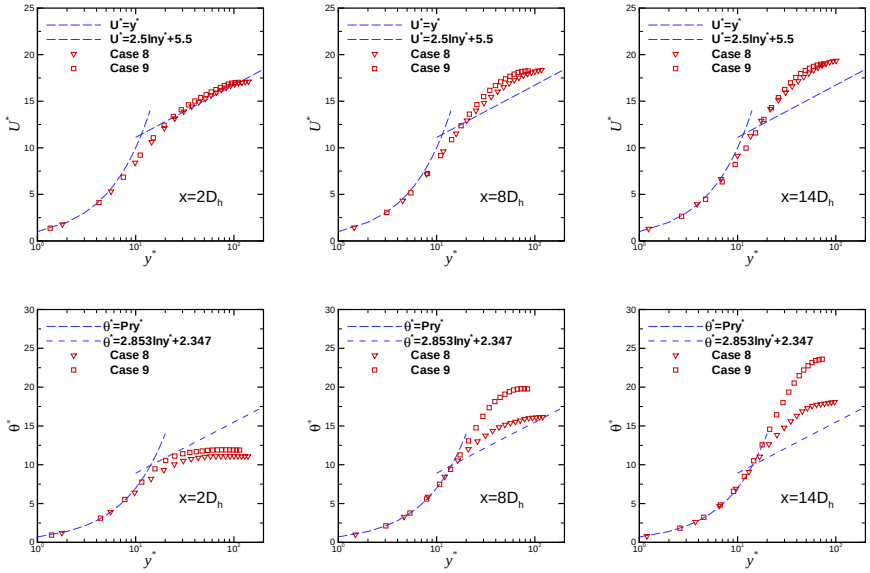

Figure 4.22 Streamwise mean velocity and temperature profiles for isoflux ducts along the wall bisector: in semi-local coordinates

diffusivity α_t:

$$Pr_t = \frac{\nu_t}{\alpha_t}, \tag{4.21}$$

where

$$\nu_t = \frac{1}{Re}\frac{\nu^*{}_t}{\nu_{ref}} = \frac{-<u'v'>}{\partial U/\partial y}, \qquad \alpha_t = \frac{1}{Re}\frac{\alpha_t^*}{\nu_{ref}} = \frac{-<v'T'>}{\partial T/\partial y}. \tag{4.22}$$

The distributions of eddy viscosity, ν_t, are shown in Fig. 4.30. From Fig. 4.29 we can see for the isothermal cases, Pr_t does not vanish at the wall. For the low heating case (case 6), $Pr_t > 1$ as $y^+ \sim 40$ while $Pr_t < 1$ as $y^+ > 40$. Comparing with the turbulent channel flow, where $Pr_t > 1$ as $y^+ \sim 60$ while $Pr_t < 1$ as $y^+ > 60$, we can see heating has a effect to decrease Pr_t. This tendency becomes more obvious for the high heating case (case 7), in which Pr_t is almost always less than unity except close to the wall. Also it can be observed that for high heating isothermal flow (case 7), the turbulent Prandtl number along the wall bisector is almost a constant, namely 0.9. For the isoflux cases, the low heating case (case 8) behaves like a isoflux turbulent channel flow (Kong et al., 2000); for the high heating case (case 9), Pr_t is also roughly a constant, and the value is about 1.0.

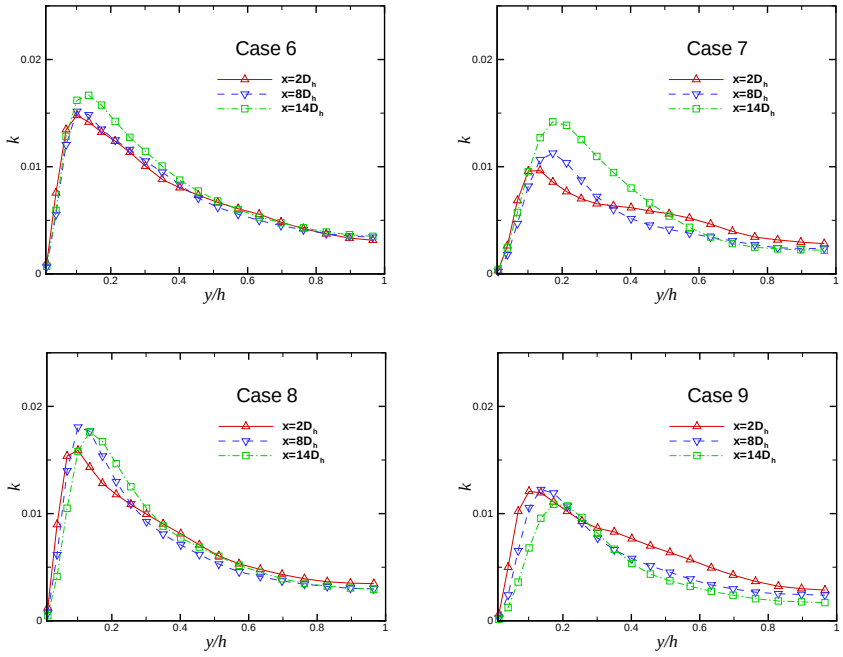

Figure 4.23 Turbulent kinetic energy

4.4 Conclusions

Large eddy simulation of hydrodynamically developed turbulent air flow thermally developing in a four-wall-heated square duct at low Mach number were carried out to study the influence of strong heating on the structure of the flow. The Navier-Stokes characteristic boundary conditions have been incorporated into finite volume LU-SGS scheme to calculate developing flow. Five isothermal (unheated) ducts were used as test cases to validate the code and numerical scheme. Very good agreement with DNS and experimental results was obtained.

Turbulent duct flows under heating with constant wall temperature and constant wall heat flux conditions were simulated. The strong heating causes significant property variations in the fluids and leads the flow to become more laminar-like. The local heat transfer coefficients decrease as the heat transfer rate increases. The mean velocity and temperature profiles approach laminar distributions downstream. The turbulent kinetic energy, temperature fluctuations and Reynolds stress also decrease. Heat transfer was found to have obvious impact on the secondary flows. The secondary flows take part in the momentum and heat transport

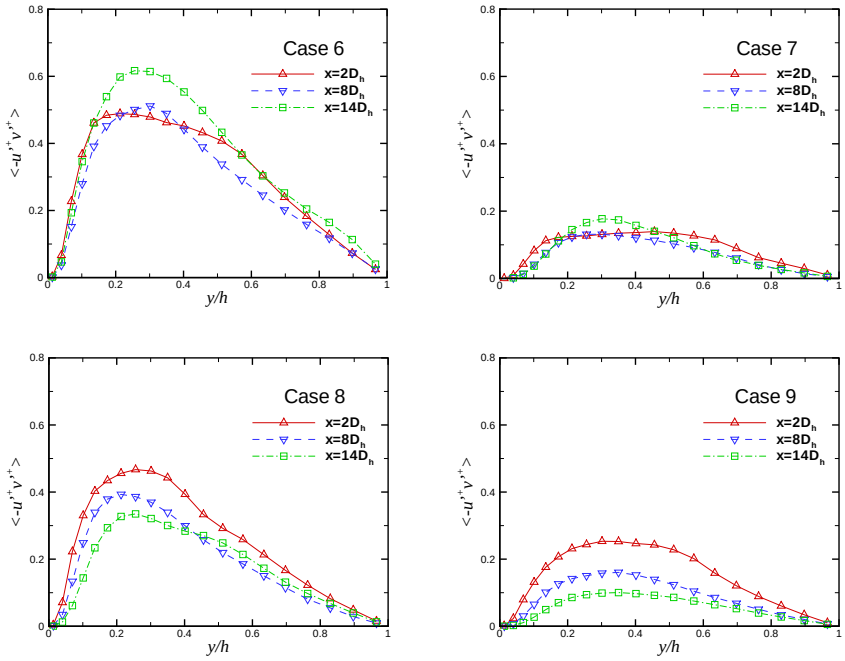

Figure 4.24 Reynolds stress

and are responsible for the modification of the distributions of wall shear stress and wall heat flux. Also heating has an effect to decrease the magnitude of turbulent Prandtl number and make its distribution more uniform.

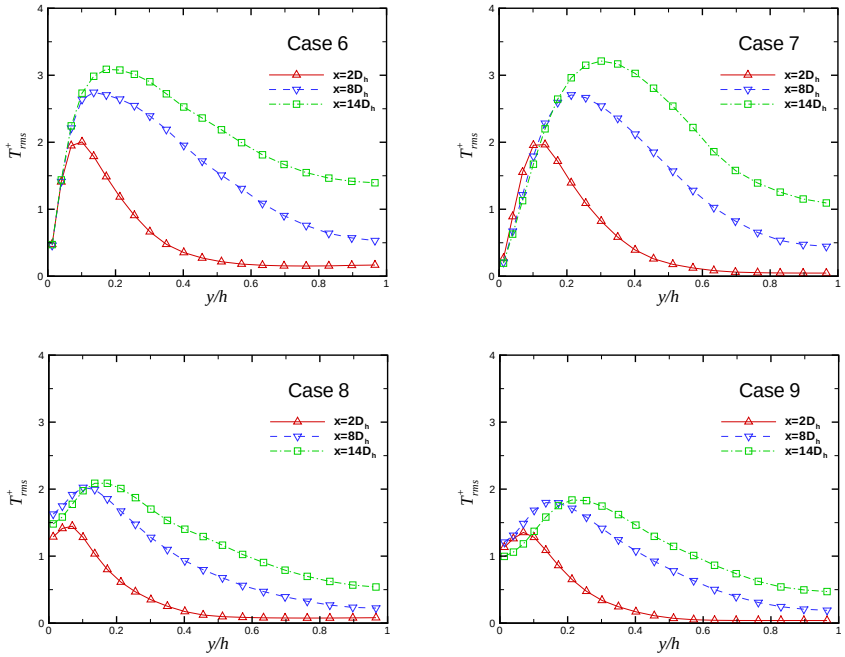

Figure 4.25 Temperature fluctuations

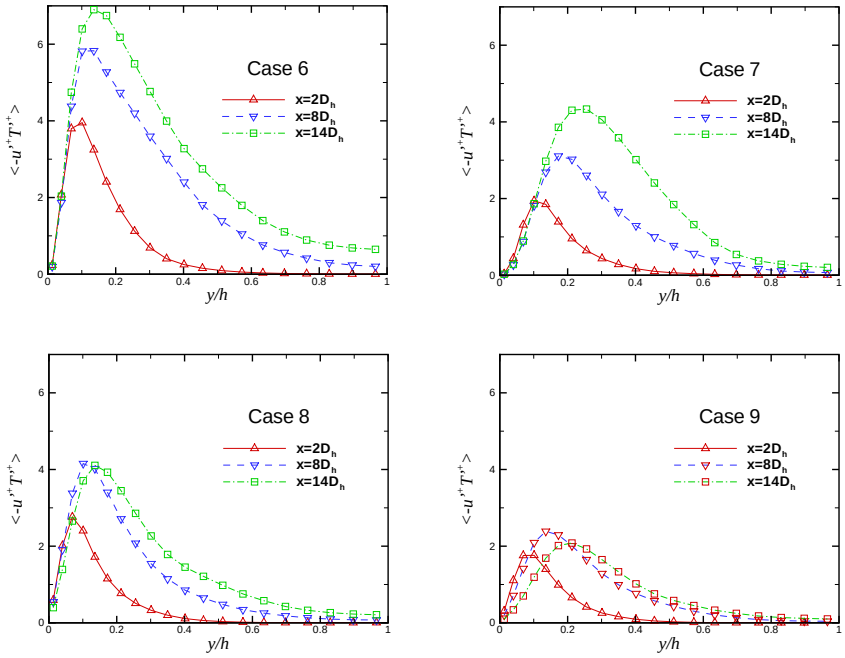

Figure 4.26 Streamwise turbulent heat flux

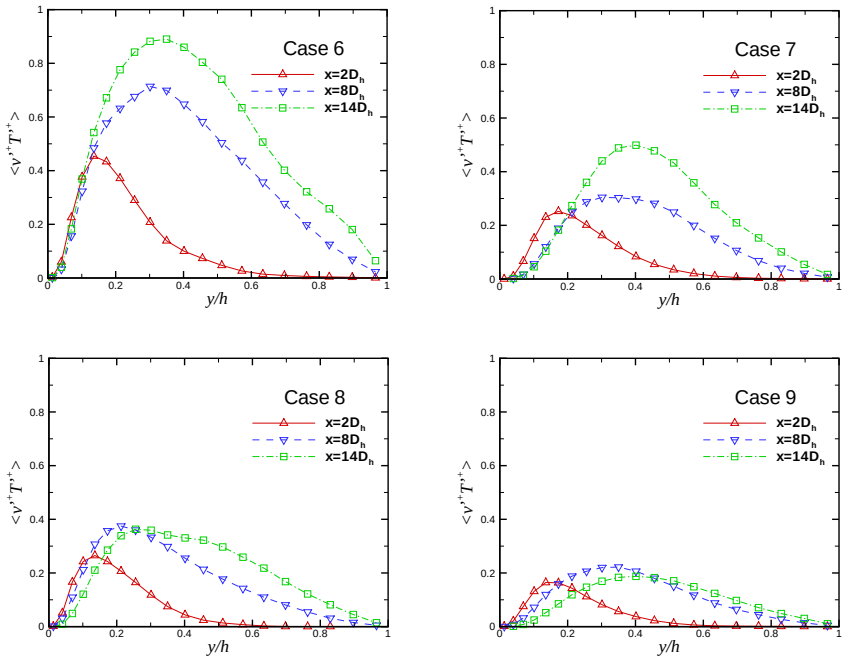

Figure 4.27 Transverse turbulent heat flux

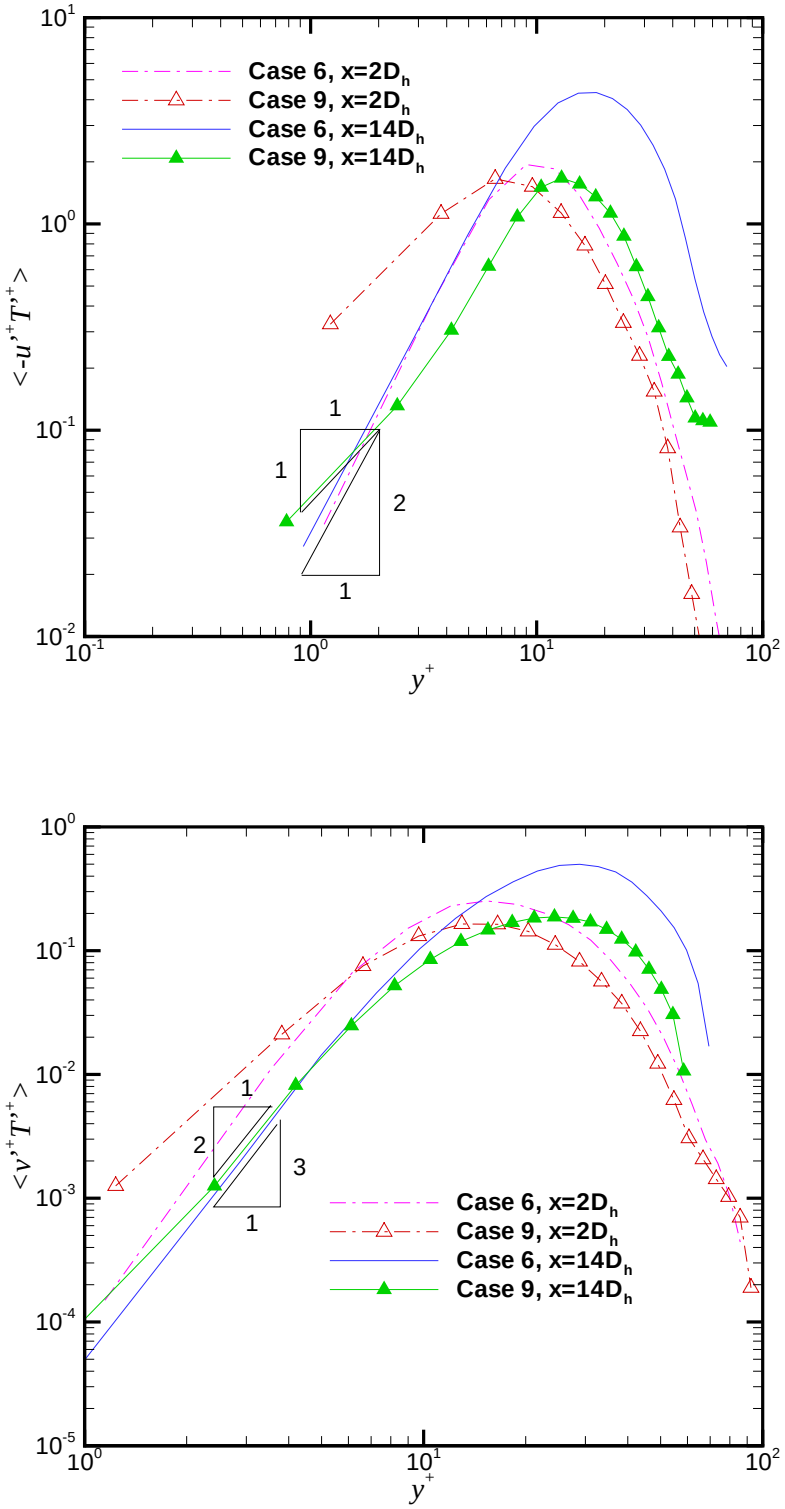

Figure 4.28 Near-wall behavior of the streamwise and transverse turbulent heat fluxes

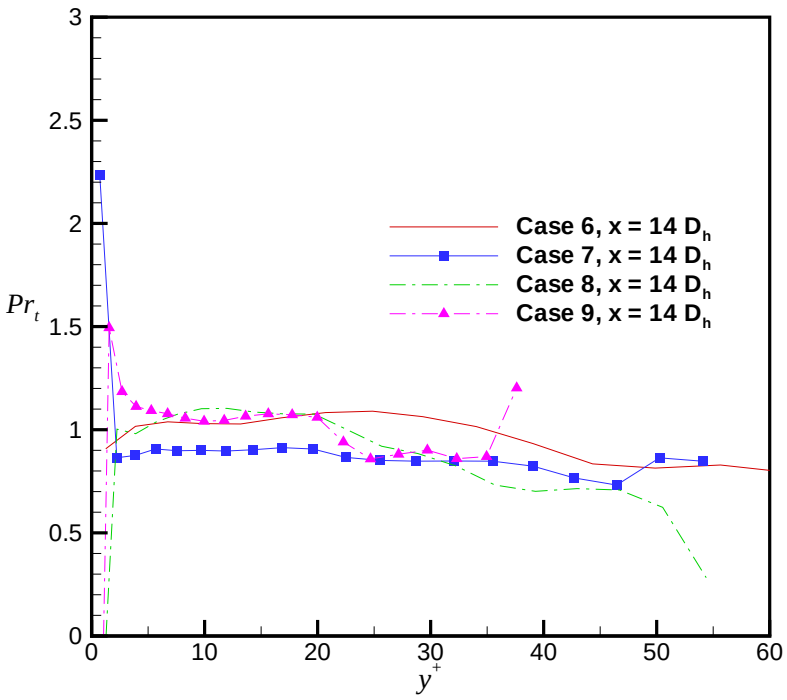

Figure 4.29 Turbulent Prandtl number

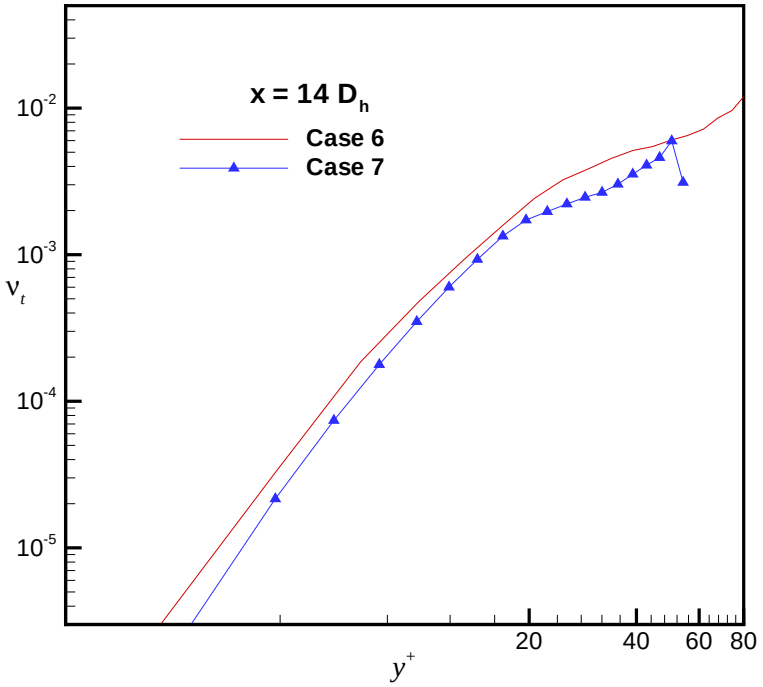

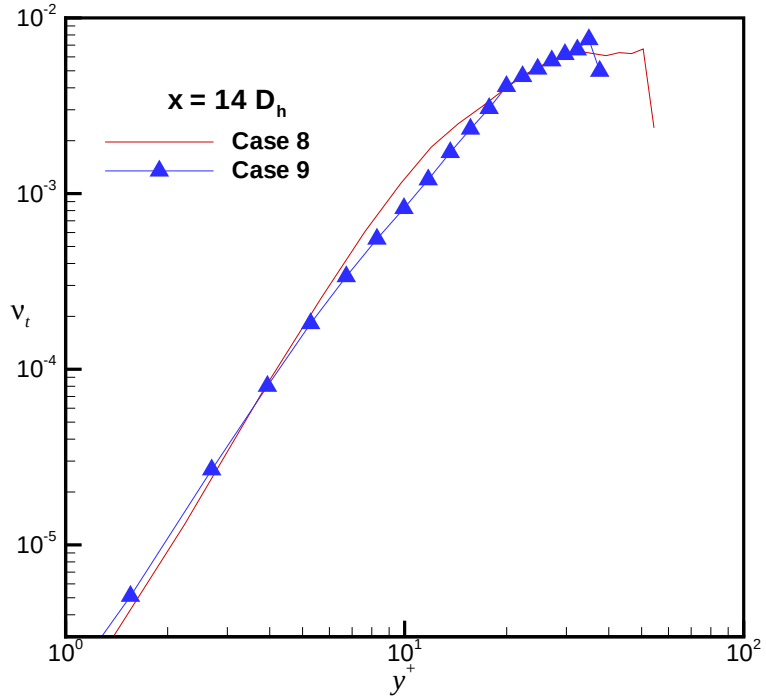

Figure 4.30 Eddy viscosity

CHAPTER 5. LARGE EDDY SIMULATION OF TURBULENT HEAT TRANSFER IN A ROTATING SQUARE DUCT

In this chapter[1], large eddy simulations of turbulent mixed convection heat transfer in a variable-property thermally developing rotating square duct are presented. A finite volume lower-upper symmetric Gauss-Seidel (LU-SGS) scheme coupled with time derivative preconditioning is used to simulate low Mach number compressible three-dimensional turbulent flow. A localized dynamic subgrid-scale (SGS) model is used to evaluate the unresolved stresses. Characteristic outflow conditions are employed so that the flow can develop further as it responds to the heating as well as rotating conditions. Several isothermal rotating duct cases were calculated and compared with previous DNS results to validate the numerical procedure. Then heated rotating ducts under constant wall heat flux are simulated. The wall heat flux is strong enough to cause the flow to separate in the outward mixed convections. A vanishing inviscid flux derivative method is designed to overcome the difficulty caused by the velocity reversal at the duct outlet when the flow separates. The Reynolds number varies from 4,500 to 10,000; The rotation number changes from 0.0133 to 0.176; The Grashof number ranges from -2.2×10^6 to 2.2×10^6. Simulation of forced and mixed convection cases shows that the flow is strongly influenced by the Coriolis and centrifugal buoyancy forces through complex and delicate mechanisms.

5.1 Introduction

Turbulent flow and related heat transfer inside a square duct rotating about an axis perpendicular to one of the walls has many engineering applications such as internal cooling of

[1]This chapter is based on the paper published in the *International Journal of Heat and Fluid Flow*, 27, 371–390, 2006.

turbine blades and automobile brakes. One of the primary concerns in these applications is the heat transfer coefficients on each wall of the rotating passage when the fluid inside is thermally developing. In turbulent duct flows, it is well known that Prandtl's secondary flow of the second kind has a significant effect on the transport of heat and momentum. This secondary flow causes distortion of the isolines of mean velocity, temperature, and their fluctuations. With rotation, Coriolis and centrifugal buoyancy forces change the mean velocity profile as well as cause a more complicated secondary flow pattern and, as a consequence, modify the heat transfer coefficient distributions on each wall.

Due to its value in military and commercial applications, the theoretical research on rotating duct flows can be traced back as far as to the 1970s. Smirnov (1978) obtained an asymptotic solution of the laminar rotating duct and gave a drag formula for this situation. Ovchinnikov and Rukolaine (1985) studied the development of laminar flow in a prismatic duct uniformly rotating about the transverse axis. Although extensive experiments (Wagner, 1991a; Morris and Ghavami-Nasr, 1991; Han and Zhang, 1992; Han et al., 1993; MacFarlane et al., 1998; Liou et al., 2001; Liou et al., 2003; Mårtensson et al. 2002) and numerical studies based on the Reynolds-averaged Navier-Stokes (RANS) equations (Prakash and Zerkle, 1992; Tekriwal, 1994; Dutta et al., 1996; Hwang et al., 1998; Lin et al., 2001; Belhoucine et al., 2004) have been carried out on this topic, relatively few direct numerical simulations (DNS) or large eddy simulations (LES) results are available, especially results in which property variations are taken into account. Kristoffersen and Andersson (1993) did direct simulations of low Reynolds number turbulent flow in a rotating channel. Tafti and Vanka (1991) carried out large eddy simulations of rotating turbulent channel flow.

Simulation of isothermal rotating ducts by Gavrilakis (2004) is the only available DNS result for rotating ducts according to the authors' knowledge. Pallares and Davidson (2000, 2002) did LES of turbulent heat transfer in both stationary and rotating square ducts. Murata and Mochizuki (1999, 2001, 2004) did large eddy simulations of turbulent heat transfer in rotating ducts with and without ribs. Most of these recent papers used the incompressible Navier-Stokes equations and periodic boundary conditions for streamwise velocity and tem-

perature because the fully developed region was their main concern. A good review on rotating internal flows without heat transfer can be found in chapter seven of *Internal flow* by Greitzer et al. (2004).

The previous researches provided much insight into the nature of the turbulent heat transfer in a fully developed rotating duct. However, a full appreciation of this phenomenon would require a more complete understanding of the details of the fluid motion. This led to the initiation of the current effort to simulate hydrodynamically developed turbulent air flow thermally developing in a four-heated-wall rotating square duct at low Mach number using large eddy simulation. The objective of this study is to develop an LES procedure to correctly predict complex turbulent flow phenomena with heat transfer and property variations and to obtain a better understanding of the physics of turbulent flow under rotating conditions. This study analyzes the air flow thermally developing in an orthogonally rotating straight smooth square duct at different Reynolds and rotation numbers. The centrifugal buoyancy effect is examined by varying the Grashof number. The constant wall heat flux condition is used in the present research. A finite volume LU-SGS scheme coupled with time derivative preconditioning is employed to solve the three-dimensional low Mach number compressible Navier-Stokes equations. Characteristic outflow boundary conditions are applied so that the flow can develop further as it responds to heating and rotating conditions. This method has been successfully implemented in the study of turbulent heat transfer in a stationary square duct (Qin and Pletcher, 2004) and LES of supercritical CO_2 pipe flow with constant wall heat flux (Wang and Pletcher, 2005). A vanishing inviscid flux derivative method is designed to avoid the possible difficulty caused by velocity reversal at the outlet which may occur as a result of an opposing centrifugal buoyancy force. To verify the code, we calculate several isothermal rotating duct cases and compare our results with DNS results. Then heated duct flow cases are simulated and the results are compared with available numerical and experimental data.

The rest of this paper is organized in two sections: the governing equations and the numerical method are described in the following section which is followed by the presentation and discussion of results.

5.2 Governing Equations and Numerical Scheme

5.2.1 Governing Equations

For gas flows with property variations, the compressible Navier-Stokes equations are applicable even if a low Mach number case is treated. The governing equations for large eddy simulation are obtained by filtering the nondimensional compressible Navier-Stokes equations in a Cartesian coordinate system. In the current research, the top-hat filter is used and Favre averaging is employed to simplify the filtered equations. The resulting equations can be written in vector form as:

$$\frac{\partial \bar{\mathbf{U}}}{\partial t} + \frac{\partial \bar{\mathbf{F}}_i}{\partial x_i} = \bar{\mathbf{S}}, \tag{5.1}$$

where

$$\bar{\mathbf{U}} = (\bar{\varrho}, \bar{\varrho}\tilde{u}, \bar{\varrho}\tilde{v}, \bar{\varrho}\tilde{w}, \bar{\varrho}\tilde{e})^T. \tag{5.2}$$

The total energy

$$\hat{e} = c_v \tilde{T} + \frac{1}{2}\tilde{u}_i \tilde{u}_i. \tag{5.3}$$

The resolved fluxes $\bar{\mathbf{F}}_i$ are

$$\bar{\mathbf{F}}_i = \begin{pmatrix} \bar{\varrho}\tilde{u}_i \\ \bar{\varrho}\tilde{u}_i\tilde{u}_1 - \hat{\sigma}_{i1} + \tau_{i1} \\ \bar{\varrho}\tilde{u}_i\tilde{u}_2 - \hat{\sigma}_{i2} + \tau_{i2} \\ \bar{\varrho}\tilde{u}_i\tilde{u}_3 - \hat{\sigma}_{i3} + \tau_{i3} \\ \bar{\varrho}\hat{e}\tilde{u}_i - \tilde{u}_j\hat{\sigma}_{ij} + \hat{q}_i + q_{ti} \end{pmatrix}, \tag{5.4}$$

where the stress tensor is

$$\hat{\sigma}_{ij} = -\bar{p}\delta_{ij} + \frac{2\bar{\mu}}{Re_r}(\bar{S}_{ij} - \frac{1}{3}\bar{S}_{kk}\delta_{ij}), \tag{5.5}$$

and $\bar{S}_{ij}$ is the strain rate tensor which is

$$\bar{S}_{ij} = \frac{1}{2}(\frac{\partial \tilde{u}_i}{\partial x_j} + \frac{\partial \tilde{u}_j}{\partial x_i}). \tag{5.6}$$

The heat flux vector is given by Fourier's law

$$\hat{q}_i = -\frac{c_p \bar{\mu}}{Re_r Pr}\frac{\partial \tilde{T}}{\partial x_i} \tag{5.7}$$

The subgrid-scale stress is

$$\tau_{ij} = \bar{\varrho}(\widetilde{u_i u_j} - \tilde{u}_i \tilde{u}_j), \tag{5.8}$$

and the subgrid-scale heat flux

$$q_{ti} = \bar{\varrho} c_v (\widetilde{T u_i} - \tilde{T} \tilde{u}_i). \tag{5.9}$$

$\bar{\mathbf{S}}$ is the resolved source term including any possible body forces. Under a rotating frame, the flow will feel both Coriolis forces and a centrifugal buoyancy force. When the rotation is in the z direction and the x coordinate is aligned with the flow direction as Fig. 5.1 shows, the source term becomes

$$\mathbf{S} = (0, 2\bar{\varrho} Ro \tilde{u}_2 + \frac{Gr}{\eta {Re_r}^2}\bar{\varrho}, -2\bar{\varrho} Ro \tilde{u}_1, 0, -\alpha - \pi - \epsilon)^T, \tag{5.10}$$

where the Reynolds number, rotation number Ro and Grashof number Gr are defined as

$$Re_r = \frac{\varrho_r V_r L_r}{\mu_r}; \;\; Ro = \frac{\omega L_r}{V_r}; \;\; Gr = \frac{{\varrho_r}^2 \beta (T_w - T_r) \omega^2 r_m {L_r}^3}{{\mu_r}^2}, \tag{5.11}$$

in which r_m is the mean rotating radius, ω the angular velocity and $\eta = \beta(T_w - T_r)$. Note we only consider the flow region far away from the rotation axis, therefore, the variations of x coordinate inside the interested flow region is negligibly small compared with the large mean rotating radius r_m. Two situations, namely outward flows and inward flows, are studied for the heated duct cases (see Fig. 5.1). For the outward flows, fluid flows away from the rotation axis and the Grashof number is positive. Since the flow is in the same direction as the centrifugal force, buoyancy acts against the high temperature fluid flow (opposing buoyancy); for the inward flows, on the contrary, fluid flows toward the rotation axis and the Grashof number is negative. Since the flow is in the opposite direction to that of the centrifugal force, buoyancy aids the high temperature fluid flow (aiding buoyancy). The last three terms in the sorce term are

$$\alpha = \tilde{u}_j \frac{\partial \tau_{ij}}{\partial x_i}, \;\; \pi = \overline{p \frac{\partial u_i}{\partial x_i}} - \bar{p} \frac{\tilde{u}_i}{x_i}, \;\; \epsilon = \overline{\sigma_{ij} \frac{\partial u_j}{\partial x_i}} - \bar{\sigma}_{ij} \frac{\partial \tilde{u}_j}{\partial x_i}. \tag{5.12}$$

For the present work, α, π and ϵ are neglected because of the low Mach number (0.001) used (Vreman et al., 1995).

For an ideal gas, the equation of state is

$$\bar{p} = \bar{\varrho} R \tilde{T}, \tag{5.13}$$

and the molecular viscosity is evaluated by the power law

$$\mu = T^{0.71}. \tag{5.14}$$

The nondimensional variables are defined as follows,

$$\begin{array}{lll} x_i = \frac{x_i{}^\star}{L_r} & t = \frac{t^\star}{L_r/V_r} & u_i = \frac{u_i{}^\star}{V_r} \\ p = \frac{p^\star}{\varrho_r {V_r}^2} & \varrho = \frac{\varrho^\star}{\varrho_r} & T = \frac{T^\star}{T_r} \\ e = \frac{e^\star}{{V_r}^2} & R = \frac{R^\star}{{V_r}^2/T_r} & c_p = \frac{{c_p}^\star}{{V_r}^2/T_r} \\ \mu = \frac{\mu^\star}{\mu_r}, & c_v = \frac{{c_v}^\star}{{V_r}^2/T_r}, & \end{array} \tag{5.15}$$

in which dimensional variables are denoted with a superscript asterisk and the subscript r denotes reference values. M_r, L_r, V_r, ϱ_r, T_r and μ_r are inflow Mach number, hydraulic diameter of the duct, inflow mean velocity, inflow mean density, inflow mean temperature and molecular viscosity evaluated by inflow mean temperature, respectively.

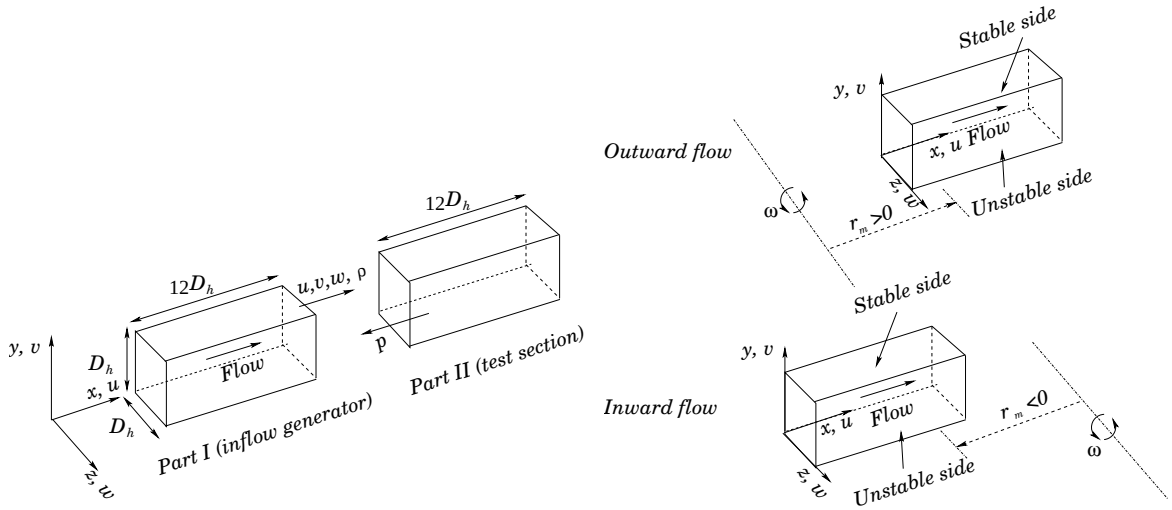

Figure 5.1 Sketch of the computational domain for rotating duct flows

5.2.2 Subgrid-Scale Modeling

The above system can be closed by modeling the subgrid-scale stress and heat flux. The localized dynamic model proposed by Piomelli and Liu (1995) is used to evaluate the subgrid-

scale stress terms. The turbulent heat flux is modeled following Wang and Pletcher (1996).

5.2.3 Numerical Scheme

The governing equations are solved with a coupled finite volume method (Qin and Pletcher, 2004). Time derivative preconditioning developed by Pletcher and Chen (1993) is adopted to overcome the singularity caused by low Mach number. This preconditioning introduces a pseudo temporal derivative into the equation. Then the preconditioned time accurate governing equation is solved by the lower-upper symmetric Gauss-Seidel (LU-SGS) scheme (Rieger and Jameson, 1988) in a dual time-stepping approach.

5.2.4 Outflow Boundary Treatment

To let the flow develop thermally, the whole computational domain is separated into two parts, as shown in Fig. 5.1. Spatially periodic boundary conditions are applied to the first (or, the inflow generator) part of the domain to generate a realistic fully developed turbulent inflow field for the second (or, the test section) part. The pressure at the test section entrance is interpolated from the interior of the domain, however. To ensure that the mass flow rate of the two parts are the same, the temperature at the entrance of the test section is recalculated according to the interpolated pressure so that the density is unchanged across the entrance section. In the inflow generator, since a periodic boundary is used, a forcing function $f(t)$ is employed in the streamwise momentum equation to maintain a constant targeted mass flow rate. This forcing function term has been widely used in numerical simulations (see e.g. Wang and Pletcher, 1996). Such a forcing function is not needed in the test section.

At the outlet of the test section, Navier-Stokes characteristic boundary conditions (NSCBC) are applied. This method, which intends to provide time-accurate boundary conditions, was proposed by Thompson (1987, 1990) and then was further developed by Poinsot and Lele (1992) and Kim and Lee (2000, 2004). This method is incorporated into the LU-SGS solver as follows.

After dropping all filtering symbols, Eq. (5.1) can be recast in terms of primitive variables

as

$$[T]\frac{\partial \mathbf{W}}{\partial t} + \frac{\partial \mathbf{F}_i}{\partial x_i} = \mathbf{S}, \tag{5.16}$$

where $\mathbf{W} = (p, u, v, w, T)^T$ and $[T] = \frac{\partial \mathbf{U}}{\partial \mathbf{W}}$ is the Jacobian matrix. The flux term $\mathbf{F}_i$ can be decomposed into two parts: the inviscid part $\mathscr{F}_i$ and another part $\mathbb{F}_i$, which takes care of the viscous and subgrid-scale terms. Consider the characteristic form of Eq. (5.16) in the x_1 direction (since the normal to the outlet is in the x_1 direction in the present work):

$$[T]\frac{\partial \mathbf{W}}{\partial t} + \frac{\partial \mathscr{F}_1}{\partial x_1} + \mathbb{C} = \mathbf{0}, \tag{5.17}$$

where $\mathbb{C}$ is the combination of the source term and flux derivative terms excluding $\frac{\partial \mathscr{F}_1}{\partial x_1}$. Define $[A]_i = \frac{\partial \mathscr{F}_i}{\partial \mathbf{W}}$, $[\mathscr{A}] = [T]^{-1}[A]_1$ and $[\Lambda] = [S]^{-1}[\mathscr{A}][S]$, where $[\Lambda]$ is the diagonal matrix whose elements are eigenvalues of $[\mathscr{A}]$, and the rows of $[S]^{-1}$ are left eigenvectors. For an ideal gas, the five eigenvalues of $[\mathscr{A}]$ are $(u_1 + c, u_1 - c, u_1, u_1, u_1)$ where c is the local sound speed. Then Eq. (5.17) can be written as

$$[S]^{-1}\frac{\partial \mathbf{W}}{\partial t} + \underbrace{\overbrace{[\Lambda][S]^{-1}}^{[\Pi]}\frac{\partial \mathbf{W}}{\partial x_1}}_{\mathscr{L}} + [S]^{-1}[T]^{-1}\mathbb{C} = \mathbf{0}. \tag{5.18}$$

By employing the characteristic form, waves with different velocities can be determined separately. At the outflow boundary, waves leaving the domain are calculated using interior points and one-sided differences. Waves propagating into the domain, however, should be estimated by available information outside the domain and also by examination of the above equation. In the current simulation, if no heating is added, $u_1 > 0$ holds for all control volumes and $\mathscr{L}_2$ is the only incoming wave since its speed is negative $(u_1 - c)$. However, if heating is added and $Gr > 0$, the opposing buoyancy force may cause the flow to separate and then the streamwise velocity becomes negative. Thus, there will be four rather than one incoming waves that need to be determined. To avoid such a situation, one can add an insulated buffer zone to the exit so that the separated region is eliminated. In the present study, instead of appending a buffer zone and then applying characteristic boundary conditions, a vanishing inviscid flux derivative method is designed for the outlet regions where $u_1 < 0$:

$$\frac{\partial \mathscr{F}_1}{\partial x_1} = 0. \tag{5.19}$$

By multiplying by $[S]$, Eq. (5.18) becomes

$$\frac{\partial \mathbf{W}}{\partial t} + [S]\mathscr{L} + [T]^{-1}\mathbb{C} = \mathbf{0}. \tag{5.20}$$

A constant pressure at infinity is used as the outlet boundary condition in the present work. This is a partially reflecting condition. From Eq. (5.20), by neglecting the source, transverse and viscous terms, which is also called the local one-dimensional inviscid (LODI) assumption, we have

$$\frac{\partial p}{\partial t} + \frac{\gamma}{\gamma - 1}\varrho(\mathscr{L}_1 + \mathscr{L}_2) = 0. \tag{5.21}$$

Let $\frac{\partial p}{\partial t} = 0$, then

$$\mathscr{L}_2 = -\mathscr{L}_1. \tag{5.22}$$

To take account of the effect of pressure at infinity, Eq. (5.22) is modified by Poinsot and Lele (1992) as

$$\mathscr{L}_2 = -\mathscr{L}_1 + K(p - p_\infty), \tag{5.23}$$

where K is a positive constant (Rudy and Strikwerda, 1980). Since $\mathscr{L} = [\Pi]\frac{\partial \mathbf{W}}{\partial x_1}$, the matrix $[\Pi]$ is changed into $[\Pi]'$ according to Eq. (5.22). The waves at the outlet boundary thus becomes

$$\mathscr{L} = [\Pi]'\frac{\partial \mathbf{W}}{\partial x_1} + \mathbf{b}, \tag{5.24}$$

where $\mathbf{b} = (0, K(p - p_\infty), 0, 0, 0)^T$ And Eq. (5.18) becomes

$$[S]^{-1}\frac{\partial \mathbf{W}}{\partial t} + [\Pi]'\frac{\partial \mathbf{W}}{\partial x_1} + \mathbf{b} + [S]^{-1}[T]^{-1}\mathbb{C} = \mathbf{0}. \tag{5.25}$$

Multiplying by $[T][S]$, Eq. (5.25) becomes

$$[T]\frac{\partial \mathbf{W}}{\partial t} + [A]'_1\frac{\partial \mathbf{W}}{\partial x_1} + \mathbb{C}' = \mathbf{0}, \tag{5.26}$$

or

$$[T]\frac{\partial \mathbf{W}}{\partial t} + \frac{\partial \mathscr{F}'_1}{\partial x_1} + \mathbb{C}' = \mathbf{0}, \tag{5.27}$$

where $[A]'_1 = [T][S][\Pi]'$, $\mathbb{C}' = \mathbb{C} + [T][S]\mathbf{b}$. Equation (5.27) is of the same form of Eq. (5.17) and should be applied at the outlet surface as Fig. 5.2 indicates. At the outlet control volume ni, the x_1 direction flux derivative term should be evaluated according to Eq. (5.17) at face $j = 3$

(interior face) and according to Eq. (5.27) at face $j = 1$ (outlet boundary face), respectively. Note that $\mathscr{F}_1'$ is unknown (though we do know $\frac{\partial \mathscr{F}_1'}{\partial x_1}$ and $\frac{\partial \mathscr{F}_1'}{\partial \mathbf{W}}$, which is $[A]_1'$), thus, we evaluate the integral of the x_1 direction flux derivative term through the boundary control volume ni as

$$\begin{aligned}\int_\Omega \frac{\partial \mathbf{F}_1}{\partial x_1} d\Omega &\approx (\mathbf{F}_{1ni}^{(m)} - \mathbf{F}_{13}^{(m)}) S_{13} \\ &+ [([A]_1 \Delta \mathbf{W})_{ni} - ([A]_1 \Delta \mathbf{W})_3] S_{13} \\ &+ \frac{\partial \mathscr{F}_1'}{\partial x_1}^{(m)} \frac{\Omega}{2} \\ &+ [([A]_1' \Delta \mathbf{W})_1 - ([A]_1' \Delta \mathbf{W})_{ni}] S_{13}, \end{aligned} \tag{5.28}$$

where S_{13} is the area of face $j = 1$ and $j = 3$. The subscript ni means the value at the center of control volume ni. For the preconditioned system, the process is essentially the same except that the eigenvalues of the matrix change. In the current LU-SGS scheme, the unsymmetry of equations used at different surfaces of the outlet control volume will cause the diagonal matrix in the $L - D - U$ decomposition to be no longer exactly diagonal. However, this difficulty can be removed by moving the non-diagonal elements to the corresponding locations in the lower and upper matrices.

5.3 Results and Discussion

5.3.1 The Isothermal Duct

Several fully developed isothermal rotating duct cases (case 1 to 4) were simulated. For these cases, step periodic boundary conditions were used. Cases 1 and 2 are compared with DNS results of Gavrilakis (2004). The computational domain is shown in Fig. 5.1. A $240 \times 40 \times 40$ grid was used for all computations. The grids were stretched toward the duct walls by using a hyperbolic tangent function (see Fig. 5.3). The effect of the grid spacing on the computed result was checked by increasing the grid number to $240 \times 60 \times 60$ for cases 1 and 2, and no major differences have been observed (see Figs. 5.5,5.6,5.7 and 5.11). The Mach number was 0.001 and the nondimensional physical time step was 8.0×10^{-3}. The computational details are in Table 5.1.

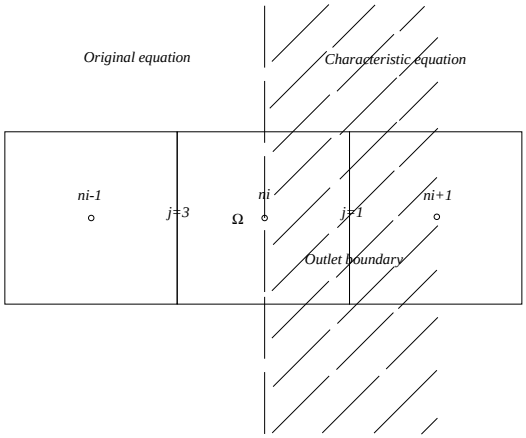

Figure 5.2 Sketch of the outlet boundary

Figure 5.4 shows the mean velocity fields (only half the fields are shown since symmetry is taken into account). A main feature is the persistent secondary flows which are constituted by two counter-rotating cells (in half the cross section). The centers of the larger cells are close to the stable wall and their location moves to the corner as rotation number increases. The smaller cells are near the unstable wall and under the corner bisectors. The strength and size of the smaller cells increase when rotation number is increased. The generation of the big cell can be attributed to the balance between pressure gradient and the Coriolis force. At the center of the duct ($z/D_h = 0.5$), the Coriolis force in the y direction is balanced by the pressure gradient. At the side walls ($z/D_h = 0$ and 1), an Ekman layer is formed since the Coriolis force is reduced as streamwise velocity decreases and the pressure gradient in the y direction drives fluid so that it is balanced by both the Coriolis force and the viscous force.

Though somewhat different from the ordinary concept of Ekman boundary layer which gives a spiral velocity variation, the Ekman layer in the current scenario is caused by the same force balance and has the same thickness as those of the traditional Ekman layer.

At the stable wall ($y/D_h = 1$), a Stewartson layer (Stewartson, 1957) comes into being to transport mass flux from the Ekman layer to the interior flow. At the unstable wall ($y/D_h = 0$),

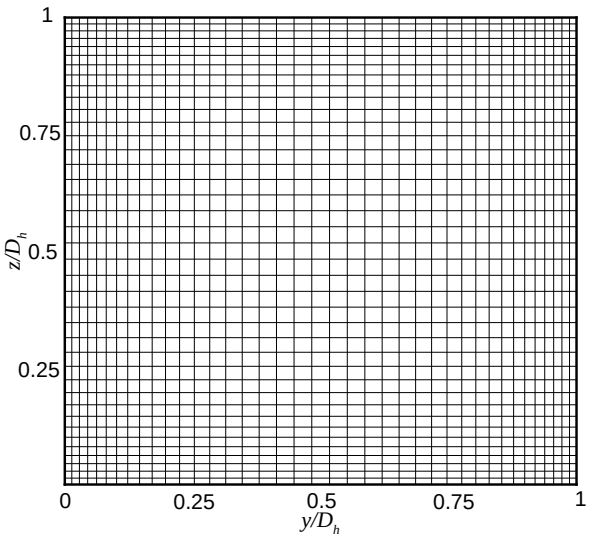

Figure 5.3 A stretched grid

secondary flow of the second kind dominates since turbulence is enhanced there.

The secondary flow convection shifts the peak value of axial velocity toward the unstable wall which results in an almost linear velocity region (see Figs. 5.5 and 5.6). The range of the linear velocity region increases with higher rotation number. The slope of the velocity profile, however, seems insensitive to the rotation rate. This can be compared with rotating turbulent channel flows, in which a linear velocity profile also shows up, however, its slope is $2Ro$ and its peak shifts toward the stable wall. When rotation rate increases, the Taylor-Proudman regime develops. That is, the interior flow field becomes uniform in the z direction (see case 4 in Fig. 5.4). This phenomenon is a result of the balance between pressure gradient and Coriolis force, which has no component in the z direction.

Figures 5.5 and 5.6 show the streamwise mean velocity profiles along the wall bisector $z/D_h = 0.5$ and Fig. 5.7 shows the streamwise mean velocity profiles along the corner bisector near the unstable wall. The mean velocity is normalized by the global wall friction velocity. The results are compared with the DNS results of Gavrilakis (2004). Very good agreement has been obtained. Figure 5.8 compares the streamwise mean velocity profiles obtained for two rotating cases with that for a non-rotating case in wall coordinates. The inner variables

Table 5.1 Simulation details of rotating duct flows

Case	Re	Ro	q_w	T_w/T_b	Gr
1	4,500	0.0133	0.0	1.0	0.0
2	4,500	0.0266	0.0	1.0	0.0
3	5,000	0.088	0.0	1.0	0.0
4	5,000	0.176	0.0	1.0	0.0
5	5,000	0.176	6.4×10^{-4}	-	0.0
6	5,000	0.176	6.4×10^{-4}	-	1.1×10^6
7	5,000	0.176	6.4×10^{-4}	-	2.2×10^6
8	5,000	0.176	6.4×10^{-4}	-	-1.1×10^6
9	5,000	0.176	6.4×10^{-4}	-	-2.2×10^6
10	5,000	0.088	6.4×10^{-4}	-	2.2×10^6
11	10,000	0.088	1.1×10^{-3}	-	2.2×10^6

U^+ and y^+ are based on the local friction velocities. The laminarization of turbulence on the stable side can be observed from the increased slope in the log-law region. On the unstable side, the enhanced turbulence causes a decrease of the slope. The degree of the laminarization and enhancement of turbulence on corresponding sides increases with rotation number. These results agree with experimental results of MacFarlane et al. (1998) and computational results of Kristoffersen and Andersson (1993) for a rotating channel. Figure 5.9 shows the average friction factor $f = 8\,(\frac{<u_\tau>}{u_b})^2$ over the duct perimeter which is normalized by the friction factor for a stationary duct of the same Reynolds number, which is given by Jones' correlation (Jones, 1976)

$$1/\sqrt{f_0} = 2log\,(1.125Re\sqrt{f_0}) - 0.8. \tag{5.29}$$

The present LES results (a $Re = 8100$, $Ro = 0.2$ case is also included) are compared with the curve which was obtained by matching the experimental data of Mårtensson et al. (2002). It can be seen that the friction factor increases rapidly with rotation number. By comparing the local friction velocities along the duct periphery under different rotation numbers, which is shown in Fig. 5.10, it can be seen that the increase of friction factor mainly takes place on the unstable wall and the side wall.

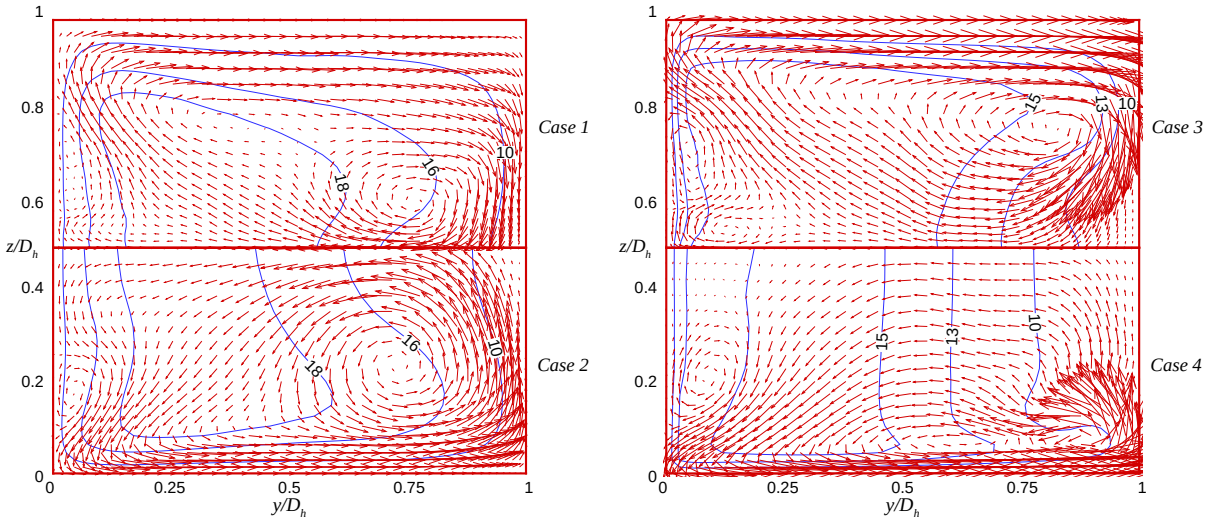

Figure 5.4 Contours of the streamwise mean velocity together with the secondary flow vector field

Figures 5.11 to 5.13 show the root mean square ($r.m.s.$) of velocity fluctuations along the wall bisector $z/D_h = 0.5$. These fluctuations are normalized by the global wall friction velocity.

A very interesting phenomenon is, unlike in a rotating channel in which cross-stream fluctuations always show maxima near the unstable wall (see Kristoffersen and Andersson, 1993; Tafti and Vanka, 1991), in a rotating duct cross-stream fluctuations are higher at the stable wall when rotation number is small. This difference can be attributed to the contribution of the secondary flows to the turbulent production in rotating duct, which are absent in a rotating channel. The interpretation of the results in Figs. 5.11 to 5.13 can be facilitated by examining the production terms in the Reynolds stress transport equations:

$$M_{ij} = P_{ij} + G_{ij}, \tag{5.30}$$

$$P_{ij} = -\varrho(\langle u_i' u_k' \rangle \frac{\partial U_j}{\partial x_k} + \langle u_j' u_k' \rangle \frac{\partial U_i}{\partial x_k}), \tag{5.31}$$

$$G_{ij} = 2\varrho Ro(\langle u_i' u_l' \rangle \epsilon_{jl3} + \langle u_j' u_l' \rangle \epsilon_{il3}), \tag{5.32}$$

where P_{ij} is caused by mean shear and G_{ij} by rotation. $\langle \cdot \rangle$ represents time averaging. The dominant components of P_{ij} and G_{ij} are shown in Table 5.2.

M_{11} and u_{rms} distributions at low and high rotation numbers are shown in Fig. 5.14. Since

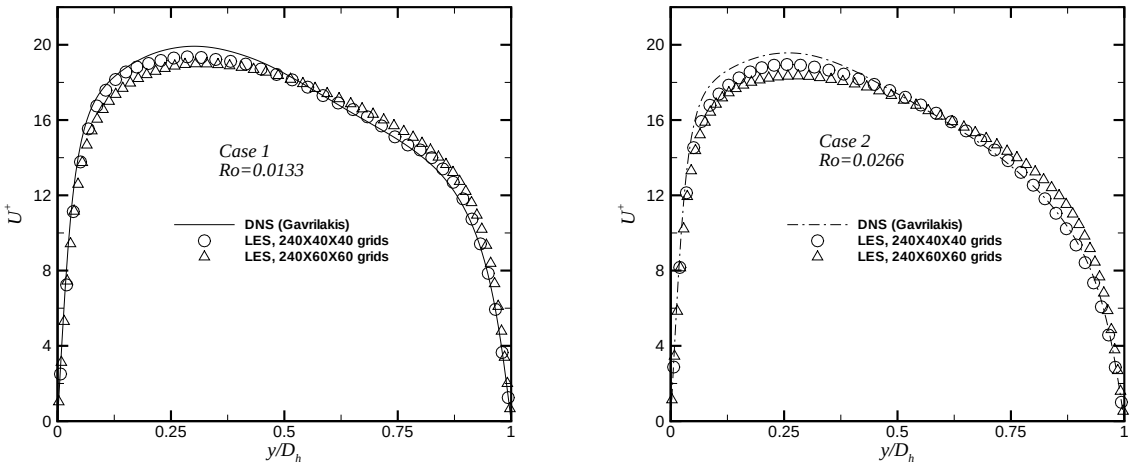

Figure 5.5 Streamwise mean velocity along wall bisector $z/D_h = 0.5$, $Ro = 0.0133$ and $Ro = 0.0266$

Table 5.2 Turbulent production terms

ij	11	22	33	12
P_{ij}	$-2\varrho(\langle u'v'\rangle\frac{\partial U}{\partial y} + \langle u'w'\rangle\frac{\partial U}{\partial z})$	$-2\varrho(\langle v'^2\rangle\frac{\partial V}{\partial y} + \langle v'w'\rangle\frac{\partial V}{\partial z})$	$-2\varrho\langle w'^2\rangle\frac{\partial W}{\partial z}$	$-\varrho\langle v'^2\rangle\frac{\partial U}{\partial y}$
G_{ij}	$4\varrho Ro\langle u'v'\rangle$	$-4\varrho Ro\langle u'v'\rangle$	0	$2\varrho Ro(\langle v'^2\rangle - \langle u'^2\rangle)$

$P_{11} \gg G_{11}$ in the current rotation number range, M_{11} is almost the same as P_{11}. Because $\langle u'v'\rangle$ is of opposite sign to $\frac{\partial U}{\partial y}$ and $\langle u'w'\rangle$ is of opposite sign to $\frac{\partial U}{\partial z}$, P_{11} is positive. Under low rotation rate, the contribution of $\frac{\partial U}{\partial z}$ to P_{11}, which causes M_{11} to attain local maximum near the horizontal wall, is of the same order as the contribution of $\frac{\partial U}{\partial y}$. When the rotation number is high, due to the Taylor-Proudman effect, the contribution of $\frac{\partial U}{\partial z}$ to P_{11} is negligible. Another feature of the M_{11} distributions is that under low rotation number, there are peak values near both stable and unstable walls while under high rotation number the peak value only appears near the unstable wall. This is because of the vanishing $\langle u'v'\rangle$ at the negative $\frac{\partial U}{\partial y}$ part under high rotation number. As for $\langle u'v'\rangle$, when the rotation rate is low, P_{12} dominates in M_{12}. At high rotation numbers (such as that in case 4), G_{12} is of the same order of magnitude as P_{12}. Furthermore, in the positive $\frac{\partial U}{\partial y}$ part, G_{12} is of the same sign as P_{12} while in the negative $\frac{\partial U}{\partial y}$

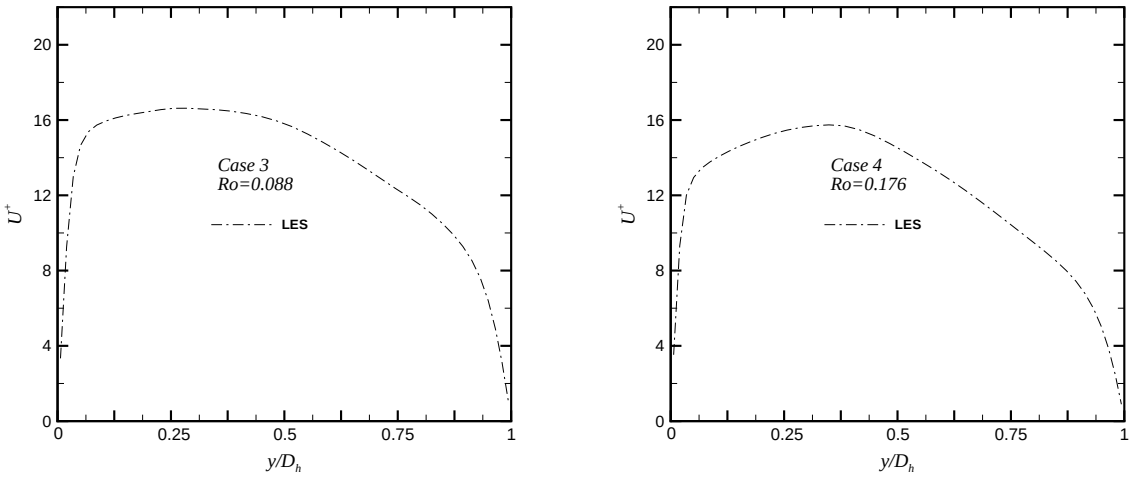

Figure 5.6 Streamwise mean velocity along wall bisector $z/D_h = 0.5$, $Ro = 0.088$ and $Ro = 0.176$

part, G_{12} is of opposite sign to P_{12} which causes M_{12} to be small and $\langle u'v' \rangle$ to vanish. These effects are shown in Fig. 5.15. $\langle v'^2 \rangle$ is affected by M_{22} as Fig. 5.16 shows. At low rotation number, the secondary flow induced P_{22} dominates in M_{22} and results in a higher v_{rms} near the stable wall. At high rotation number, G_{22} dominates in M_{22} and as a result, v_{rms} shows only one peak near the unstable wall.

5.3.2 The Heated Duct

The domain for the heated rotating duct cases are the same as that of the isothermal cases which is shown in Fig. 5.1. Heat is applied to all four walls of the test section. The constant wall heat flux condition is employed. As mentioned above, rotation reduces/increases streamwise velocity at the stable/unstable wall which results in relatively higher/lower local temperature at the stable/unstable wall. Density differences arise as a consequence of this local temperature difference. The buoyancy acts in the aiding/opposing direction to the mean flow at the unstable/stable side, respectively, if the Grashof number is positive (outward flow) and the situation is reversed when the Grashof number is negative (inward flow). In comparison with the buoyancy-free flow, the opposing buoyancy at the stable side in the outward flow

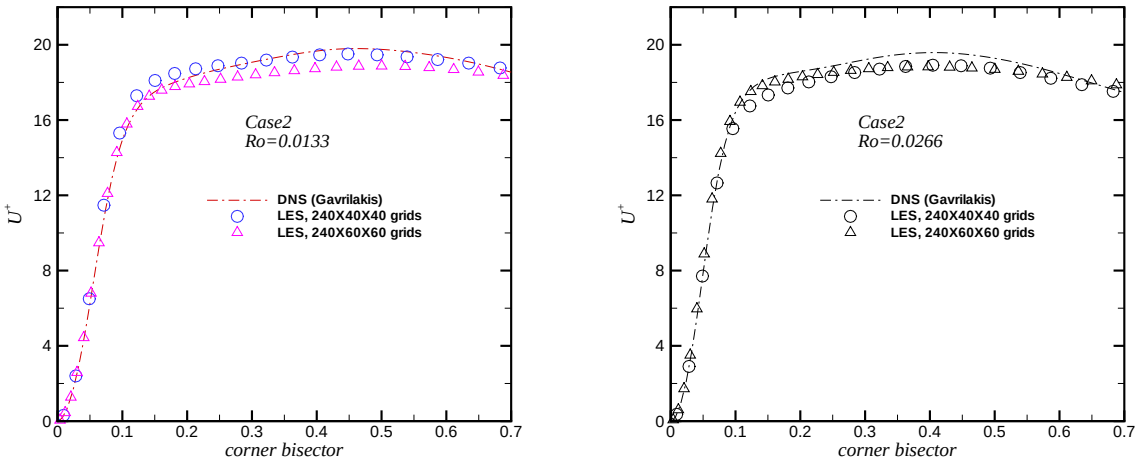

Figure 5.7 Streamwise mean velocity along corner bisector

causes the streamwise velocity there to decrease and eventually the flow separates under the current Grashof numbers. As a result, a significant temperature rise appears at the stable side near the inlet of the heated section ($x/D_h = 2$). This reduces the Nusselt number on the stable wall. However, farther downstream the temperature at the stable wall decreases somewhat. This is due to the enhancement of the near-wall turbulent kinetic energy and the turbulent transport near the stable wall, which causes a slight increase in Nusselt number (see Figs. 5.17, 5.21, 5.22 and 5.24). For the inward flow, the aiding buoyancy increases the streamwise velocity near the stable side and as a result the temperature/Nusselt number at the stable side is much lower/higher than that of the buoyancy-free flow at the same streamwise location.

These effects can be seen from Figs. 5.17 and 5.18 which present mean streamwise velocity and temperature profiles at the wall bisector $z/D_h = 0.5$ for forced and mixed convection cases.

The cross section distributions of the mean velocity (contours of U^+ and vectors of secondary flow) and temperature θ at station $x/D_h = 10$ are shown in Fig. 5.19. Here the nondimensional temperature is defined as $\theta = \frac{T-\langle T_w \rangle}{\langle T_\tau \rangle}$ where $\langle T_w \rangle$ is the average wall temperature and $\langle T_\tau \rangle$ is the average friction temperature. It can be seen that compared with the buoyancy-free flow, the secondary flow patterns become more complex because of buoyancy. In the outward mixed flows, the small rotating cell at the unstable side is suppressed and the

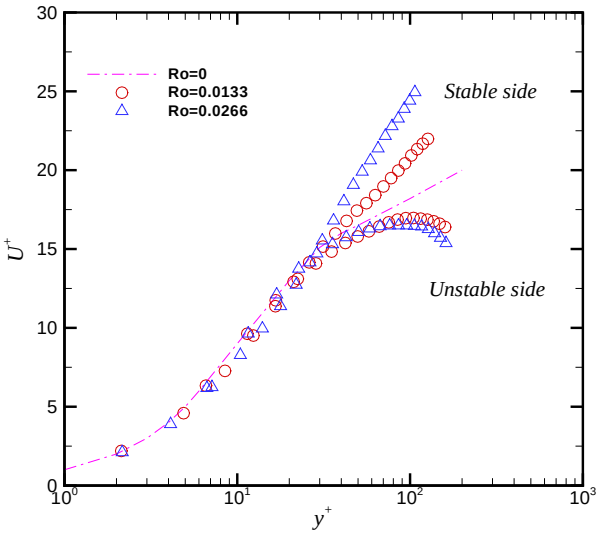

Figure 5.8 Streamwise mean velocity along wall bisector $z/D_h = 0.5$

large rotating cell near the stable side is also weakened in strength and moved toward the unstable side. In the inward mixed flows, the small rotating cell does not change much compared with forced flow and the large rotating cell is strengthened. At high Grashof number (case 9), a new cell appears near the center of the stable wall in the inward flow. These secondary flow pattern changes have significant impacts on the streamwise velocity and temperature distributions which can be most obviously observed in the inward flows where streamwise velocity isolines are severely distorted from the original Taylor-Proundman regime.

These phenomena can be explained by the force balance mentioned above. As Fig. 5.19 shows (where P means pressure gradient, C means Coriolis force), in the outward flows, the flow separation near the stable side causes the Coriolis force to reverse direction which promotes a pressure gradient toward the unstable wall. This adverse pressure gradient does not favor the development of Ekman layer at the side wall. As a result, the impingement of fluid from Ekman layer toward the stable wall is impaired. The rotating cell at the corner is then weakened and shifted toward the unstable side. In the inward flows, on the contrary, the aiding buoyancy at the stable side accelerates the local streamwise velocity and results in increased Coriolis force and pressure gradient. This enhanced favorable pressure gradient helps the development of the

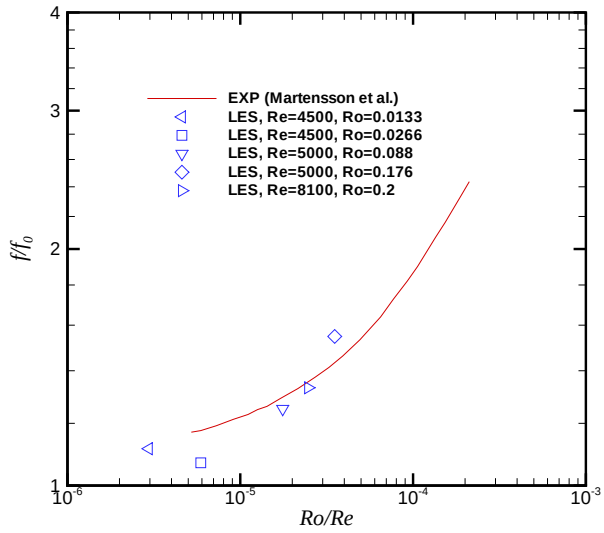

Figure 5.9 Average friction factor over duct perimeter

Ekman layer as well as the flow impingement toward the stable wall. Thus, the corner vortex is strengthened.

The variations of the secondary flow pattern affect the temperature and Nusselt number distributions at the stable wall as follows. The Stewartson layer transports hot fluid from the stable wall to the duct interior and the Ekman layer transports cold fluid from the duct center to the stable wall corner. Thus in the buoyancy-free flows, the temperature peak appears at the center of stable wall and the Nusselt number maximum shows up at the corner. In the outward flows, the Ekman layer is hindered as analyzed above; therefore, the temperature peak on the stable wall shifts to the corner and the Nusselt number maximum shows up near the stable wall-bisector. In the inward flows, the Ekman layer is strengthened. As a result, the impingement of cold fluid toward the stable wall corner is also strengthened; therefore, the temperature peak on the stable wall is located near the wall-bisector. In the case of Grashof number -2.2×10^6, a new rotating cell appeared near the stable wall center and it also transports relatively cold fluid toward the stable wall, which is responsible for the shift of the local stable wall temperature maximum from the wall bisector toward the corner.

The local temperature and Nusselt number distributions along the duct perimeter are

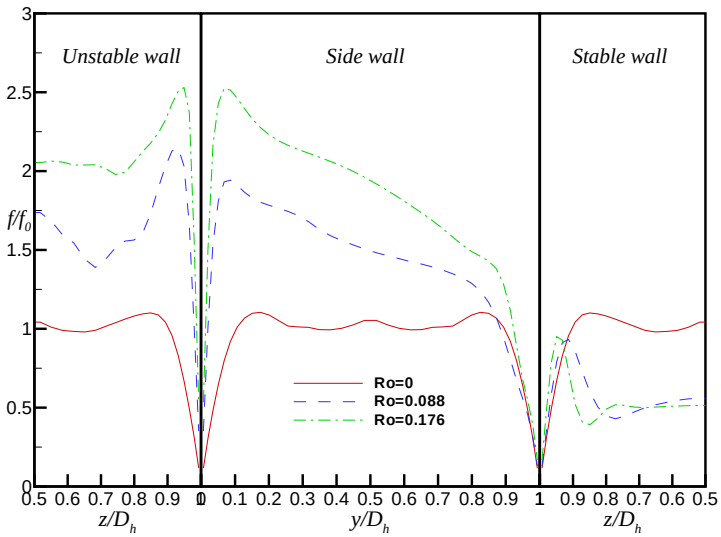

Figure 5.10 Local friction factor along duct perimeter

shown in Fig. 5.20 and Fig. 5.25, respectively, in which the phenomena mentioned above can be observed.

The variations of the secondary flow pattern also influence the mean shear stress distribution on the stable wall. Since the Ekman layer transports high speed fluid from the duct interior to the stable wall and the Stewartson layer transports low speed fluid from the stable side to the duct interior, in the buoyancy-free flows, the mean shear stress on the stable wall obtains its peak value at the corner. In the inward flows, the strengthened secondary flow results in high temperature near the central stable wall as mentioned above. And the aiding buoyancy accelerates the hot fluid; thus, a high shear stress appears near the central stable wall in the inward flows.

In summary, rotation causes the streamwise velocity to increase/decrease near the unstable/stable side. The different balances between Coriolis force, pressure gradient and viscous force give rise to persistent secondary flow patterns. Under heating the streamwise velocity differences cause temperature differences (and as a result, density differences) across the duct. The buoyancy effects due to these density differences change streamwise velocity distributions and through the force balance change the secondary flow patterns. The modified velocity field

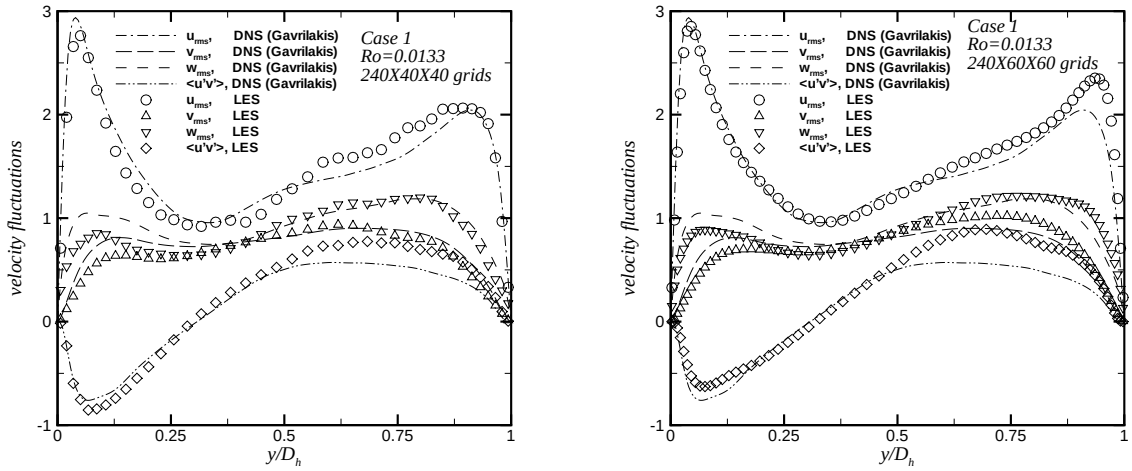

Figure 5.11 Turbulent intensities of velocity along wall bisector $z/D_h = 0.5$, $Ro = 0.0133$

changes the temperature field through convection and the modified temperature field in turn affects velocity field through buoyancy force. At the same time, the velocity and temperature fluctuations are also influenced by buoyancy.

The turbulent kinetic energy $k = \frac{1}{2}\langle u_i' u_i' \rangle$ distributions and the production term of the Reynolds averaged T.K.E. (turbulent kinetic energy) equation at the wall bisector $z/D_h = 0.5$ are shown in Fig. 5.21. The production term M is composed of two parts: P, the production due to mean shear and G, production due to buoyancy. These terms are given in the following equation:

$$M = P + G, \tag{5.33}$$

$$P = -\varrho \langle u_i' u_k' \rangle \frac{\partial U_i}{\partial x_k}, \tag{5.34}$$

$$G = \frac{Gr}{\epsilon {Re_r}^2} \langle \varrho' u' \rangle. \tag{5.35}$$

Coriolis force makes no contribution to the turbulent energy production term. The production term P also can be divided into two parts:

$$P = P_{accel} + P_{shear}, \tag{5.36}$$

$$P_{accel} = -\varrho(\langle u'^2 \rangle \frac{\partial U}{\partial x} + \langle v'^2 \rangle \frac{\partial V}{\partial y} + \langle w'^2 \rangle \frac{\partial W}{\partial z}). \tag{5.37}$$

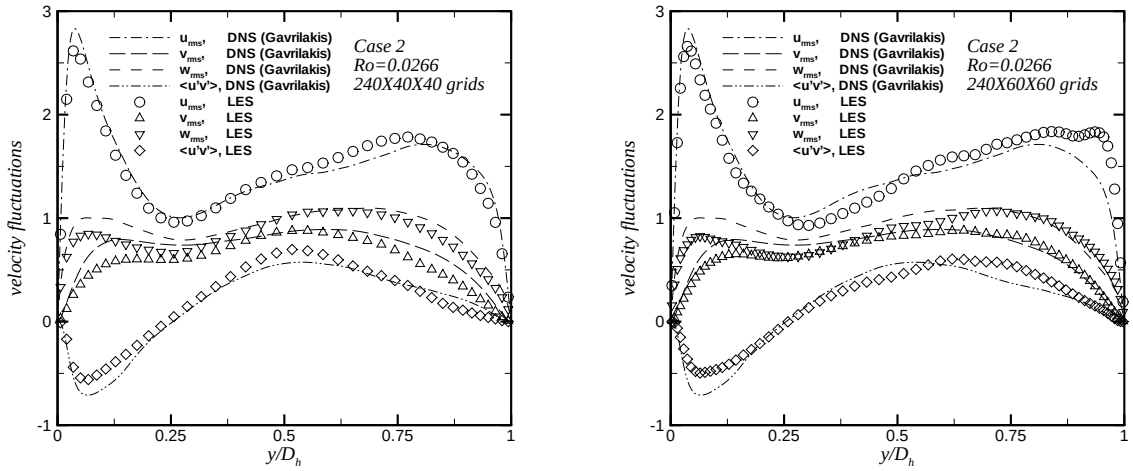

Figure 5.12 Turbulent intensities of velocity along wall bisector $z/D_h = 0.5$, $Ro = 0.0266$

The first part is the T.K.E. absorption rate caused by mean flow acceleration and the second part is the terms determined by shear stress. The T.K.E. absorption rate is always negative when the flow is under heating. The reason is that the density of the fluid keeps decreasing under heating, so the velocity of the flow keeps increasing so that a constant mass flow rate can be maintained. In the present study, P_{shear} dominates the production term. The production term caused by buoyancy, though only about 10% of the total production currently, can dominate when the buoyancy parameter $\frac{Gr}{\epsilon Re_r{}^2}$ becomes larger. In the outward flows, P_{shear} increases near the stable side because of the strong shear gradient caused by the flow separation. In contrast, in the inward flow, P_{shear} decreases slightly near the unstable side because of the reduced shear gradient.

The temperature fluctuation intensities T_{rms} and their production term along the wall bisector $z/D_h = 0.5$ are shown in Fig. 5.22. The production term M_t is given by

$$M_t = -\varrho \langle u_i{}' T' \rangle \frac{\partial T}{\partial x_i}. \tag{5.38}$$

Unlike in the thermally fully-developed flows, the contribution from the streamwise turbulent heat flux and temperature gradient, $-\varrho\langle u'T'\rangle\frac{\partial T}{\partial x}$ together with the contribution from the vertical components $-\varrho\langle v'T'\rangle\frac{\partial T}{\partial y}$ dominates the production term in the present developing heat

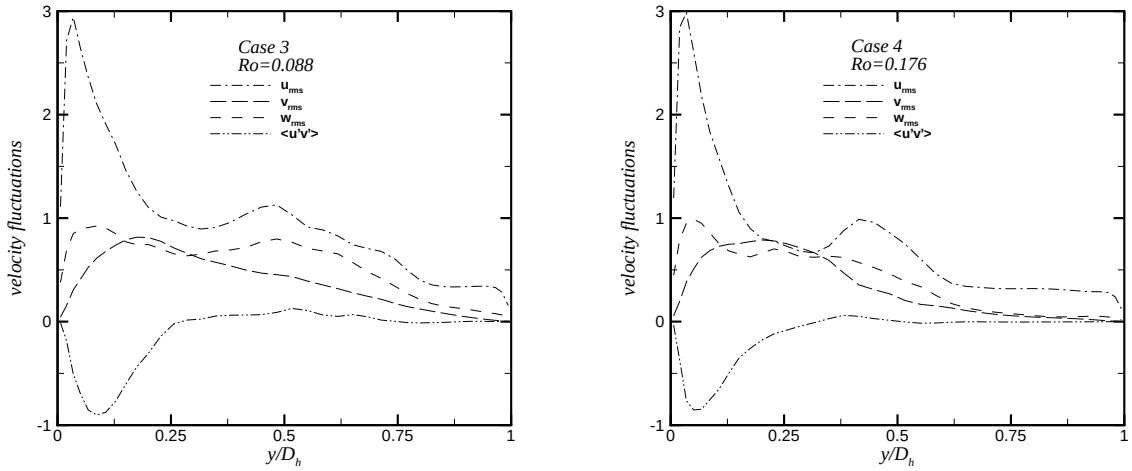

Figure 5.13 Turbulent intensities of velocity along wall bisector $z/D_h = 0.5$, $Ro = 0.088$ and $Ro = 0.176$

transfer situations. It can be seen that the temperature fluctuations, like turbulent kinetic energy, are suppressed near the stable side in the forced flow. This is due to the distributions of the turbulent heat flux components, which are also suppressed near the stable side. In the outward mixed flows, the temperature fluctuations are markedly higher than that of forced flow near the stable side which is due to the enhanced streamwise and vertical components of turbulent heat flux as a result of the augmented mixing. This helps to compensate for the effect of mean flow separation which reduces the Nusselt number near the stable wall. In the inward mixed flows, the temperature fluctuations increase near the stable side which can be attributed to the strengthening of the corner rotating cell. To aid in understanding the relation of secondary flows to the temperature fluctuations, the distributions of temperature fluctuation and the vertical component of turbulent heat flux $-\langle v'T'\rangle$ together with the secondary flow vectors in the cross section are shown in Fig. 5.23. These results were obtained at the location $x/D_h = 10$. A very strong relation between secondary flows and the vertical component of turbulent heat flux can be observed. A negative $-\langle v'T'\rangle$ zone appears near the unstable wall and a positive $-\langle v'T'\rangle$ zone appears near the stable wall. The size of the negative $-\langle v'T'\rangle$ zone is controlled by the size of the small rotating cell near the unstable side. In the

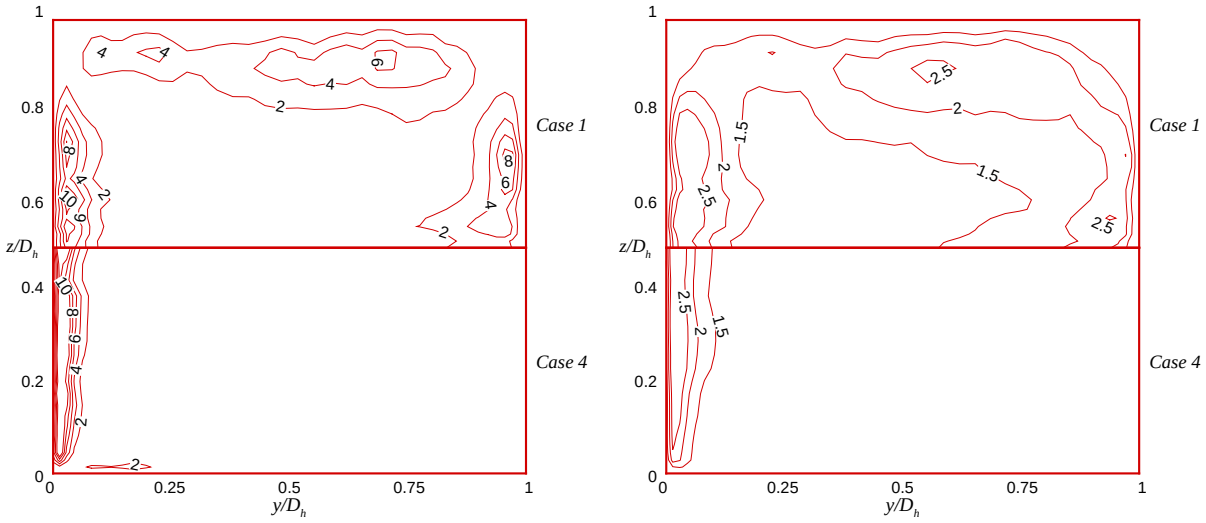

Figure 5.14 Contours of M_{11} (left) and u_{rms} (right)

outward mixed flow, the small rotating cell is suppressed which results in the reduction of this zone. The positive $-\langle v'T'\rangle$ zone is related to the large rotating cell near the stable side. In the outward mixed flow, the large rotating cell and the positive $-\langle v'T'\rangle$ zone are both displaced towards the unstable side. In the inward mixed flow, the strengthened stable side rotating cell causes an intensified positive $-\langle v'T'\rangle$ zone, which is responsible for the augmentation of temperature fluctuations near the stable side compared with the forced flow.

The streamwise distribution of the wall-averaged Nusselt number ratio Nu_x/Nu_s is shown in Fig. 5.24. The Reynolds number and the rotation number are fixed at $Re = 5000$ and $Ro = 0.176$, respectively. Nu_x is the local peripherally averaged Nusselt number. The reference Nusselt number Nu_s is the fully developed Nusselt number for stationary straight pipe flow correlated by Dittus-Boelter/McAdams as $Nu_s = 0.023Re^{0.8}Pr^{0.4}$. The triangles are the experimental data of Han and Zhang (1992). Compared with buoyancy-free flow, the heat transfer coefficient is enhanced at the unstable wall in the outward mixed flows as well as the stable wall in the inward mixed flows due to the increased mean shear, which is caused by the aiding buoyancy. The opposing buoyancy near the stable side in the outward mixed flows causes the flow to separate. The slow speed flow close to the stable wall reduces the Nusselt number at first; however, as the flow goes downstream, the situation is improved

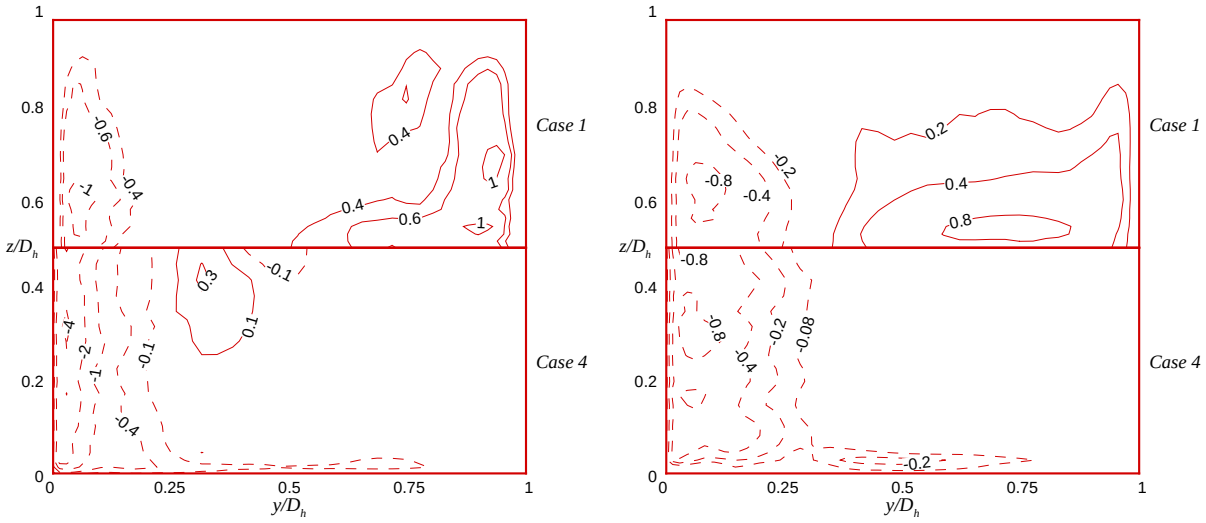

Figure 5.15 Contours of M_{12} (left) and $\langle u'v' \rangle$ (right)

because of the enhanced turbulent kinetic energy near the stable side. As can be observed, the stable wall Nusselt number of the $Gr = 2.2 \times 10^6$ case surpasses the $Gr = 1.1 \times 10^6$ case at $x/D_h = 1.4$ and then surpasses the forced flow at $x/D_h = 8$. The Nusselt numbers at the side wall of the outward mixed flows are lower than that of the forced flow. The four-wall averaged Nusselt number of the outward mixed flow is lower than that of the forced flow at first but eventually becomes higher than the forced flow. For the inward mixed flows, the unstable wall Nusselt number is less than that of the forced flow because the opposing buoyancy retards the streamwise mean velocity near the unstable side. However, in the current developing situation, there is no obvious differences in the side wall and four-wall averaged Nusselt number between the inward mixed and forced flow.

The local Nusselt number ratio Nu/Nu_s and mean shear stress τ/τ^a distribution along the duct perimeter at $x/D_h = 10$ are shown in Fig. 5.25. Here τ is obtained by calculating the value of $\mu\frac{U}{\delta}$ of the nearest point from the wall (δ is the distance from the wall) and τ^a is the peripherally averaged shear stress. Note that the negative shear stress at the side wall near $y/D_h = 1$ and the stable wall in the outward mixed flows are due to the mean streamwise velocity reversal. A strong correlation between the two distributions can be found, especially near the unstable wall and side wall. At the stable wall, turbulent transport is also important

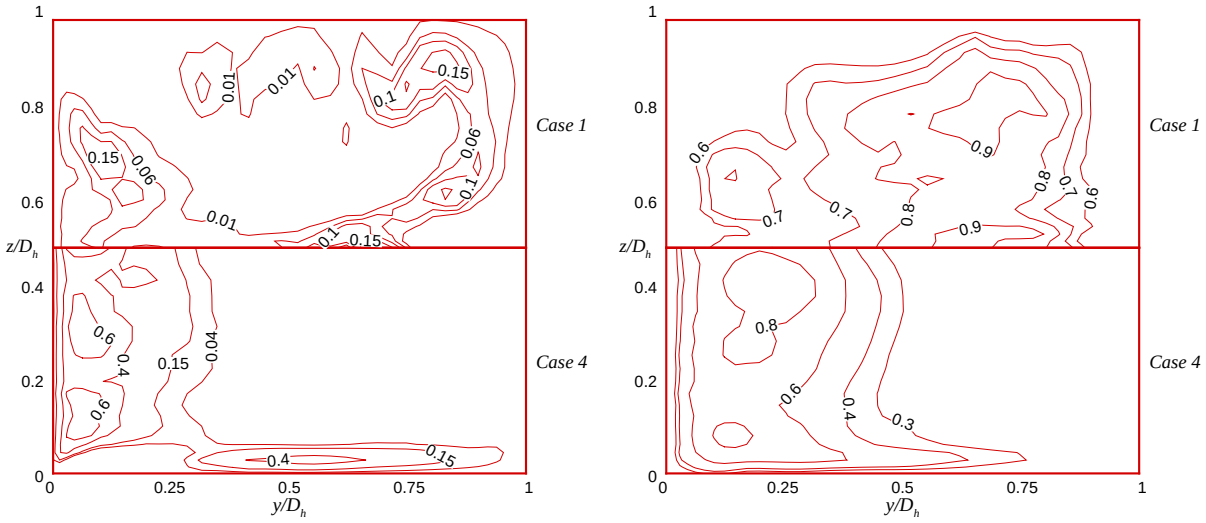

Figure 5.16 Contours of M_{22} (left) and v_{rms} (right)

in addition to the mean shear for the outward mixed flows as mentioned.

Attention is now turned to the effects of rotation number and Reynolds number on heat transfer. As shown in Fig. 5.26, at the same Reynolds number and Grashof number, the differences between the heat transfer coefficients on the unstable and stable walls increase with increasing rotation number; at the same rotation number and Grashof number, the Reynolds number shows little impact on local heat transfer coefficients, which agrees well with the physical meaning of rotation number (which is the measurement of the relative strength of Coriolis force to inertia force) and experimental results (Han and Zhang, 1992).

5.4 Summary and Conclusions

Turbulent mixed convection heat transfer in a variable-property thermally developing rotating square duct was investigated using large eddy simulation. The effects of Coriolis force and rotational buoyancy on the mean flow structure, turbulent fluctuation intensities and heat transfer behavior were studied. Fairly satisfactory agreement between prediction and experimental results has been achieved. The discrepancy may be due to the uncertainty of measurements in experiments (up to 20-25% according to Han and Zhang, 1992) and the boundary condition differences between experiments and simulations. Based on the analysis

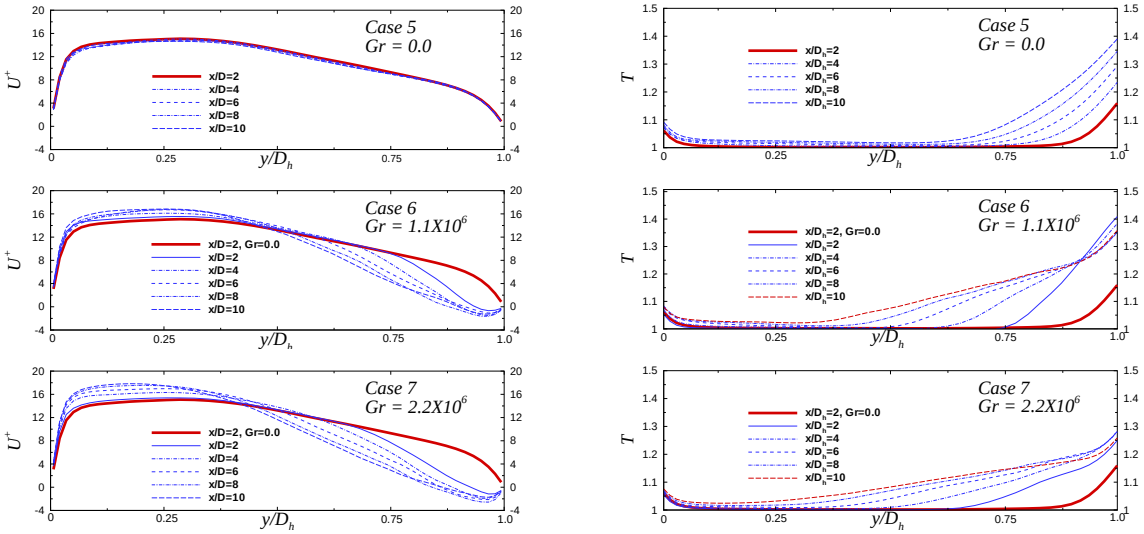

Figure 5.17 Streamwise mean velocity and temperature along wall bisector $z/D_h = 0.5$, case 5, 6 and 7

of the present LES results, the following conclusions can be drawn.

1). In the fully developed isothermal rotating duct flows, the cross-stream fluctuations ($\langle v'^2 \rangle$ and $\langle w'^2 \rangle$) obtain their peak values near the stable side rather than near the unstable side when the rotation number is small. This is due to the contribution of secondary flows on the turbulent production.

2). Buoyancy changes the secondary flow pattern through a delicate force balance. In the outward flows, the opposing buoyancy retards or even reverses the flow near the stable side. This results in a reduced or even reversed Coriolis force and in turn, a reduced favorable or even adverse pressure gradient which does not favor the development of the Ekman layer at the side wall and, as a result, weakens the stable wall corner rotating cell. In the inward flows, the aiding buoyancy accelerates fluids close to the stable wall giving rise to an enhanced favorable pressure gradient which strengthens the Ekman layer as well as the stable wall corner rotating cell.

3). Buoyancy influences the temperature (and as a result, Nusselt number) and mean shear stress distribution on the stable wall not only by changing the streamwise velocity directly, but also by modifying secondary flow patterns. Since the Ekman layer transports cold and

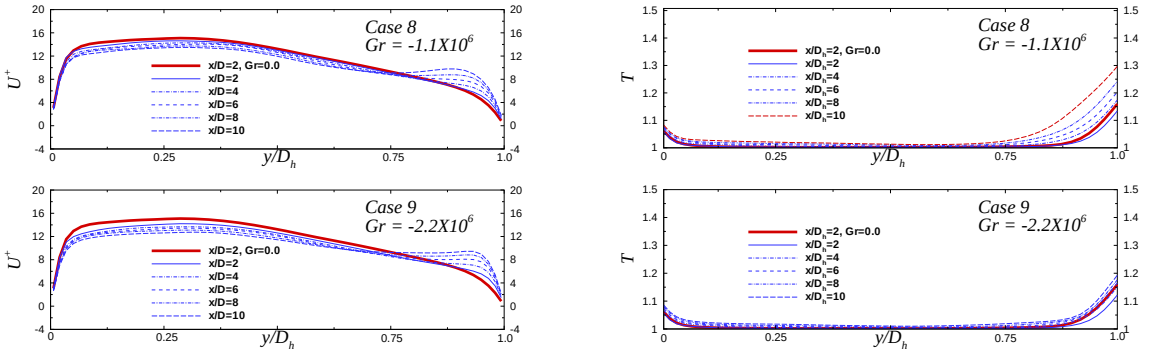

Figure 5.18 Streamwise mean velocity and temperature along wall bisector $z/D_h = 0.5$, case 8 and 9

high speed fluid from the duct interior to the stable wall and the Stewartson layer transports hot and low speed fluid from the stable side to the duct interior, in the buoyancy-free flows, the Nusselt number and mean shear stress on the stable wall obtains their peak values at the corner, while the temperature maximum appears at the wall-bisector. In the outward flows, the weakened secondary flow results in high temperature near the stable side corner and a Nusselt number maximum at the wall-bisector. In the inward flows, the strengthened secondary flow results in high temperature near the central stable wall. The aiding buoyancy accelerates the hot fluid; thus, a high shear stress appears near the stable wall-bisector in the inward flows. This explains the discrepancy between the Nusselt number and shear stress distributions at the stable wall.

4). Buoyancy affects turbulent kinetic energy and temperature fluctuation distributions through its contributions to the relevant production terms. Buoyancy influences the production of turbulent kinetic energy in two ways: by modifying the mean shear and by acting directly as a buoyancy production term. The latter can dominate if the buoyancy parameter $\frac{Gr}{\epsilon Re_r^2}$ becomes large. It has been found that the secondary flow pattern has a strong relationship with the vertical heat flux $-\langle v'T'\rangle$, which is vital in the production term of the temperature fluctuations. Buoyancy thus impacts the temperature fluctuation indirectly by altering the secondary flow pattern.

5). There is a strong correlation between the peripheral distributions of local Nusselt num-

ber and mean shear stress at the unstable wall and the side wall. The discrepancy between the Nusselt number and shear stress distributions at the stable wall is explained in conclusion 3.

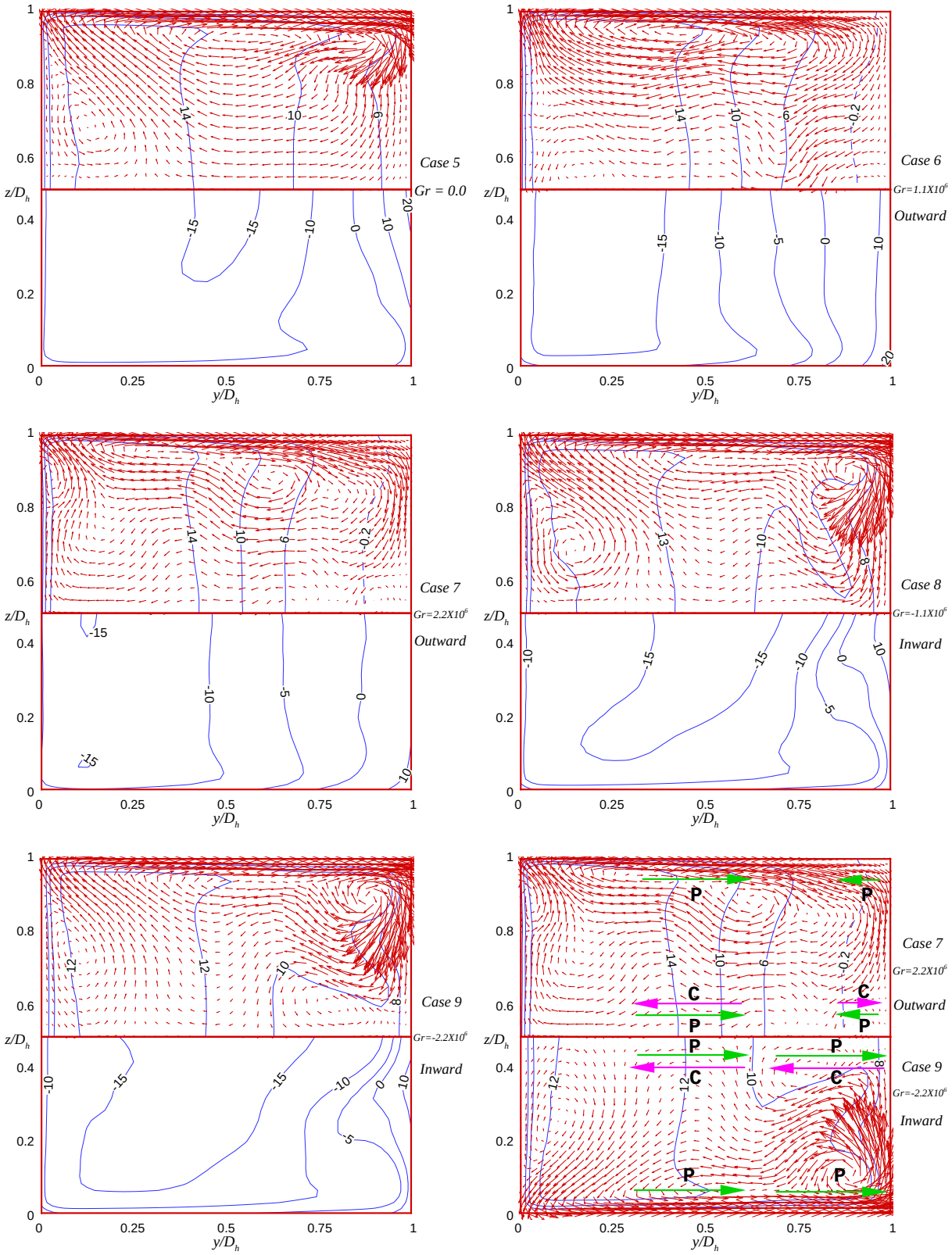

Figure 5.19 Mean velocity (up) and temperature (below) at $x/D_h = 10$ and schematic of the mechanism of the variations of secondary flows

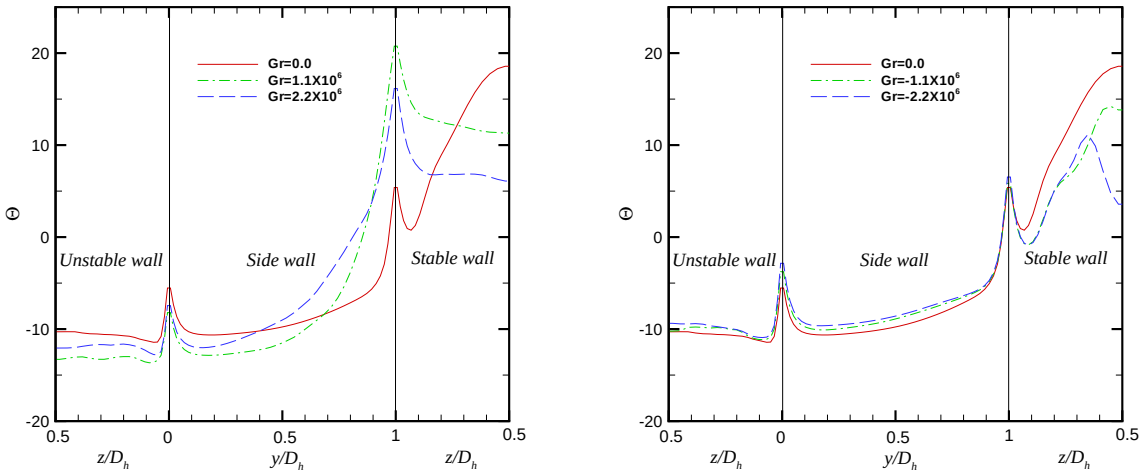

Figure 5.20 Local temperature distributions along duct perimeter at $x/D_h = 10$

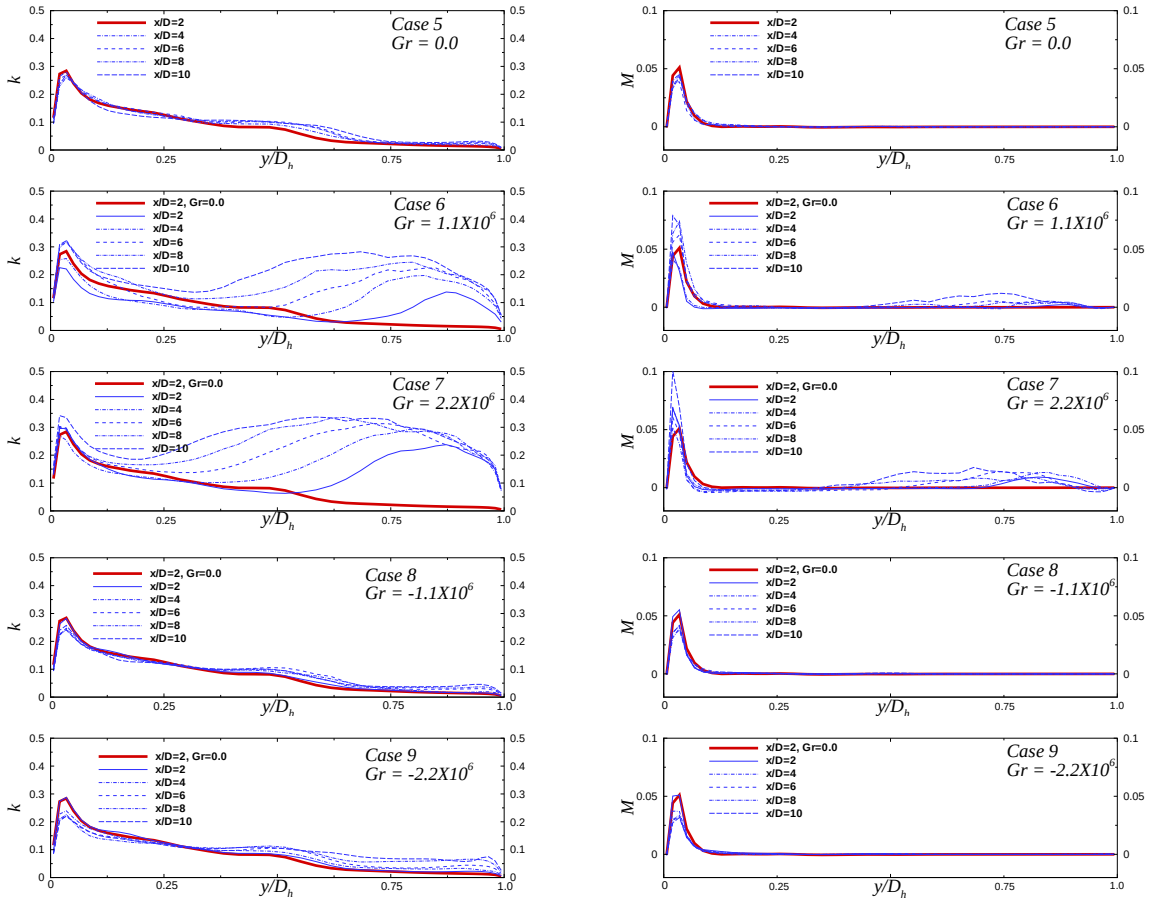

Figure 5.21 Turbulent kinetic energy (left) and its production term (right) along wall bisector $z/D_h = 0.5$

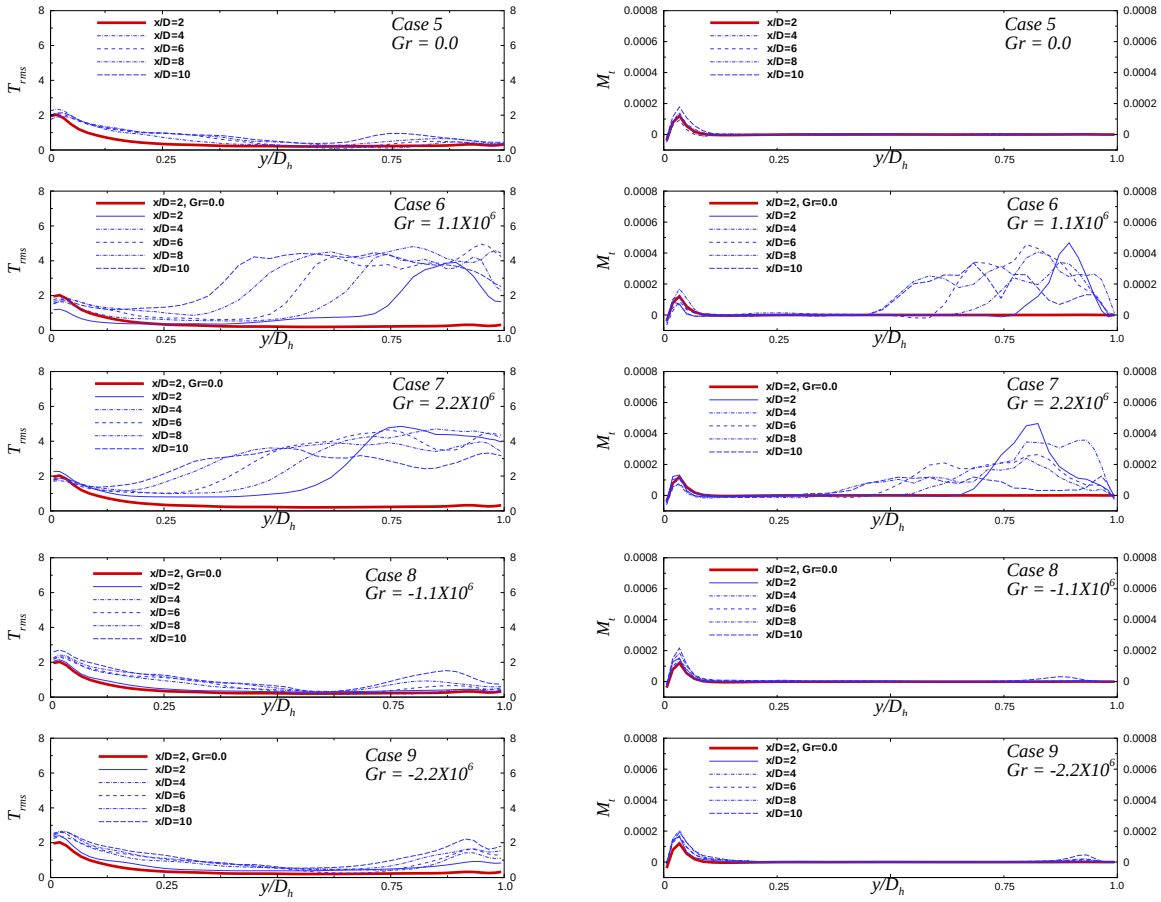

Figure 5.22 Temperature fluctuation intensity (left) and its production term (right) along wall bisector $z/D_h = 0.5$

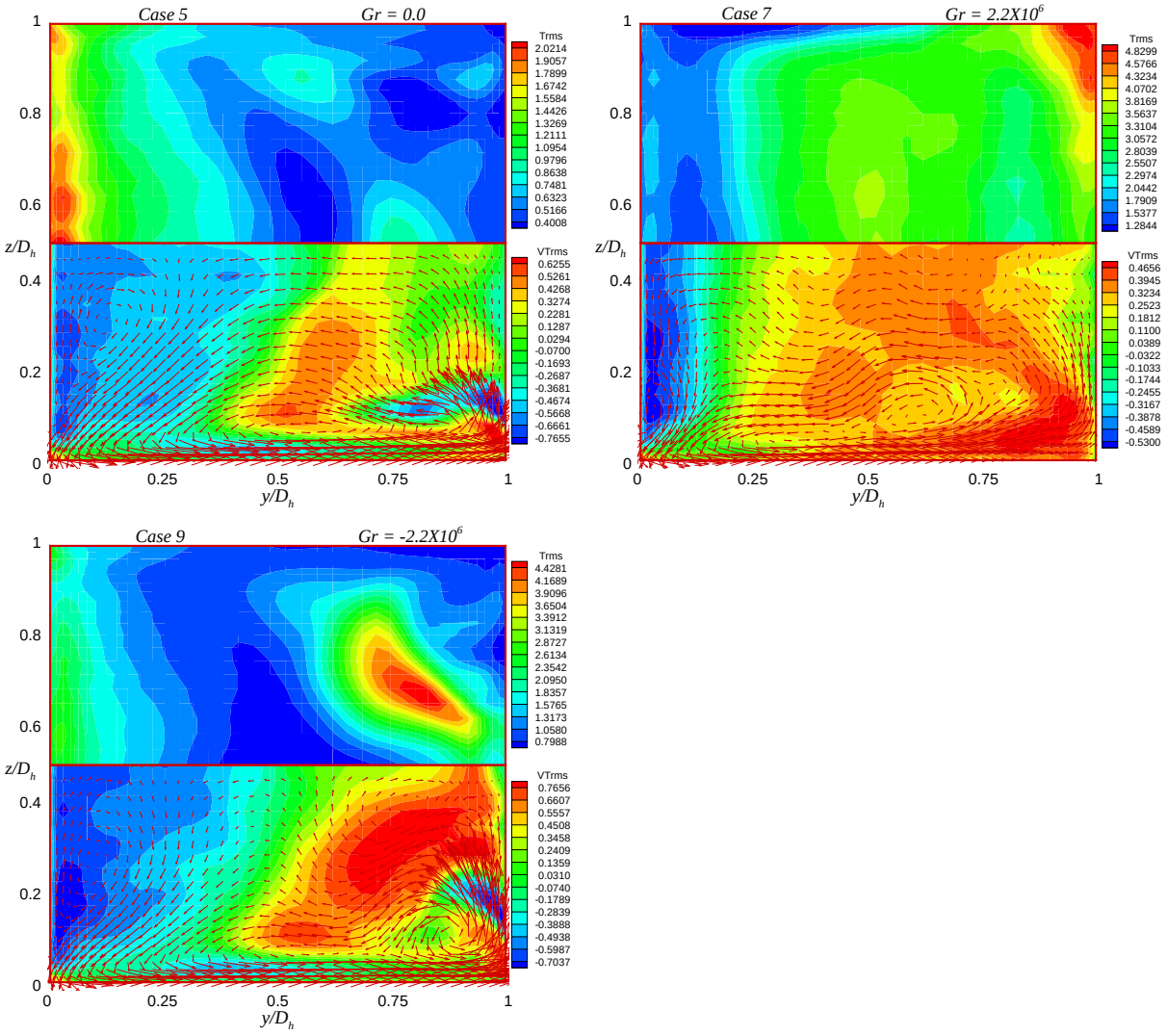

Figure 5.23 Temperature fluctuation intensity (up) and vertical turbulent heat flux (below) at $x/D_h = 10$

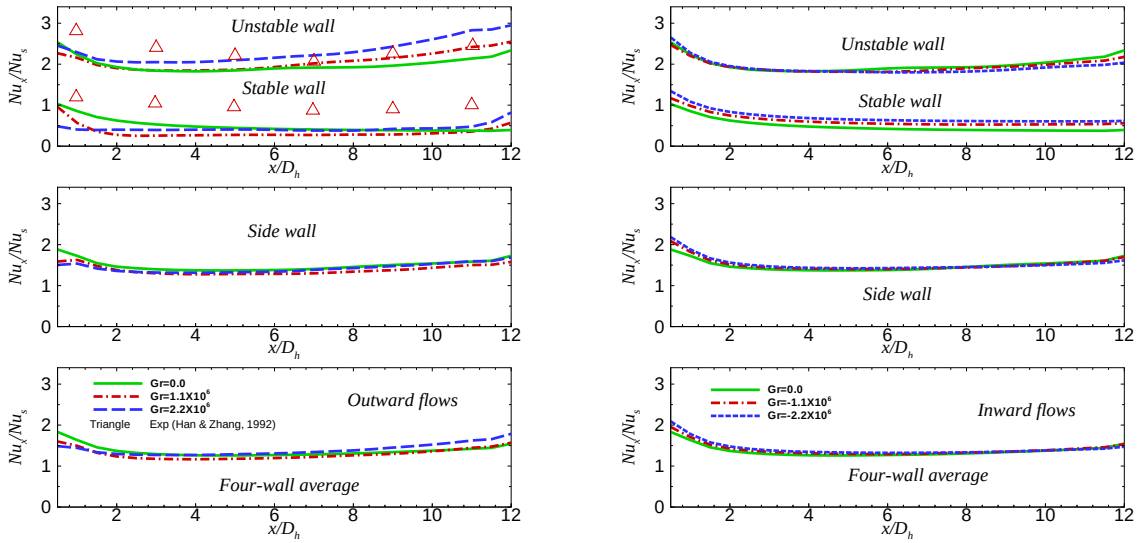

Figure 5.24 Streamwise distribution of wall-averaged Nusselt number

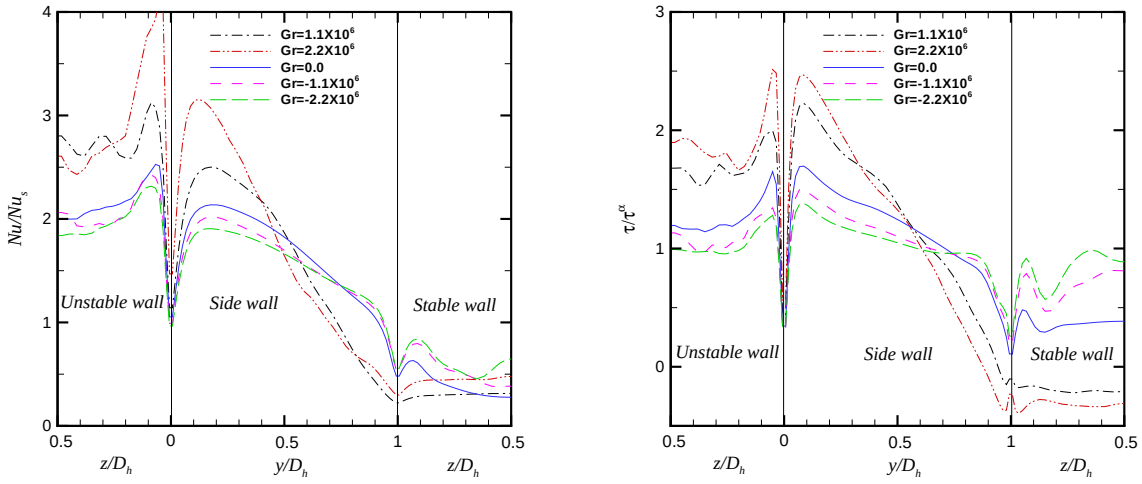

Figure 5.25 Local Nusselt number (left) and shear stress (right) along the duct perimeter at $x/D_h = 10$

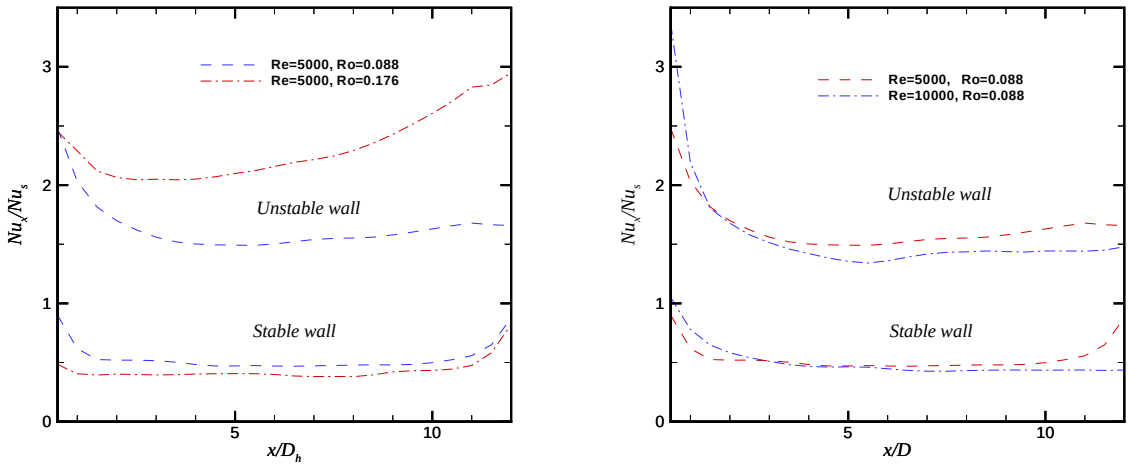

Figure 5.26 Streamwise distribution of wall-averaged Nusselt number at different rotation and Reynolds numbers

CHAPTER 6. THE VELOCITY FIELD AND INSTABILITY OF ROTATING DUCT FLOW

Abstract

The velocity field and the instability of the flow in a rotating square duct were investigated. The velocity profiles were obtained for Ekman numbers less than 1/16 by combining a linear Stewartson layer solution, a non-linear Ekman layer solution and a local similarity assumption. The transition of the secondary-flow pattern from one pair of vortices to two pairs of vortices was studied with the conventional linearized equations for small disturbances. The resultant sixth order equation was solved numerically. The onset of the instability of the Ekman layer was also studied and found to be relevant to the class A and class B waves. The present theory was compared with the experimental results of Smirnov and Yurkin (1983). The critical rotation numbers for marginal stability of both the Stewartson layer and the Ekman layer were found in good agreement with measurements.

The experiments of Smirnov and Yurkin (1983) also revealed a boundary in the parameter space corresponding to the sudden change of the slopes of the drag curves, which was found at least partially related to the wavy instability of the Stewartson layer. A quasi-geostrophic method was used to include the effects of Ekman friction in the instability formula. The critical rotation numbers obtained were in qualitative agreement with experimental measurements. Another phenomenon the experiments discovered was the pulsation of the four-vortex pattern as a certain critical Reynolds number was exceeded. This phenomenon has not yet been explained by the present analysis.

6.1 Introduction

Experiments by Smirnov and Yurkin (1983) and numerical simulations of Kheshgi and Scriven (1985) revealed the existance of two different secondary flow patterns and the transition from one to another in a rotating square duct. For a duct rotating about an axis perpendicular to one of its walls, for example, the situation shown in Fig. 6.1, the Coriolis force component in the negative y direction is balanced by pressure gradient in the central duct region. Close to the top and bottom walls, this Coriolis force component decreases with velocity so that the pressure gradient drives the fluid to the stable wall of the duct ($y/D = 1$) so that it can be balanced by both the Coriolis force and the viscous force. Due to these mechanisms, a double-vortex secondary flow pattern is formed, as sketched in Fig. 6.1. However, a four-vortex pattern can also arise under certain conditions. A transition process between these two patterns is shown

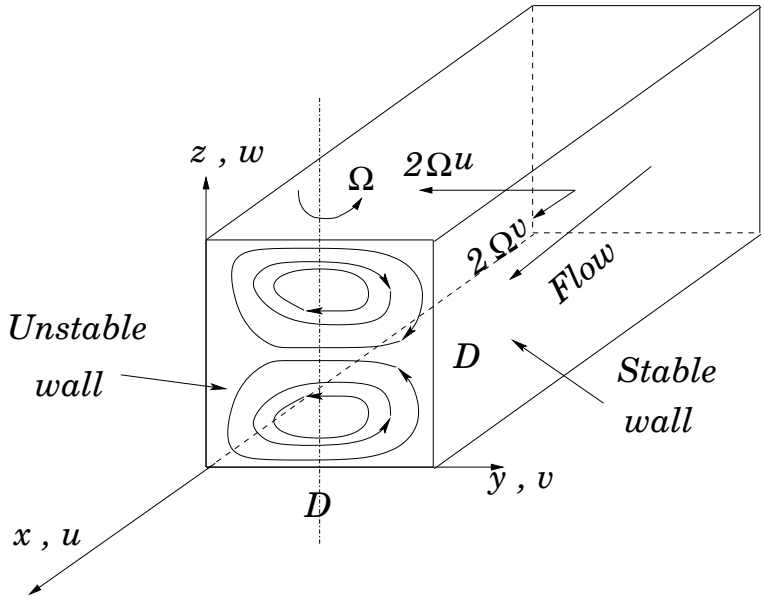

Figure 6.1 Flow in a rotating square duct

in Fig. 6.2. These results were obtained by using a low Mach number preconditioned finite volume code with a lower-upper symmetrical Gauss-Seidel scheme (Qin and Pletcher, 2006). This code was designed for large eddy simulations (LES) of turbulent flows but could also be used for laminar flow simulations if the subgrid-scale model was disabled. In the following

text the results obtained this way will be denoted as "LES results" without causing confusion. Four different combinations of Reynolds number and rotation number were simulated. The

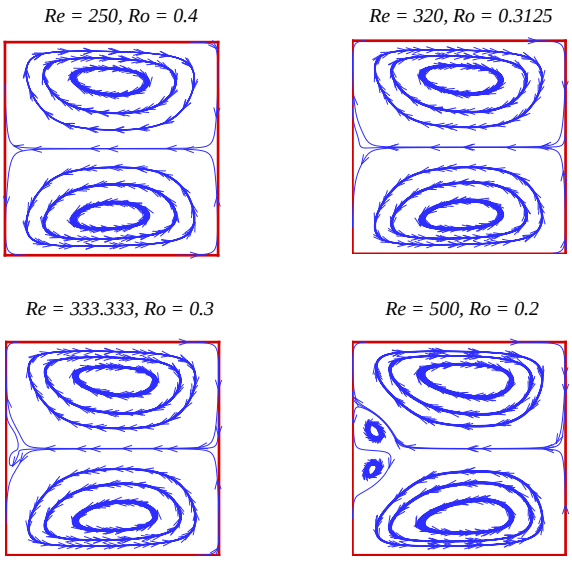

Figure 6.2 Transition between double-vortex and four-vortex patterns

definitions of these numbers will be given shortly. It may be noticed that the products of Reynolds and rotation number are the same, namely 100, for all these four cases. It can be observed that as rotation number reduces to 0.3125, close to the the high pressure wall at $y = 0$ the fluid begins to meander around the center line $z = 0.5D$ which suggests the onset of flow instability in the Stewartson layer (the boundary layers at the vertical walls). As the rotation number decreases further, the four-vortex pattern appears. This instability boundary was denoted as boundary "S_1" in Fig. 6.3, which summarized the experimental results of Smirnov and Yurkin (1983). Experiments of Smirnov and Yurkin (1983) indicated that this four-vortex pattern was steady for all rotation numbers as $Re < 650$. Above this critical Reynolds number this pair of vortices began to pulsate and eventually broke up. The instability boundary "S_2" in Fig. 6.3 shows when such transitions happen.

The visualization of the experiments by Smirnov and Yurkin (1983) showed that below the hatched region "S_3" in Fig. 6.3 there were no oscillations in the positive absolute vorticity

area (that is, the negative du/dy area. See Fig. 6.4). Also, the experiments of Döbner (1959) demonstrated another critical line existing in the parameter space (line "S_4" in Fig. 6.3) which corresponds to the sudden change of the slopes of the drag curves. And this critical line had been reasonably associated with the transition to turbulence of the Ekman layer (the boundary layers at the horizontal walls) by Smirnov and Yurkin (1983) since the drag in a rotating duct is mainly determined by the shear stress in the Ekman layer (Smirnov, 1978).

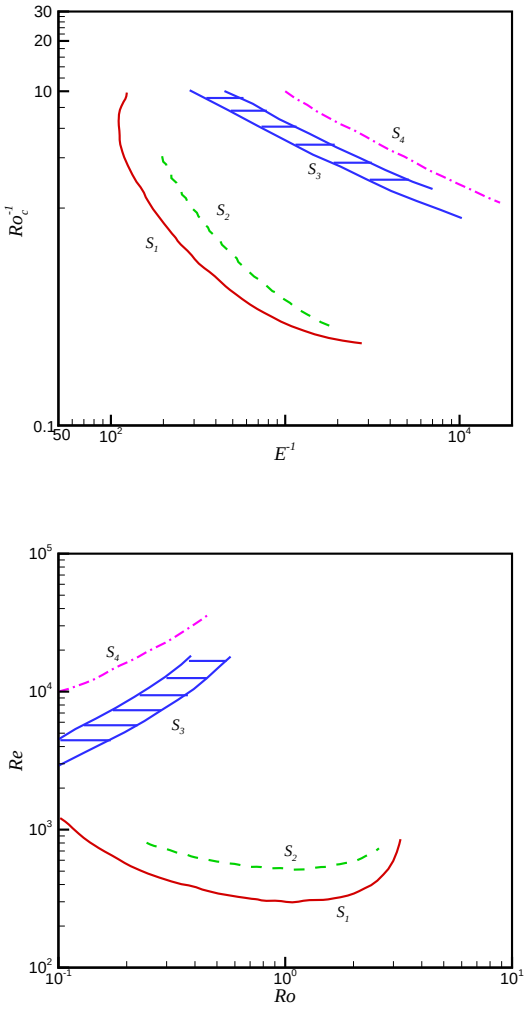

Figure 6.3 Critical lines from experiments by Smirnov and Yurkin (1983)

To facilitate a better understanding of the various instabilities mentioned above, a linear stability analysis was carried out. This required the velocity field inside the rotating duct to

be known in advance. Smirnov (1978) solved the linearized equations of motion by neglecting all convection terms and reached an asymptotic solution. The convection of the secondary flow, however, should not be ignored since it has a major effect on the streamwise velocity distributions as shown in Fig. 6.4, which shows u velocity profiles at several different rotation numbers. The maximum u velocity is displaced by the secondary flow toward the unstable wall ($y = 0$) and an almost constant slope region in u profiles can be identified which occupies the

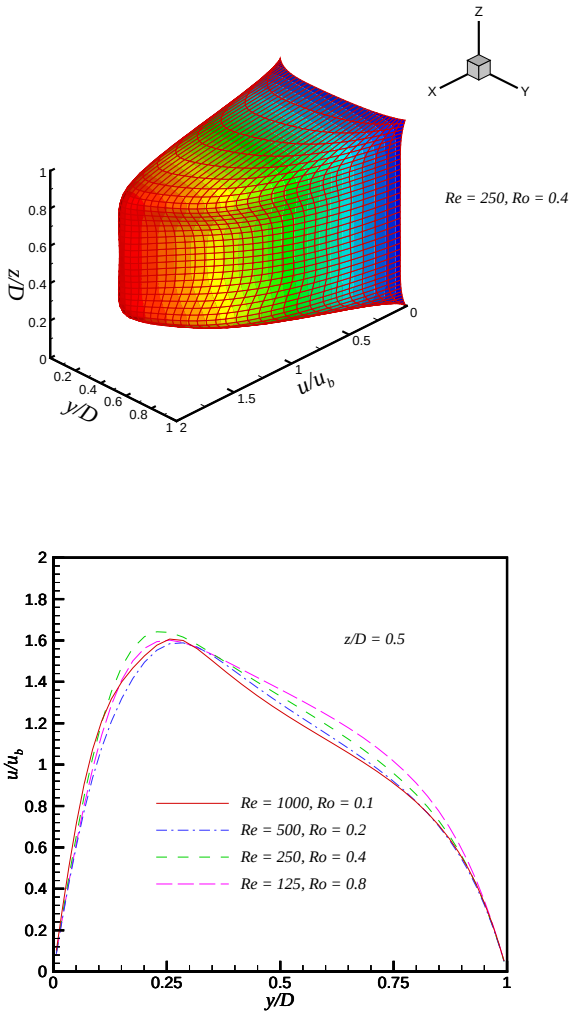

Figure 6.4 Streamwise velocity

majority of the duct. As a result, in order to predict the streamwise velocity accurately, the profile as well as magnitude of the secondary flow needs to be determined, which will be done

in Sec. 6.2 by combining a linear Stewartson layer solution, a non-linear Ekman layer solution and a local similarity assumption. With the velocity field known, the onset of the instabilities mentioned above were predicted with linear theory for disturbances of small magnitude in Sec. 6.3. Hart (1971) as well as Lezius and Johnston (1976) carried out analysis for "roll-cell" instabilities in rotating laminar (Hart, 1971; Lezius and Johnston, 1976) and turbulent (Lezius and Johnston, 1976) channel flows. A similar process was employed in the present research for the S_1 instability boundary although the situation was complicated by the presence of secondary flow. The resultant ordinary differential eigenvalue problem was solved numerically by a matrix deduction method with a Laguerre rootfinder. The S_3 instability boundary was studied by considering the non-linear Ekman layer subjected to banded disturbances which propagated at a constant angle with the base flow. In this case, the base flow changes in the principal component direction of the Coriolis force and is more complex than the usual linear Ekman or von Kármán boundary layers. Also in this section the wavy instability of the Stewartson layer was explored to explain the S_4 drag change boundary since the unstable Stewartson layer also contributes a significant part of the total drag. Bulk rather than local velocity field was considered by assuming the flow to be quasi-geostrophic. The method of Niino and Misawa (1984) were used and the theoretical results qualitatively agree with experimental measurements. The concluding remarks are given in Sec. 6.4.

6.2 Velocity Field in a Rotating Square Duct

6.2.1 Governing Equations and Flow Regions

The dimensionless Navier-Stokes equations for incompressible viscous flow in a coordinate system rotating with the duct (see Fig. 6.1) are

$$\nabla \cdot \mathbf{q} = 0, \tag{6.1}$$

$$\frac{\partial \mathbf{q}}{\partial t} + \mathbf{q} \cdot \nabla \mathbf{q} + 2Ro\hat{\mathbf{k}} \times \mathbf{q} = -\nabla p + \frac{1}{Re}\nabla^2 \mathbf{q}, \tag{6.2}$$

where $\mathbf{q}$ is the velocity vector. The reference length, velocity and time are duct side width D, bulk velocity u_b and D/u_b, respectively. The Reynolds number and rotation number are

defined as $Re = u_b D/\nu$ and $Ro = \Omega D/u_b$. The Ekman number is defined as $E = 1/(Re \cdot Ro)$. Obviously, the flow is completely controled by any two of these three non-dimensional parameters. By taking the curl of the equation of motion, we obtain the vorticity equation:

$$\frac{\partial \mathbf{B}}{\partial t} + \mathbf{q} \cdot \nabla \mathbf{B} - \mathbf{B} \cdot \nabla \mathbf{q} - 2Ro \frac{\partial \mathbf{q}}{\partial z} = \frac{1}{Re} \nabla^2 \mathbf{B}, \tag{6.3}$$

where $\mathbf{B} = \nabla \times \mathbf{q}$.

For a steady, fully-developed flow, the velocity vector assumes the form

$$\mathbf{q} = u(y,z)\hat{\mathbf{i}} + \nabla \times \left[\varphi(y,z)\hat{\mathbf{i}}\right], \tag{6.4}$$

where φ is the stream function. The $x-$momentum and $x-$vorticity equations are

$$\frac{\partial \varphi}{\partial z}\frac{\partial u}{\partial y} - \frac{\partial \varphi}{\partial y}\frac{\partial u}{\partial z} - 2Ro\frac{\partial \varphi}{\partial z} = -\frac{\partial p}{\partial x} + \frac{1}{Re}\nabla^2 u, \tag{6.5}$$

$$\frac{\partial \varphi}{\partial z}\frac{\partial \nabla^2 \varphi}{\partial y} - \frac{\partial \varphi}{\partial y}\frac{\partial \nabla^2 \varphi}{\partial z} + 2Ro\frac{\partial u}{\partial z} = \frac{1}{Re}\nabla^4 \varphi. \tag{6.6}$$

As mentioned above, the duct cross section can be divided into three regions based on the flow characteristics in each region (see Fig. 6.5, in which the secondary flow is shown in the upper half of the duct and the u velocity distributions along the y and z directions are shown in the lower half). The boundary layers close the horizontal walls are Ekman layers, which have a characteristic thickness of $E^{1/2}$. Adjacent to the vertical walls are Stewartson layers which have a double-layer structure (Stewartson, 1957). And the characteristic thicknesses are $E^{1/3}$ and $E^{1/4}$ for the inner and outer layers, respectively. Outside of these boundary layers is the central core, in which viscosity is usually negligible. The fluid from the central core flows to the Ekman layer through the unstable wall Stewartson layer, and then comes back to the central core through the stable wall Stewartson layer. In derivations to follow we will use subscripts 1, 2, 3 to denote the central core, the Ekman layers and the Stewartson layers, respectively. In most applications of practical interest, the Ekman numbers are usually much less than unity. Therefore the Stewartson layer is thicker than the Ekman layer. If $E^{1/4} > 1/2$, that is $E > 1/16$, the two Stewartson layers merge and the central core disappears. For this situation the perturbed Poisson equation method as adopted by Hart (1971) for flow through slowly rotating channels may be more appropriate. We will restrict our study in the range $E < 1/16$ since all instability boundaries fall in this region.

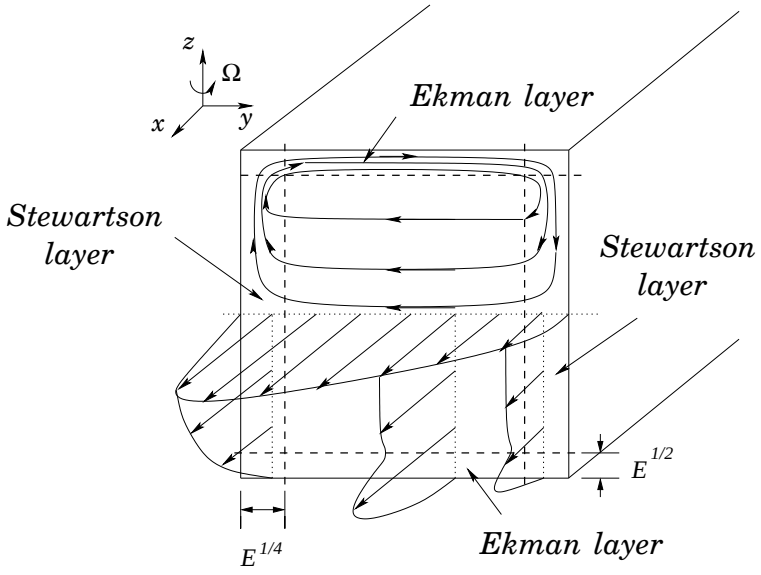

Figure 6.5 Different flow regions

6.2.2 The Central Core

In the central core, as $Ro \gg 1$ and $E \ll 1$, from Eqs. (6.2) and (6.3), we have

$$\mathbf{q}_1 = \frac{1}{2Ro}\hat{\mathbf{k}} \times \nabla p, \tag{6.7}$$

$$\frac{\partial \mathbf{q}_1}{\partial z} = 0. \tag{6.8}$$

Equation (6.8) is simply the Taylor-Proudman theorem (Greenspan, 1968). For fully-developed flow, $\partial p/\partial x$ is a constant everywhere inside the flow; also because of symmetry, $w(z = 1/2) = 0$. As a result, we have

$$\varphi_1 = g_1 E^{\frac{1}{2}} \left(z - \frac{1}{2} \right), \tag{6.9}$$

$$v_1 = g_1 E^{\frac{1}{2}}, \tag{6.10}$$

$$w_1 = 0, \tag{6.11}$$

$$\frac{\partial p}{\partial x} = 2Rog_1 E^{\frac{1}{2}}, \tag{6.12}$$

where g_1 is a constant. The scaling $E^{\frac{1}{2}}$ is appropriate due to the mass balance between the central core and the Ekman layer which will be clear shortly.

For the central core at moderate rotation numbers, $Ro \sim O(1)$, the convection term vdu/dy (the partial derivative $\partial u/\partial y$ can be replaced by an ordinary derivative du/dy in the central

core) in the $x-$momentum equation is of the same order as the Coriolis term and cannot be neglected. As mentioned before, there exists a linear slope region (du_1/dy =constant) in the u profile which occupies most the central core. Hence we have

$$\varphi_1 = g_1 E^{\frac{1}{2}} \left(z - \frac{1}{2} \right), \tag{6.13}$$

$$v_1 = g_1 E^{\frac{1}{2}}, \tag{6.14}$$

$$w_1 = 0, \tag{6.15}$$

$$\frac{\partial p}{\partial x} = \left(2Ro - \frac{du_1}{dy} \right) g_1 E^{\frac{1}{2}}. \tag{6.16}$$

6.2.3 The Ekman Layer

In the Ekman layers adjacent to the central core, if $Ro \gg 1$ and $E \ll 1$, the convection terms in Eqs. (6.5) and (6.6) can be ignored and $\partial/\partial z \gg \partial/\partial y$. Equations (6.5) and (6.6) become

$$-2Ro \frac{\partial \varphi_2}{\partial z} = \frac{1}{Re} \frac{\partial^2 u_2}{\partial z^2}, \tag{6.17}$$

$$2Ro \frac{\partial u_2}{\partial z} = \frac{1}{Re} \frac{\partial^4 \varphi_2}{\partial z^4}, \tag{6.18}$$

which can be reduced to

$$E^2 \frac{\partial^6 \varphi_2}{\partial z^6} + 4 \frac{\partial^2 \varphi_2}{\partial z^2} = 0. \tag{6.19}$$

By substituting $\eta = E^{-a} z$ into the above equation, we have $a = 1/2$. Thus, the Ekman layer is of a characteristic thickness $E^{\frac{1}{2}}$. Also the stream function φ must be of the same order $E^{\frac{1}{2}}$ since $u \sim 1$. By using $\eta = z/E^{\frac{1}{2}}$ and $\Phi = \varphi/E^{\frac{1}{2}}$, Eq.(6.19) becomes

$$\frac{\partial^6 \Phi_2}{\partial \eta^6} + 4 \frac{\partial^2 \Phi_2}{\partial \eta^2} = 0, \tag{6.20}$$

with boundary conditions

$$\eta = 0, \quad u_2 = \Phi_2 = \frac{\partial \Phi_2}{\partial \eta} = 0, \tag{6.21}$$

$$\eta \to \infty, \quad u_2 \to u_1, \Phi_2 \to \Phi_1(z=0), \frac{\partial \Phi_2}{\partial \eta} \to v_1. \tag{6.22}$$

The second condition of Eq. (6.22) comes from the mass balance of the secondary flow:

$$\int_0^{\frac{1}{2}} v dz = 0. \tag{6.23}$$

and the fact that as $E \ll 1$, the Ekman layer is very thin. Also from this condition it can be concluded that the stream function in the central core, φ_1, like φ_2, is of order $E^{\frac{1}{2}}$. This justified the scaling of φ_1 used above. Notice only the Ekman layer at $z = 0$ is considered since the layer at $z = 1$ can be solved exactly the same way. The solution is

$$u_2 = u_1 \left[1 - exp(-\eta) cos\eta\right], \tag{6.24}$$

$$\Phi_2 = \Phi_1 \left[1 - \sqrt{2} exp(-\eta) cos(\eta - \frac{\pi}{4})\right], \tag{6.25}$$

$$u_1 = -g_1 \sim 1. \tag{6.26}$$

Equation (6.26) is the compatibility condition on the fluid velocities in the central core when linear theory applies, from which we can see that the fluid in the central core moves axially as a plug flow when it reaches the rapid rotating limit $Ro \gg 1$. According to Greenspan (1968), the velocity at a surface, say Σ, induced by Ekman pumping is

$$\hat{\mathbf{n}} \cdot \tilde{\mathbf{q}}_2 = \frac{1}{2} E^{\frac{1}{2}} \hat{\mathbf{n}} \cdot \nabla \times \left\{ \left[\hat{\mathbf{n}} \times \mathbf{q}_1 + \frac{\hat{\mathbf{n}} \cdot \hat{\mathbf{k}}}{\left| \hat{\mathbf{n}} \cdot \hat{\mathbf{k}} \right|} \mathbf{q}_1 \right] \left| \hat{\mathbf{n}} \cdot \hat{\mathbf{k}} \right|^{-\frac{1}{2}} \right\}_{\Sigma}, \tag{6.27}$$

where $\hat{\mathbf{n}}$ is the outward unit vector normal to the surface. Under the current settings $\hat{\mathbf{n}} = \hat{\mathbf{k}}$ at the top surface and $\hat{\mathbf{n}} = -\hat{\mathbf{k}}$ at the bottom surface. To balance this induced flow, we have

$$w_2 = -\tilde{w}_2 = \frac{\hat{\mathbf{n}} \cdot \hat{\mathbf{k}}}{\left| \hat{\mathbf{n}} \cdot \hat{\mathbf{k}} \right|} \frac{E^{\frac{1}{2}}}{2} \frac{du_1}{dy}. \tag{6.28}$$

Since in the rapid rotating limit $du_1/dy = 0$, there is no normal flow inside the Ekman layer, except close to the vertical walls.

For the Ekman layer at moderate rotation numbers, the convection term $v\partial u/\partial y$ as well as the pressure gradient in $x-$momentum equation cannot be ignored. By using scalings $\Phi = \varphi/E^{\frac{1}{2}}$, $\eta = z/E^{\frac{1}{2}}$ and $\xi = 2Roy$, Eq. (6.6) becomes

$$\frac{\partial(\Phi_2 - \Phi_1)}{\partial \eta} (\frac{\partial u_2}{\partial \xi} - 1) = \frac{1}{2} \frac{\partial^2 u_2}{\partial \eta^2}, \tag{6.29}$$

$$\frac{\partial u_2}{\partial \eta} = \frac{1}{2} \frac{\partial^4 (\Phi_2 - \Phi_1)}{\partial \eta^4}. \tag{6.30}$$

The boundary conditions are still Eqs. (6.21) and (6.22). One method to solve this equation is to assume $(\partial u_2/\partial y) \mid_{y=y_0} = (du_1/dy) \mid_{y=y_0}$ throughout the whole Ekman layer at any specific

location $y = y_0$. If $(du_1/dy)\mid_{y=y_0} < 2Ro$, which is the case in most part of the duct, we have

$$\Phi_2 = \Phi_1 + exp(-\sigma\eta)\left[\frac{g_1}{2}cos(\sigma\eta) + (\frac{g_1}{2} - \frac{v_1}{\sigma})sin(\sigma\eta)\right], \tag{6.31}$$

$$u_2 = u_1 + \sigma^3 exp(-\sigma\eta)\left[(g_1 - \frac{v_1}{\sigma})cos(\sigma\eta) - \frac{v_1}{\sigma}sin(\sigma\eta)\right], \tag{6.32}$$

$$u_1 = -\sigma^3(g_1 - \frac{v_1}{\sigma}), \tag{6.33}$$

where $\sigma = (1 - du_1/d\xi)^{1/4}$. Equation (6.33) gives a compatibility condition on the fluid velocities in the central core for moderate rotation numbers. Using Eq. (6.33), the velocity distributions in the Ekman layer can be further simplified and expressed as

$$u_2 = u_1\left[1 - cos(\sigma E^{-\frac{1}{2}}z)exp(-\sigma E^{-\frac{1}{2}}z)\right] - v_1\sigma^2 sin(\sigma E^{-\frac{1}{2}}z)exp(-\sigma E^{-\frac{1}{2}}z), \tag{6.34}$$

$$v_2 = v_1\left[1 - cos(\sigma E^{-\frac{1}{2}}z)exp(-\sigma E^{-\frac{1}{2}}z)\right] + \frac{u_1}{\sigma^2}sin(\sigma E^{-\frac{1}{2}}z)exp(-\sigma E^{-\frac{1}{2}}z). \tag{6.35}$$

If $(du_1/dy)\mid_{y=y_0} > 2Ro$, the result is

$$\Phi_2 = \Phi_1\left[1 - exp(-\sqrt{2}\sigma\eta)\right], \tag{6.36}$$

$$u_2 = u_1\left[1 - exp(-\sqrt{2}\sigma\eta)\right], \tag{6.37}$$

$$u_1 = -\frac{\sqrt{2}}{2}\sigma^3\Phi_1, \tag{6.38}$$

where $\sigma = (du_1/d\xi - 1)^{1/4}$.

From the above results we can see the thickness of the non-linear Ekman layer ($\sim \sigma^{-1}E^{1/2}$) is thinner than that of the linear one ($\sim E^{1/2}$). Also there exists asymmetry inside the Ekman layer: the velocity profile changes with y coordinate. This feature has been reflected in Fig. 6.5. Since the Stewartson layer is much thicker than the Ekman layer, these solutions still serve as good approximations as the Ekman layer enters the Stewartson layer, that is, at the corner of the duct. We will see later that this method is good enough to predict the u velocity profile; however, it may not be optimum for calculating the magnitude of secondary flow. Also this method has a singular point at $\sigma = 0$. We will use a local similarity method to improve the prediction of the Ekman layer.

For this non-linear Ekman layer, following the method of Greenspan (1968), the induced normal flow at the wall can be obtained, which is

$$w_2 = \frac{\hat{\mathbf{n}}\cdot\hat{\mathbf{k}}}{\left|\hat{\mathbf{n}}\cdot\hat{\mathbf{k}}\right|}\frac{E^{\frac{1}{2}}}{2\sigma^3}\frac{du_1}{dy}, \quad \text{if } du_1/dy < 2Ro \tag{6.39}$$

or,

$$w_2 = \frac{\hat{\mathbf{n}}\cdot\hat{\mathbf{k}}}{\left|\hat{\mathbf{n}}\cdot\hat{\mathbf{k}}\right|}\frac{\sqrt{2}E^{\frac{1}{2}}}{\sigma^3}\frac{du_1}{dy}, \quad \text{if } du_1/dy > 2Ro \tag{6.40}$$

where

$$\sigma = \left|1 - \frac{1}{2Ro}\frac{du_1}{dy}\right|^{\frac{1}{4}}. \tag{6.41}$$

The importance of Eqs. (6.39) and (6.40) should not be underestimated since they are counterparts of the equation of Greenspan, Eq. (6.28), and are expected to find applications in many other similar situations.

6.2.4 The Stewartson Layer

Now let us turn to the Stewartson layer. Let $\bar{z} = z - \frac{1}{2}$, $\bar{u}_3 = u_3 - u_1$ and $\bar{\varphi}_3 = \varphi_3 - \varphi_1 = \varphi_3 - g_1 E^{\frac{1}{2}}\bar{z}$, then as $Ro \gg 1$, $E \ll 1$, the linear problem is

$$-\frac{2}{E}\frac{\partial\bar{\varphi}_3}{\partial\bar{z}} = \left\{\frac{\partial^2}{\partial y^2} + \frac{\partial^2}{\partial\bar{z}^2}\right\}\bar{u}_3, \tag{6.42}$$

$$\frac{2}{E}\frac{\partial\bar{u}_3}{\partial\bar{z}} = \left\{\frac{\partial^2}{\partial y^2} + \frac{\partial^2}{\partial\bar{z}^2}\right\}^2\bar{\varphi}_3. \tag{6.43}$$

with the boundary conditions

$$at \;\; \bar{z} = \pm\frac{1}{2}, \quad \bar{u}_3 = -u_1, \bar{\varphi}_3 = -\varphi_1, \frac{\partial\bar{\varphi}_3}{\partial\bar{z}} = -g_1 E^{\frac{1}{2}}, \tag{6.44}$$

$$at \;\; y = 0, \quad \bar{u}_3 = -u_1, \bar{\varphi}_3 = -\varphi_1, \frac{\partial\bar{\varphi}_3}{\partial y} = 0. \tag{6.45}$$

Notice it is enough to consider the Stewartson layer at $y = 0$ only since the layer at $y = 1$ can be easily obtained by substituting $\bar{y} = 1 - y$ into above formulae. Also it will be easier to find solutions only satisfying the conditions out of the Ekman layers first. We will add a subscript

"s" to such solutions. Since the Ekman layer is thin as $E \ll 1$, the condition, Eq. (6.44), is replaced by

$$at \quad \bar{z} = \pm\frac{1}{2}, \quad \bar{u}_{3s} = \bar{\varphi}_{3s} = 0, \frac{\partial\bar{\varphi}_{3s}}{\partial\bar{z}} = -g_1 E^{\frac{1}{2}} \doteq 0. \tag{6.46}$$

Following the method of Stewartson (1957), the above system can be solved. The solution is

$$u_{3s} = u_1 \left[1 - exp(-\sqrt{2}\xi) - \sqrt{2}E^{\frac{1}{4}}F(\theta, z)\right], \tag{6.47}$$

$$\varphi_{3s} = g_1 E^{\frac{1}{2}} \left\{(z - \frac{1}{2})[1 - exp(-\sqrt{2}\xi)] - 2^{\frac{1}{6}}E^{\frac{1}{12}}G(\theta, z)\right\}, \tag{6.48}$$

$$F(\theta, z) = \sum_{n=1}^{\infty} \frac{cos(2n\pi z)}{2n\pi} \left[exp(-c_n\theta) - exp(-\frac{c_n\theta}{2})cos(\frac{\sqrt{3}}{2}c_n\theta + \pi/3)\right], \tag{6.49}$$

$$G(\theta, z) = \sum_{n=1}^{\infty} \frac{sin(2n\pi z)}{(2n\pi)^{4/3}} \left[exp(-c_n\theta) - exp(-\frac{c_n\theta}{2})cos(\frac{\sqrt{3}}{2}c_n\theta - \pi/3)\right], \tag{6.50}$$

$$c_n = (4n\pi)^{1/3}, \quad \xi = y/E^{\frac{1}{4}}, \quad \theta = y/E^{\frac{1}{3}}. \tag{6.51}$$

Then the solution satisfying the original boundary conditions, Eqs. (6.44) and (6.45), can be obtained by incorporating the linear Ekman layer solution, Eqs. (6.24) and (6.25):

$$u_3 = u_{3s}\left[1 - exp(-\eta)cos\eta\right], \tag{6.52}$$

$$\varphi_3 = \varphi_{3s}\left[1 - \sqrt{2}exp(-\eta)cos(\eta - \frac{\pi}{4})\right]. \tag{6.53}$$

All the linear results above (that is, as $Ro \gg 1$ and $E \ll 1$) had also been obtained by Smirnov (1978). The other results are new.

For the Stewartson layer under moderate rotation numbers, the convection term $v\partial u/\partial y$ cannot be ignored in the $x-$momentum equation. Therefore, the u velocity profile, Eq. (6.52), will be far from realistic as $Ro \sim O(1)$. However, from our calculations, it seems that the secondary flow obtained from linear theory is a rather good estimation of the real situation for a wide range of rotation numbers. Figure 6.6 shows the comparison of the contours of stream function and vectors of secondary flow between large eddy simulation (upper half) and linear theory (lower half) for a $Re = 250$, $Ro = 0.4$ case. From this figure we can see although the vortex center is slightly displaced toward the unstable side by convection in

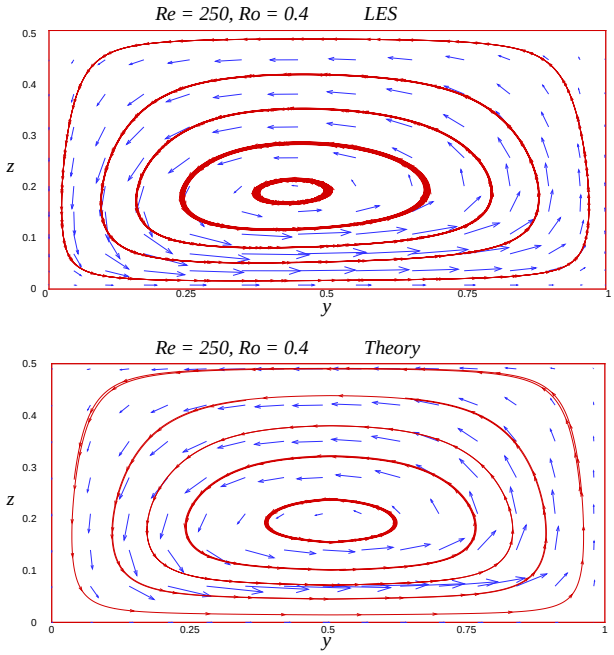

Figure 6.6 Stream function contours and secondary flow vectors

the real situation, which the linear theory is not able to reproduce, the other features of the secondary flow pattern are satisfactorily duplicated. Figure 6.7 shows the comparison between LES and the linear theory of v and w velocity profiles at different z locations for the $Re = 250$, $Ro = 0.4$ case. As we can see, the agreement is good for $z > E^{1/2} = 0.1$, that is, out of the Ekman layer. And one may notice the case we chose here is, in fact, unfavorable for the linear theory: the Ekman number is not very low and the rotation number is not very high. One may expect the agreement to improve if the non-linear rather than linear Ekman layer solutions are incorporated with the linear Stewartson layer solution for this moderate rotation number situation. In fact, it is the case. However, we will not pursue along this line further since a better method to solve for the non-linear Ekman layer will be introduced.

Now we turn to the problem of determining the u velocity in the Stewartson layer at moderate rotation numbers. For this purpose, the appropriate equation for the Stewartson layer out of the Ekman layer is

$$\frac{\partial \varphi_3}{\partial z}\left(\frac{\partial u_3}{\partial y} - 2Ro\right) = \frac{d\varphi_1}{dz}\left(\frac{du_1}{dy} - 2Ro\right) + \frac{1}{Re}\frac{\partial^2 u_3}{\partial y^2}, \tag{6.54}$$

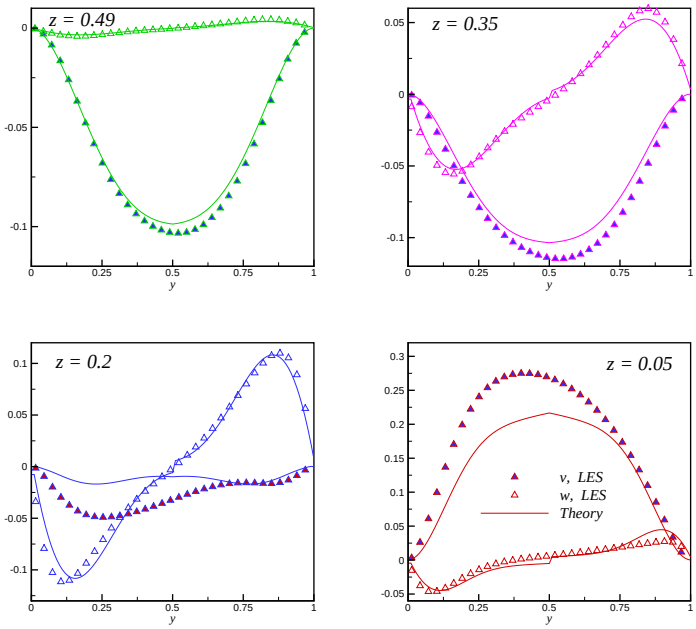

Figure 6.7 Secondary flow velocities

with the boundary conditions $u_3 = 0$ at vertical walls. It is easy to verify that $v_3 = \partial\varphi_3/\partial z$ varies little with z out of the Ekman layer. As a result, u_3 also does not change much with z in this region. Thus, the partial derivatives $\partial u_3/\partial y$ and $\partial^2 u_3/\partial y^2$ can be replaced by corresponding ordinary derivatives in the above equation. Since the stream function, φ_3, from the linear theory is still valid for the non-linear cases as discussed previously, this equation is very simple to solve numerically. Figure 6.8 shows a u velocity profile calculated this way, which is in good agreement with LES.

6.2.5 Determination of Key Parameters

All velocity field calculations discussed previously were dependent on two parameters: the u velocity gradient in the central part of the duct, du_1/dy, and the magnitude of v velocity, $g_1 E^{\frac{1}{2}}$. In order to determine these two parameters, two equations (or conditions) are needed. One is a compatibility equation relating du_1/dy and g_1, and another condition is that the bulk velocity u_b should be equal to unity since it is the reference velocity. The compatibility relation comes from the balance between the Ekman layer and the central duct, for example Eq.

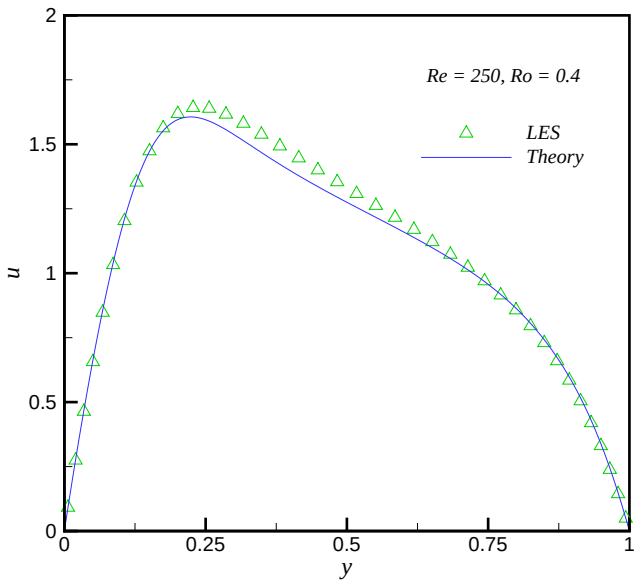

Figure 6.8 Streamwise velocity

(6.33). Equation (6.33) should work well as the flow conditions are close to $Ro \gg 1$, $E \ll 1$, to which the linear theory can apply. However, under flow conditions away from the linear limit, Eq. (6.33) fails to give satisfactory estimations of du_1/dy and g_1. The reason is due to the assumption of $(\partial u_2/\partial y)\,|_{y=y_0} = (du_1/dy)\,|_{y=y_0}$ throughout the whole Ekman layer, which may not be valid. A better choice may be the local similarity assumption proposed by Bennetts and Hocking (1973). The same authors had employed this method to investigate pressure-induced flows at high rotation numbers (Bennetts and Hocking, 1974). The innovation of the present study is that we incorporate the Stewartson layer solution into the local similarity procedure, which is able to give good estimations of du_1/dy and g_1.

Within the bottom wall Ekman layer away from the vertical walls, by using scalings $\Phi = \varphi/E^{\frac{1}{2}}$, $\eta = z/E^{\frac{1}{2}}$, and $\xi = 2Roy$, the appropriate equations are

$$\frac{\partial \Phi_2}{\partial \eta}\left(\frac{\partial u_2}{\partial \xi} - 1\right) - \frac{\partial \Phi_2}{\partial \xi}\frac{\partial u_2}{\partial \eta} = \frac{\partial \Phi_1}{\partial \eta}\left(\frac{du_1}{d\xi} - 1\right) + \frac{1}{2}\frac{\partial^2 u_2}{\partial \eta^2}, \tag{6.55}$$

$$\frac{\partial \Phi_2}{\partial \eta}\frac{\partial^3 \Phi_2}{\partial \eta^2 \partial \xi} - \frac{\partial \Phi_2}{\partial \xi}\frac{\partial^3 \Phi_2}{\partial \eta^3} + \frac{\partial u_2}{\partial \eta} = \frac{1}{2}\frac{\partial^4 \Phi_2}{\partial \eta^4}. \tag{6.56}$$

The boundary conditions are

$$\eta = 0, \quad u_2 = \Phi_2 = \frac{\partial \Phi_2}{\partial \eta} = 0, \tag{6.57}$$

$$\eta \to \infty, \quad u_2 \to u_1, \Phi_2 \to \Phi_1, \frac{\partial \Phi_2}{\partial \eta} \to v_1. \tag{6.58}$$

Let $u_1 = F(\xi)$ and $\Phi_1 = g_1(z - 1/2)G(\xi)$, then $v_1 = g_1 E^{\frac{1}{2}} G(\xi)$. The effects of the Stewartson layer on the central core are included by adding a function $G(\xi)$ to the stream function. From the Stewartson layer solutions, we have

$$G = 1 - exp(-\sqrt{2}\zeta) - 2^{\frac{1}{6}} E^{\frac{1}{12}} \sum_{n=1}^{\infty} \frac{cos(2n\pi z)}{(2n\pi)^{1/3}} \left[exp(-c_n\theta) - exp(-\frac{c_n\theta}{2}) cos(\frac{\sqrt{3}}{2} c_n\theta - \pi/3) \right], \tag{6.59}$$

$$c_n = (4n\pi)^{1/3}, \quad \zeta = y_w/E^{\frac{1}{4}}, \quad \theta = y_w/E^{\frac{1}{3}}. \tag{6.60}$$

Here y_w is the distance from the nearest vertical wall. Since G varies little with respect to z out of the Ekman layer, we can use $z = 1/2$ in the above expression. Thus, G is a function only of y, or ξ. Assuming $u_2 = F(\xi)f(\eta)$ and $\Phi_2 = g_1 G(\xi)\bar{g}(\eta)$ and substituting them into Eqs. (6.55) and (6.56), we have

$$\frac{dg}{d\eta}(\alpha f - 1) - \beta g \frac{df}{d\eta} = \frac{dg}{d\eta} \mid_{\eta\to\infty} (\alpha - 1) + \frac{1}{2}\frac{d^2 f}{d\eta^2}, \tag{6.61}$$

$$\beta \left(\frac{dg}{d\eta}\frac{d^2 g}{d\eta^2} - g\frac{d^3 g}{d\eta^3} \right) + \frac{df}{d\eta} = \frac{1}{2}\frac{d^4 g}{d\eta^4}, \tag{6.62}$$

$$\alpha = \frac{dF}{d\xi}, \quad \beta = \frac{F}{G}\frac{dG}{d\xi}, \quad \bar{g} = \frac{F}{g_1 G} g. \tag{6.63}$$

The boundary conditions for f and g are

$$\eta = 0, \quad f = g = \frac{dg}{d\eta} = 0, \tag{6.64}$$

$$\eta \to \infty, \quad f = 1, \frac{dg}{d\eta} = \frac{g_1 E^{\frac{1}{2}} G}{F}, \tag{6.65}$$

$$\eta = \eta_m, \quad g = 0, \tag{6.66}$$

where η_m is the point corresponding to $z = 1/2$. Equations (6.61) and (6.62) serve as an eigenvalue problem with du_1/dy and g_1 as eigenvalues. The process to determine these two parameters is as follows.

(1) Guess an α;

(2) Guess a g_1, then v_1 can be obtained from $v_1 = g_1 E^{\frac{1}{2}} G(\xi)$;

(3) Calculate the u velocity in the central part of the duct by solving Eq. (6.54), which gives F. Then β can be computed at any y location;

(4) Solve Eqs. (6.61) and (6.62) and check if boundary conditions for f and g are all satisfied. If they are satisfied, go ahead to step (5); if not, go back to step (2) to choose another g_1;

(5) Use the Ekman layer solutions, Eqs. (6.32) and (6.37), to calculate the bulk velocity u_b. If $u_b \neq 1$, then go back to step (1) to choose another α; if u_b does equal 1, then α and g_1 are obtained.

Of course, iterations may be needed to reach satisfactory solutions. More details of step (4) are given below. Equation (6.62) can be integrated from $\eta = \eta_m$ to η once:

$$\beta \left(g \frac{d^2 g}{d\eta^2} - \frac{dg}{d\eta}\frac{dg}{d\eta} + \frac{g_1^2 E G^2}{F^2} \right) + (f-1) = \frac{1}{2}\frac{d^3 g}{d\eta^3}. \tag{6.67}$$

Define $q = dg/d\eta$ then

$$q(\alpha f - 1) - \beta \frac{df}{d\eta} \int_0^\eta q d\eta = \frac{g_1 E^{\frac{1}{2}} G}{F}(\alpha - 1) + \frac{1}{2}\frac{d^2 f}{d\eta^2}, \tag{6.68}$$

$$\beta \left(\frac{dq}{d\eta} \int_0^\eta q d\eta - q^2 + \frac{g_1^2 E G^2}{F^2} \right) + (f-1) = \frac{1}{2}\frac{d^2 q}{d\eta^2}, \tag{6.69}$$

with

$$\eta = 0, \quad f = q = 0, \tag{6.70}$$

$$\eta \to \infty, \quad f = 1, q = \frac{g_1 E^{\frac{1}{2}} G}{F}. \tag{6.71}$$

In practice, the above system is solved in an interval from 0 to η_{max}, which is much larger than η_m. After reaching convergence, the boundary conditions will be changed to

$$\eta > \eta_m, \quad f = 1, q = \frac{g_1 E^{\frac{1}{2}} G}{F}, \frac{df}{d\eta} = \frac{dq}{d\eta} = 0. \tag{6.72}$$

That is, we drop the boundary conditions at $\eta = 0$ and set $f = 1$ and $q = g_1 E^{\frac{1}{2}} G/F$ for $\eta > \eta_m$. Then q is obtained by integrating Eq. (6.69) backwards from $\eta = \eta_{max}$ to $\eta = 0$. The

criterion of reaching a satisfactory solutions is

$$\int_0^{\eta_m} q d\eta = 0. \tag{6.73}$$

The above procedure is designed to avoid the influence of the rapidly changing f profile close to $\eta = 0$. Although this procedure does not guarantee that q will always satisfy boundary conditions at $\eta = 0$, it can give good estimations of α and g_1. As we have mentioned, the above system is essentially an eigenvalue problem so we only expect it to give precise eigenvalues. After these eigenvalues (α and g_1) are obtained, the system changes back to a boundary-value problem and can be used to yield more accurate velocity profiles.

Some results of du_1/dy and g_1 obtained from the above procedure are listed in Table 6.1 Among these results are the parameters for the $Re = 250$ and $Ro = 0.4$ case, which have

Table 6.1 Flow parameters

E = 0.001			E = 0.005			E = 0.01		
Ro	du_1/dy	g_1	Ro	du_1/dy	g_1	Ro	du_1/dy	g_1
0.5	-1.29	-0.74	0.1	-1.27	-0.34	0.1	-1.11	-0.45
0.6	-1.29	-0.79	0.2	-1.32	-0.52	0.15	-1.15	-0.56
0.8	-1.27	-0.87	0.3	-1.36	-0.63	0.2	-1.17	-0.67
1.0	-1.25	-0.93	0.4	-1.37	-0.73	0.22	-1.17	-0.7
1.2	-1.23	-0.98	0.5	-1.38	-0.81	0.24	-1.17	-0.75
1.4	-1.21	-1.02	0.6	-1.4	-0.85	0.26	-1.17	-0.78
1.6	-1.2	-1.04	0.7	-1.4	-0.92	0.4	-1.16	-1.0
1.8	-1.17	-1.08	0.8	-1.4	-0.97	0.5	-1.16	-1.12
2.0	-1.17	-1.08	0.9	-1.42	-1.0	0.8	-1.09	-1.42
2.4	-1.13	-1.13						
2.8	-1.11	-1.15						

been used for some theoretical calculations in previous sections. From these results it can be observed that du_1/dy is roughly a constant at a given Ekman number over wide range of rotation numbers.

Figures 6.9 and 6.10 show the results of u and v velocity profiles in the Ekman layer based on the flow parameters obtained. We can see that the local similarity assumption gives a better shape for the u velocity profile than Eq. (6.32) does as compared with LES. However,

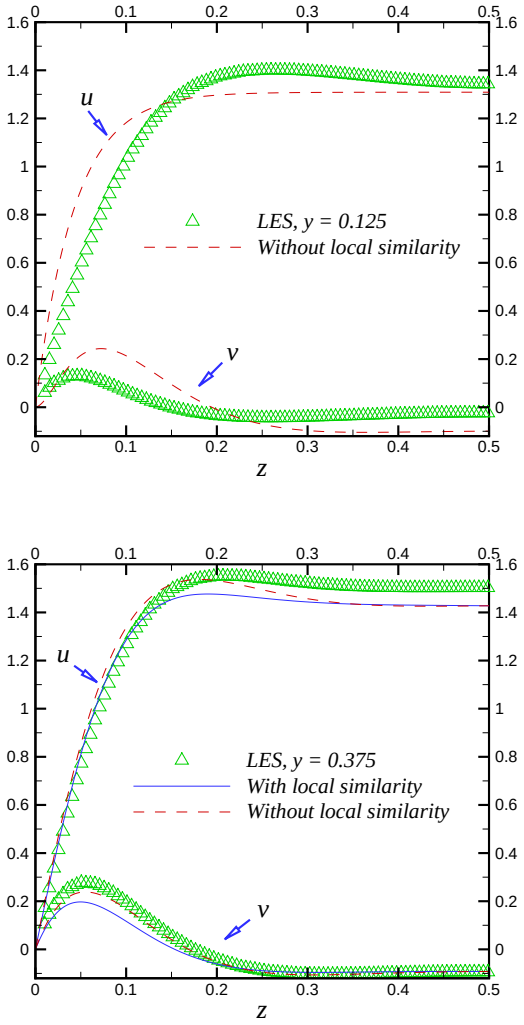

Figure 6.9 Velocity profiles in the Ekman layer

close to the vertical walls the derivatives with respect to y become important which makes the situation much more complex; also, the increasing of β as the vertical walls are being reached will dramatically slow down the convergence speed of the local similarity equations. For these reasons, the local similarity formulas are not used close to the vertical walls. As mentioned earlier, Eqs. (6.32) and(6.37) are usually good enough for predicting the u velocity profile and for calculating the bulk velocity.

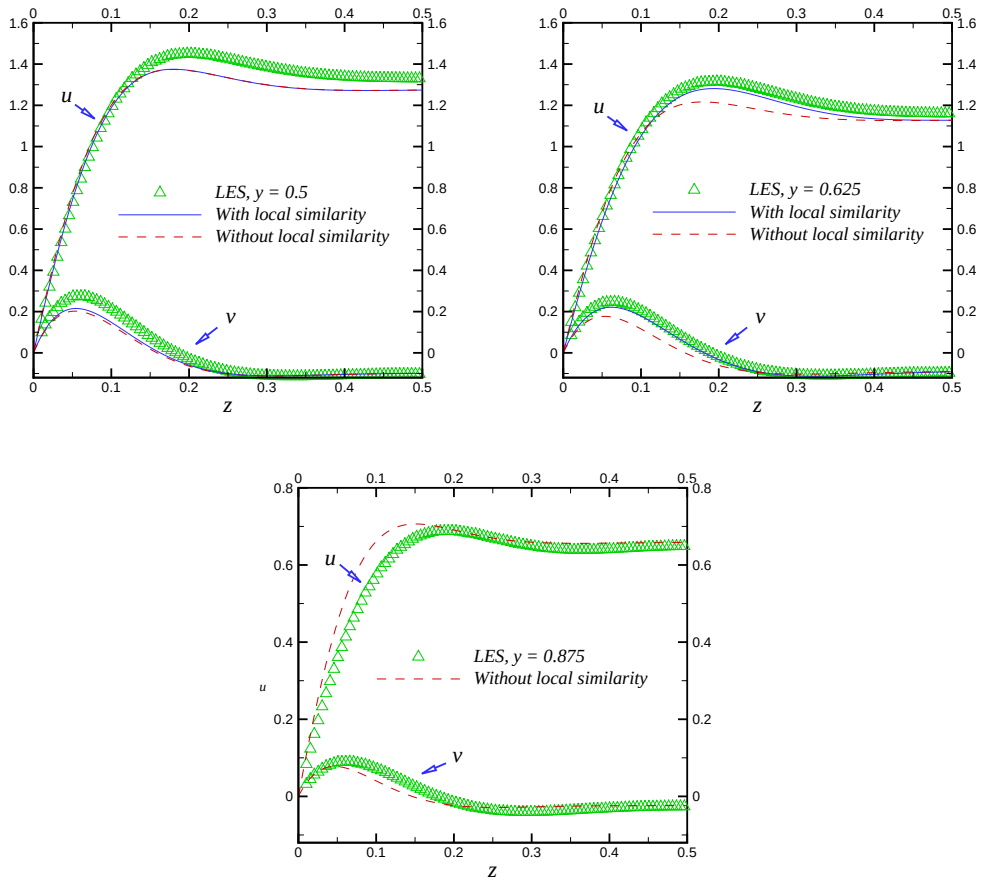

Figure 6.10 Velocity profiles in the Ekman layer, contld

6.2.6 Pressure Drop

Before closing Sec. 6.2, it is of interest to verify our velocity field calculation with experimental and numerical results. Mårtensson et al. (2002) measured the pressure drop in a rapidly rotating square duct. Pallares et al. (2005) gave a drag formula, $f = 4E^{1/2}(Ro/1.09)^{0.8}$, based on their large eddy simulations. As one can see in Fig. 6.3, even with a slight rotation, say $Ro = 0.1$, the threshold of transition to turbulence of the flow in a square duct will be increased to $Re \doteq 10^4$. Therefore, we can expect the above obtained analytic laminar flow field will be valid for the purpose of determining drag in a wide range of Reynolds and rotation numbers. The present theoretical friction coefficients, which are calculated from the velocity gradients at each wall, are compared with experimental and numerical results in Fig. 6.11, which shows

favorable agreement. Here the friction coefficients are defined as $f = 8(u_\tau/u_b)^2$, where u_τ is the friction velocity, and they are normalized by the friction coefficients for a stationary square duct at the same Reynolds number.

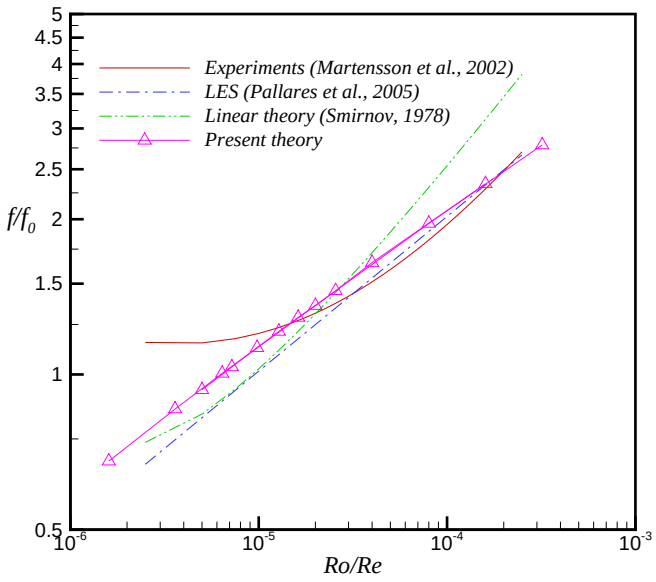

Figure 6.11 Friction coefficients

6.3 Instability of the Rotating Square Duct Flow

6.3.1 Linear Instability Analysis

Conventional linear instability analysis was implemented by superimposing infinitesimal disturbances $\tilde{\mathbf{q}}$ and $\tilde{p}$ on the base flow, which is denoted by $\mathbf{q}_l$ and p_l. In the present research only temporal modes were considered. The instantaneous velocity and pressure are

$$\mathbf{q} = \mathbf{q}_l + \tilde{\mathbf{q}}, \quad p = p_l + \tilde{p}. \tag{6.74}$$

Substituting this equation into Eqs. (6.1), (6.2) and (6.3), we have

$$\nabla \cdot \tilde{\mathbf{q}} = 0, \tag{6.75}$$

$$\frac{\partial \tilde{\mathbf{q}}}{\partial t} + \mathbf{q}_l \cdot \nabla \tilde{\mathbf{q}} + \tilde{\mathbf{q}} \cdot \nabla \mathbf{q}_l + 2Ro\hat{\mathbf{k}} \times \tilde{\mathbf{q}} = -\nabla \tilde{p} + \frac{1}{Re}\nabla^2 \tilde{\mathbf{q}}, \tag{6.76}$$

$$\frac{\partial \tilde{\mathbf{B}}}{\partial t} + \mathbf{q}_l \cdot \nabla \tilde{\mathbf{B}} - \tilde{\mathbf{B}} \cdot \nabla \mathbf{q}_l + \tilde{\mathbf{q}} \cdot \nabla \mathbf{B}_l - \mathbf{B}_l \cdot \nabla \tilde{\mathbf{q}} - 2Ro \frac{\partial \tilde{\mathbf{q}}}{\partial z} = \frac{1}{Re} \nabla^2 \tilde{\mathbf{B}}. \tag{6.77}$$

By assuming the disturbance is of a wave form then the substitution of the perturbations into the above equations results in an eigenvalue problem. The imaginary part of the complex phase speed of the perturbation wave determines if the superimposed disturbances grow or attenuate with time, that is, whether the flow is stable or unstable.

There are many methods to solve the instability eigenvalue problem; for example, the compound matrix method (Drazin and Reid, 2004). This method can be easily realized if there is only one equation and its order is not too high. However, we consider the method which will be introduced next as more satisfactory since it can be used in more general situations.

The method we used to solve all equations to follow was a finite-difference method, very similar to that of Gary and Helgason (1970). Lagrangian interpolation was used to generate a nine-point scheme so that both the equation and boundary conditions could be discretized with small truncation errors. After replacing the ordinary differential equations with finite difference equations, the system was transformed into the eigenvalue problem $|\mathbf{A} - c\mathbf{B}| = 0$. The implementation of the boundary conditions causes singularities of the coefficient matrix $\mathbf{B}$, which can be removed by the matrix deduction method of Gary and Helgason (1970). The difference between our method and that of Gary and Helgason is that instead of using a $Q-R$ algorithm, we employed Laguerre's method (Parlett, 1964) to find the eigenvalues of $\mathbf{B}^{-1}\mathbf{A}$. If the grids are not fine enough, spurious eigenvalues may arise together with the genuine one. However, the genuine eigenvalue can be easily recognized because they usually have a much larger or smaller real part than that of the spurious eigenvalues.

6.3.2 The S_1 Instability Boundary

The S_1 instability boundary is related to the instability of the Stewartson layer, which is analogous to the "roll-cell" instability in rotating channel flows (Lezius and Johnston, 1976). There are two differences, however, between these two situations. First, the base flow in a rotating channel is Poiseuille flow, which is simpler than the base flow in a rotating duct.

Secondly, there exist Ekman layers in rotating ducts so that the "free-stream" velocity profiles outside Stewartson layers are not constant but change from place to place. Therefore, the instability analysis has to be a "local" one by assuming the disturbances are not affected by environments away from the location of interest. In the rotating ducts, this location of interest is the duct center line $z = 1/2$, since the onset of instability always happens there.

Assume the disturbances do not vary in the streamwise direction and are of the form

$$\tilde{\mathbf{q}} = \tilde{u}\hat{\mathbf{i}} + \nabla \times (\tilde{\varphi}\hat{\mathbf{i}}), \tag{6.78}$$

$$\tilde{u} = u(y)exp[i\alpha(z - ct)], \tag{6.79}$$

$$\tilde{\varphi} = \varphi(y)exp[i\alpha(z - ct)], \tag{6.80}$$

$$\tilde{p} = p(y)exp[i\alpha(z - ct)], \tag{6.81}$$

in which α is the wave number and c the complex phase speed.

Substituting Eqs. (6.78) to (6.81) into (6.76) and (6.77) gives

$$(D^2 - \alpha^2)u = i\alpha Re\left[(w_l - c)u + \left(u_l' - 2Ro\right)\varphi\right] + Rev_l Du, \tag{6.82}$$

$$(D^2 - \alpha^2)^2\varphi = i\alpha Re\left[(w_l - c)(D^2 - \alpha^2)\varphi + 2Rou\right] + Rev_l(D^2 - \alpha^2)D\varphi - Rev_l'' D\varphi \tag{6.83}$$

where $D = d/dz$ and $(\cdot)' = d(\cdot)/dy$. The boundary conditions are

$$u = \varphi = D\varphi = 0 \quad \text{at } y = 0,\ 1. \tag{6.84}$$

Close to the line $z = 1/2$, $w_l \doteq 0$.

Equations (6.82) to (6.84) define an eigenvalue problem with c as the eigenvalue. Given any Re, Ro and α, there may exist one or more c so that the equations have solutions satisfying both boundary conditions at $y = 0$ and $y = 1$. If the imaginary part of c is positive, the disturbance will increase with time exponentially and the flow is unstable; if the imaginary part of c is negative, the disturbance will be damped eventually and the flow is stable. Our interest is to find out the marginal stability state, that is, when the the imaginary part of c vanishes. Extensive calculations have been carried out with the matrix deduction and Laguerre's method mentioned above. The marginal stability curves are shown in Fig. 6.12.

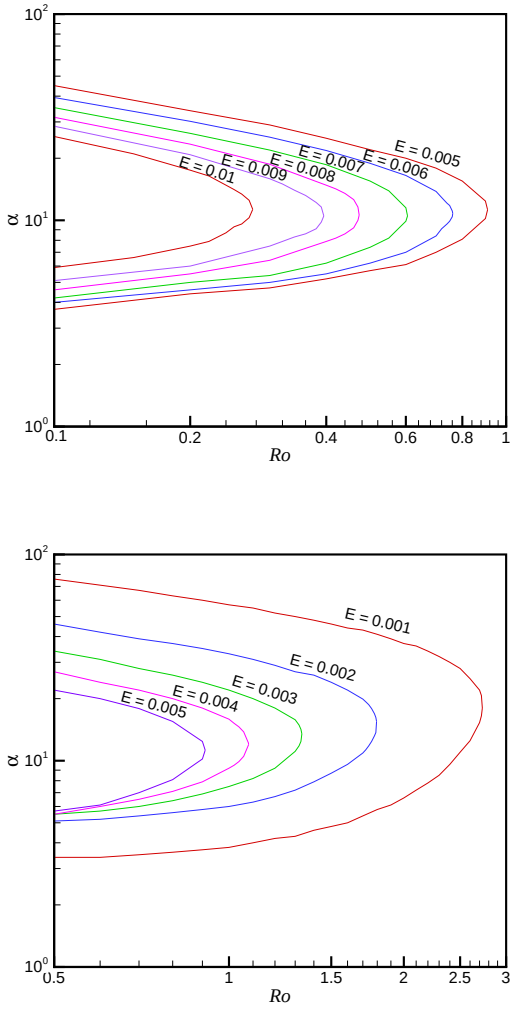

Figure 6.12 Marginal stability curves

In all these calculations the real parts of c are always of order 10^{-17} to 10^{-15} by using 200 grid points, which means the disturbance waves are stationary. This agrees with both the experimental observations of Smirnov and Yurkin (1983) and numerical simulations of Kheshgi and Scriven (1985), which showed that the flow pattern after the onset of the Stewartson instability was a steady one.

The critical rotation number for each given Ekman number is the one located at the "nose" of the corresponding marginal curve. A comparison between the present theory and the experimental data of Smirnov and Yurkin (1983) is shown in Fig. 6.13, where a reasonably

good agreement has been reached. The minimum critical Reynolds number is about 297 in

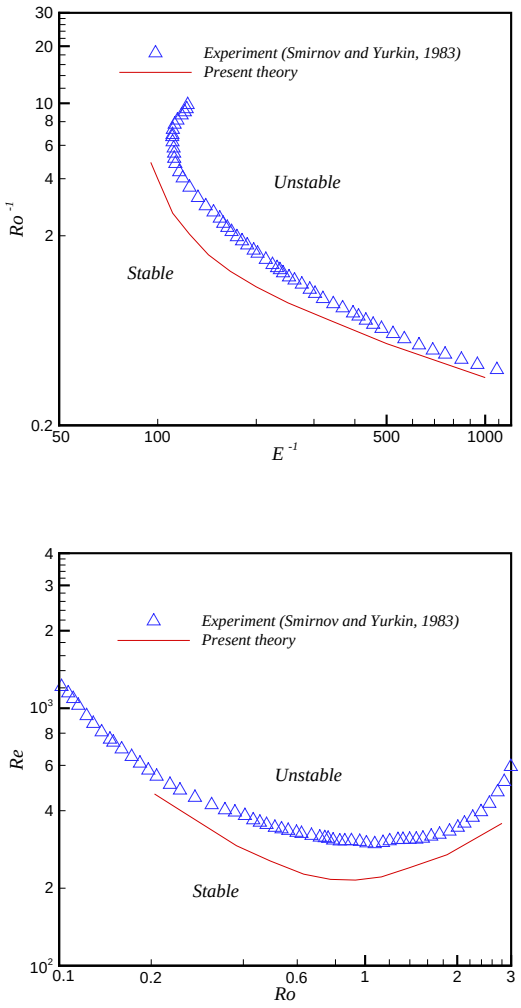

Figure 6.13 Comparison between experiment and theory

experiments and our theoretical value is 215. By neglecting v_l and repeating the calculations, it has been found that the effect of the secondary flow is to delay the occurrence of the instability. Comparing with the rotating channel case, where the critical Reynolds number is 88.53 (Lezius and Johnston, 1976), the particular u velocity profile induced by the secondary flow in a rotating duct increases the critical Reynolds number considerably.

6.3.3 The S_2 Instability Boundary

As the Stewartson layer becomes unstable, small disturbances can absorb energy from the base flow and grow with time until they are no longer small. A new steady state, the four-vortex pattern, arises as the result of such interactions between the disturbances and the base flow. The S_2 instability boundary in Fig. 6.3 shows when these two new vortices begin to pulsate. For the S_2 instability boundary, which has a shape similar to the S_1 boundary, one may suspect that it is caused by waves propagating at an angle with the z axis. However, the calculations showed that the only two angles at which the instability can occur are 0 and $\pi/2$. The former corresponds to the S_1 instability and the latter corresponds to the wave propagating in the streamwise direction and homogeneous in the z direction. This wave may cause a wavy deformation of the vortices at the unstable wall, but should not be able to produce the pulsation of the vortices. Therefore, this wave should not be responsible for the appearance of the S_2 instability boundary. Another possibility, namely the secondary instability, seems to be a more plausible explanation.

The steady four-vortex flow pattern arising from the S_1 instability, of course, is also subject to disturbances from background noise and can become unstable. One of such secondary instabilities which is of the greatest relevance to the current S_2 instability boundary may be the Eckhaus instability (Eckhaus, 1965). It considers the steady vortices subject to small z direction propagating waves. Guo and Finlay (1991) studied the Eckhaus instability of the finite-amplitude vortices in a rotating channel flow. Their results showed that the Eckhaus stability region was a small closed area tangent to the primary marginal instability curve. Since the flow can only be unstable outside of this region, the secondary critical Reynolds number is higher than the primary critical Reynolds number. We can expect a similar mechanism exists for the current rotating duct flow. However, to determine the amplitude of the two new vortices arising from the S_1 instability involves complex non-linear processes, not only from the Reynolds stress but also from the mean flow convection, which is beyond the scope of the present study and has to be deferred to future research.

6.3.4 The S_3 Instability Boundary

The S_3 instability boundary, which indicates when pulsations can be observed in the flow region where $du_1/dy - 2Ro < 0$, can be described by a single parameter $R_E = \sqrt{Re/Ro}$. R_E is indeed a Reynolds number based on the thickness of Ekman layer. The hatched region S_3 in Fig. 6.3 is in fact defined by $163 < R_E < 208$. Therefore it is not unreasonable for one to relate the S_3 boundary with the onset of Ekman layer instability.

The instability of Ekman layer has been studied for a long time. Two types of instabilities, namely the class A and the class B instabilities, have been identified. The class A instability is related to the interaction between Coriolis and shear forces and the class B instability is associated to the inflection point in the boundary layer velocity profile. These instabilities cause traveling vortex lines within the Ekman layer, which have been extensively studied experimentally and theoretically. For a review of various analyses and experiments on this topic, one is referred to the paper of Lingwood (1995).

The Ekman layer profile in a rotating square duct changes not only with z but also with y, as shown in Fig. 6.5, which is different from the situation that has been the focus of most previous researches. However, since flow in the central part of the duct shows a linear u velocity profile and the Ekman layer is controled by the gradient du_1/dy, instead of trying to calculate the instability at each y location, we only give a calculation for an "average" velocity profile, which is the velocity profile at the plane $y = 1/2$. The effects of the velocity variation with y are taken into account by retaining the $\partial u_l/\partial y$ term in governing equations.

By using a new length scale $DE^{1/2}$ and still using u_b as the velocity scale, the time scale is $DE^{1/2}/u_b$ and the equations for the small disturbances are

$$\nabla \cdot \tilde{\mathbf{q}} = 0, \tag{6.85}$$

$$R_E\left(\frac{\partial \tilde{\mathbf{q}}}{\partial t} + \mathbf{q}_l \cdot \nabla \tilde{\mathbf{q}} + \tilde{\mathbf{q}} \cdot \nabla \mathbf{q}_l\right) + 2\hat{\mathbf{k}} \times \tilde{\mathbf{q}} = -\nabla \tilde{p} + \nabla^2 \tilde{\mathbf{q}}, \tag{6.86}$$

$$R_E\left(\frac{\partial \tilde{\mathbf{B}}}{\partial t} + \mathbf{q}_l \cdot \nabla \tilde{\mathbf{B}} - \tilde{\mathbf{B}} \cdot \nabla \mathbf{q}_l + \tilde{\mathbf{q}} \cdot \nabla \mathbf{B}_l - \mathbf{B}_l \cdot \nabla \tilde{\mathbf{q}}\right) - 2\frac{\partial \tilde{\mathbf{q}}}{\partial \eta} = \nabla^2 \tilde{\mathbf{B}}. \tag{6.87}$$

We use Eqs. (6.34) and (6.35) to approximate the base flow field $\mathbf{q}_l$ and its derivative:

$$u_l = u_{lc}\left[1 - cos(\sigma\eta)exp(-\sigma\eta)\right], \tag{6.88}$$

$$v_l = \frac{u_{lc}}{\sigma^2} sin(\sigma\eta)exp(-\sigma\eta), \tag{6.89}$$

$$\frac{\partial u_l}{\partial \xi} = \frac{du_1}{d\xi}\left[1 - cos(\sigma\eta)exp(-\sigma\eta)\right], \tag{6.90}$$

$$\eta = z/E^{1/2}, \quad \xi = y/E^{1/2}, \quad \sigma = \left(1 - \frac{1}{2Ro}\frac{du_1}{dy}\right)^{1/4}, \quad u_{lc} = u_1(y = 1/2). \tag{6.91}$$

We assume the disturbances are of banded form and the bands are homogeneous in the longitudinal direction which is at a constant angle ϵ with the x axis. The disturbances propagate in the direction normal to the band longitude, which is at an angle ϵ with the y axis, as shown in Fig. 6.14. The longitudinal and propagating directions are denoted as x' and y' coordinates,

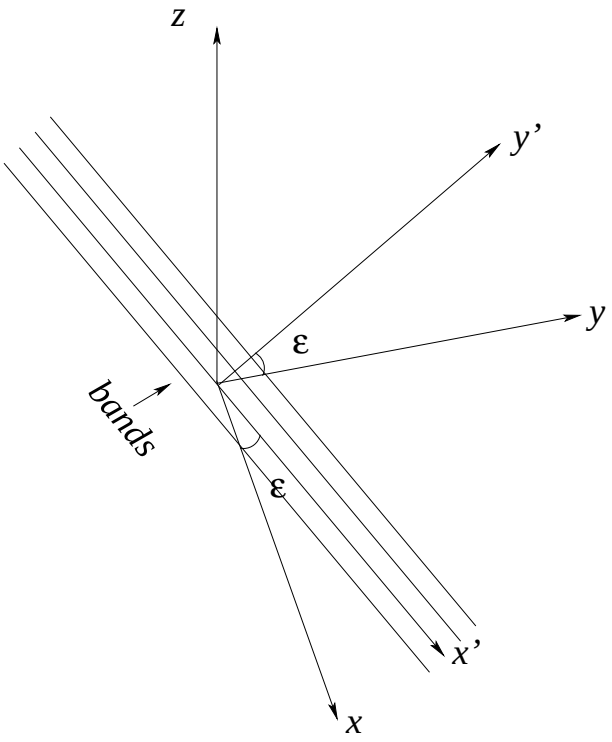

Figure 6.14 The banded disturbances

respectively. Therefore, we have

$$\tilde{\mathbf{q}} = \tilde{u}\hat{\mathbf{i}}' + \nabla \times (\tilde{\varphi}\hat{\mathbf{i}}'), \tag{6.92}$$

$$\tilde{u} = u(\eta)exp[i\alpha(\xi' - ct)], \tag{6.93}$$

$$\tilde{\varphi} = \varphi(\eta)exp[i\alpha(\xi' - ct)], \tag{6.94}$$

$$\tilde{p} = p(\eta)exp[i\alpha(\xi' - ct)], \tag{6.95}$$

$$\xi' = y'/E^{1/2}, \tag{6.96}$$

in which $\hat{\mathbf{i}}'$ is the unit vector in the x' direction, α the wave number and c the complex phase speed. Substitution of Eqs. (6.92) to (6.95) into Eqs. (6.85) to (6.87) gives

$$\begin{aligned}(D^2-\alpha^2)u = i\alpha R_E\left[(v_l cos\epsilon - u_l sin\epsilon - c)u - \left(\frac{\partial u_l}{\partial \eta}cos\epsilon + \frac{\partial v_l}{\partial \eta}sin\epsilon\right)\varphi\right] + \\ + R_E sin\epsilon cos\epsilon \frac{\partial u_l}{\partial \xi}u + \left(R_E cos^2\epsilon \frac{\partial u_l}{\partial \xi} - 2\right)D\varphi,\end{aligned} \tag{6.97}$$

$$\begin{aligned}(D^2-\alpha^2)^2\varphi = -R_E sin\epsilon cos\epsilon \frac{\partial u_l}{\partial \xi}(D^2-\alpha^2)\varphi + i\alpha R_E\left[(v_l cos\epsilon - u_l sin\epsilon - c)(D^2-\alpha^2)\varphi - \right. \\ \left. - \left(\frac{\partial^2 v_l}{\partial \eta^2}cos\epsilon - \frac{\partial^2 u_l}{\partial \eta^2}sin\epsilon\right)\varphi\right] - R_E sin\epsilon cos\epsilon \frac{\partial^2 u_l}{\partial \xi \partial \eta}D\varphi - \\ - R_E sin^2\epsilon \frac{\partial^2 u_l}{\partial \xi \partial \eta}u + \left(2 - R_E sin^2\epsilon \frac{\partial u_l}{\partial \xi}\right)Du,\end{aligned} \tag{6.98}$$

where $D = d/d\eta$. These two equations together with the boundary condition

$$\eta = 0, \quad u = \varphi = D\varphi = 0, \tag{6.99}$$

$$\eta \to \infty, \quad Du = \varphi = D^2\varphi = 0 \tag{6.100}$$

constitute an eigenvalue problem. Eigenvalues have been calculated for different combinations of E, Ro, α and ϵ. The marginal stability curves are shown in Fig. 6.15. The critical rotation numbers are shown in Fig. 6.16. The Reynolds number, wave number, phase speed and band orientation angle at each critical point are listed at Table 6.3.4. The results for the linear Ekman layer in Table 6.3.4 are due to Lilly (1966) and one can refer to the paper of Serre et al. (2004) for more recent and more accurate values.

From these numerical results it can be observed that the non-linear Ekman layer behaves quite differently from its linear counterpart. The critical Reynolds numbers of the non-linear Ekman layer for both type A and type B instabilities are considerably larger than those of linear Ekman layer. Roll vortices form in the Ekman layer as a result of these instabilities.

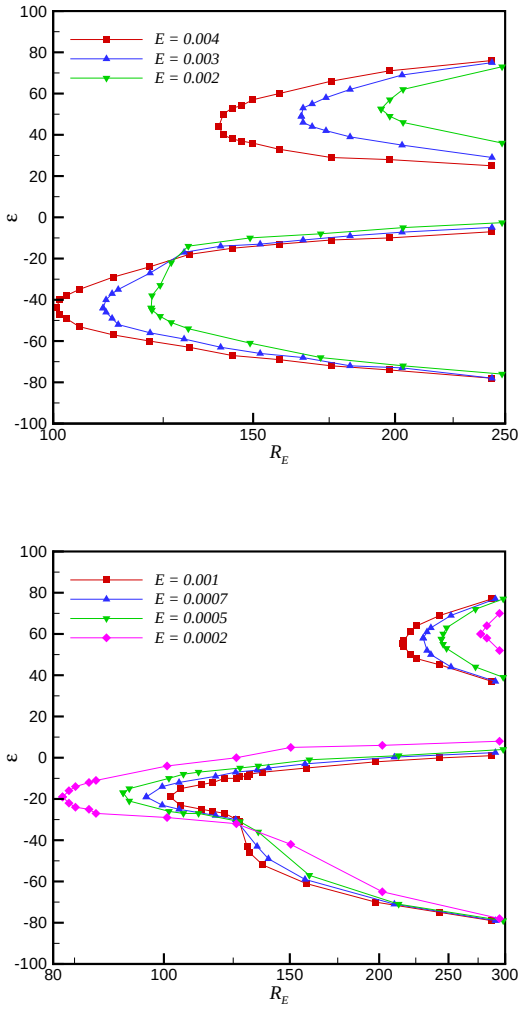

Figure 6.15 Marginal stability curves

Both phase speed and orientation angle of these roll vortices in the non-linear Ekman layer are greater than those in the linear Ekman layer.

As $E > 0.001$ the type A instability occurs at the critical disturbance orientation angle $\epsilon \doteq -44°$. As $E < 0.001$, the critical angle of the type A instability begins shifting to the linear Ekman layer limit, $\epsilon \doteq -21°$. The other critical parameters of the type A instability experience similar changes around $E = 0.001$. Although the critical parameters of the non-linear type B instability eventually converge to their linear limits as $E \to 0$, this transition process does not happen when the Ekman number is higher than 0.0002.

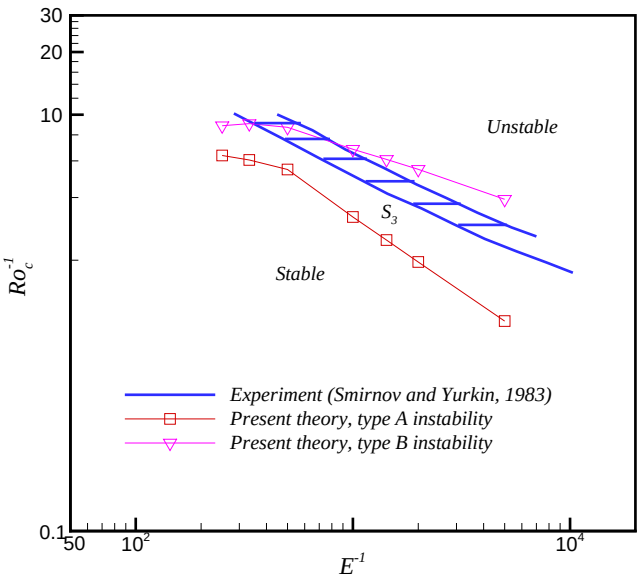

Figure 6.16 Comparison between experiment and theory

Figure 6.16 shows that the S_3 instability boundary is almost coincident with the type B instability boundary of the Ekman layer, which is reasonable since type B waves are located farther from the wall than type A waves. Therefore they can be more easily observed in laboratory. However, to draw a definite conclusion, further experimental measurements are needed to provide more details of the roll vortices caused by the S_3 instability so that the parameters obtained from the present theory may be tested.

6.3.5 The S_4 Instability Boundary

The experiments of Döbner (1959) showed that an abrupt change in the slope of the drag curves in a rotating square duct occured at a critical Reynolds number $R_E \doteq 280$. This is the S_4 instability boundary shown in Fig. 6.3. This boundary has been reasonably associated with the onset of the transition to turbulence of the Ekman layer in Smirnov and Yurkin, 1983, since most resistance in a rotating duct comes from the shear stress in the Ekman layer.

Two mechanisms are most likely to contribute to the occurrence of the S_4 instability boundary, namely the absolute instability of the Ekman layer and the wavy instability of the Stew-

Table 6.2 Critical parameters.

E	type	R_E	α	c_r	ϵ (deg)
0.004	A	101	0.87	0.85	-43.5
	B	140	1.05	-0.837	44.0
0.003	A	111	0.8	0.847	-44.0
	B	166	0.95	-0.89	49.0
0.002	A	122	0.725	0.837	-44.0
	B	194	0.80	-0.923	52.5
0.001	A	102	0.48	0.474	-19.0
	B	216	0.7	-0.954	55.5
0.0007	A	95	0.46	0.484	-19.0
	B	230	0.65	-0.973	58.0
0.0005	A	88	0.4	0.475	-17.0
	B	244	0.58	-0.961	57.5
0.0002	A	72	0.37	0.529	-19.0
	B	277	0.49	-0.972	60.0
Linear Ekman layer	A	65	0.31	0.567	-20.5
	B	110	0.53	0.094	7.5

artson layer. The absolute instability considers if a disturbance generated at a given location can grow exponentially in time and spread both upstream and downstream of this location. If it is the case, the instability will contaminate the entire flow field and lead to transition. Otherwise the unstable disturbance is being swept away from the perturbation source and the transition will not occur. Lingwood (1995) has studied the absolute instability of the Ekman layer on a rotating disk. The flow transition between a rotating and a stationary disk has been studied by Serre et al. (2004). The absolute instability is, however, beyond the scope of the present research since we will restrict attention to the temporal mode disturbances.

Another possibility that may cause the S_4 instability boundary is the wavy instability of the Stewartson layer, that is, the instability due to the streamwise-propagating disturbances. One reason that such a possibility may exist is that the unstable wall Stewartson layer also contributes a significant portion of the total drag besides the Ekman layers, as shown in Fig. 6.17, which gives the LES results of the local shear stress distribution along duct perimeter for a $Re = 5000$, $Ro = 0.176$ case. Therefore the instability of the Stewartson layer may change

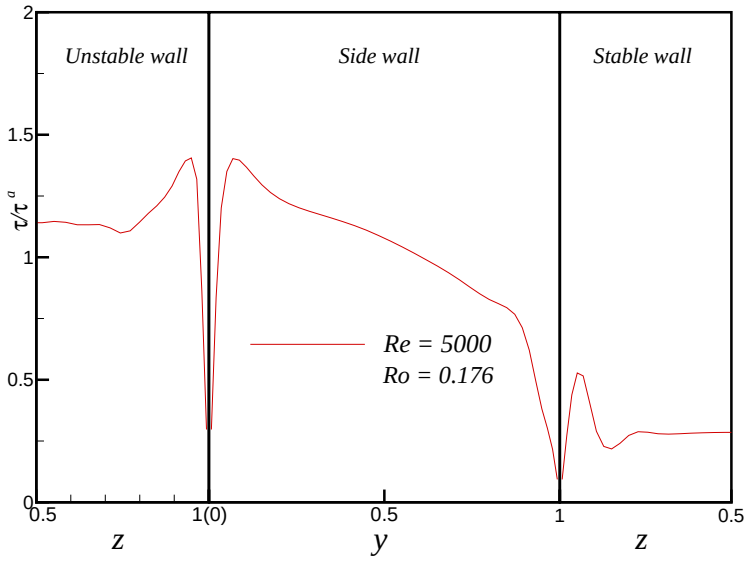

Figure 6.17 Local shear stress distribution

the drag curves. Another reason is due to the asymptotic behavior of the drag curves: since the abrupt change of the drag curve as $Ro \to 0$ (the stationary duct flow) is triggered by the streamwise-propagating disturbances, one may expect they still play a similar role in rotating duct flows.

The wavy instability of the shear layer in rotating cylindrical tanks has been studied extensively and is still an area of active research. In this scenario it is often called barotropic instability and the shear layer studied is driven by the differential rotation in the horizontal wall of the tank relative to a background rotation of the entire system. This shear layer is a Stewartson layer. One may refer to the paper of Niino and Misawa (1984) and that of Früh and Read (1999) for more information on this topic.

Busse (1968) studied the shear layer caused by differential rotation of a disc inside a rotating cylinder filled with fluid. He included the effects of Ekman friction and internal dissipation in the analysis and obtained an Orr-Sommerfeld type equation (Eq. (3.4) in his paper). Busse's method was generalized by Greenspan (1968) and formed the foundation of much theoretical work thereafter. Niino and Misawa (1984) proposed a quasi-geostrophic

model to compute the onset of the barotropic instability, which has been shown to be able to give favorable agreement with experimental results (Früh and Read, 1999). We will apply the quasi-geostrophic method to the present wavey instability problem.

The starting point is again the governing equations for fluid motion. However, we will use Ω^{-1} as the reference time scale instead of using D/u_b. The reference length and velocity scales are still duct side width D and bulk velocity u_b. Then, the $z-$component of vorticity equation is

$$\frac{\partial B_z}{\partial t} + \epsilon(\mathbf{q}\cdot\nabla B_z - \mathbf{B}\cdot\nabla w) - 2\frac{\partial w}{\partial z} = E\nabla^2 B_z, \tag{6.101}$$

where $\epsilon = 1/Ro$, which is the Rossby number. The suffix x, y and z here and hereafter are the $x-$, $y-$ and $z-$components of the corresponding vector. The "quasi-geostrophic" assumption is that u, v and B_z are considered as independent of z and w varies linearly with z. This assumption is valid in the duct region out of the Ekman layers and as $E \ll 1$.

Taking the $z-$average of Eq. (6.101) and using quasi-geostrophic assumptions, we have

$$\frac{\partial B_z}{\partial t} + \epsilon\left(u\frac{\partial B_z}{\partial x} + v\frac{\partial B_z}{\partial y}\right) - (2+\epsilon B_z)\langle\frac{\partial w}{\partial z}\rangle = E\nabla^2 B_z, \tag{6.102}$$

where $\langle\cdot\rangle = \int_0^1 \cdot dz$.

Now by using the equation for the induced normal flow at the wall in a non-linear Ekman layer, Eq. (6.39), together with the assumption that w changes linearly with z, we have

$$\langle\frac{\partial w}{\partial z}\rangle \doteq -\frac{E^{1/2}}{\sigma^3}B_z, \tag{6.103}$$

$$\sigma \doteq \left(1 - \frac{1}{2Ro}\frac{du_1}{dy}\right)^{1/4}. \tag{6.104}$$

Note we do not use Eq. (6.40) because as $E \ll 1$ the negative constant du_1/dy region occupies most of the duct.

Substituting Eq. (6.103) into Eq. (6.102) results in

$$\frac{\partial B_z}{\partial t} + \epsilon\left(u\frac{\partial B_z}{\partial x} + v\frac{\partial B_z}{\partial y}\right) + \frac{E^{1/2}}{\sigma^3}(2+\epsilon B_z)B_z = E\nabla^2 B_z. \tag{6.105}$$

If a small disturbance $\tilde{\mathbf{q}}$, $\tilde{B}_z$ is superposed on the base flow $\mathbf{q}_l$, B_z, the equation for such small disturbances is

$$\frac{\partial \tilde{B}_z}{\partial t} + \epsilon u_l\frac{\partial \tilde{B}_z}{\partial x} + \epsilon\left(v_l\frac{\partial \tilde{B}_z}{\partial y} + \tilde{v}\frac{\partial B_z}{\partial y}\right) + 2\frac{E^{1/2}}{\sigma^3}(1+\epsilon B_z)\tilde{B}_z = E\nabla^2\tilde{B}_z.$$

(6.106)

Note it is a common practice to drop the vorticity stretching term $\epsilon B_z \langle \partial w/\partial z \rangle$ in the derivation; however, this term is retained in the current study since there is no reason to drop it. Also one may notice that the base flow $\mathbf{q}_l$, especially v_l and w_l, have been significantly modified by the S_1 and S_2 instabilities. Since the modified flow field cannot be obtained within the scope of the present study, the original undisturbed flow field is used as the base flow here. Although this is not fully satisfactory, we can still expect that some useful and at least qualitative information can be extracted from the computation.

For the wavy instability we assume the disturbances are of the form

$$\tilde{\mathbf{q}} = \nabla \times (\tilde{\varphi}\hat{\mathbf{k}}) + \tilde{w}\hat{\mathbf{k}}, \tag{6.107}$$

$$\tilde{\varphi} = \varphi(y) exp\left[i\alpha(x - \epsilon ct)\right], \tag{6.108}$$

$$\tilde{B}_z = -\nabla^2 \tilde{\varphi} = -(D^2 - \alpha^2)\varphi exp\left[i\alpha(x - \epsilon ct)\right], \tag{6.109}$$

then we have

$$\begin{aligned}(D^2 - \alpha^2)^2\varphi = i\alpha Re\left[(u_l - c)(D^2 - \alpha^2)\varphi - u_l''\varphi\right] + Rev_l(D^2 - \alpha^2)D\varphi + \\ + \frac{2R_E}{\sigma^3}(Ro - u_l')(D^2 - \alpha^2)\varphi,\end{aligned} \tag{6.110}$$

where $D = d/dy$ and $(\cdot)' = d(\cdot)/dy$. The boundary condition is $\varphi = D\varphi = 0$ at $y = 0$ and $y = 1$.

The marginal stability curves at different Ekman numbers are shown in Fig. 6.18. For all Ekman numbers considered, the real parts of the eigenvalue c at the critical points are approximately the same, which is about 0.67.

The critical rotation numbers are shown in Fig. 6.19, which show qualitative agreement with the experimental S_4 instability boundary.

If one follows the method of Busse (1968) and Greenspan (1968), one will expand the disturbances in the powers of $E^{1/2}$ and end up with the following equation:

$$(D^2 - \alpha^2)^2\varphi = i\alpha Re\left[(u_l - c)(D^2 - \alpha^2)\varphi - u_l''\varphi\right] + Rev_l(D^2 - \alpha^2)D\varphi +$$

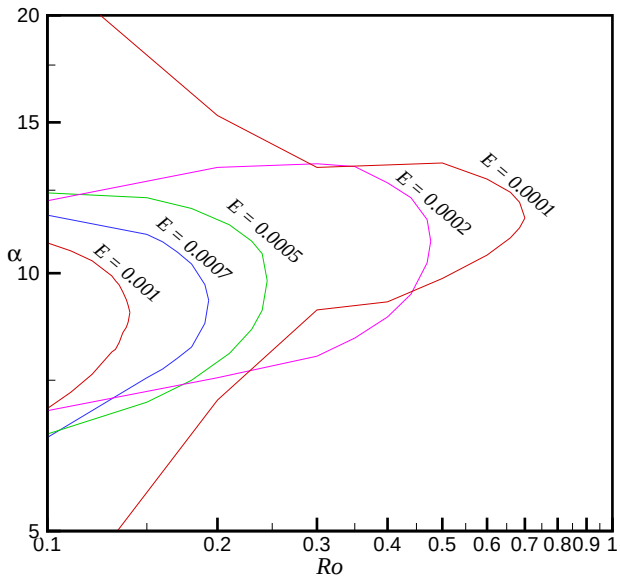

Figure 6.18 Marginal stability curves

$$+Re(\frac{2}{R_E}+v_l')(D^2-\alpha^2)\varphi. \tag{6.111}$$

It can be observed that the non-linear Ekman layer effect, which is expressed by the σ^3 term in Eq. (6.110), is absent in the above equation; also the factor before v_l' is 1 in the above equation while that before u_l' is 2 in Eq. (6.110) (Note $R_E Ro = Re/R_E$ and $E^{1/2}u_l \doteq -v_l$ as $E \ll 1$ and $Ro \gg 1$). We also tested Eq. (6.111) and the resultant critical Rossby number increases as Ekman number decreases, at least in some Ekman number ranges. This erroneous result implies that the non-linear Ekman layer effect is very important and cannot be ignored. Of course, as $E \ll 1$ and $Ro \gg 1$ both methods give the same results.

6.4 Conclusion

The present study gives a detailed theoretical analysis of the velocity field and the onset of instabilities of the flow in a rotating square duct. By combining the solutions of linear Stewartson layer, non-linear Ekman layer and a local-similarity assumption, we are able to give

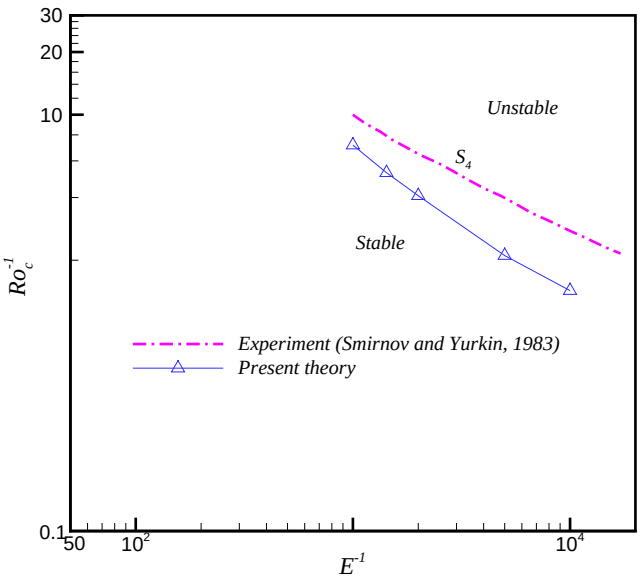

Figure 6.19 Critical rotation number

the two key parameters, du_1/dy and g_1, that control the entire velocity field. The theoretical predictions of the velocity field agree well with numerical simulations and experimental results.

By using linear stability analysis, we give the prediction of the onset of the instability of the Stewartson layer. Comparing with the rotating channel flow, the secondary flow and the particular u velocity profile in a rotating duct have the effects of increasing the critical Reynolds number. The steady four-vortex secondary flow pattern arising from this instability becomes unstable at a higher critical Reynolds number. This supercritical instability is very possible an Eckhaus instability. Unfortunately, it is a formidable task to theoretically determine the velocity field of the four-vortex secondary flow, which is needed to verify this speculation.

For the instabilities observed in the central part and stable side of a rotating duct, we propose that they are caused by the Ekman layer instabilities. We find that both type A and type B waves in the current non-linear Ekman layer are quite different with their counterparts in the linear Ekman layer: the former have considerably larger critical Reynolds number, phase speed and orientation angle. However, the characteristics of the type A wave become more and more close to their linear limits as $E < 0.001$. Such a transition does not happen to the

type B wave when $E > 0.0002$.

We relate the abrupt changes of the slopes of the drag curves to the wavy instability of the Stewartson layer, besides another possibility, namely the absolute instability of the Ekman layer. A quasi-geostrophic formula is used to include the effects of Ekman friction. From computation we find that the equation for the non-linear Ekman layer induced normal velocity should be used, otherwise no reasonable results can be obtained.

The present theoretical results invite tests by more advanced experimental measurements. Also the Eckhaus instability of the four-vortex pattern and the absolute instability of the Ekman layer require further analysis. Another possibility which may deserve attention is combining the Busse-Greenspan method with the quasi-geostrophic formula, so that a more accurate prediction of the wavy (barotropic) instability of the Stewartson layer can be reached.

CHAPTER 7. CONCLUSIONS AND RECOMMENDATIONS

The present study is summarized in Section 7.1 and the major contributions are listed in Section 7.2. The conclusions which can be drawn from the current work are given in Section 7.3. Finally, the recommended future work is discussed in Section 7.4.

7.1 Summary

The current thesis presented the idea and realization of large eddy simulation (LES) of turbulent flows with rotation and heat transfer. Also a theoretical treatment of the velocity field and instabilities of the rotating duct flow was given.

The common methodology of large eddy simulation was introduced with a special emphasis on the subgrid-scale (SGS) modeling and boundary conditions. And then the Navier-Stokes characteristic boundary condition (NSCBC) was introduced. The objective was to incorporate the NSCBC into the current LES code so that it could handle the thermally developing turbulent flow and at the same time retain the accuracy and efficiency of the implicit LU-SGS scheme. The details of such incorporation were given and the new code was then validated with simulations of stationary isothermal turbulent duct flow. The results were compared to experimental data and DNS results.

The LES formulation was then applied to the stationary turbulent duct flow with wall heating. Two different heating conditions, constant wall temperature and constant wall heat flux, were used. For each heating conditions, two heating levels, one small and one large enough to cause significant property variations, were simulated. The Nusselt numbers obtained were compared with correlations in the literature.

The turbulent heat transfer in a rotating square duct flow was then simulated. The effects

of centrifugal buoyancy forces were examined by varying the Grashof number. The resultant Nusselt number distributions were compared with experimental data.

The velocity field and instabilities of the flow in a rotating square duct was investigated theoretically. The theory was compared with numerical simulations and experiments.

7.2 Contributions

• The Navier-Stokes characteristic boundary condition (NSCBC) was incorporated into the lower-upper symmetric Gauss-Seidel (LU-SGS) scheme, which largely extended the capability of the LES code to simulate the turbulent flows in complex geometry and developing flows. Based on the author's work, Wang and Pletcher (2005) further expanded the idea to simulate supercritical fluid flows. An improvement to the current NSCBC, the so called "vanishing inviscid flux derivative" method, was made so that the code can handle flow reversal without any buffer zones.

• To the author's knowledge, this work gives the first report of LES of thermally developing turbulent duct flow with constant high heating. There are even no appropriate empirical correlations in the literature to compare with our results. The current results therefore are expected to call for more experimental researches in this area. The present work explored the "relaminarization" phenomenon in turbulent flow under high heating.

• The large eddy simulations of turbulent heat transfer in a rotating square duct was carried out. This is the first LES simulation of rotating turbulent duct flow with property variations. Fairly satisfactory agreement between prediction and experimental results of Nusselt number was achieved. The interaction between the buoyancy, flow pattern and temperature was interpreted.

• This work is also the first one to give a complete theoretical treatment of the velocity field and instability of the flow in a rotating duct. The velocity field was determined from first principles and the pressure drop (drag) obtained without resorting to any empirical formulas. The instabilities of the Stewartson layer and the Ekman layer were investigated with linear instability analysis and good agreement between theory and experimental data was reached.

7.3 Conclusions

From the present work, the following conclusions can be drawn.

• The NSCBC strategy should be incorporated into the original scheme rather than being used separately. And the current incorporation of NSCBC and LU-SGS scheme is able to maintain the friction velocity level in the computational domain and can be used to simulate turbulent flows in complex geometry and developing flows. This scheme was tested by simulating isothermal stationary and rotating square duct flows and very good agreement between our results and previous DNS and experimental data has been achieved.

• Turbulent duct flows under heating with constant wall temperature and constant wall heat flux conditions were simulated. The strong heating causes significant property variations in the fluids and leads the flow to become more laminar-like. The local heat transfer coefficients decrease as the heat transfer rate increases. The mean velocity and temperature profiles approach laminar distributions downstream. The turbulent kinetic energy, temperature fluctuations and Reynolds stress also decrease. Heat transfer was found to have obvious impact on the secondary flows. The secondary flows take part in the momentum and heat transport and are responsible for the modification of the distributions of wall shear stress and wall heat flux. Also heating has an effect to decrease the magnitude of turbulent Prandtl number and make its distribution more uniform.

• In the fully developed isothermal rotating duct flows, the cross-stream fluctuations ($\langle v'^2 \rangle$ and $\langle w'^2 \rangle$) obtain their peak values near the stable side rather than near the unstable side when the rotation number is small. This is due to the contribution of secondary flows on the turbulent production.

• In the turbulent flow in a heated rotating duct, buoyancy changes the secondary flow pattern through a delicate force balance. In the outward flows, the opposing buoyancy retards or even reverses the flow near the stable side. This results in a reduced or even reversed Coriolis force and in turn, a reduced favorable or even adverse pressure gradient which does not favor the development of the Ekman layer at the side wall and, as a result, weakens the stable wall corner rotating cell. In the inward flows, the aiding buoyancy accelerates fluids close to the

stable wall giving rise to an enhanced favorable pressure gradient which strengthens the Ekman layer as well as the stable wall corner rotating cell.

• In the turbulent flow in a heated rotating duct, buoyancy influences the temperature (and as a result, Nusselt number) and mean shear stress distribution on the stable wall not only by changing the streamwise velocity directly, but also by modifying secondary flow patterns. Since the Ekman layer transports cold and high speed fluid from the duct interior to the stable wall and the Stewartson layer transports hot and low speed fluid from the stable side to the duct interior, in the buoyancy-free flows, the Nusselt number and mean shear stress on the stable wall obtains their peak values at the corner, while the temperature maximum appears at the wall-bisector. In the outward flows, the weakened secondary flow results in high temperature near the stable side corner and a Nusselt number maximum at the wall-bisector. In the inward flows, the strengthened secondary flow results in high temperature near the central stable wall. The aiding buoyancy accelerates the hot fluid; thus, a high shear stress appears near the stable wall-bisector in the inward flows. This explains the discrepancy between the Nusselt number and shear stress distributions at the stable wall.

• In the turbulent flow in a heated rotating duct, buoyancy affects turbulent kinetic energy and temperature fluctuation distributions through its contributions to the relevant production terms. Buoyancy influences the production of turbulent kinetic energy in two ways: by modifying the mean shear and by acting directly as a buoyancy production term. The latter can dominate if the buoyancy parameter $\frac{Gr}{\epsilon Re_r^2}$ becomes large. It has been found that the secondary flow pattern has a strong relationship with the vertical heat flux $-\langle v'T'\rangle$, which is vital in the production term of the temperature fluctuations. Buoyancy thus impacts the temperature fluctuations indirectly by altering the secondary flow pattern.

• In the turbulent flow in a heated rotating duct, there is a strong correlation between the peripheral distributions of local Nusselt number and mean shear stress at the unstable wall and the side wall.

• By combining the solutions of linear Stewartson layer, non-linear Ekman layer and a local-similarity assumption, we are able to give the two key parameters, du_1/dy and g_1, that

control the entire velocity field. The theoretical predictions of the velocity field agree well with numerical simulations and experimental results.

• By using linear stability analysis, we give the prediction of the onset of the instability of the Stewartson layer. Compared with the rotating channel flow, the secondary flow and the particular u velocity profile in a rotating duct have the effects of increasing the critical Reynolds number. The steady four-vortex secondary flow pattern arising from this instability becomes unstable at a higher critical Reynolds number. This supercritical instability is very possible an Eckhaus instability. Unfortunately, it is a formidable task to theoretically determine the velocity field of the four-vortex secondary flow, which is needed to verify this speculation.

• For the instabilities observed in the central part and stable side of a rotating duct, we propose that they are caused by the Ekman layer instabilities. We find that both type A and type B waves in the current non-linear Ekman layer are quite different from their counterparts in the linear Ekman layer: the former have a considerably larger critical Reynolds number, phase speed and orientation angle. However, the characteristics of the type A wave become closer and closer to their linear limits as $E < 0.001$. Such a transition does not happen to the type B wave when $E > 0.0002$.

• We relate the abrupt changes of the slopes of the drag curves to the wavy instability of the Stewartson layer, besides another possibility, namely the absolute instability of the Ekman layer. A quasi-geostrophic formula is used to include the effects of Ekman friction. From computation we find that the equation for the non-linear Ekman layer induced normal velocity should be used, otherwise no reasonable results can be obtained.

7.4 Recommendations for Future Work

• The turbulent heat transfer in a stationary square duct needs more simulations for more heating levels. One may give a Nusselt number correlation from these numerical results.

• In this work only fairly satisfactory agreement between LES and experiments has been reached for the Nusselt number distributions at each wall of a rotating duct. A possible reason is that we did not consider the conduction of the duct wall. Such a coupled conduction-

convection simulation is very desired so that more accurate predictions can be made.

• The Eckhaus instability of the four-vortex pattern and the absolute instability of the Ekman layer require further analysis. Another possibility which may deserve attention is combining the Busse-Greenspan method with the quasi-geostrophic formula, so that a more accurate prediction of the wavy (barotropic) instability of the Stewartson layer can be reached.

• It is of great interest to theoretically determine the four-vortex pattern, which arises from non-linear disturbance-flow interactions. However, this task may be too difficult and one may begin with the rotating channel flow. In this way, one has the opportunity to test the theories of Malkus (1956), of Stuart (1958), etc. and to link the many clues of instability and transition processes together to give a great insight into turbulent flows.

APPENDIX A. JACOBIAN MATRICES

Notice all the over-bars denoting the filtered variables such as $\overline{(\cdot)}$, $\tilde{(\cdot)}$, $\hat{(\cdot)}$ have been droped for simplicity. However, their meanings should not be confused with the original unfiltered variables.

The transformation matrix between the conservative and the primitive variables (see Eq. 2.64) is

$$[T] = \begin{bmatrix} 1/T & 0 & 0 & 0 & -p/T^2 \\ u/T & p/T & 0 & 0 & -pu/T^2 \\ v/T & 0 & p/T & 0 & -pv/T^2 \\ w/T & 0 & 0 & p/T & -pw/T^2 \\ c_v + \frac{1}{2}(u^2+v^2+w^2)/T & pu/T & pv/T & pw/T & -\frac{1}{2}(p/T^2)(u^2+v^2+w^2) \end{bmatrix} \tag{A.1}$$

Its inverse is

$$[T]^{-1} = \begin{bmatrix} (u^2+v^2+w^2)/(2c_v) & -u/c_v & -v/c_v & -w/c_v & 1/c_v \\ -uT/p & T/p & 0 & 0 & 0 \\ -vT/p & 0 & T/p & 0 & 0 \\ -wT/p & 0 & 0 & T/p & 0 \\ (T/p)\left[(u^2+v^2+w^2)/(2c_v) - T\right] & -uT/(pc_v) & -vT/(pc_v) & -wT/(pc_v) & T/(pc_v) \end{bmatrix} \tag{A.2}$$

The preconditiong matrix (see Eq. 2.83) is

$$[\Gamma] = \begin{bmatrix} R/T & 0 & 0 & 0 & -p/T^2 \\ R/T & p/T & 0 & 0 & -pu/T^2 \\ R/T & 0 & p/T & 0 & -pv/T^2 \\ Rw/T & 0 & 0 & p/T & -pw/T^2 \\ R\left[c_v + \frac{1}{2}(u^2+v^2+w^2)/T\right] & pu/T & pv/T & pw/T & -\frac{1}{2}(p/T^2)(u^2+v^2+w^2) \end{bmatrix} \tag{A.3}$$

Its inverse is

$$[\Gamma]^{-1} = \begin{bmatrix} (u^2+v^2+w^2)/(2Rc_v) & -u/(Rc_v) & -v/(Rc_v) & -w/(Rc_v) & 1/(Rc_v) \\ -uT/p & T/p & 0 & 0 & 0 \\ -vT/p & 0 & T/p & 0 & 0 \\ -wT/p & 0 & 0 & T/p & 0 \\ (T/p)\left[(u^2+v^2+w^2)/(2c_v) - T\right] & -uT/(pc_v) & -vT/(pc_v) & -wT/(pc_v) & T/(pc_v) \end{bmatrix} \tag{A.4}$$

The flux Jacobian matrices (see Eq. 2.87) are

$$[A] = \begin{bmatrix} u/T & p/T & 0 & 0 & -pu/T^2 \\ u^2/T + R & 2pu/T & 0 & 0 & -pu^2/T^2 \\ uv/T & pv/T & pu/T & 0 & -puv/T^2 \\ uw/T & pw/T & 0 & pu/T & -puw/T^2 \\ uH/T & (p/T)(H+u^2) & puv/T & puw/T & -\frac{1}{2}(pu/T^2)(u^2+v^2+w^2) \end{bmatrix} \tag{A.5}$$

$$[B] = \begin{bmatrix} v/T & 0 & p/T & 0 & -pv/T^2 \\ vu/T & pv/T & pu/T & 0 & -pvu/T^2 \\ v^2/T + R & 0 & 2pv/T & 0 & -pv^2/T^2 \\ vw/T & 0 & pw/T & pv/T & -pvw/T^2 \\ vH/T & pvu/T & (p/T)(H+v^2) & pvw/T & -\frac{1}{2}(pv/T^2)(u^2+v^2+w^2) \end{bmatrix} \tag{A.6}$$

$$[C] = \begin{bmatrix} w/T & 0 & 0 & p/T & -pw/T^2 \\ wu/T & pw/T & 0 & pu/T & -pwu/T^2 \\ wv/T & 0 & pw/T & pv/T & -pwv/T^2 \\ w^2/T + R & 0 & 0 & 2pw/T & -pw^2/T^2 \\ wH/T & pwu/T & pwv/T & (p/T)(H + w^2) & -\frac{1}{2}(pw/T^2)(u^2 + v^2 + w^2) \end{bmatrix} \quad \text{(A.7)}$$

where

$$H = c_p T + \frac{1}{2}(u^2 + v^2 + w^2) \quad \text{(A.8)}$$

APPENDIX B. MATRICES FOR NSCBC

Using the formulas of $[T]^{-1}$ and $[A]$ in Appendix A, we have

$$[\Pi] = [T]^{-1}[A] = \begin{bmatrix} u & \gamma p & 0 & 0 & 0 \\ 1/\rho & u & 0 & 0 & 0 \\ 0 & 0 & u & 0 & 0 \\ 0 & 0 & 0 & u & 0 \\ 0 & (\gamma-1)T & 0 & 0 & u \end{bmatrix} \tag{B.1}$$

where γ is the specific heat ratio, which is $\gamma = c_p/c_v = 1 + R/c_v$.

Let $[\Pi] = [S][\Lambda][S]^{-1}$, where $[\Lambda]$ is a diagonal matrix with elements which are eigenvalues of $[T]^{-1}[A]$, then the rows of $[S]^{-1}$ are the corresponding eigenvectors.

$$[\Lambda] = \begin{bmatrix} u+c & 0 & 0 & 0 & 0 \\ 0 & u-c & 0 & 0 & 0 \\ 0 & 0 & u & 0 & 0 \\ 0 & 0 & 0 & u & 0 \\ 0 & 0 & 0 & 0 & u \end{bmatrix} \tag{B.2}$$

where c is the local sound speed which is $c = \sqrt{\gamma RT}$.

$$[S] = \begin{bmatrix} (p/T)[\gamma/(\gamma-1)] & (p/T)[\gamma/(\gamma-1)] & 0 & 0 & 0 \\ c/[(\gamma-1)T] & -c/[(\gamma-1)T] & 0 & 0 & 0 \\ 0 & 0 & 0 & 1 & 0 \\ 0 & 0 & 0 & 0 & 1 \\ 1 & 1 & 1 & 0 & 0 \end{bmatrix} \tag{B.3}$$

$$[S]^{-1} = \begin{bmatrix} (\gamma-1)T/(2\gamma p) & (\gamma-1)T/(2c) & 0 & 0 & 0 \\ (\gamma-1)T/(2\gamma p) & -(\gamma-1)T/(2c) & 0 & 0 & 0 \\ -(\gamma-1)T/(\gamma p) & 0 & 0 & 0 & 1 \\ 0 & 0 & 1 & 0 & 0 \\ 0 & 0 & 0 & 1 & 0 \end{bmatrix} \tag{B.4}$$

The "wave vector "$\mathcal{L}$ is defined by $\mathcal{L} = [\Xi]\frac{\partial \mathbf{W}}{\partial x} = [\Lambda][S]^{-1}\frac{\partial \mathbf{W}}{\partial x}$. The matrix $[\Xi]$ is

$$[\Xi] = \begin{bmatrix} (u+c)(\gamma-1)T/(2\gamma p) & (u+c)(\gamma-1)T/(2c) & 0 & 0 & 0 \\ (u-c)(\gamma-1)T/(2\gamma p) & -(u-c)(\gamma-1)T/(2c) & 0 & 0 & 0 \\ -u(\gamma-1)T/(\gamma p) & 0 & 0 & 0 & u \\ 0 & 0 & u & 0 & 0 \\ 0 & 0 & 0 & u & 0 \end{bmatrix} \tag{B.5}$$

and its inverse is

$$[\Xi]^{-1} = \begin{bmatrix} \frac{p}{(u+c)T}\frac{\gamma}{\gamma-1} & \frac{p}{(u-c)T}\frac{\gamma}{\gamma-1} & 0 & 0 & 0 \\ \frac{c}{(u+c)(\gamma-1)T} & -\frac{c}{(u-c)(\gamma-1)T} & 0 & 0 & 0 \\ 0 & 0 & 0 & 1/u & 0 \\ 0 & 0 & 0 & 0 & 1/u \\ 1/(u+c) & 1/(u-c) & 1/u & 0 & 0 \end{bmatrix} \tag{B.6}$$

APPENDIX C. MOLECULAR DYNAMICS SIMULATIONS OF FLUID FLOW IN A ROTATING CHANNEL

Introduction

In this chapter[1], molecular dynamics (MD) simulations of a Lennard-Jones liquid flowing through a rotating nano-scale channel are presented.

Fluid flows under a rotating frame are of engineering interest and have been extensively studied. The researches in this field can be put into three categories: theoretical, experimental and numerical. Traditionally, macroscopic hydrodynamic equations such as the Navier-Stokes equations are used in numerical simulations. In the past two decades, MD simulation has attracted more and more attention for it can provide detailed information about the flow field. Most previous MD simulations focused on unidirectional flows, such as Couette and Poiseuille flows (Thompson and Troian, 1997; Xu et al., 2004). The present study tries to extend the MD method to the rotating flows.

Compared with non-rotating flows, the frame rotation will cause fictional centrifugal and Coriolis forces inside the fluids. The Coriolis force is an apparent force the fluid feel according to an observer rotating with the frame. A well known example of the effects of Coriolis force is the wind circulation. The Coriolis force is given by $-2m\vec{\Omega} \times \vec{V}$ where m is the mass of the particle, $\vec{\Omega}$ the angular velocity vector of rotation and $\vec{V}$ is the particle velocity vector. In the present simulation, the channel is rotating around y axis (see Fig. C.1), thus, the Coriolis forces are along x and z directions with magnitudes $2m\Omega V_z$ and $2m\Omega V_x$, respectively.

The centrifugal force and all other driving forces like pressure drop are combined into

[1]This chapter is based on a paper published in the *Proceedings of ASME Integrated Nanosystems Conference*, September 2005, University of California, Berkeley.

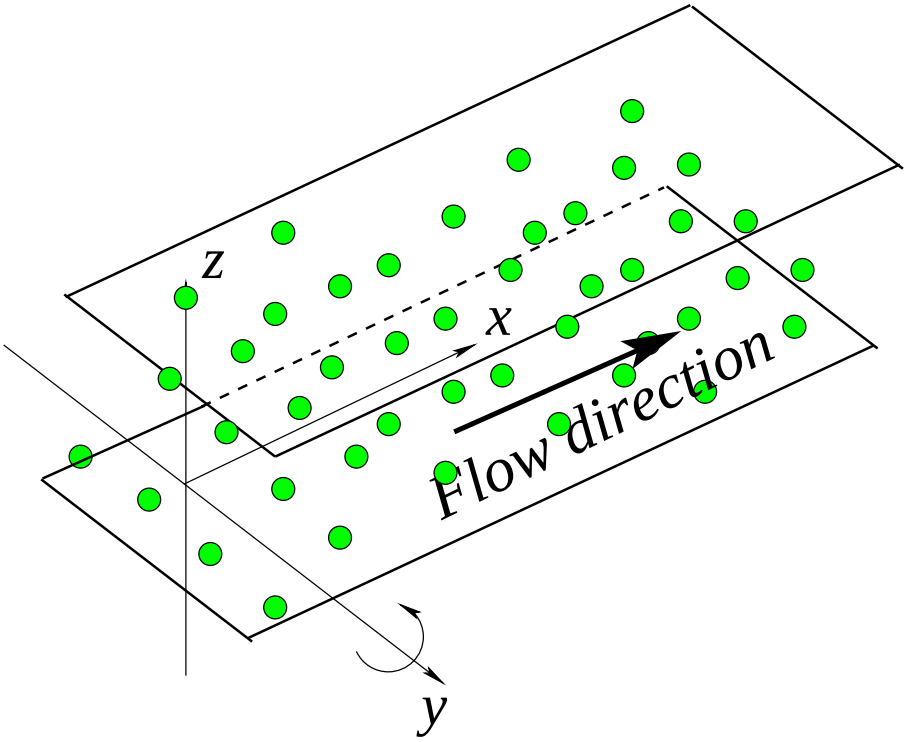

Figure C.1 Domain of the rotating channel

one "gravity" g in the x direction to drive the flow. It has been found in the macroscopic rotating channel flow that the Coriolis force causes a stream wise velocity gradient $\frac{dV_x}{dz} = 2\Omega$ in the central part of the channel which can be easily deduced from the reduced Navier-Stokes equation of x momentum:

$$V_z \frac{dV_x}{dz} = 2\Omega V_z \tag{C.1}$$

The pressure gradient $\frac{dP}{dz}$ is equal to $-2\Omega V_x$ so that it can balance the Coriolis force. Near the walls, the viscous force balances the other forces and the non-slip condition holds.

By doing the molecular dynamics simulation, it is hoped that a better understanding of the phenomenon in the rotating channel can be obtained. It is also of interest to compare the MD results with results from macroscale calculations.

Simulation Method

Potential Model

As Fig. C.2 shows, any fluid particle i will interact with liquid particle j and wall particle j_w. Besides these particle-particle interactions, the liquid molecule also will feel external forces, namely, the "gravity" force and Coriolis force. The Lennard-Jones pairwise potential is used for the interactions between fluid/fluid and fluid/wall molecules, which is written as

$$V(r) = 4\epsilon[(\frac{\sigma}{r})^{12} - (\frac{\sigma}{r})^{6}]. \tag{C.2}$$

The force between two fluid molecules i and j is

$$F_{ij}(r) = \begin{cases} 24\frac{\epsilon}{\sigma}[2(\frac{\sigma}{r})^{13} - (\frac{\sigma}{r})^{7}]\vec{r_{ij}}/|\vec{r_{ij}}|, & \text{if } r < r_c \\ 0, & otherwise \end{cases} \tag{C.3}$$

where $r_{ij} = |\vec{r_{ij}}|$, $\vec{r_{ij}} = \vec{r_i} - \vec{r_j}$. The interaction between fluid molecule and wall molecule has similar expression:

$$F_{ij_w}(r) = \begin{cases} 24\frac{\epsilon_{wf}}{\sigma_{wf}}[2(\frac{\sigma_{wf}}{r})^{13} - (\frac{\sigma_{wf}}{r})^{7}]\vec{r_{ij_w}}/|\vec{r_{ij_w}}|, & \text{if } r < r_{cw} \\ 0, & otherwise \end{cases} \tag{C.4}$$

where σ_{wf} and ϵ_{wf} are the length scale and energy scale for the fluid-wall system. The cut-off distance r_c between liquid molecules is set to be 2.5σ and the cut-off distance r_{cw} between liquid and wall molecules is set to be $2.5\sigma_{wf}$. The equations of motion are solved by the Verlet algorithm. It is convenient to use the reduced quantities

$$\begin{array}{cccc} r^\star = \frac{r}{\sigma} & t^\star = \frac{t}{\sigma}\sqrt{\epsilon} & F^\star = \frac{F\sigma}{\epsilon} & g^\star = \frac{mg\sigma}{\epsilon} \\ V^\star = V\sqrt{m/\epsilon} & T^\star = \frac{k_B T}{\epsilon} & Ro = 2\Omega\sigma\sqrt{m/\epsilon} & n^\star = n\sigma^3 \end{array} \tag{C.5}$$

and omit the asterisk if no confusion can occur. Thus, the total force acting on a fluid molecule i is $24\sum_{j\neq i,j=1}^{N}\left(\frac{2}{|r_{ij}{}^{13}|} - \frac{1}{|r_{ij}{}^{7}|}\right)\frac{(\vec{r_i}-\vec{r_j})}{|r_{ij}|} + 24\frac{\epsilon_{wf}/\epsilon}{\sigma_{wf}/\sigma}\sum_{j_w=1}^{N_w}\left[(\frac{\sigma_{wf}}{\sigma})^{13}\frac{2}{|r_{ij_w}{}^{13}|} - (\frac{\sigma_{wf}}{\sigma})^{7}\frac{1}{|r_{ij_w}{}^{7}|}\right]\frac{(\vec{r_i}-\vec{r_{j_w}})}{|r_{ij_w}|} + (g + Ro\cdot V_z)\vec{i} - Ro\cdot V_x\vec{k}$. Here $\vec{i}$ and $\vec{k}$ are the unit vector of the x and z axes, respectively. N is the number of fluid particles and N_w is that of wall particles. It can be seen that the rotating channel flow is controlled by the parameters of liquid particle number N, wall particle number N_w, length scale ratio σ_{wf}/σ, energy scale ratio ϵ_{wf}/ϵ, non-dimensional gravity force g, rotation number Ro and the geometry.

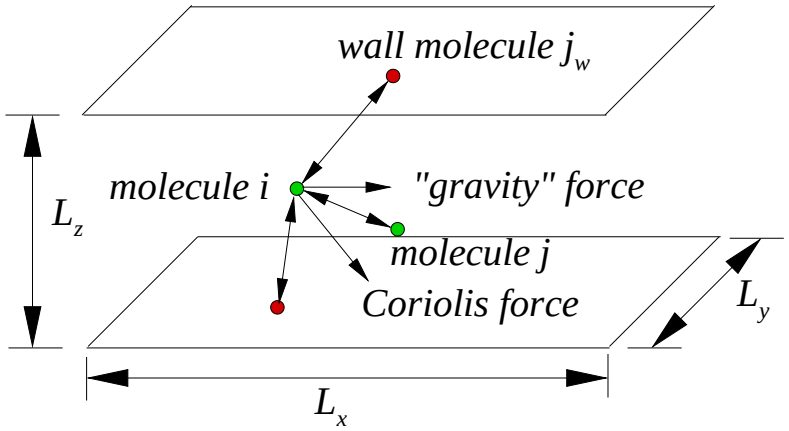

Figure C.2 Sketch of the forces acted on molecule i

Initial Conditions

The initial configuration of wall molecules is assigned so that molecules are evenly located on the two walls. All fluid molecules are initially located at the sites of a FCC lattice with a random distributed displacement. This arrangement always causes unphysically large potentials. To avoid this, a Monte Carlo-like process is used to reduce the system potential until a more reasonable new structure is achieved. Randomly distributed fluid particle velocities are assumed to initiate the calculation. In the beginning of the simulation the fluid molecules are allowed to move without applying external forces until the thermodynamic equilibrium is reached. At the same time, the fluid molecule velocities are rescaled so that the fluid temperature is equal to the initial fluid temperature. The program will store the results such as locations and velocities of molecules in a restart file so that it can be read when the program is restarted.

Boundary Conditions

Periodic boundary conditions are applied on the fluid boundary (x and y directions) of the computational domain. On the wall boundary (z direction), specular wall conditions are used. In fact, when the liquid particle is close to the solid wall surface, the repulsive force between it and wall particles will push the liquid particle away from the wall. However, it is still possible for some liquid particles to "leak" from the box. If it happens, then the program will reflect them back into the box, as Fig. C.3 shows.

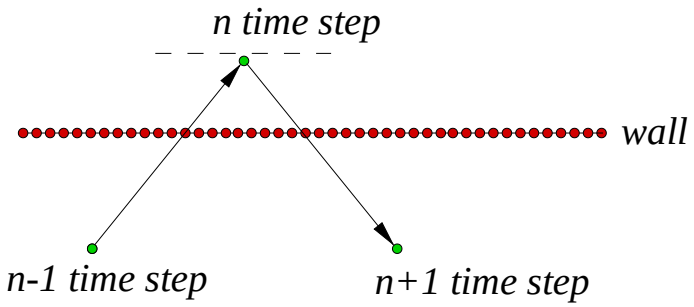

Figure C.3 Reentry mechanism

A crucial problem is the dissipation of the heat generated by the driving force. The work done by the external force is partly converted into heat and increases the temperature of the fluid. It is a common practice to use a thermostat to keep the temperature constant. However, a thermostat requires additional free parameters which maybe result in some arbitrariness in the results. In the present simulation, a more physically meaningful approach, wall temperature

scaling (WTS) is adopted following Heinbuch and Fischer (1989). That is, the velocities are scaled down to keep the local kinetic temperature constant in the fluid layer closest to the wall and equal to the initial equilibrium temperature. In the present simulation, the fluid molecules with distance away from wall less than 1 will be rescaled.

Parameter Averaging

The MD simulation needs a suitable time step. In the current simulation, a time step $\Delta t = 0.0005$ was chosen. After integrating for about $200,000$ steps, the system reached steady-state. The mean value distribution of variables such as velocity, number density are computed as a function of z. An identity function $H_n(i,j)$ is defined as

$$H_n(i,j) = \begin{cases} 1, & if (n-1)\Delta z < z_i^j < n\Delta z \\ 0, & otherwise \end{cases} \tag{C.6}$$

where n means the n^{th} slab in z direction, i means the i^{th} fluid particle and j represents the j^{th} time step. The average number density in the n^{th} slab from time step J_n to J_m is

$$n = \frac{\sum_{j=j_n}^{j_m} \sum_{i=1}^{N} H_n(i,j)}{L_x L_y \Delta z (J_m - J_n + 1)} \tag{C.7}$$

The slab average velocity from time step J_n to J_m is

$$u(n) = \frac{\sum_{j=j_n}^{j_m} \sum_{i=1}^{N} H_n(i,j) V_{x,i}^j}{\sum_{j=j_n}^{j_m} \sum_{i=1}^{N} H_n(i,j)} \tag{C.8}$$

Results

Verification of the Present MD Code

Two cases were performed to verify the current MD code. The first is the slip flow confined between two parallel plates, which is compared with the results of Thompson and Troian (1997). The geometry considered is two parallel walls with one stationary and another one moving at a constant speed in the x direction. The domain is $12.51\sigma \times 7.22\sigma \times 24.57\sigma$. 1000 fluid particles with 100 wall particles were used in this case. The other parameters are $\epsilon_{wf}/\epsilon = 0.6$, $\sigma_{wf}/\sigma = 1.0$.

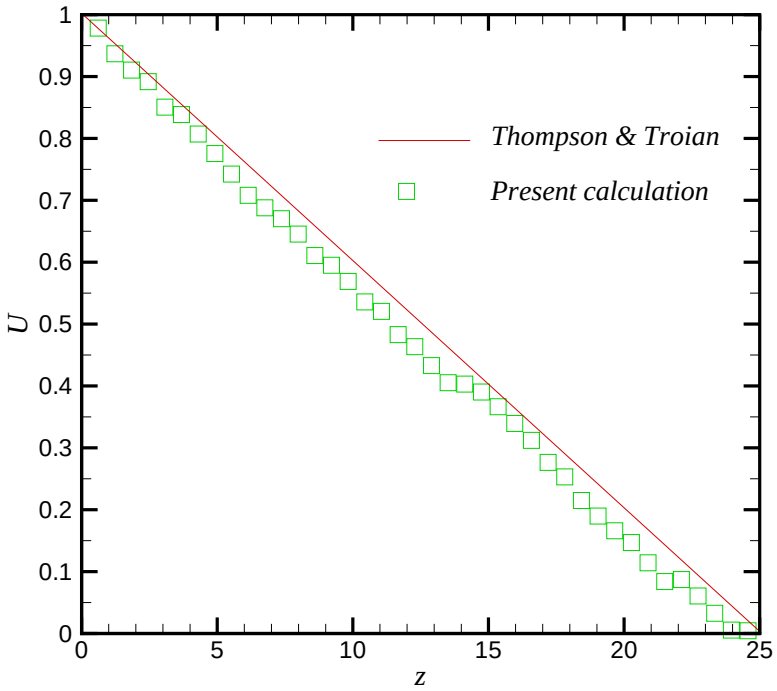

Figure C.4 Mean axial velocity distributions (Couette flow)

The result is shown in Fig. C.4. It can be observed that good agreement between the current simulation and the previous one is obtained. The small wiggles in the present result are due to the not-long-enough averaging steps.

Another test case is Poiseuille flow. That is, a flow is confined between two parallel plates and driven by a constant body force g. This type of flow also can be considered a special rotating channel flow with rotation number 0. The non-dimensional driving force $g = 0.1$. The other parameters are the same as the Couette flow case. The present MD simulation results are compared with the solution to the Navier-Stokes equations. The results are shown in Fig. C.5. The average number density distribution is shown in Fig. C.6, from which we can see that a sticking layer is formed close the walls, however, the number density distribution is still symmetrical in the z direction.

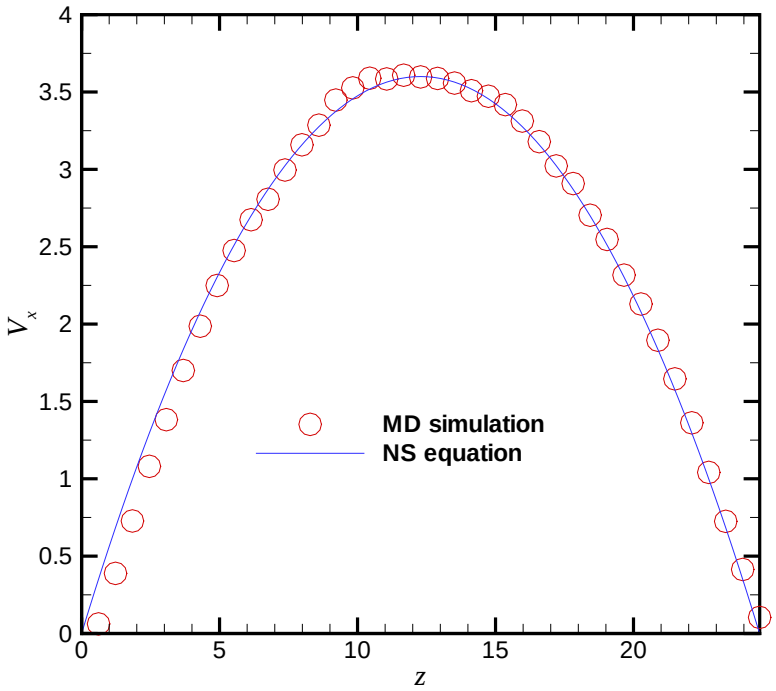

Figure C.5 Mean axial velocity distributions (Poiseuille flow)

Rotating Channel Cases

Several rotating channel cases were simulated. They belong to two different geometries. One is the same as the above setting, $12.51\sigma \times 7.22\sigma \times 24.57\sigma$ and another is a cubic with side length 12σ. The number of wall particles for the cubic geometry is 400. The results of the former geometry are shown in Fig. C.7 and Fig. C.8. Here two different rotation numbers, 0.1 and 0.5 are used.

From above results we can see that as the rotation number increases, the velocity shifts more toward the top wall, which agrees with the macroscale situation. Rotation causes high density near the bottom wall and the higher rotation number causes a steeper density gradient. These phenomena also agree with the macroscale behavior.

The corresponding results for the $12\sigma \times 12\sigma \times 12\sigma$ cubic are shown in Fig. C.9 and Fig. C.10. Some new features appeared in these results. One is the coupling region near the

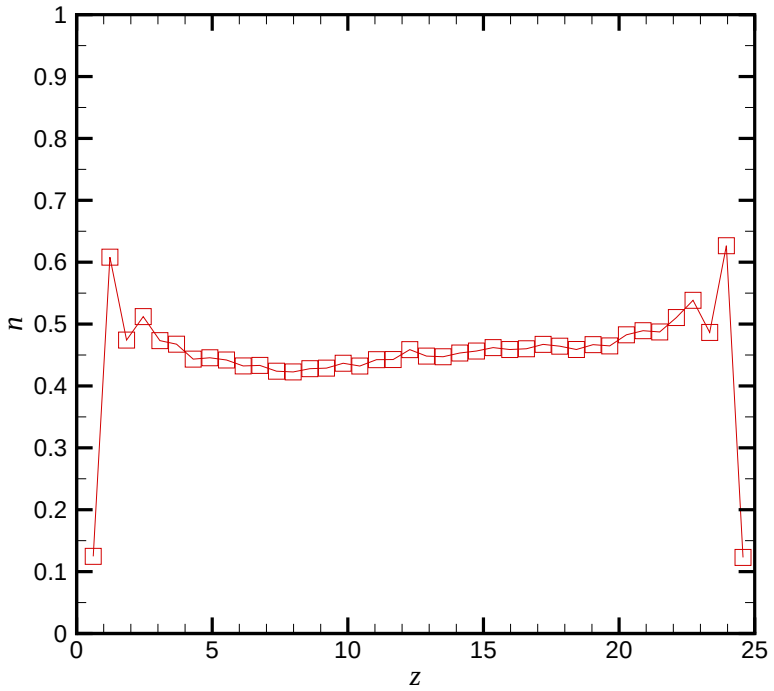

Figure C.6 Number density distribution (Poiseuille flow)

wall, which shows discontinuity in the velocity and density profile. This is caused by the stronger interaction between fluid particles with wall particles. It is of interest that when the fluid/wall molecules interactions are strong, even the forces between them are repulsive, the fluid particles behave like they feel attractive forces. This had been proved by Boltzmann (1896 & 1898). Another feature is that the density near the bottom wall shows much fluctuation, especially at high rotation number, while the fluctuations at the top wall decrease as rotation number increases. The fluctuation is due to the strong fluid/wall molecules interactions that cause the layered structures near wall surface. However, it is difficult to explain why the fluctuation numbers change across the channel. It also can be observed that the frequency of the fluctuation does not change much when rotation number varies. Finally, the kinetic energy distributions are shown for the cubic geometry in Fig. C.11. It can be seen that the kinetic energy distributions are similar to the axial velocity distributions but more continuous. This

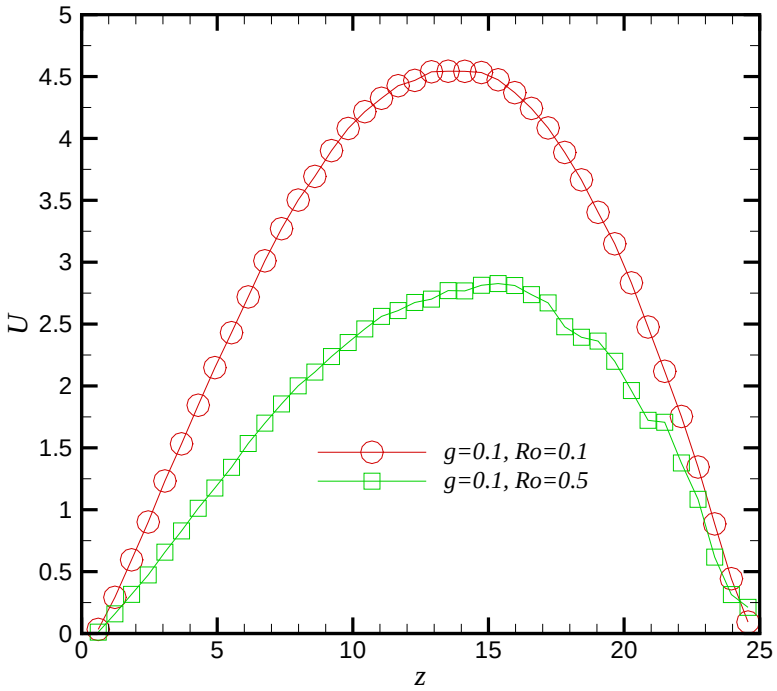

Figure C.7 Mean axial velocity distributions (rectangular box)

distribution implies that, as their macroscale counterpart, the heat transfer is higher on the top wall than that on the bottom wall.

Final Remarks

In this study, the molecular dynamics (MD) simulation was employed to investigate a flow of liquid in rotating nanoscale channels. Several features of the simulation code include: wall particles; boundary conditions other than periodic boundary conditions; reentry mechanism; wall temperature rescale; parameter averaging, etc.

Two simple flows, Couette flow and Poiseuille flow were used to verify the code. Good agreement between the present calculations and exact solutions has been obtained. Then rotating channel cases were simulated. The simulations have been conducted in two geometries. It has been found that geometry, magnitude of driving force and rotation number, particle

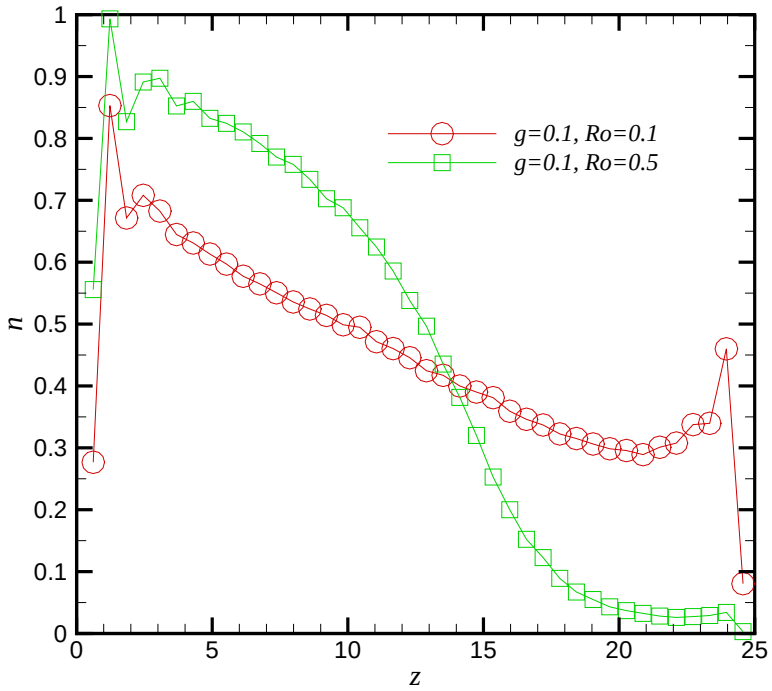

Figure C.8 Number density distribution (rectangular box)

numbers and scale parameters have enormous effects on the results.

When the rotation number increases, the streamwise velocity profile shifts more toward the top wall and becomes more unsymmetrical. At the same time the number density gradient increases. It is also observed that the near-bottom-wall multi-layer structures under strong fluid/wall interactions become more obvious when rotation number increases. The structures near the top wall show a contrary trend. There is a need to develop theoretical models to explain such phenomena.

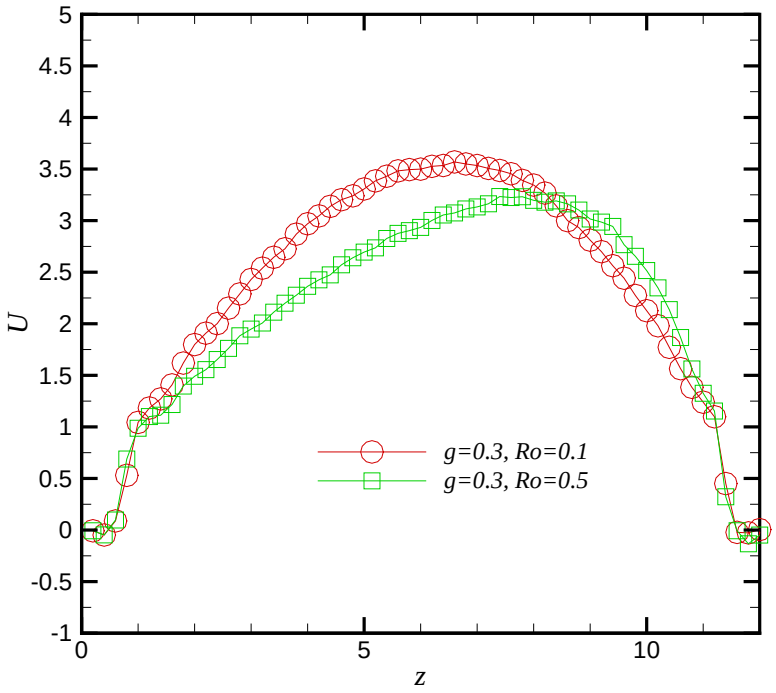

Figure C.9 Mean axial velocity distributions (cubic box)

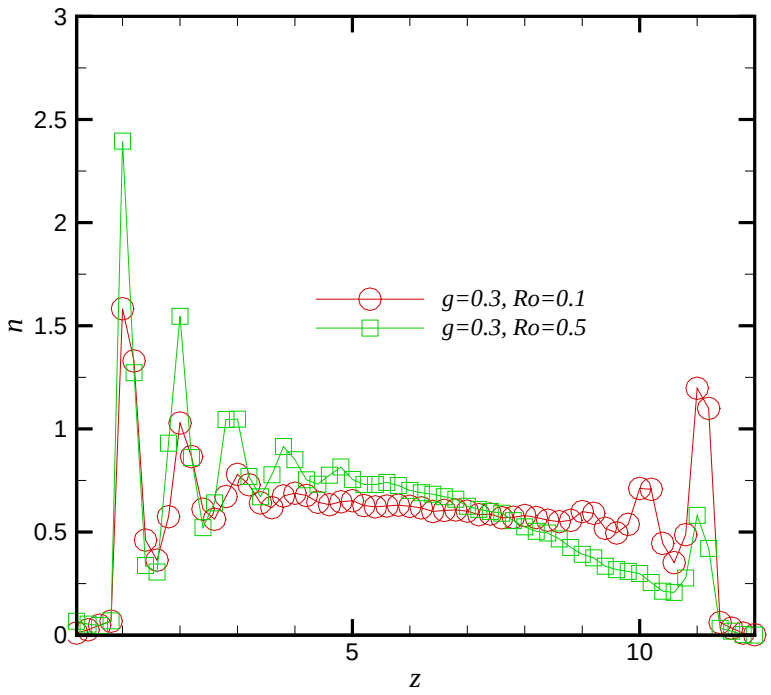

Figure C.10 Number density distribution (cubic box)

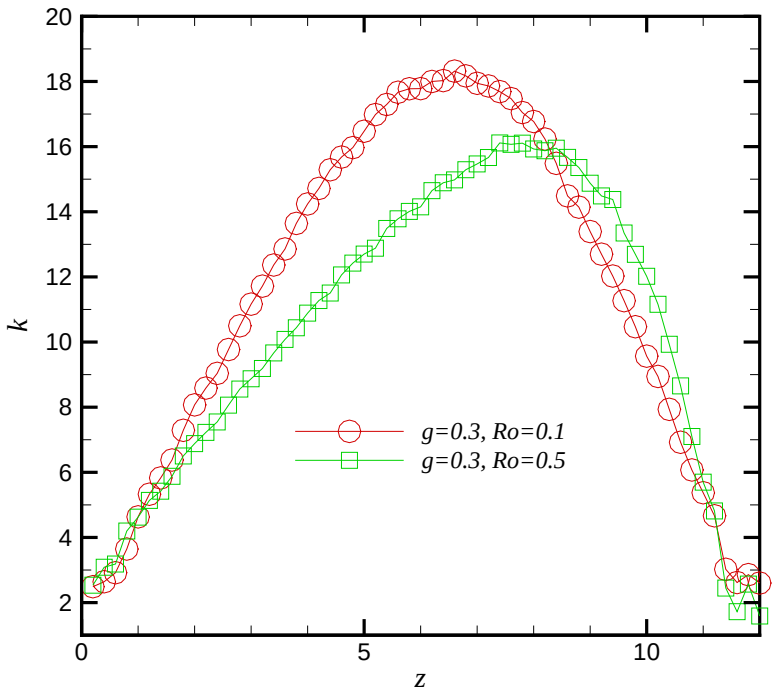

Figure C.11 Kinetic energy distribution (cubic box)

BIBLIOGRAPHY

Al-Arabi, M. (1982). Turbulent heat transfer in the entrance region of a tube. *Heat Transfer Engineering*, *3*, 76–83.

Alvelius, K. (1999). Studies of turbulence and its modeling through large eddy and direct numerical simulation. *Ph.D. thesis*, Department of Mechanics, Royal Institute of Technology, Stockholm, Sweden.

Anderson, J. D. (1995). *Computational fluid dynamics*. McGraw-Hill.

Belhoucine, L., Deville, M., Elazehari, A. R. and Bensalah, M. O. (2004). Explicit algebraic Reynolds stress model of incompressible turbulent flow in rotating square duct. *Computers and Fluids*, *33*, 179–199.

Bennetts, D. A. and Hocking, L. M. (1973). On nonlinear Ekman and Stewartson layers in a rotating fluid. *Proceedings of Royal Society*, *333*, 469–489.

Bennetts, D. A. and Hocking, L. M. (1974). Pressure-induced flows at low Rossby numbers. *Physics of Fluids*, *17*, 1671–1676.

Benocci, C. and Pinelli, A. (1990). The role of the forcing term in the large eddy simulation of equilibrium channel flow. *Engineering Turbulence Modeling and Experiments*, W. Rodi and E. N. Ganic (Eds), New York, 287–296.

Benton, G. S. and Boyer, D. (1966). Flow through a rapidly rotating conduit of arbitrary cross-section. *Journal of Fluid Mechanics*, *26*, 69–79.

Berenger, J. P. (1994). A perfect matched layer for the absorption of electromagnetic waves. *Journal of Computational Physics 114*, 185–200.

Bo, T., Iacovides, H. and Launder, B. E. (1995). Developing buoyancy-modified turbulent flow in ducts rotating in orthogonal mode. *Journal of Turbomachinery*, *117*, 474–484.

Boltzmann, L., *Lectures on gas theory*. Dover Publications.

Bons, J. P. and Kerrebrock, J. L. (1998). Complementary velocity and heat transfer measurements in a rotating cooling passage with smooth walls. *Journal of Turbomachinery*, *121*, 651–662.

Busse, F. H. (1968). Shear flow instabilities in rotating systems. *Journal of Fluid Mechanics*, *33*, 577–589.

Cebeci, T. and Smith, A. M. O. (1974). *Analysis of turbulent boundary layers*. Academic Press.

Chandrasekhar, S. (1961). *Hydrodynamic and hydromagnetic stability*. Oxford.

Cheesewright, R., McGrath G. and Petty, D. G. (1990). LDA measurements of turbulent flow in a duct of square cross section at low Reynolds number. *Aeronautical Engineering Department Report ER 1011.*, Queen Mary Westfield College. University of London, London, Britain.

Choi, Y.-H. and Merkle, C. L. (1993). The application of preconditioning in viscous flows. *Journal of Computational Physics*, *105*, 207–223.

Churchill, S. W. (1977). Comprehensive correlating equations for heat, mass and momentum transfer in fully developed flow in smooth tubes. *Industrial and Engineering Chemistry Fundamentals*, *16*, 109–116.

Colonius, T. (2004). Modeling artificial boundary conditions for compressible flow. *Annual Review of Fluid Mechanics*, *36*, 315–345.

Colonius, T. and Ran, H. (2002). A super-grid-scale model for simulating compressible flow on unbounded domains. *Journal of Computational Physics*, *182*, 191–212.

Dailey, L. D. (1997). Large eddy simulation of turbulent flows with variable property heat transfer using a compressible finite volume formulation. *Ph.D. Thesis*, Iowa State University, Ames, Iowa, U.S.A.

Dailey, L. D., Meng, N. and Pletcher, R. H. (2003). Large eddy simulation of constant heat flux turbulent channel flow with property variations : quasi-developed model and mean flow results. *Journal of Heat Transfer*, *125*, 27–38.

Deardorff, J. W. (1970). A numerical study of three-dimensional turbulent channel flow at large Reynolds numbers. *Journal of Fluid Mechanics*, *41*, 453–480.

Dittus, P. W. and Boelter, L. M. K. (1930). Heat transfer in automobile radiators of the tubular type. *University of California Publications*, *2*, 443-461.

Döbner, E. (1959). Über den Strömungswiderstand in einem rotierenden Kanal. *Dissertation*, Technische Hochschule, Darmstadt.

Drazin, P. G. and Reid, W. H. (2004). *Hydrodynamic stability*. Cambridge University Press.

Dutta, S., Andrews, M. J. and Han, J. C. (1996). Prediction of turbulent heat transfer in rotating smooth square duct. *International Journal of Heat and Mass Transfer*, *39*, 2505–2514.

Eckhaus, W. (1965). *Studies in non-linear stability theory*. Springer-Verlag.

Ekman, V. W. (1905). On the influence of the earth's rotation on ocean-currents. *Arkiv för matematik, astronomi och fysik*, *2*, 1–52.

Favre, A. (1983). Turbulence: space-time statistical properties and behavior in supersonic flows. *Physics of Fluids*, *26*, 2851–2863.

Feng, J. and Merkle, C. L. (1990). Evaluation of preconditioning methods for time-marching methods. *AIAA Paper*, 90-0016.

Früh, W.-G. and Read P. L. (1999). Experiments on a barotropic rotating shear layer. Part 1. Instability and steady vortices. *Journal of Fluid Mechanics*, *383*, 143–173.

Gary, J. and Helgason, R. (1970). A matrix method for ordinary differential eigenvalue problems. *Journal of Computational Physics*, *5*, 169–187.

Gavrilakis, S. (2004). Direct numerical simulations of turbulent flow in rotating straight square duct using spectral methods. *Private Communication.*

Gavrilakis, S. (1992). Numerical simulations of low-Reynolds-number turbulent flow through a straight square duct. *Journal of Fluid Mechanics*, *244*, 101–129.

Germano, M., Piomelli, U., Moin, P. and Cabot, W. H. (1991). A dynamic subgrid-scale eddy viscosity model. *Physics of Fluids*, *3*, 1760–1765.

Germano, M. (1992). Turbulence: the filtering approach. *Journal of Fluid Mechanics*, *238*, 325–336.

Ghosal, S. and Moin, P. (1995). The basic equations for the large eddy simulation of turbulent flows in complex geometry. *Journal of Computational Physics*, *118*, 24–37.

Ghosal, S., Lund, T. S., Moin, P. and Akselvoll, K. (1995). A dynamic localization model for large-eddy simulation of turbulent flows. *Journal of Fluid Mechanics*, *286*, 229–255.

Givoli, D. (1991). Non-reflecting boundary conditions. *Journal of Computaional Physics*, *94*, 1–29.

Gnielinski, V. (1976). New equations for heat and mass transfer in turbulent pipe and channel flow. *International Chemical Engineering*, *16*, 359–368.

Greitzer, E. M., Tan, C. S. and Graf M. B. (2004). *Internal flow.* Cambridge.

Greenspan, H. P. (1968). *The theory of rotating fluids.* Cambridge.

Guo, Y. and Finlay, W. H. (1991). Splitting, merging and wavelength selection of vortices in curved and/or rotating channel flow due to Eckhaus instability. *Journal of Fluid Mechanics*, *228*, 661–691.

Guo, Y., Adams, N. A. and Kleiser, L. (1994). Direct numerical simulation of transition in a spatially growing compressible boundary layer using a new fourier method. *Direct and Large Eddy Simulation*, Ed. Voke, P. R., Kleiser, L. and Chollet, J. P. *1*, 249–259. Kluwer Academic, Dordrecht.

Gustafsson, B. (1975). Convergence rate for difference approximations to mixed initial boundary-value problems. *Mathematics of Computation*, *29*, 396–406.

Hagstrom, T. (1999). Radiation boundary conditions for the numerical simulation of waves. *Acta Numerica*, *8*, 47–106.

Han, J.-C. and Zhang, Y. M. (1992). Effect of uneven wall temperature on local heat transfer in a rotating square channel with smooth walls and radial outward flow. *Journal of Heat Transfer*, *114*, 850–858.

Han, J.-C., Zhang, Y. M. and Kalkuehler, K. (1993). Uneven wall temperature effect on local heat transfer in a rotating two-pass square channel with smooth walls. *Journal of Heat Transfer*, *115*, 912–920.

Han, J.-C., Zhang, Y. M. and Lee, C. (1994). Influence of surface heating condition on local heat transfer in a rotating square channel with smooth walls and radial outward flow. *Journal of Turbomachinery*, *116*, 149–158.

Hart, J. E. (1971). Instability and secondary motion in a rotating channel flow. *Journal of Fluid Mechanics*, *45*, 341–351.

Hedstrom, G. W. (1979). Non-reflecting boundary conditions for non-linear hyperbolic system. *Journal of Computational Physics*, *30*, 222–237.

Heinbuch, U. and Fischer, J. (1989). Liquid flow in pores: slip, no-slip, or multilayer sticking. *Physical Review A*, *40*, 1144–1146.

Hirota, M., Fujita, H., Yokosawa, H., Nakai, H. and Itoh, H. (1997). Turbulent heat transfer in a square duct. *International Journal of Heat and Fluid Flow*, *18* (1), 170–180.

Hu, F. Q. (1996). On absorbing boundary conditions for linearized Euler equations by a perfectly matched layer. *Journal of Computational Physics*, *129*, 201–219.

Huang, P. G., Coleman, G. N. and Bradshaw, P. (1995). Compressible turbulent channel flow– A close look using DNS data. *AIAA paper*, 95-0584.

Humble, L. V., Lowdermilk, W. H. and Desmon, L. G. (1951). Measurement of average heat transfer and friction coefficients for subsonic flow of air in smooth tubes at high surface and fluid temperatures. *NACA report*, 1020.

Huser, A. and Biringen, S. (1993). Direct numerical simulation of turbulent flow in a square duct. *Journal of Fluid Mechanics*, *257*, 65–95.

Hwang, J. J., Lia, T. Y. and Chen, S. H. (1998). Prediction of turbulent fluid flow and heat transfer in a rotating periodical two-pass square duct. *International Journal of Numerical Methods for Heat and Fluid Flow*, *8*, 519–538.

Iacovides, H. and Launder, B. E. (1991). Parametric and numerical study of fully developed flow and heat transfer in rotating rectangular ducts. *Journal of Turbomachinery*, *113*, 331–338.

Johnston, J. P., Halleen, R. M. and Lezius, D. K. (1972). Effects of spanwise rotation on the structure of two-dimensional fully developed turbulent channel flow. *Journal of Fluid Mechanics*, *56*, 533–557.

Jones, O. C. (1976). An improvement in the calculation of turbulent friction in rectangular ducts. *Journal of Fluids Engineering*, *98*, 173–181.

Kakaç, S., Shah, R. K. Aung, W. (Editors) (1987) . *Handbook of single-phase convective heat transfer*. John Wiley & Sons.

Kasagi, N., Kuroda, A. and Hirata, M. (1989). Numerical investigation of near-wall turbulent heat transfer taking into account the unsteady heat conduction in the solid wall. *Journal of Heat Transfer*, *111*, 385–392.

Kays, W. M., Crawford, M. E. and Weigand, B. (2005). *Convective heat and mass transfer, 4th edition*. McGraw-Hill.

Kheshgi, H. S. and Scriven, L. E. (1985). Viscous flow through a rotating square channel. *Physics of Fluids*, *28* (10), 2968–2979.

Kim, J. W. and Lee, D. J. (2000). Generalized characteristic boundary conditions for computational aeroacoustics. *AIAA Journal*, *38*, 2040–2049.

Kim, J. W. and Lee, D. J. (2004). Generalized characteristic boundary conditions for computational aeroacoustics, part 2. *AIAA Journal*, *42*, 47–55.

Kong, H., Choi, H. and Lee, J. S. 2000. Direct numerical simulation of turbulent thermal boundary layers. *Physics of Fluids*, *12* (10), 2555–2568.

Kristoffersen, R. and Andersson, H. I. (1993). Direct simulations of low-Reynolds-number turbulent flow in a rotating channel. *Journal of Fluid Mechanics*, *256*, 163–197.

Launder, B. E. and Ying, W. M. (1973). Prediction of flow and heat transfer in ducts of square cross-section. *Heat and Fluid Flow*, *3*, 115–121.

Lee, J. S., Meng, N., Pletcher, R. H. and Liu, Y. (2004). Numerical study of the effects of rotation on heat transfer in channels with and without ribs. *International Journal of Heat and Mass Transfer*, *47* (22), 4673–4684.

Lezius, D. K. and Johnston, J. P. (1976). Roll-cell instabilities in rotating laminar and turbulent channel flows. *Journal of Fluid Mechanics*, *77*, 153–174.

Lilly, D. K. (1966). On the instability of Ekman boundary flow. *Journal of Atomospheric Sciences*, *23*, 481–494.

Lilly, D. K. (1992). A proposed modification of the Germano subgrid-scale closure method. *Physics of Fluids*, *4*, 633–635.

Lin, C. C. (1955). *The theory of hydrodynamic stability*. Cambridge.

Lin, Y.-L., Shih, T. I.-P., Stephens, M. A. and Chyu, M. K. (2001). A numerical study of flow and heat transfer in a smooth and ribbed U-duct with and without rotation. *Journal of Heat Transfer*, *123*, 219–232.

Lingwood, R. J. (1995). Absolute instability of the boundary layer on a rotating disk. *Journal of Fluid Mechanics*, *299*, 17–33.

Liou, T.-M., Chen, C.-C., Tzeng, Y.-Y. and Tsai, T.-W. (2000). Non-intrusive measurements of near-wall fluid flow and surface heat transfer in a serpentine passage. *International Journal of Heat and Mass Transfer*, *43*, 3233–3244.

Liou, T.-M., Chen, C.-C. and Chen, M.-Y. (2001). TLCT and LDV measurements of heat transfer and fluid flow in a rotating sharp turning duct. *International Journal of Heat and Mass Transfer*, *44*, 1777–1787.

Liou, T.-M., Chen, C.-C. and Chen, M.-Y. (2003). Rotating effect on fluid flow in two smooth ducts connected by a 180-degree bend. *Journal of Fluids Engineering*, *125*, 138–148.

Liu, K. L. (2006). The large eddy simulation of turbulent boundary layers and film cooling. *Ph.D. Thesis*, Iowa State University, Ames, Iowa, U.S.A.

Lumley, J. L. and Newman, G. W. (1977). The return to isotropy of homogeneous turbulence. *Journal of Fluid Mechanics*, *82*, 161–178.

McEligot, D. M., Magee, P. M. and Leppert, G. (1965). Effect of large temperature gradients on convective heat transfer: the downstream region. *Journal of Heat Transfer*, *87*, 67–76.

MacFarlane, I., Joubert, P. N. and Nickels, T. B. (1998). Secondary flows and developing, turbulent boundary layers in a rotating duct. *Journal of Fluid Mechanics*, *373*, 1–32.

Malkus, W. V. R. (1956). Outline of a theory of turbulent shear flow. *Journal of Fluid Mechanics*, *1*, 521–539.

Mårtensson, G. E., Gunnarsson, J., Johansson, A. V. and Moberg, H. (2002). Experimental investigation of a rapidly rotating turbulent duct flow. *Experiments in Fluids*, *33*, 482–487.

Mårtensson, G. E., Brethouwer, G. and Johansson, A. V. (2002). Direct numerical simulation of rotating turbulent duct flow. *Electronic version available at http://www2.mech.kth.se/~gustaf/download.html*.

Medwell, J. O., Morris, W. D., Xia, J. Y. and Taylor, C. (1991). An investigation of convective heat transfer in a rotating coolant channel. *Journal of Turbomachinery*, *113*, 354–359.

Meneveau, C. and Katz J. (2000). Scale-invariance and turbulence models for large-eddy simulation. *Annual Review of Fluid Mechanics*, *32*,1–32

Moin, P., Squires, K., Cabot, W. and Lee, S. (1991). A dynamic subgrid-scale model for compressible turbulence and scalar transport. *Physics of Fluids*, *3*, 2746–2757.

Monin, A. S. and Yaglom, A. M. (1971). *Statistical fluid mechanics*. MIT.

Morris, W. D. and Ayhan, T. (1979). Observations on the influence of rotation on heat transfer in the coolant channels of gas turbine rotor blades. *Proceedings of the Institution of Mechanical Engineers*, *193*, 303–311.

Morris, W. D. and Ghavami-Nasr, G. (1991). Heat transfer measurements in rectangular channels with orthogonal mode rotation. *Journal of Turbomachinery*, *113*, 339–345.

Murata, A. and Mochizuki, S. (1999). Effects of cross-sectional aspect ratio on turbulent heat transfer in an orthogonally rotating rectangular smooth duct. *International Journal of Heat and Mass Transfer*, *42*, 3803–3814.

Murata, A. and Mochizuki, S. (2001). Effects of centrifugal buoyancy on turbulent heat transfer in an orthogonally rotating square duct with transverse or angled rib turbulators. *International Journal of Heat and Mass Transfer*, *44*, 2739–2750.

Murata, A. and Mochizuki, S. (2004). Centrifugal buoyancy effect on turbulent heat transfer in a rotating two-pass smooth square channel with sharp 180-deg turns. *International Journal of Heat and Mass Transfer*, *47*, 3215–3231.

Myong, H. K. (1991). Numerical investigation of fully developed turbulent fluid flow and heat transfer in a square duct. *International Journal of Heat and Fluid Flow*, *12* (4), 344–352.

Niino, H. and Misawa, N. (1984). An experimental and theoretical study of barotropic instability. *Journal of Atmospheric Sciences*, *41* (12), 1992–2011.

Oliger, J. and Sundstrom, A. (1978). Theoretical and practical aspects of some initial boundary value problems in fluid dynamics. *SIAM Journal of Applied Mathematics*, *35*, 419–446.

Ovchinnikov, O. N. and Rukolaine A. V. (1985). Initial section in a square duct rotating about the transverse axis. *Mekhanika Zhidkosti i Gaza*, *5*, 41–46.

Pallares, J. and Davidson, L. (2000). Large-eddy simulations of turbulent flow in a rotating square duct. *Physics of Fluids*, *12*, 2878–2894.

Pallares, J. and Davidson, L. (2000). Large-eddy simulations of turbulent heat transfer in stationary and rotating square ducts. *Physics of Fluids*, *14*, 2804–2816.

Pallares, J., Grau, F. X. and Davidson, L. (2005). Pressure drop and heat transfer rates in forced convection rotating square duct flows at high rotation rates. *Physics of Fluids 17*, p075102.

Parlett, B. (1964). Laguerre's method applied to the matrix eigenvalue problem. *Mathematics of Computation*, *18* (87), 464–485.

Perkins, K. R. (1975). Turbulence structure in gas flows laminarizing by heating. *Ph.D. Thesis*, University of Arizona, Tucson, Arizona, U.S.A.

Piller, M. and Nobile, E. (2002). Direct numerical simulation of turbulent heat transfer in a square duct. *International Journal of Numerical Methods for Heat and Fluid Flow*, *12* (6), 658–686.

Piomelli, U. and Liu, J. (1995). Large-eddy simulation of rotating channel flows using a localized dynamic model. *Physics of Fluids*, *7*, 839–848.

Pletcher, R. H. and Chen, K.-H. (1993). On solving the compressible Navier-Stokes equations for unsteady flows at very low Mach numbers. *AIAA Paper*, 93-3368.

Poinsot, T. J. and Lele, S. K. (1992). Boundary conditions for direct simulations of compressible viscous flows. *Journal of Computational Physics*, *101*, 104–129.

Prakash, C. and Zerkle, R. (1992). Prediction of turbulent flow and heat transfer in a radially rotating square duct. *Journal of Turbomachinery*, *114*, 835–846.

Prakash, C. and Zerkle, R. (1995). Prediction of turbulent flow and heat transfer in a ribbed rectangular duct with and without rotation. *Journal of Turbomachinery*, *117*, 255–264.

Qin, Z. H. and Pletcher, R. H. (2004). Large eddy simulation of turbulent heat transfer in a square duct. *Proceedings of 2004 ASME International Mechanical Engineering Congress and RD&D Expo*, Anaheim, U.S.A.

Qin, Z. H. and Pletcher, R. H. (2006). Large eddy simulation of turbulent heat transfer in a rotating square duct. *International Journal of Heat and Fluid Flows*, *27*, 371–390.

Ravikanth, V. R. A. and Pletcher, R. H. (2002). Large eddy simulation of the turbulent flow past a backward-facing step with heat transfer and property variations. *International Journal of Heat and Fluid Flows*, *23*, 601–614.

Reynolds, H. C., Swearingen, T. B. and McEligot, D. M. (1969). Thermal entry for low Reynolds number turbulent flow. *Journal of Basic Engineering*, *91*, 87–94.

Rieger, H. and Jameson, A. (1988). Solution of steady three dimensional compressible Euler and Navier Stokes equations by an implicit LU scheme. *AIAA Paper*, 88-0619.

Rokni, M. and Gatski, T. B. (2001). Predicting turbulent convective heat transfer in fully developed duct flows. *International Journal of Heat and Fluid Flow*, *22*, 381–392.

Rokni, M. and Sunden, B. (2003). Investigation of a two-equation turbulent heat transfer model applied to ducts. *Journal of Heat Transfer*, *125*, 194–200.

Rudy, D. H. and Strikwerda, J. C. (1980). A nonreflecting outflow boundary condition for subsonic Navier-Stokes calculations. *Journal of Computational Physics*, *36*, 55–70.

Salinas Vázquez, M. and Métais, O. (2002). Large-eddy simulation of the turbulent flow through a heated square duct. *Journal of Fluid Mechanics*, *453*, 201–238.

Satake, S., Kunugi, T., Shehata, A. M. and McEligot, D. M. (2000). Direct numerical simulation for laminarization of turbulent forced gas flows in circular tubes with strong heating. *International Journal of Heat and Fluid Flow*, *21*, 526–534.

Serre, E., Tuliszka-Sznitko, E. and Bontoux, P. (2004). Coupled numerical and theoretical study of the flow transition between a rotating and a stationary disk. *Physics of Fluids*, *16* (3), 688–706.

Sewall, E. A. and Tafti, D. K. (2005). Large eddy simulation of flow and heat transfer in the developing region of a rotating gas turbine blade internal cooling duct with coriolis forces and buoyancy forces. *Proceedings of ASME Turbo Expo 2005*, Reno, U.S.A.

Shehata, A.M. and McEligot, D.M. (1998). Mean structure in the viscous layer of strongly-heated internal gas flows. Measurements. *International Journal of Heat and Mass Transfer*, *41*, 4297–4313.

Smagorinsky, J. (1963). General circulation experiments with the primitive equations. I. The basic experiment. *Monthly Weather Review*, *91*, 99–164.

Smirnov, E. M. (1978). Asymptotic drag formulas for rapidly rotating radial channels of rectangular cross section. *Mekhanika Zhidkosti i Gaza*, *6*, 42–49.

Smirnov, E. M. and Yurkin, S. V. (1983). Fluid flow in a rotating channel of square section. *Mekhanika Zhidkosti i Gaza*, *6*, 24–30.

Spalart, P. R. (1988). Direct numerical study of leading edge contamination. *Fluid Dynamics of Three-Dimensional Turbulent Shear Flows and Transition*, *AGARD-CP-438*, 5.1–5.13. Neuilly-Sur-Seine, Agard, France.

Sparrow, E. M., Garcia, A., and Chuck W. (1986). Numerical and experimental turbulent heat transfer results for a one-sided heated rectangular duct. *Numerical Heat Transfer*, *9*, 301–322.

Spyropoulos, E. T. and Blaisdell, G. A. (1995). Evaluation of the dynamic subgrid-scale model for large eddy simulation of compressible turbulent flows. *AIAA Paper*, 95-0355.

Stewartson, K. (1957). On almost rigid rotations. *Journal of Fluid Mechanics*, *3*, 17–26.

Strikwerda, J. C. (1977). Initial boundary value problems for incompletely parabolic systems. *Communications on Pure and Applied Mathematics*, *30*, 797–822.

Stuart, J. T. (1958). On the non-linear mechanics of hydrodynamic stability. *Journal of Fluid Mechanics*, *4*, 1–21.

Tafti, D. K. and Vanka, S. P. (1991). A numerical study of the effects of spanwise rotation on turbulent channel flow. *Physics of Fluids*, *3*, 642–656.

Tannehill, J. C., Anderson, D. A. and Pletcher, R. H. (1997). *Computational fluid mechanics and heat transfer*. Taylor & Francis.

Taylor, G. I. (1923). Stability of a viscous liquid contained between two rotating cylinders. *Philosophical Transactions of the Royal Society of London A*, *223*, 289–343.

Tekriwal, P. (1994). Heat transfer predictions with extended $k-\epsilon$ turbulence model in radial cooling ducts rotating in orthogonal mode. *Journal of Heat Transfer*, *116*, 369–380.

Thompson, K. W. (1987). Time dependent boundary conditions for hyperbolic systems. Part 1. *Journal of Computational Physics*, *68*, 1–24.

Thompson, K. W. (1990). Time dependent boundary conditions for hyperbolic systems. Part 2. *Journal of Computational Physics*, *89*, 439–461.

Thompson, P. A. and Troian, S. M. (1997). A general boundary condition for liquid flow at solid surfaces. *Letters to Nature*, *389* (25), 360–362.

Tolpadi, A. K. (1994). Calculation of heat transfer in a radially rotating cooling passage. *AIAA Paper*, 94-0261.

Tsynkov, S. V. (1998). Numerical solution of problems on unbounded domains. A review. *Applied Numerical Mathematics*, *27*, 465–532.

Turkel, E. (1987). Preconditioned methods for solving the incompressible and low speed compressible equations. *Journal of Computational Physics*, *72*, 277–298.

Vázquez, M. S. and Métais, O. (2002). Large-eddy simulation of the turbulent flow through a heated square duct. *Journal of Fluid Mechanics*, *453*, 201–238.

Vreman, A. W., Geurts, B. J. and Kuerten, H. (1995). Subgrid-modeling in LES of computational flow. *Applied Scientific Research*, *54*, 191–203.

Wagner, J. H., Johnson, B. V. and Hajek, T. J. (1991). Heat transfer in rotating passages with smooth walls and radial outward flow. *Journal of Turbomachinery*, *113*, 42–51.

Wagner, J. H., Johnson, B. V. and Kopper, F. C. (1991). Heat transfer in rotating serpentine passages with smooth walls. *Journal of Turbomachinery*, *113*, 321–330.

Wang, W.-P. (1995). Coupled compressible and incompressible finite volume formulations of the large eddy simulation of turbulent flow with and without heat transfer. *Ph.D. Thesis*, Iowa State University, Ames, Iowa, U.S.A.

Wang, W.-P. and Pletcher, R. H. (1996). On the large eddy simulation of a turbulent channel flow with significant heat transfer. *Physics of Fluids*, *8*, 3354–3366.

Wang, X. H. and Pletcher, R. H. (2005). Large eddy simulation of supercritical CO2 pipe flow with constant wall heat flux. *Proceedings of 35th AIAA Fluid Dynamics Conference and Exhibit*, Toronto, Canada.

Xu, X. F. (2003). Large eddy simulation of compressible turbulent pipe flow with heat transfer. *Ph.D. Thesis*, Iowa State University, Ames, Iowa, U.S.A.

Xu, X. F., Lee, J. S., Pletcher, R. H., Shehata, A. M. and McEligot, D. M. (2004). Large eddy simulation of turbulent forced gas flows in vertical pipes with high heat transfer rates. *International Journal of Heat and Mass Transfer*, *47*, 4113–4123.

Xu, J. L., Zhou, Z. Q. and Xu, X. D. (2004). Molecular dynamics simulation of micro-Poiseuille flow for liquid argon in nanoscale. *International Journal of Numerical Methods for Heat and Fluid Flow*, *14* (5), 664–688.

Yahyaoui, A. M., Maekawa, H. and Yamamoto, K. (2001). Direct numerical simulations of subsonic plane Poiseuille flows undergoing transition. *JSME International Journal*, *44*, 72–80.

Yoon, S. and Jameson, A. (1987). An LU-SSOR scheme for the Euler and Navier-Stokes equations. *AIAA Paper*, 87-600.

ACKNOWLEDGEMENTS

It is my pleasure to take this opportunity to express my gratitude to those who helped me so much in the last five years.

First of all, I thank the LORD, who gives me enough mental power and patience as well as His consistent help so that I can try to understand a very small portion of His creation, namely rotating duct flow. I would like to thank my major professor, Dr. Richard Pletcher. I will never forget his care of my life, research, teaching and job hunting; his willingness to help whenever I need and his unique sense of humor. I always hope I can become a professor in the future and if it comes true, I hope I treat my students as Dr. Pletcher treated me. Special thanks go to my committee members, Drs. Francine Battaglia, Michael Olsen, Tom I-P. Shih and John Tannehill for their service and many good suggestions on my thesis. I am indebted to Dr. Francine Battaglia for her very kind help when I taught for the first time in 2005. I thank my PFF mentor, Dr. Joseph C.-S. Chen, for his invaluable advices and the many talks between us on my life, teaching and career. I am grateful for the financial support from Air Force Office of Scientific Research under grant F49620-01-1-0113 and the National Science Foundation under grant CTS-9806989. The computer resources provided by the Iowa State High Performance Computing Center and the Minnesota Supercomputing Institute are highly appreciated.

I would like to thank my colleagues in the CFD lab, with whom I had some of the happiest years in my life. I thank my former students in the ME 436 and ME 330 classes, who were very nice to me. Last, but not least, I would like to thank my parents, parents-in-law, my brothers, relatives, and my sweet wife, Jialin Shen, for their love during the past years.